Tomography of the Solar Wind using Interplanetary Scintillations

Divya Oberoi

July 2000

DECLERATION

I hereby declare that the work presented in this thesis is entirely original, and it has been carried out by me at the National Centre for Radio Astrophysics, TIFR, Pune, under the auspices of the Joint Astronomy Programme of the Department of Physics, Indian Institute of Science, Bangalore. I furthur declare that this has not formed the basis of award of any degree, diploma, membership, associateship or similar title of any University or Institution.

Divya Oberoi

Department of Physics,
Indian Institute of Science,
Bangalore - 560 012,
INDIA.

Acknowledgements

It has been a rewarding experiance to have worked with Pramesh Rao, my thesis supervisor. His critiscism and a balanced approach have benifited this work enormously. I much appreciate the freedom which he allowed me during the course of this work, right from the choice of the problem to the manner in which to tackle it. I hope it has been an interesting experiance for him as well.

I thank V. Balasubramainam for making the Ooty Radio Telsecope available for my observations for almost five uninterrupted months and for providing his catalogue of scintillating sources. Thanks are due to P. K. Manoharan for providing information about several other sources which were included in the observations. I am indebted to the observing and technical staff at Radio Astronomy Centre, Ooty, for making these observations possible. I would in particular, like to thank Bilal, Magesh, Ravi, Srinivas and VVS who helped my carry out the rather gruelling observations. Amongst the engineeering staff I would like to thank Mr. A. J. Selvanayakam, Mr. D. Nandgopal, Mr. Kalyansundaram.

It is a pleasure to acknowledge the many illuminating and frutiful discussions which I had with Rajaram Nityananda, I only wish that I had interacted with him more. I wish to thank Chanda Jog and Arnab Rai Choudhuri for their help on various occassions.

This research would not have been possible without the extensive use of the large body of *free* software made available by the Free Software Foundation and also by other individuals and organisations. I acknowledge the efforts and the spirit of the authors of the free software used, too numerous to name individually. This research has made use of NASA's Astrophysics Data System Abstract Service. Data from ULYSSES and WIND space missions used in this work have been obtained from the archives of National Space Science Data Center, a part of NASA. The SOHO/LASCO data used here are produced by a consortium of the Naval Research Laboratory (USA), Max-Planck-Institut fuer Aeronomie (Germany), Laboratoire d'Astronomie (France), and the University of Birmingham (UK). SOHO is a project of international cooperation between ESA and NASA.

I have learnt large amounts from Sanjay Bhatnagar and Rajiv Singh about both software and larger things in life. The friends and fellow students (of which rather few remain) are fondly remembered.

I thank my parents for providing me with an opportunity to do what I wanted to do, something which was denied to them. Thanks are due to Jayshree, my wife, for tolerating me all through and even being enthusiastic about it.

List of Publications

1. A. P. Rao, S. Ananthakrishnan, V. Balasubramanian, W. A. Coles and **D. Oberoi**, 1995 Very long baseline IPS observations of the Solar Wind speed in the fast polar streams, Solar Wind 8, AIP Conference Proceedings 382, 511-514, 1995.

2. **D. Oberoi** and A. P. Rao, 1999, Tomography of the Solar Wind using Interplanetary Scintialltion, to appear in proceedings of the IAU Colloquium 179 on *Cyclic evolution of the Solar magnetic fields: advances in theory and observations*, December 1999.

3. **D. Oberoi** and A. P. Rao, 1999, Tomography of the Solar Wind using the technique of Interplanetary Scintialltion, to appear in proceedings of the IAU Symposium 199 on *The Universe at low radio frequencies*, December 1999.

Contents

List of Figures

List of Tables

List of symbols used

Sun - The Sun
Earth - The Earth
α -
β -
ϵ - elongation
θ_0 - angular size of the source
$\theta_\odot$ - heliographic latitude
$\phi_\odot$ - heliographic longitude
μ - refractive index
ν - temporal frequency
τ - optical depth
ξ - average counts per Jansky for a day
ξ_i - counts per Jansky for a scan on a calibrator source
AR - axial ratio
$A_{P(\nu)}$ - area under the power spectrum of intensity fluctuations
C_n^2 -
f_1 - the first moment of $P(\nu)$
f_2 - the second moment of $P(\nu)$
g - the g value!
k - wavenumber $(2\pi/\lambda)$
m - scintiallation index
n_e - number density of electrons in the Solar Wind
δn_e - fluctuations in the number density of electrons in the Solar Wind
$P_z(\nu)$ - power spectrum of intensity fluctuations due to a thin screen
$P(\nu)$ - power spectrum of intensity fluctuations due to the entire *l.o.s.*
q -
q_x -
q_y -
$R_\odot$ - Solar radius
S_{327} - flux density at $327MHz$
V_p - the component of the velocity $\perp$ to the *l.o.s.*
z - the distance coordinate along the *l.o.s.*

Chapter 1

Introduction

1.1 Interplanetary Scintillations

The Solar Wind is a neutral plasma which constantly flows out from the Sun and permeates the interplanetary space. The density inhomogeneities in this plasma cause the plane wavefront from a distant compact radio source to develop phase corrugations as it travels through it. By the time the corrugated wavefront travels to the plane of observation, at the Earth, the phase corrugations develop into an interference pattern. The scenario is shown schematically in figure 1.1. The motion of the Solar Wind causes this interference pattern to sweep past the telescope, translating the spatial variations of the interference pattern into temporal intensity scintillations. These intensity scintillations are referred to as Interplanetary Scintillations (IPS). This phenomenon finds a good analogy in the twinkling of stars due to turbulence in the atmosphere.

Hewish, Scott and Wills (Hewish et al., 1964) are credited with the discovery of this phenomenon and offering the explanation for its cause. Since its discovery in the mid sixties, IPS has been extensively used as a remote sensing technique to study the Solar Wind. IPS has been used to study a variety of aspects of the Solar Wind ranging from the large scale properties of the *normal* Solar Wind to characterising the disturbances in the interplanetary medium due to transient activities on the Sun. Considerable information about the global structure of the Solar Wind and its changes with solar cycle has been obtained using IPS studies. Physical parameters of the interplanetary disturbances and their associations with events on the Sun have also been an active area of research. An excellent review of the work done in the pre 1978 period is provided by Coles (Coles, 1978). A more recent review by Kojima and Kakinuma (Kojima and Kakinuma, 1990) incorporates almost all major developments and focuses mainly on studies of global structure and solar cycle dependence of the Solar Wind, as learnt from IPS observations.

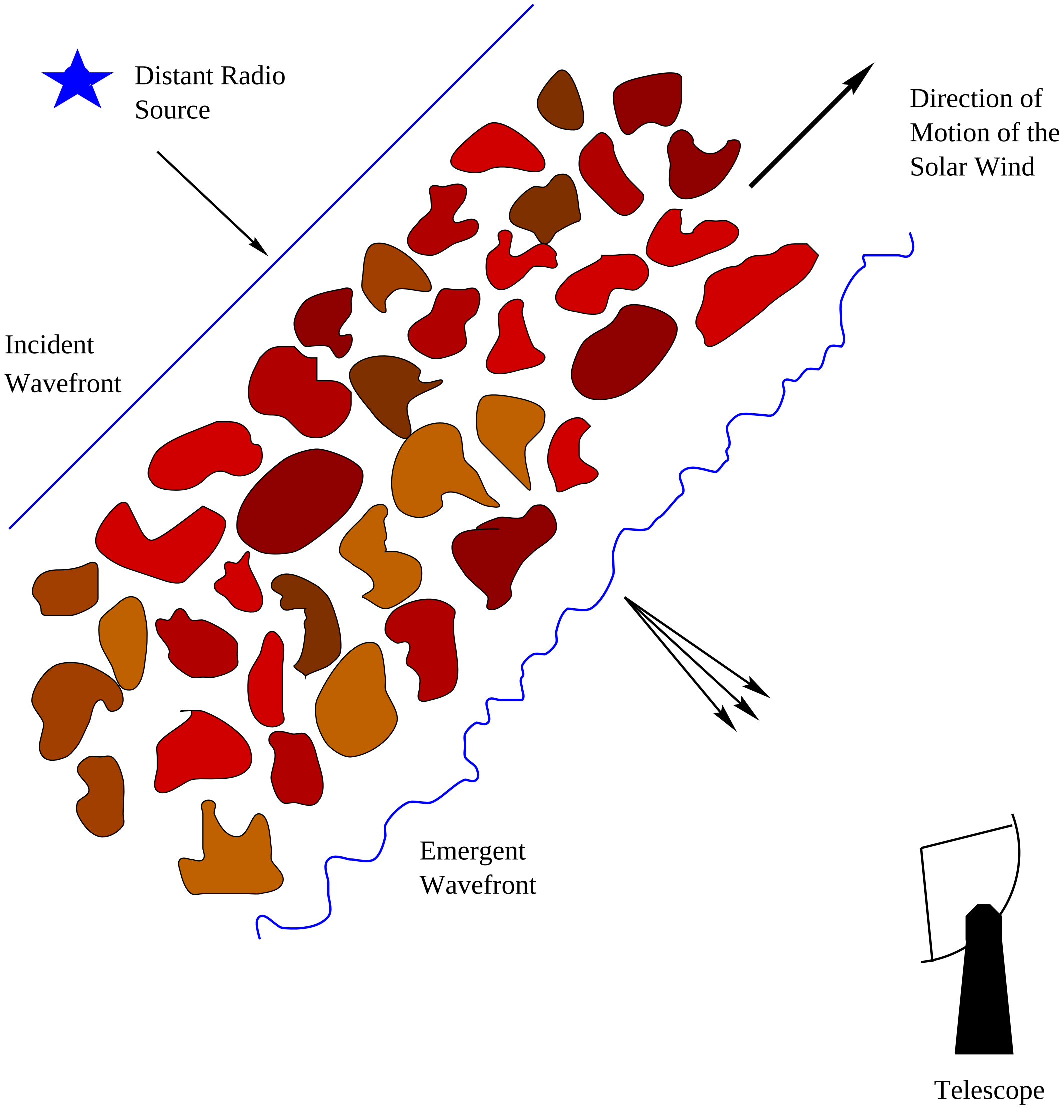

Figure 1.1: **The origin of Interplanetary Scintillations - A schematic illustration** – The Solar Wind acts as a medium with fluctuating refractive index to the incident plane wavefront from a distance radio source. The emergent wavefront carries an imprint of these fluctuations as phase corrugations which develop into an interference pattern by the time it arrives at the observing plane. The motion of the Solar Wind causes this interference pattern to sweep past the telescope giving rise to Interplanetary Scintillations.

The intensity scintillations also depend on the structure of the scintillating source. There have, therefore, been many studies which have used IPS to try to unravel the structure the source, assuming average properties for the Solar Wind. Before the advent of Very Long Baseline Interferometry (VLBI), IPS and Lunar occultation studies were the only means of obtaining sub arc second resolutions. An added advantage which stands even today is that IPS gives high resolution information at low frequencies where rather few VLBI studies have been undertaken. Major surveys were undertaken by Little and Hewish (Little and Hewish, 1968) at 178 MHz, Cohen (Cohen et al., 1968) at 430 MHz and Bhandari et. al. (Bhandari et al., 1974) at 327 MHz which derived the structures of the scintillating sources in late 1960s and early 1970s.

A large number of instruments, both ground and space based, are dedicated to study the solar disc and the corona over a large range of the electromagnetic spectrum. The many Earth orbiting satellites at 1 AU [1] measure various physical properties of the local Solar Wind. IPS provides measurements of the Solar Wind in the intervening region from about 0.1 AU out to 1.0 AU and thus provide the missing link to allow the observations close to the Sun to be related to the Solar Wind observed at 1 AU. These observations can also help in studying the evolution of the Solar Wind plasma as it travels out from the Sun.

1.2 Motivation for this thesis

IPS measurements carry an integrated information of the Solar Wind along the *line-of-sight* (*l.o.s.*) to the radio source. It is conceptually simple to realise that if IPS measurements are made along a large number of *l.o.s.*s distributed such that they sample a large volume of the heliosphere adequately, such a data-set must have the information of the global structure of the Solar Wind in the entire inner heliosphere hidden in it. The problem of extracting this information from the data-set is conceptually similar to that of *tomography*, where one tries to reconstruct the structure of a N dimensional object from its projections in $N-1$ dimensions.

The proposition of reconstructing the global structure of Solar Wind using IPS is aided by the following facts – IPS can sample a large fraction of the heliosphere at any given time and the rotation of the Sun presents many different perspectives of the same physical regions of the heliosphere to the observer. The epoch of observation available to us was close to the solar minima, this is the epoch when the time evolution of the features on the Sun is expected to be the least. The fact that Solar Wind can be modelled well by a purely radial outflow with a constant velocity allows one to make a simple model for propagation of the Solar Wind. Most attempts at

---

[1] $1\ AU = 1.49 \times 10^8\ km$

modelling the Solar Wind, in the past, implicitly assume it to have a relatively simple structure which can be represented adequately with a few features.

If one is able to achieve a reliable reconstruction of the Solar Wind in the inner heliosphere, there are a fair number of issues on which such the results of such an exercise can shed light. The most important among these are :

1. The radial evolution of the Solar Wind as it traverses out from close to the Sun to 1 *AU* is still poorly studied, mainly because of the lack of a suitable data-set. These observations can provide a data-set suitable for such studies.

2. Close to the solar minima, well defined and stable Co-rotating Interaction Regions (CIRs) are formed near the solar equator. The CIRs are usually detected in the plasma data obtained from satellites at 1 *AU* or beyond and are correlated with the locations of the coronal holes on the solar disc. Their evolution and properties are yet to studied in significant detail in the inner heliosphere. A study which can be made possible by this data-set.

3. IPS is sensitive to the level of turbulence in the Solar Wind. Correlations with other synoptic observations is expected to lead to some information about the features on the solar disc which contribute significant turbulence in the Solar Wind.

4. As the data-set will span a large duration, it is very likely that some transient events take place during the course of the observations. As the observing strategy would be optimised to get the best possible coverage of the heliosphere, the interplanetary disturbance will also be very well sampled along an entire range of heliospheric distances. Data-sets with such extensive coverage of transients can yield comparatively well constrained models for the disturbance and its evolution with heliospheric distances.

Such a detailed study using the IPS data may lead to some surprises as well, as most of the data-sets available in the past have usually been too sparse to look for fine features.

A data-set suitable for such an exercise shall necessarily require large amounts of observing time on a sensitive telescope, in order to achieve a good coverage of the heliosphere. We had our disposal practically unlimited observing time at the *Ooty Radio Telescope*, which is a very sensitive instrument for this exercise. This exercise provided a good opportunity to exploiting this advantage to the hilt.

1.3 The present work

It was argued in the previous section that IPS observations can generate a data-set which has the information of the global structure of the Solar Wind in the entire inner heliosphere. The reconstruction of the global structure of the Solar Wind from such data relies crucially on the assumption that the time evolution, in the minimum duration of the period which is required to obtain a complete coverage of the heliosphere, is not significant enough to render the data-set inconsistent. Other, equally crucial, inputs to the reconstruction process are the laws of propagation of the Solar Wind. The most important aspects which have been dealt with in the present work are enumerated below :

1. The starting point of this exercise was to acquire an IPS data-set which is suited to the requirements of attempting a tomographic reconstruction of the Solar Wind in the inner heliosphere. Such a data-set has been obtained using the Ooty Radio Telescope, India. The data-set has extensive coverage of the relevant parts of the inner heliosphere, spans more than 4 Carrington rotations, amounts to $5,418$ observations of scintillating sources and calibrators and used $\sim 1,500\ hrs$ of telescope time. This data-set is one of the few of its kind which provide a dense coverage of the inner heliosphere for extended periods of time.

2. An automated procedure to estimate the parameters of the featureless Solar Wind model which represent the best fit to the observed data has been developed. The procedure has been tested rigorously and has been demonstrated to work efficiently. This procedure provides, for the first time, an objective means of arriving at the parameters of best fit featureless Solar Wind model. The availability of such a procedure reduces the possibilities of human errors and biases and also the drudgery involved in fitting models to large volumes of data. It forms an important part of the tomographic reconstruction procedure and has made it possible to run many more simulations and experiments than would have been possible otherwise.

3. It was required to develop an analysis procedure which uses the IPS data as input and provides a global model for 3D distribution of the physical properties of the Solar Wind consistent with the data-set as the output. An analysis procedure which fulfils these requirements has been developed. This procedure has been extensively tested using simulated data which satisfies the assumption of no time and radial evolution made by the analysis procedure. It has been established that the analysis procedure is sensitive to stable structures in the Solar Wind and the coverage of the heliosphere obtained by the data-set is adequate to reconstruct the structure of the Solar Wind in the equatorial belt of the Sun.

4. Having ascertained the effectiveness of the reconstruction procedure on simulated data, it was next required to establish if the assumptions required by the procedure are met by the IPS data obtained. The effects of violations of the assumptions and the reliability of the tomographically reconstructed models for the Solar Wind in the inner heliosphere have been studied.

5. The data-set obtained being very well suited for studying the radial evolution of the Solar Wind properties, we performed a careful analysis to study the radial evolution of the average velocity of the Solar Wind. This exercise led to the conclusion that the average IPS velocity of the Solar Wind shows a trend to decrease slightly between 0.3 and 1 AU. This conclusion is at variance with the standard models for the Solar Wind which predict the velocity to increase slightly in the range of the radial distances studied. We present an explanation for the trend seen in the data.

Any transient events on the Sun during the course of the observations which give rise to disturbances which propagate through the Interplanetary Medium are quite likely to sampled very well by the data-set. The data corresponding to the events can be used independently to build a detailed model for the Interplanetary Disturbances. Two significant transient events which led to Interplanetary Disturbances (Section 1.6) took place during the period of the observations and have both been very well sampled by the data-set.

1.4 Solar Wind

1.4.1 Early Developments

The earliest hints about events on the Sun having a significant effect on the Earth came about 150 years ago. Carrington, in 1859, noticed that a major geomagnetic storm began about 1.5 days after a solar flare was observed on the Sun. He tentatively suggested a causal relationship between the solar and geomagnetic events. Subsequent investigations revealed numerous examples of apparent associations between solar flares and large geomagnetic storms. Lindemann tried to explain this relationship by suggesting that the geomagnetic storms result from an interaction between the geomagnetic field and the high speed plasma ejected into the Interplanetary Space by solar activity. A periodicity of 27 days, the rotation period of the Sun as observed from Earth, was also noticed fairly early in the studies of geomagnetic activity. The persistent presence of some form of auroral and geomagnetic activity led to the suggestion that the charged particles from the Sun impact and perturb the geomagnetic field almost continuously. Variations in the cosmic ray intensity, measured on the surface of the Earth, were found to follow an ~ 11 year cycle, 180° out of phase with the solar activity cycle. One possible explanation of this fact was that the magnetic fields embedded in plasma clouds emitted from the Sun during flares sweep away the cosmic rays from the interstellar space.

The first evidence for a continuous outflow of plasma from the Sun came from Biermann's observations of ionic comet tails in early 1950s. He noticed that the comet tails always point away from the Sun, independent of the orbital inclination, and offered an explanation in terms of an interaction between the material emitted from the comets and the plasma continuously moving away from the Sun. Biermann estimated a particle flux of $\sim 10^9$ protons $cm^{-2}\ s^{-1}$ at 1 AU, remarkably close to the modern day estimates from *in-situ* satellite observations at 1 AU of $\sim 4 \times 10^8$ protons $cm^{-2}\ s^{-1}$.

1.4.2 Parker's model

On the theoretical front, most theories of solar atmosphere treated the corona as static and gravitationally bound till late 1950s. The main stumbling block for this model was that it required the pressures at very large distances from the Sun to be seven to eight orders of magnitude larger than the estimated pressure of the interstellar plasma. This mismatch in pressure at large heliocentric distances inspired Parker to reason that the solar corona could not be in static equilibrium and therefore must be expanding. In 1958 Parker presented his theoretical model for the Solar Wind which used hydrodynamic equations for conservation of mass, momentum and energy for a hot solar corona. Figure showing velocity evolution of the Solar Wind as a function of radial distance from the Sun is reproduced from his original work. His model gave a picture in which the velocity of the Solar Wind is low close to the Sun and becomes supersonic as it traverses away from the Sun and has vanishingly small pressure at large heliocentric distances. Parker coined the term *Solar Wind* to emphasise the fluid character of the solutions which describe the continuous supersonic coronal expansion. Firm observational evidence for existence of Solar Wind was presented by Snyder and Neugebauer by direct measurements using the plasma analyser onboard the Mariner-2 space probe in 1962.

1.5 Means of studying the Solar Wind

The Solar Wind has been studied using both direct sampling methods using space observatories and remote sensing techniques. Numerous satellites have been launched in order to study the physical properties of the Sun and the Solar Wind. The payloads on board these satellites perform a variety of different measurement and

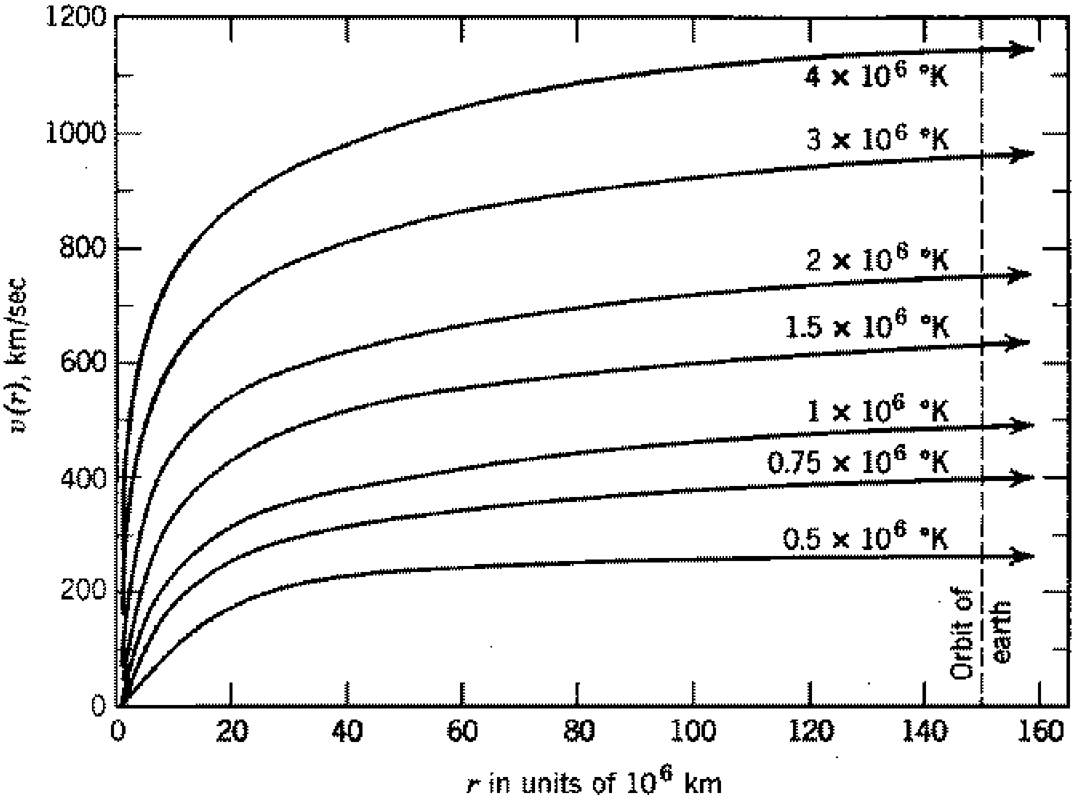

Figure 1.2: **Speed of the Solar Wind with heliocentric distance** – The figure shows Parker's original solutions for speed of the Solar Wind as a function of the heliocentric distance for different values of coronal temperatures. This figure has been reproduced from *Interplanetary Dynamical Processes, 1963.*

can be categorised broadly into plasma analysers and flux monitoring or imaging instruments. The plasma analysers perform *in-situ* measurements of the local Solar Wind plasma. They measure physical parameters like number density, velocity, temperature of electrons and protons and magnetic field orientation and magnitude. The other instruments monitor the flux of the Sun in various wavebands ranging from UV to hard X rays and image of the solar disc and the corona in a range of wavelengths from UV to hard X rays. Among the remote sensing tools, IPS is the most important and often used technique to study the Solar Wind.

Both, direct sampling and remote sensing observation techniques, used to study the Solar Wind, have their respective advantages and disadvantages. Direct sampling by satellites provides data which is much less dependent on the various assumptions which are crucial for interpreting the indirect observations. Satellites, on the other hand, provide only spot measurements of plasma parameters, which, in principle, cannot distinguish between temporal and spatial variations in a model independent manner. The vast expanse of the heliosphere is sampled very poorly by our existing set of satellites and their locations, relative to each other, are rarely suitable for investigating large scale structure in the Solar Wind. IPS, on the other hand, has the advantage that it has a large fraction of the inner heliosphere accessible to it any given time and IPS measurements are inherently sensitive to the distribution of Solar Wind properties along the entire $l.o.s.$. IPS thus forms an ideal and low cost tool to investigate the large scale structure of the Solar Wind, which cannot be studied by any other existing means. As IPS is an indirect measurement technique, IPS observables can be related to Solar Wind parameters only in a model dependent manner. The current state of the knowledge about the Solar Wind constrains the values of some of the parameters of the IPS model for Solar Wind to lie in a small range, so the uncertainties in interpretation, due to the dependence on model parameters, is not large.

1.6 Properties of the Solar Wind

A large body of information has been gathered about the Solar Wind from both ground and space based observations since the first direct observational evidence for Solar Wind in 1962. This section discusses some of the rather well established properties which are of relevance to this work and are often referred to in the following chapters. An excellent treatment of the subject is available in considerable detail along with a useful set of references in a set of two volumes edited by Schwenn and Marsch (Schwenn and Marsch, 1990a,b).

General properties

Solar Wind has traditionally been thought of as being composed of two distinct components, a smooth and featureless ambient or quiescent component which is ubiquitous and has reasonably well known and stable large scale properties and a disturbed component which constitutes primarily of transients and is superposed on the ambient Solar Wind. Most of the discussion in this section relates to the ambient Solar Wind and especially to its properties close to the minima of the solar activity cycle. The simplest models of the Solar Wind assume the ambient medium to be a featureless steady outflow of magnetised coronal plasma. For such models the radial profiles for velocity and density of the plasma are well known. The acceleration region of the Solar Wind lies close to the Sun and most observations have found the Solar Wind to be already accelerated to its velocity at 1 AU by the time it reaches $\sim 20\ R_{\odot}$. The Solar Wind velocity is almost purely radial, the non-radial components of the velocity are usually smaller than a few percent of the radial component. Beyond the acceleration region, the ambient Solar Wind plasma is believed to flow outwards with practically a constant velocity. As a consequence of the radial outflow with a constant velocity, the number density of the ambient Solar Wind plasma falls of as R^{-2}, where R is the heliocentric distance. It has now been established that the ambient wind is endowed with considerable structure and that its large scale properties change with the phase of the solar activity cycle. There is now a growing consensus that the ambient wind comprises of two distinct kinds of the Solar Wind, the slow wind and the fast wind which differ in their physical properties and sites and mechanisms of origin and can be clearly distinguished between by the present observations.

Structure of Interplanetary Magnetic Field

The plasma comprising the Solar Wind is a very good electrical conductor. As the consequence, the solar magnetic field is *frozen* in the plasma. As the coronal plasma expands away, it carries along with it the solar magnetic field. The near radial motion of the Solar Wind and the rotation of the Sun cause the magnetic field lines to bend into spirals, in the plane of the solar equator. The pitch angle of the spiral is related to the angular speed of rotation of the Sun, $\Omega_{\odot}$ [2] and the velocity of the Solar Wind, V_{SW}, by the relation :

$$d\theta = \Omega_{\odot} dt = \Omega_{\odot} \frac{dR}{V_{SW}} \tag{1.1}$$

where $d\theta$ is the change in the azimuthal angle in time dt and dt is the time taken to travel a radial distance of dR with a constant radial velocity, V_{SW}. Such spi-

---

[2] $\Omega_{\odot} = 1.642 \times 10^{-4} deg\ sec^{-1}$

rals, which turn through equal angles in equal radial distances, are referred to as *Archimedean spirals.* Figure 1.3 shows the structure of the magnetic field in the Interplanetary Medium in the solar equatorial plane, as seen from the solar North pole. A constant radial speed of 400 $km\ sec^{-1}$ has been used to generate the spirals. The magnetic field lines of force are inclined at $\sim 45°$ to the radial direction from the Sun at 1 AU. The magnetic field lines trace out the locus of the plasma packets arising from a given fixed point on the solar surface, while the individual plasma packets themselves move radially outwards. The field lines outside the plane of the solar equator are also spirals wrapped around the solar rotation axis. This picture is in reasonable agreement with the observed average orientation of magnetic field at a range of heliocentric distances and latitudes, though the instantaneous values of the magnetic field undergo large deviations.

Stream Structure

It was realised quite early, from the photographs of the solar corona taken at the times of solar eclipse, that the solar corona is highly structured and changes very significantly during the solar activity cycle. It is, therefore, reasonable to expect that this structure and time variability should also manifest itself in the Solar Wind which the corona expands into. While the Parker's model describes a featureless Solar Wind, the real Solar Wind is known to have considerable structure. In the ecliptic plane, the Solar Wind tends to be organised in alternating low and high velocity streams, especially close to the solar minima. The high speed streams originate in the *coronal holes.* Coronal holes are regions of large spatial extent in the solar atmosphere with practically unipolar field and are comparatively inactive regions of the solar surface. These regions appear dark in coronographs because the coronal density in them is rather low. The low density arises because the plasma in the coronal hole regions can expand with comparative ease by flowing along the field lines. The closed magnetic field lines, on the other hand, restrain the plasma from freely expanding away and the slow wind arises from above these more active regions of the Sun and shows much higher variability of all its properties. The high speed streams are therefore unipolar in nature while sharp long lived field reversals take place in the intervening slow speed wind streams.

The Ballerina Skirt Model

The magnetic field of the Sun can be described by a dipolar magnetic field, to a first order. Close to the minima of solar activity cycles, the following scenario holds. The magnetic poles of the Sun are covered by large coronal holes, areas of open magnetic field lines. Some of the coronal holes migrate to low latitude regions, well into the equatorial regions. This is due to the fact the global solar dipole axis is

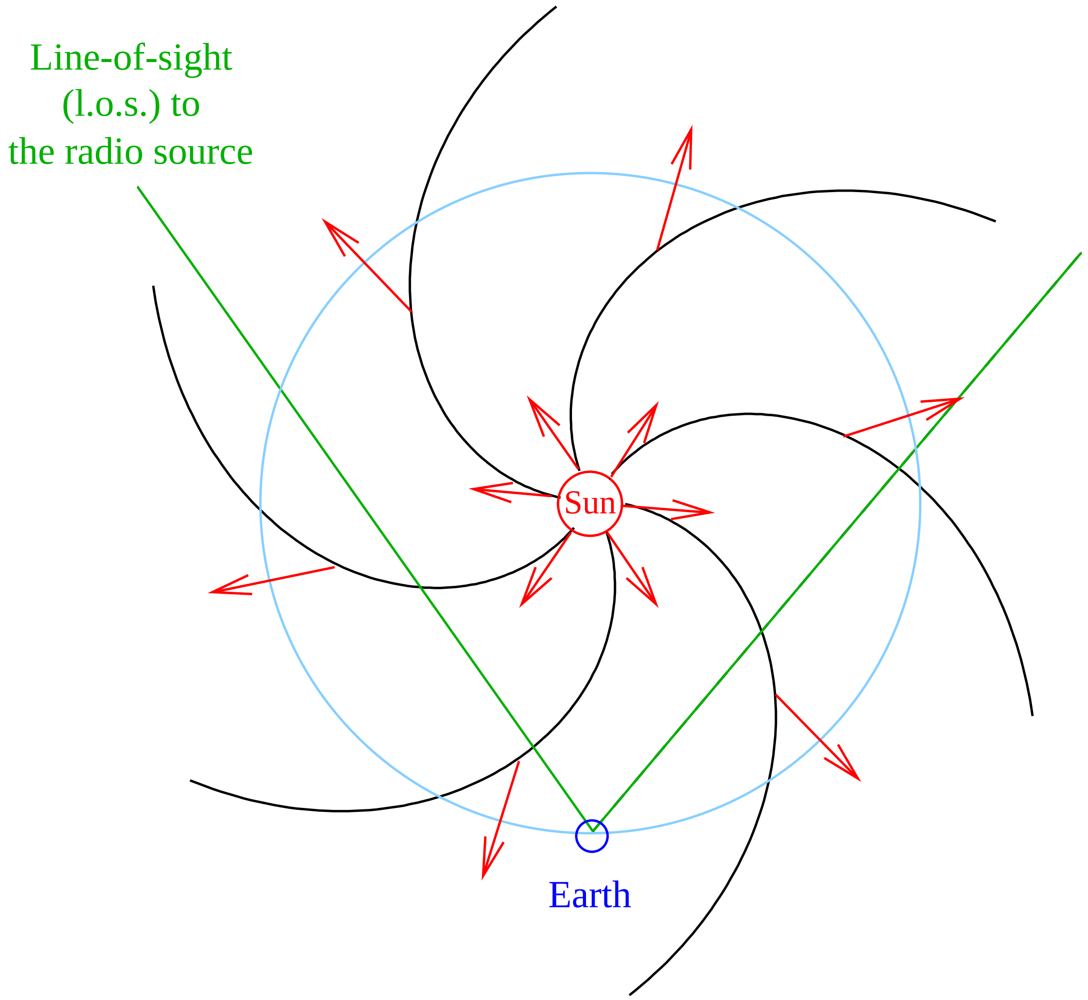

Figure 1.3: **Structure of the magnetic field in the Interplanetary Medium** – A view of the structure of the magnetic field in the solar equatorial plane, as seen from the North pole is shown. The velocity of the Solar Wind is assumed to be a constant and along the radial direction and is shown by the arrows. A velocity of 400 $km\ sec^{-1}$ has been used to generate this figure. The radial velocity of the Solar Wind causes the magnetic field lines frozen in the plasma to bend into Archimedean spirals. For a velocity of 400 $km\ sec^{-1}$, the magnetic field lines make an angle of $\sim 45°$ with the radial direction from the Sun at 1 AU.

titled with respect to the solar rotation axis, though tilt is small at solar minima. The active regions, with their closed magnetic field configurations, are confined to the equatorial regions on the Sun. There is a thin boundary which separates the hemisphere with positive open field lines from the one with negative open field lines. This boundary takes the form of a sheet as the Solar Wind is convected away and is referred to as the *Heliospheric Current Sheet* (HCS). The warps in the HCS make it appear like the skirt of a twirling ballerina. This skirt is generally *attached* to the corona in the middle of the near-equator activity belt and in between the large coronal holes. This model, referred to as the *Ballerina Model* was first proposed by Alfven (Alfven, 1977). The undulations in the HCS, lead to the consequence that the magnetic field detected by the Earth orbiting satellites is organised into alternating regions of positive and negative polarities. The HCS is usually detected in the satellite plasma data as a region of high plasma density with long lived structures of opposite magnetic field polarities sandwiching it. This organisation of the magnetic field is referred to as sector structure of the Solar Wind and the size and the number of structures is closely related to the structure of the underlying corona.

Latitudinal Structure

Historically, the first indication for the variation of Solar Wind properties with heliographic latitude came from IPS studies by Dennison and Hewish, in 1967, when they reported for the first time a trend for velocity of the Solar Wind to increase at high latitudes (Dennison and Hewish, 1967). Coles and Rickett presented convincing evidence, using IPS data, for an increase in the velocity of the Solar Wind out of the equatorial plane (Coles and Rickett, 1976). Many subsequent observations have now established the latitudinal structure of the Solar Wind on a firm footing (Kojima and Kakinuma, 1990; Ananthkrishnan et al., 1995).

In view of the fact that the embedded magnetic field in the Solar Wind can strongly influence its properties by channelling the coronal expansion (Hundhausen, 1972), many investigations were carried out to study the association of the Solar Wind structure with the *heliomagnetic*, rather than *heliographic*, latitude. In the current context, the term heliomagnetic latitude, denotes the local latitudinal separation from the warped HCS, the heliomagnetic equator. As the solar activity cycle progresses from a minima to a maxima, the angle between the heliomagnetic axis and the axis of rotation of the Sun increases. This leads to increasing warps of larger amplitudes in the HCS and causes the sector structure to extend to much higher latitudes. Most of these studies exploited these warps in the HCS to sample a substantial range of heliomagnetic latitudes using spacecrafts confined to the ecliptic. Many such studies were compared by Bruno (Bruno et al., 1986) and all of them had the common characteristic that the *slow* Solar Wind is found in a belt with a width of about ±20° around the heliomagnetic equator and only *high* speed wind is found outside this region. Kojima and Kakinuma (Kojima and Kakinuma, 1990) also arrive at a similar conclusion using IPS data. Close to the solar minima, the heliomagnetic equator is close to the heliographic equator, hence heliomagnetic and heliographic latitudes do not differ much from each other.

Co-rotating Interaction Regions

As has been mentioned before, close to the minimum of the solar activity cycle, some of the coronal holes migrate down to the equatorial belt. These coronal holes are often stable over time scales of many solar rotations [3] and lead to the high and low speed streams described earlier. When the coronal expansion is spatially variable but time stationary, steady flow patterns develop in the equatorial plane, due to interaction of the slow and the fast Solar Wind. These long lived patterns co-rotate with the Sun.

The curvature of the flux tubes is inversely proportional to the velocity of the plasma contained in the flux tube (equation 1.1). The flux tubes with plasma at higher velocities are less tightly wound than the ones with plasma at slower velocities, their angular separation, therefore, changes as they propagate radially outwards. To provide a feel for the magnitude of this effect, the separation between Archimedean spirals followed by two streams with velocities 300 and 600 $km\ sec^{-1}$, respectively, changes by 41° as they travel from the solar surface to 1 AU. The rotation of the Sun, therefore, causes the Archimedean flux tubes containing plasma at a higher velocity to collide and interact with slower plasma ahead of it, as shown in Figure 1.4. As the fast moving Solar Wind tries to overtake the slower plasma ahead of it and moves away from the slower plasma behind it, the structure of Solar Wind along the longitude, its longitude profile, changes as the wind moves outwards. The fast wind cannot stream though the slow wind because the two are threaded by different magnetic field lines which are frozen in them. The longitude profile of velocity evolves towards a rapid rise and slow decay shape, this is referred to as *steepening* of the velocity profile of the wind. The plasma on the rising part of the high speed stream has high density and is compressed and the plasma on the slow decay part of the high speed stream has a lower density than the ambient Solar Wind. The difference in velocity of the plasma in different flux tubes, thus, leads to the development of regions of compression and rarefaction, of both the plasma and the magnetic field. The compression regions in such a pattern are referred to as *Co-rotating Interaction Regions* (CIRs).

In presence of compressions and rarefactions the number density evolution of the Solar Wind streams differs significantly from the R^{-2} dependence, expected

---

[3] One solar rotation period is $\sim 27 days$ and is also referred to as *Carrington period*

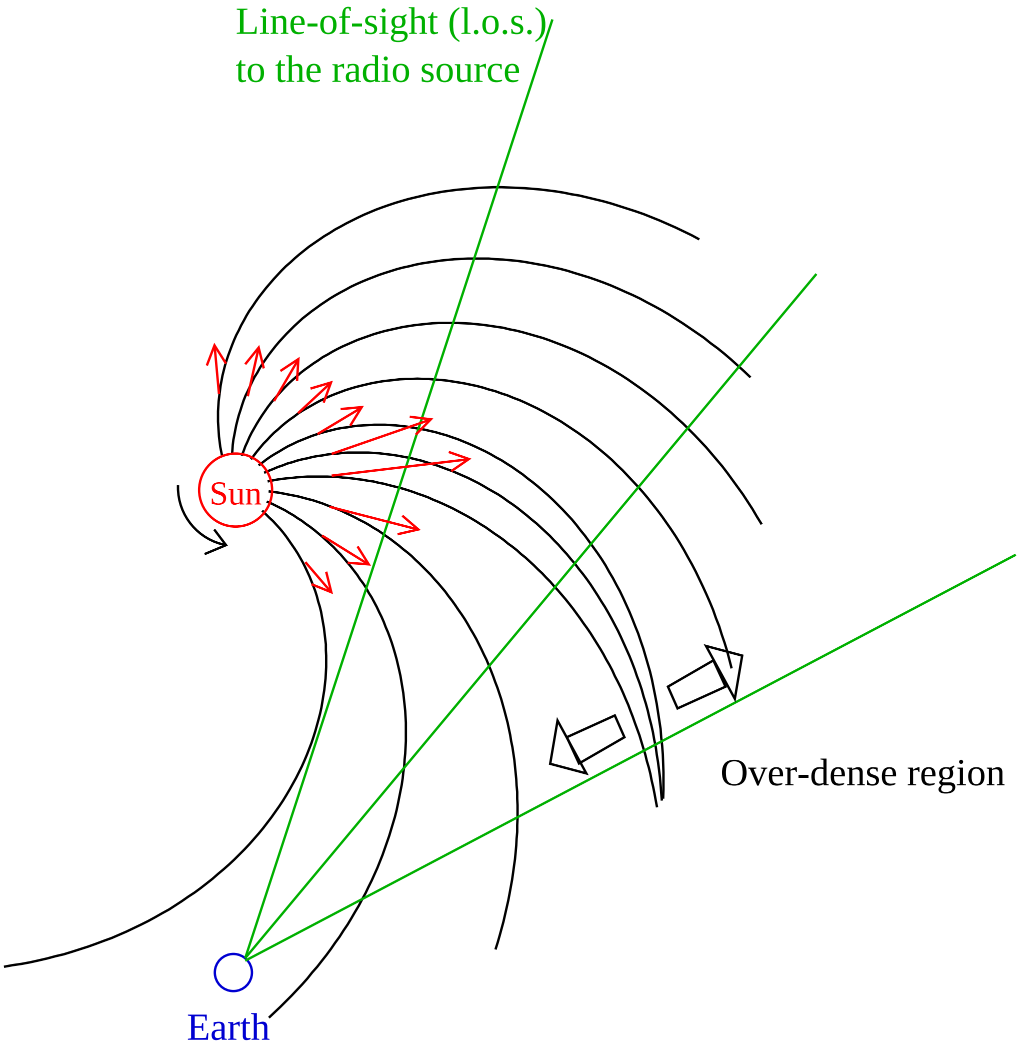

Figure 1.4: **Formation of Co-rotating Interaction Regions** – The figure illustrates, schematically, the scenario which leads to formation of quasi-stationary Co-rotating Interaction Regions (CIRs) in the plane of the ecliptic. The curves represent the Archimedean spirals which the magnetic field lines get bent into and the arrows the magnitude of the radial velocity vector. The sense of rotation of the Sun is also marked. The higher velocity streams push against the slower moving plasma ahead of it and lead to the formation of compression regions. The excess pressure in these over-dense regions leads to development of pressure gradients which impart non-radial velocities to the Solar Wind plasma. The figure also shows the Earth with a few *l.o.s.* to distant sources passing through the CIRs.

from spherical symmetry, and longitudinal pressure gradients also develop. These pressure gradients tend to fill in the rarefaction regions and also impart non radial velocities to the plasma on either side of the CIRs. As interaction is not significant in rarefied medium, the radial evolution of the trailing edges of the high speed streams is not effected significantly by the longitudinal pressure gradients. The situation is dramatically different for the leading edges of the high speed streams. The matter involved in a CIR may originate from a coronal longitude range of 70° or more by the time it reaches 1 *AU* and the longitude range from where the CIR receives contribution increases with heliocentric distance. The leading edge of the high speed streams slows down due to piling up of the slower moving plasma ahead of it.

If the amplitude of the high velocity stream is large enough, the pressure in the leading edge of the high velocity stream increases non-linearly as velocity profile of the stream steepens and pair of shock waves form on either side of the high pressure region. The shock at the front of the CIR is referred to as the *forward shock* and it propagates into the plasma ahead of it, the shock on the rarefaction side of the CIR, which propagates towards the Sun, is referred to as the *reverse shock*. Both these shocks are convected away by the large bulk velocity of the Solar Wind. Few high velocity streams steepen sufficiently to develop into shocks within 1 *AU*. By ~ 2 *AU* most of the CIRs have shocks associated with them and beyond ~ 5 *AU* a large fraction of the mass in Solar Wind has been swept up by the shocks and is found within the compression regions bounded by shock waves on the rising part of the damped high speed streams.

Transients - Interplanetary Disturbances

Apart from the recurrent variations in the Solar Wind, which can be understood in terms of spatial variations in the co-rotating structures, there are sporadic disturbances which involve true temporal variations. These are referred to as *Interplanetary Disturbances* (IPDs). The most striking of these are the Interplanetary shock waves which propagate outwards from the Sun. Such a shock is seen by an observer as an abrupt change in the values of the physical properties of the Solar Wind like speed, density, temperature and the strength and orientation of the magnetic field. The change in the values of the physical properties persist for time scales of many hours after the shock front has passed through, at 1 *AU*. An example of such a shock, from the period of observations presented in this work, is shown in Figure 1.5. It is now believed shock waves with thickness much smaller than the collision length scales can form in magnetised plasma of the Solar Wind, such shocks have been given the name *Collisionless shocks*. A shock front moving outwards through the Solar Wind overtakes the slow wind ahead of it and accelerates and heats up the material which passes through it. The shock thus transfers energy and momentum

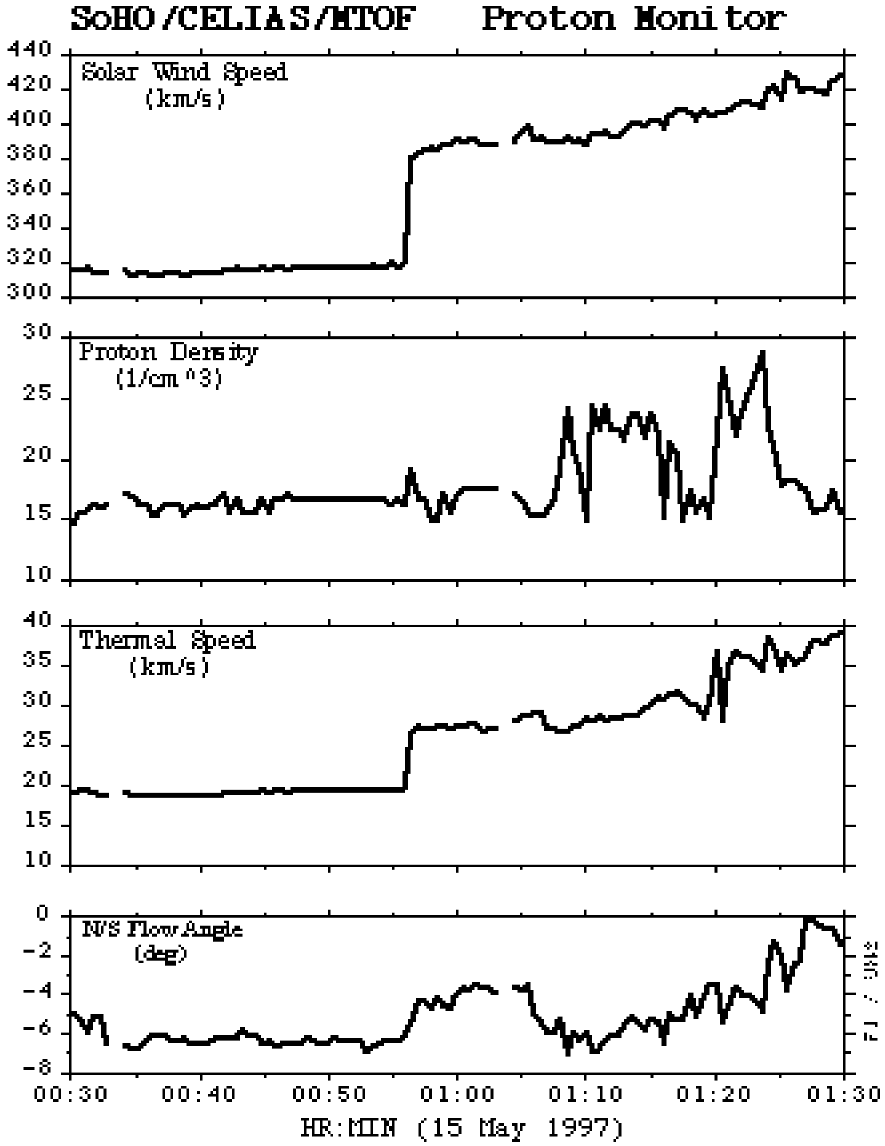

Figure 1.5: **An Interplanetary Disturbance, as seen in Solar Wind plasma at 1 AU** – The figure shows the time series of Solar Wind speed, proton density, thermal speed and N/S flow angle seen by the CELIAS/MTOF instrument onboard the SOHO satellite. This event has been identified to be an Earth directed Coronal Mass Ejection which was launched from the Sun on the 12^{th} May 1997 and was seen at 1 AU on the 15^{th} of May 1997.

to the Solar Wind *shocked* medium. Unless the momentum and the energy of the shock are continually replenished, the shock must decelerate as it moves outwards.

The solar origins of these shocks have been a subject of considerable interest for the past many years. Traditionally they were believed to be associated with solar flares. It has, however, remained difficult to establish a definite connection between the flares and interplanetary shocks and their association does not find much favour now. The availability of space borne coronal instruments, which provided images of the corona with unprecedented angular and temporal resolution, led to the discovery of major class of temporal disturbances of the coronal plasma, the *Coronal Mass Ejections* (CMEs). These instruments provide spectacular time-series of images which show "relatively dense and discretely bounded coronal material being propelled irretrievably into interplanetary space" (Bird and Edenhofer, 1990). The ejection speeds of the CMEs range from less than $\sim$ 50 to 2000 $km\ sec^{-1}$ at $\sim 5\ R_{\odot}$ and the mass of the ejected solar material lies in the range 10^{15} to 10^{16} gm. The faster CMEs are believed to be a primary source of transient Solar Wind disturbances, typically 1/3 of the CMEs in the ecliptic plane have sufficiently high speeds to develop into shocks by the time they reach 1 AU. The frequency of CMEs is closely related to the solar activity cycle - while an average of 3.5 day^{-1} CMEs are launched close to the peak of the solar activity cycle, their number reduces to 0.5 day^{-1} close to the minima. Opening angle of a typical CMEs is $\sim 45°$, though some of them may have opening angles as large as 90° by 5 $R_{\odot}$. Flares and CMEs are not always observed in association with solar flares, this fact does not allow them to be related to each other as cause and effect or *vice-versa*. It is natural to expect CMEs to develop into IPDs as they propagate away from the Sun, but whether CMEs are the only causes of IPDs remains an open question.

Physical parameters of the quiet SW at 1 AU

A large number of satellite missions have been devoted to the study of the Solar Wind, since early 1960s. An overwhelming majority of these satellites are Earth orbiting and therefore sample the Solar Wind only in the ecliptic plane and at 1 AU. Over the past many years a vast database of measurements of physical properties of Solar Wind has been generated using the plasma analysers on-board these satellites. The statistical properties of the Solar Wind at 1 AU derived from these measurements in the ecliptic plane are listed in Table 1.1. This table is reproduced from Gosling (Gosling, 1997). The table includes the mean values, standard deviations about the mean values, most probable values, median values and the 5–95% range limits for the parameters. The parameters listed are number density of protons (n), the velocity of the Solar Wind (V_{SW}), the magnetic field strength (B), the α particle abundance relative to protons (A_{He}), the temperatures of protons, electrons and α

Table 1.1: **Statistical properties of the Solar Wind at 1 AU in the plane of the ecliptic** – The table gives statistical values of various physical parameters of the Solar Wind, as determined by *in-situ* satellite measurements at 1 AU in the ecliptic plane. The first column identifies the parameter, the second gives the mean values, the third the standard deviations about the mean values, the fourth the most probable values, the fifth the median values and the last the 5–95% range limits for the parameter. n is number density of protons, V_{SW} the velocity of the Solar Wind, B the magnetic field strength, A_{He} the α particle abundance relative to protons, T_p, T_e and T_α the temperatures of protons, electrons and α particles respectively, nS_{SW} the flux of the Solar Wind and C_s and C_A the sound and the Alfven speeds respectively. This table is reproduced from Gosling (Gosling, 1997).

Parameter	Mean	rms	Most probable	Median	5 – 95 %
$n\ (cm^{-3})$	8.7	6.6	5.0	6.9	3.0 – 20.0
$V_{SW}\ (km\ sec^{-1})$	468	116	375	442	320 – 710
$B\ (nT)$	6.2	2.9	5.1	5.6	2.2 – 9.9
A_{He}	0.047	0.019	0.048	0.047	0.017 – 0.078
$T_p\ (\times 10^5\ K)$	1.2	0.9	0.5	0.95	0.1 – 3.0
$T_e\ (\times 10^5\ K)$	1.4	0.4	1.2	1.33	0.9 – 2.0
$T_\alpha\ (\times 10^5\ K)$	5.8	5.0	1.2	4.5	0.6 – 15.5
T_e/T_p	1.9	1.6	0.7	1.5	0.37 – 5.0
T_α/T_p	4.9	1.8	4.8	4.7	2.3 – 7.5
$nV_{SW}\ (\times 10^8\ cm^{-2}s^{-1})$	3.8	2.4	2.6	3.1	1.5 – 7.8
$C_s\ (km\ sec^{-1})$	63	15	59	61	41 – 91
$C_A\ (km\ sec^{-1})$	50	24	50	46	30 – 100

particles (T_p, T_e and T_α), the flux of the Solar Wind (nV_{SW}) and C_s and C_A the sound and the Alfven speeds (C_s and C_A). As is evident from this table, the Solar Wind parameters vary over a considerable range. The speed of the Solar Wind is much larger than sound speed and Alfven speed at 1 AU, the flow is thus both supersonic and superalfvenic. It is also interesting to note the average values of T_e, T_p and T_α are not equal.

1.7 Organisation of the thesis

The thesis is organised in eight chapters, the basic thrust of each of them is briefly described below.

The present chapter introduces the technique of IPS and offers a very brief historic account of the development of the subject. This chapter also presents the motivation for the present work, introduces the Solar Wind and describes a few established properties of the Solar Wind of relevance to this work.

The second chapter discusses the theory of IPS. The emphasis has been on presenting the final frame work of the formulation used and discussing it in some depth rather than developing the formalism. The formalism is justified using physical arguments rather than mathematical rigour. The assumptions relied upon and their domains of validity are clearly highlighted. The effects of each of the parameters of the Solar Wind model on the observed power spectra are also discussed.

The third chapter begins with a discussion of the estimation of the properties of the Solar Wind from single station studies of IPS, the applications they have been used for and their limitations. It goes on to point out violations of the assumptions made by these models in the actual Solar Wind scenarios. The formulation of the problem of tomography is presented and the basic requirements for an observable to be useful for a tomographic reconstruction are discussed. The feasibility of using IPS data for a tomography reconstruction of the Solar Wind in the inner heliosphere is discussed. The data, software and computing requirements for such an exercise are estimated. The advantages and limitations of such a reconstruction are presented.

The fourth chapter describes the data-set which was obtained to attempt a tomographic reconstruction of the Solar Wind. The criterion for source selection and the coverage of inner heliosphere achieved by the data-set are discussed. The data processing carried out to compute the basic IPS observables, the scintillation index and the power spectra of intensity fluctuations is described along with computation of their respective statistical uncertainties. Computation of g values is also described.

Chapter five discusses the automated procedure developed to estimate the best fit IPS model for the observed power spectra. This procedure is basically a χ^2 minimisation procedure with the χ^2 defined in an appropriate manner. The criterion which a suitable definition of the χ^2 must satisfy are presented. Our implementation of the procedure is discussed in considerable detail. The extensive simulations carried out to validate the automated procedure and their results are described. The results of using the procedure on the observed data are shown and a discussion on their interpretation is presented. The reliability of the automated procedure is clearly established by presenting a large number of power spectra which provide a fair sample of the observed data-set. A glimpse of the observed data-set is provided in the form of time series of IPS parameters estimated for individual sources.

The sixth chapter describes our results regarding the radial evolution of the Solar Wind. We see a significant trend for decrease in the average IPS velocity of the equatorial Solar Wind as it travels outwards. The observed decrease in the average velocity with radial distance is critically examined. It is shown that the trend is a genuine feature of the data-set and is not an artifact of the analysis procedure or the sampling of the heliosphere. Our interpretation of this result is also presented.

Chapter seven discusses our formulation of the problem of tomographic reconstruction and highlights the differences from and improvements over the previous attempts. The large set of simulation done to validate both the software and the methodology developed are presented. The results of the simulations which established the efficacy the both the software and our procedure are discussed in detail. The results of application of the methodology to the observed data-set are presented and some comparisons with other independent data-sets are made. The conclusions drawn from these results and their implications are discussed in depth.

The final chapter summarises the conclusions arrived at in this work and makes some comments on the utility of tomography as a routine investigation tool for the Solar Wind.

Chapter 2

Theory of Interplanetary Scintillations

2.1 The geometry of IPS observations

The relative positions of the Sun, the Earth and the *line-of-sight*, *l.o.s.*, to the radio source define the geometry of IPS observations. The Heliographic coordinate system, with its origin fixed on the Sun, is the one most suited for the problem. The geometry is shown schematically in Figure 2.1. The angle between the Sun – Earth line and the direction to the distant radio source is referred to as elongation, ϵ. It is a measure of how close the *l.o.s.* to the source passes to the Sun. The point on the *l.o.s.* closest to the Sun is labelled by P and is referred to as the *P-point* in the literature. The distance of the P-point from the Sun, p, is given by the expression :

$$p = R \ \sin(\epsilon) \tag{2.1}$$

where R is the Sun – Earth distance. The eccentricity of the Earth's orbit being very small, R differs from its mean value of $1AU$ by at most $\sim 2.0\%$. Therefore $\sin(\epsilon) \simeq p$ expressed in AU, to a good approximation. We have however chosen not to make this approximation.

In order to understand the origin of IPS, consider a plane electromagnetic wave of wavelength, $\lambda = 2\pi/k$, from a point radio source at infinity propagating along the $-Z$ direction and encountering a thin screen of thickness Δz at a distance Z. The electron density fluctuations in the screen give rise to phase fluctuation on the emergent wavefront. These phase fluctuations develop into intensity fluctuations by the time the wavefront arrives at the observing plane at $Z = 0$. The electron density fluctuations in the thin screen sweep past the observer with a velocity V, the velocity of the Solar Wind. The motion of the electron density fluctuations cause the interference pattern to sweep past the telescope. The motion of the interference pattern past the telescope gives rise to the intensity fluctuations observed.

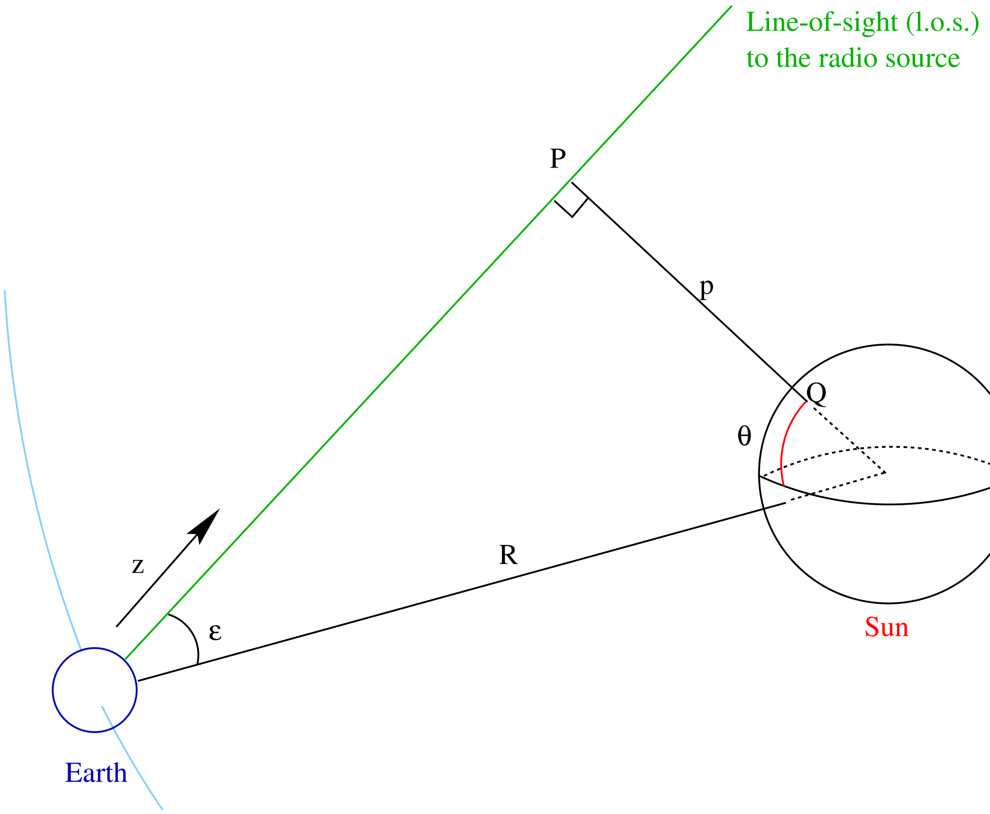

Figure 2.1: **The Sun, the Earth and the *l.o.s.* geometry** – The figure shows the relative positions of the Sun, the Earth and the *l.o.s.*, to the distant radio source. Sun–Earth distance is denoted by R and the elongation by ϵ. z measures the distance of a point on the *l.o.s.* from the Earth. P is the point on the *l.o.s.* closest to the Sun and p is its distance from the Sun. Q is the geometric projection of P-point on the solar surface and gives its heliographic co-ordinates. Heliographic latitude of Q is marked by θ.

We follow the convention that the sources on the East of the Sun have positive elongation and those on the West have negative elongation. The elongation of an ecliptic source changes approximately by a degree per day, a consequence of fact that the revolution of the Earth around the Sun takes a year.

The point Q, where the line joining the P-point to the centre of the Sun cuts the surface of the Sun, defines the geometrically projected heliographic latitude, $\theta_\odot$, and the heliographic longitude, $\phi_\odot$, of the P-point. The entire *l.o.s.* can be geometrically projected on to the solar surface in a similar manner, as shown in Figure 2.2, to give the geometric *footpoints* of *l.o.s.* on the solar surface.

The heliographic equator and the ecliptic make an angle of $\sim 7^\circ$ to each other. This small angle has the consequence that the *l.o.s.*s to ecliptic sources always sample regions close to the equator on the Sun. Non-ecliptic sources also sample low heliographic latitudes at large elongations but the *l.o.s.*s to them move to higher heliographic latitudes with decreasing elongations as shown in Figure 2.3. Figure 2.4 shows how the geometrically projected footpoints of *l.o.s.*s to an ecliptic and high latitude source change with elongation. This figure shows clearly that the Solar Wind sampled by any given *l.o.s.* arises from a region of considerable spatial extent on the Sun.

As the distance of different points on the *l.o.s.* from the Sun is significantly different, the time taken for the Solar Wind plasma to travel from the Sun to different parts of the *l.o.s.* can differ by as much as a few days (the propagation time from the Sun to 1 AU is ~ 4 $days$ for Solar Wind travelling at 400 $km\ sec^{-1}$). Figure 2.5 shows the footpoints of the *l.o.s.*s with the propagation delay accounted for. The propagation time, t_p, is given by :

$$t_p = \frac{R(z)}{v_r} \tag{2.2}$$

where $R(z)$ is the distance of a point on the *l.o.s.* from the fiducial source surface and v_r is the radial component of the velocity of propagation of the Solar Wind. In the time t_p, the region from where the Solar Wind would have reached the *l.o.s.* would have rotated by an amount given by :

$$\phi_{t_p} = \omega_\odot t_p \tag{2.3}$$

where $\omega_\odot$ is the angular rotation velocity of the Sun. The regions of the solar surface sampled by a *l.o.s.* differ from the geometric footpoints of the *l.o.s.* by an amount ϕ_{t_p}. A featureless Solar Wind model with a constant velocity of 400 $km\ s^{-1}$ has been used and radial evolution has been assumed to be absent. A given *l.o.s.* therefore not only samples the Solar Wind arising from a region of considerable spatial extent but different parts of the *l.o.s.* also sample the Solar Wind which originated from the Sun over times spread over a few days.

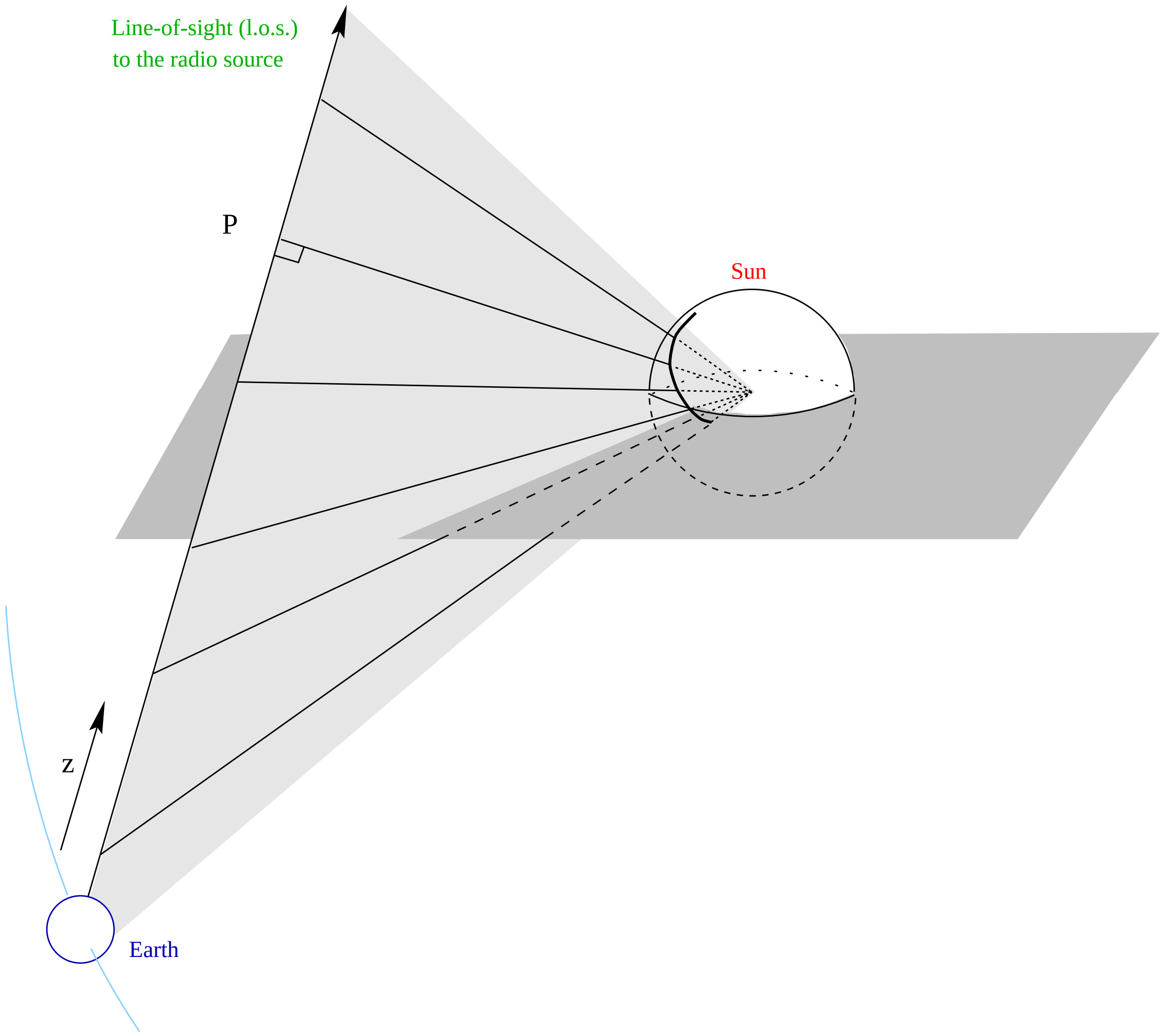

Figure 2.2: **The geometric projection of *l.o.s.* on the solar surface** – The locus of the points where the line joining each of the points on the *l.o.s.* to the solar centre intersects the solar surface defines the geometric projection of the *l.o.s.* on the Sun. It is marked by the bold line on the surface of the Sun. The equatorial plane of the Sun is shaded dark gray and the plane containing the *l.o.s.* and the Sun is shaded light gray. A few representative lines from the *l.o.s.* to the centre of the Sun are also shown. The *l.o.s.* shown here is to a non-ecliptic source, consequently the geometric projection of the *l.o.s.* samples a large range of heliographic latitude.

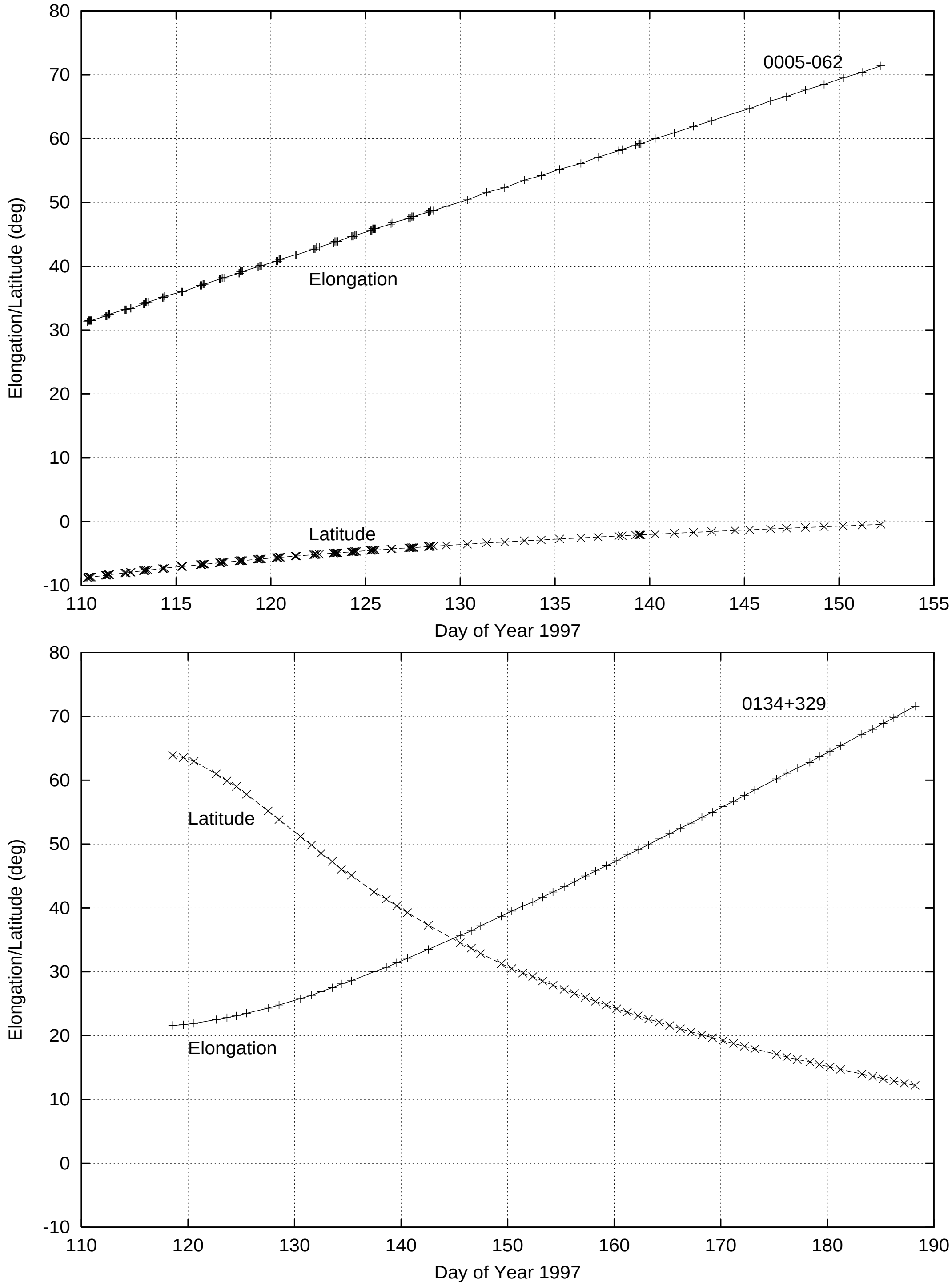

Figure 2.3: **Change in the heliographic latitude of the P-point with elongation** – The elongation and heliographic latitude for an ecliptic source (first panel) and a high heliographic latitude source (second panel) are presented as a function of the time of observation (Day of Year 1997). 0005-062 was chosen to represent the behaviour for ecliptic sources and 0134+329 ($3C48$) for the high latitude sources. The + and × symbols represent the values of elongation and heliographic latitude, respectively, for actual observations. Both the panels are plotted to the same scale, along the Y axis, to facilitate comparison. The elongations for both the sources span a very similar range. The heliographic latitude for the ecliptic source always remains in the range -10° to 0° while that for the high latitude source changes from $\sim 10^\circ$ at large elongations to $\sim 65^\circ$ at small elongations.

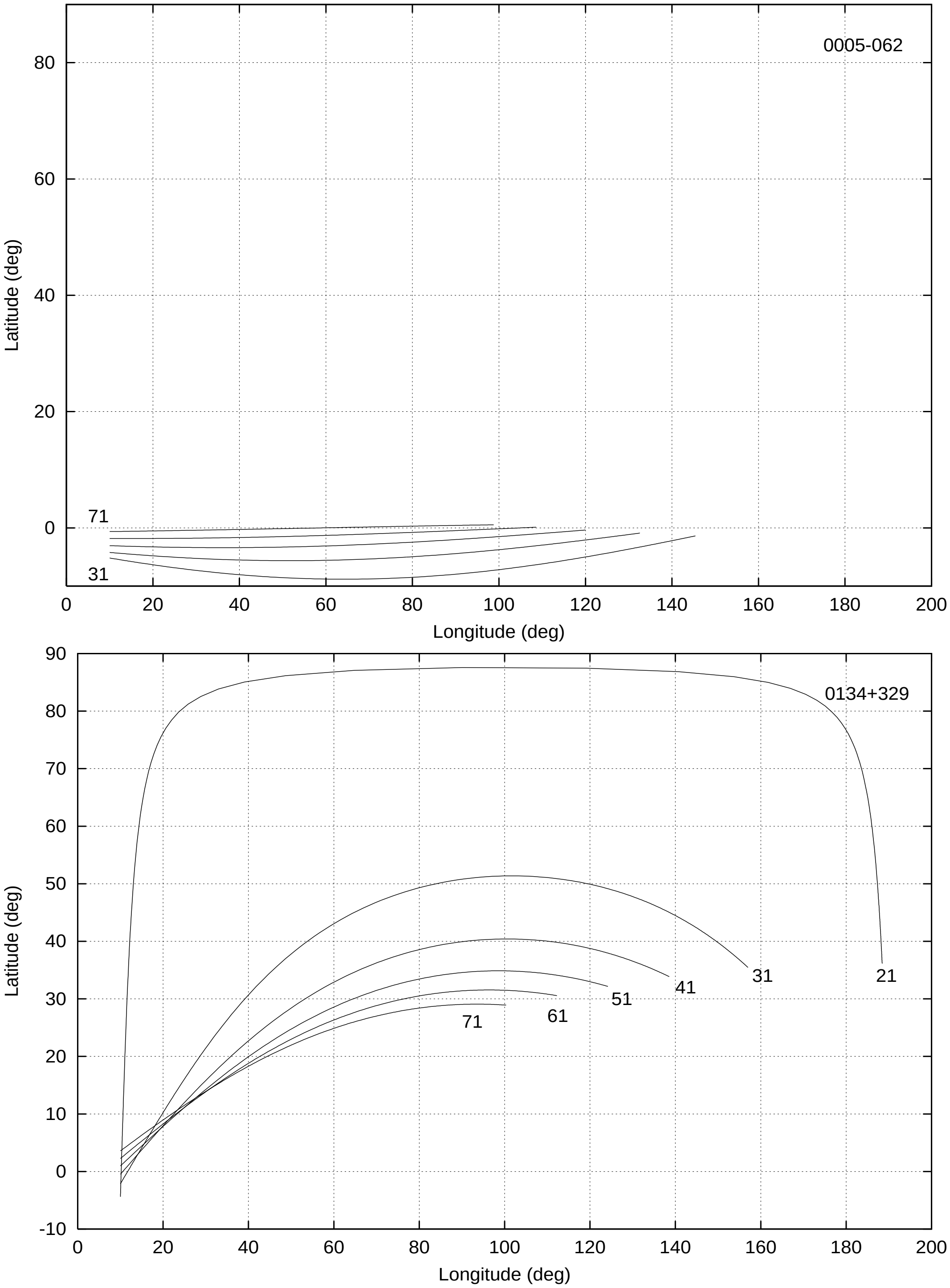

Figure 2.4: **Behaviour of the geometrically projected footpoints of the *l.o.s.*s with elongation** – This figure illustrates the changes in the geometrically projected footpoints of the *l.o.s.* to a source as the elongation of the source changes. The first panel shows the *l.o.s.*s to an ecliptic source, 0005-062, and the second to a high latitude source, 0134+329. The *l.o.s.*s for elongations in the range $\sim 20^\circ$ – 70° have been plotted at $\sim 10^\circ$ interval. The *l.o.s.* has been plotted out to 2 AU, starting from close to the position of the Earth. The apparent increase in length of the *l.o.s.*, as it moves to higher latitudes, is an artifact of representing a spherical surface on a 2D plot. The small spread in the $\theta_\odot$s at which the *l.o.s.*s begin is because of the changes in the $\theta_\odot$ of the Earth. Both the panels are plotted to the same scale.

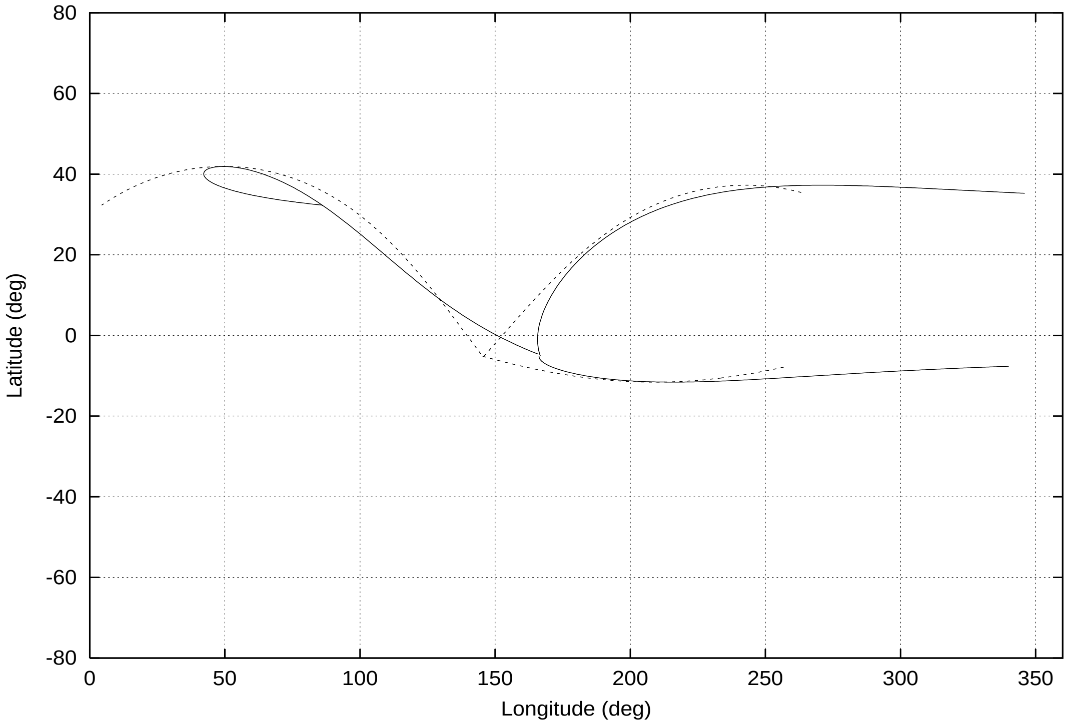

Figure 2.5: **Projected *l.o.s.* with propagation delay accounted for** – The figure shows the changes in the geometric footpoints of *l.o.s.*s to three different sources observed on the same day on taking the propagation time of the Solar Wind from the solar surface to the *l.o.s.* into account. The dashed lines are the geometric footpoints of *l.o.s.*s and the solid lines the footpoints after accounting for the propagation delay. The point where the three *l.o.s.*s meet is the footpoint of the Earth. A featureless Solar Wind model with a constant radial velocity of 400 $km\ sec^{-1}$ has been assumed and the fiducial surface has been placed at $0.3AU$.

In order to locate the regions on the Sun which influence the IPS measurables for a given *l.o.s.*, one necessarily needs the following information:

1. The distribution of Solar Wind velocity along the *l.o.s.*. Each point on the *l.o.s.* can then be traced back to the Sun along an Archimedean spiral and its place of origin on the solar surface located (Section 1.6).
2. The Archimedean spiral mentioned above is actually a mathematical abstraction, valid only for the structure-less Solar Wind. The real Solar Wind is often endowed with considerable structure of both transient and long lived nature. The structure in the Solar Wind may cause the locus of the plasma emanating from a given location on the solar surface to differ significantly from Archimedean spiral. In order to trace back each point on the *l.o.s.* appropriately, the laws of propagation of the Solar Wind also need to be known.

IPS can be used to attempt to solve the inverse problem - given the IPS measurements along one or more *l.o.s.*, one can try to find out both the velocity distribution and the laws of propagation of the Solar Wind. Usually, the number of free parameters involved in such an exercise is much larger than the number of available constraints. It therefore becomes necessary to use simple models for the Solar Wind in order to reduce the number of free parameters to a manageable number.

2.2 IPS observables

The primary observable of IPS is the time series of intensity fluctuations. Scintillations being a stochastic process, the information about the Solar Wind is derived not from the detailed investigations of the time series itself but from its statistical properties, in both time and frequency domain. The definitions presented in this section apply to ideal noiseless data and serve to illustrate the concept. The modifications required in presence of noise, as is the case with real data, are presented in Section 4.5.6. The Scintillation index, m, is a measure of the strength of intensity fluctuations, due to IPS, observed on a particular source and is defined by equation 2.4 :

$$m = \frac{\sigma_{IPS}}{mean\ intensity\ of\ the\ source} \tag{2.4}$$

where σ_{IPS} represents the rms of intensity fluctuations due to IPS and is given by the expression :

$$\sigma_{IPS} = \sqrt{\frac{\sum_{i=1}^{N} \{I_\circ - I(t)\}^2}{N-1}} \tag{2.5}$$

where $I_\circ$ is the mean intensity of the source, defined by :

$$I_\circ = \frac{\sum_{i=1}^{N} I(t)}{N} \tag{2.6}$$

and N is the number of points available in the time series.

The time series of intensity fluctuations sampled by a telescope represents a track in the interference pattern on the ground, as it is swept past the telescope. The *auto-correlation function* of these randomly varying intensity fluctuation, in space and time, is a characteristic of scintillations and is defined as :

$$\rho(\mathbf{r}', t') = \int\int \triangle I(\mathbf{r}, t)\ \triangle I(\mathbf{r}+\mathbf{r}', t+t')\ d\mathbf{r}\ dt \tag{2.7}$$

where $\triangle I(\mathbf{r}, t)$ is defined as :

$$\triangle I(\mathbf{r}, t) = I(\mathbf{r}, t) - I'_{\circ} \tag{2.8}$$

and $I'_{\circ}$ represents the mean intensity of the source, defined by :

$$I'_{\circ} = \frac{\int\int I(\mathbf{r}, t)\ d\mathbf{r}\ dt}{\int\int d\mathbf{r}\ dt} \tag{2.9}$$

The power spectrum of temporal intensity fluctuations, $P(\nu)$, measured at a single spatial location and $\rho(\mathbf{0}, t)$ are related by a Fourier transform relationship :

$$P(\nu) = \frac{1}{2\pi}\int \rho(\mathbf{0}, t)\ exp(-i2\pi\nu t)\ dt \tag{2.10}$$

From the definition σ_{IPS} (equation 2.5) it follows that :

$$\sigma^2_{IPS} = \rho(\mathbf{0}, 0) \tag{2.11}$$

hence m can be expressed as :

$$m = \frac{\sqrt{\rho(\mathbf{0}, 0)}}{I_{\circ}} \tag{2.12}$$

Substituting for $\rho(\mathbf{0}, 0)$ using equation 2.10 m can be expressed as :

$$m^2 = \frac{1}{I^2_{\circ}}\int P(\nu)\ d\nu \tag{2.13}$$

The area under the power spectrum of intensity fluctuations, thus, gives the variance of the intensity fluctuations. The square root of this variance normalised by the intensity of the source, gives the scintillation index .

2.3 Basic IPS scenario

The rigorous treatment of the theory of IPS requires solving for wave propagation through a scattering medium with random refractive index fluctuations in both space and time. In order to make the problem tractable several assumptions need to be made. These assumptions allow us to build a theoretical framework which can be used to interpret the observations. We first present the formalism for a plane quasi-monochromatic wavefront from a distant point source incident on a *thin* weakly scattering screen and then extend it to incorporate spatially extended scattering medium, finite source size and finite bandwidth.

In this and the next few sections we present only the final results, along with some implications of their mathematical form, rather than a complete development of the subject with rigorous derivations. The material in these sections has contributions from a large number of previous researchers. It is difficult, if not impossible, to draw a complete list of contributors. The list of people to whom this work is attributed is likely to be fraught with omissions. The aspects of solving the wave equation in a random medium received considerable contributions from Tatarsky (Tatarsky, 1961, 1971) Marians (Marians, 1975) and Uscinski (Uscinski, 1977). The theory of IPS was first presented in a comprehensive manner by Salpeter (Salpeter, 1967) using a Gaussian form for the spectrum of intensity fluctuations. Rumsey (Rumsey, 1975) and Marians (Marians, 1975) considered a power law form the spectrum of intensity fluctuations. For a more detailed discussion of the subject, the reader is referred to Rao (Rao, 1975) and Manoharan (Manoharan, 1991).

In order to provide a mental picture which the reader can relate to in the following discussion, the situation is shown schematically in Figure 2.6 and is described briefly. Consider a plane wave incident normally on a thin slab of scattering material of thickness Δz. The scattering material imposes space dependent phase fluctuations on the incident wavefront. The emergent radiation has a range of wavevectors spread over an angle ψ_s, which define the *angular spectrum* of the emergent radiation The extremes of ψ_s are shown by the two bold arrows at the screen. The observing plane is at a distance z from the scattering screen. At a large enough z, the path differences between different waves in the angular spectrum grow sufficiently large to produce interference effects and the phase fluctuations imposed by the scattering screen develop into amplitude fluctuations. A given point on the observing plane receives contribution from a patch of size $z\psi_s$ on the scattering screen, as shown in the figure. An important length scale, referred to as the *Fresnel length*, r_f, defines the size of the region on the thin screen which dominates the amplitude interference seen on the observing plane. Fresnel length is given by $\sqrt{z\lambda}$ and is schematically shown by the dark patch of radius r_f in Figure 2.6. It is instructive to think in term of a typical scale size of electron density fluctuation on the screen, this is represented by a light patch of size a_0. $\mathbf{s}$ represents an arbitrary point on the scattering screen. The scattering screen is swept across the *l.o.s.* with the velocity of the Solar Wind, as shown in the figure. The interference pattern it gives rise to on the observing plane, therefore, also sweeps past a stationary observer on the observing plane. This

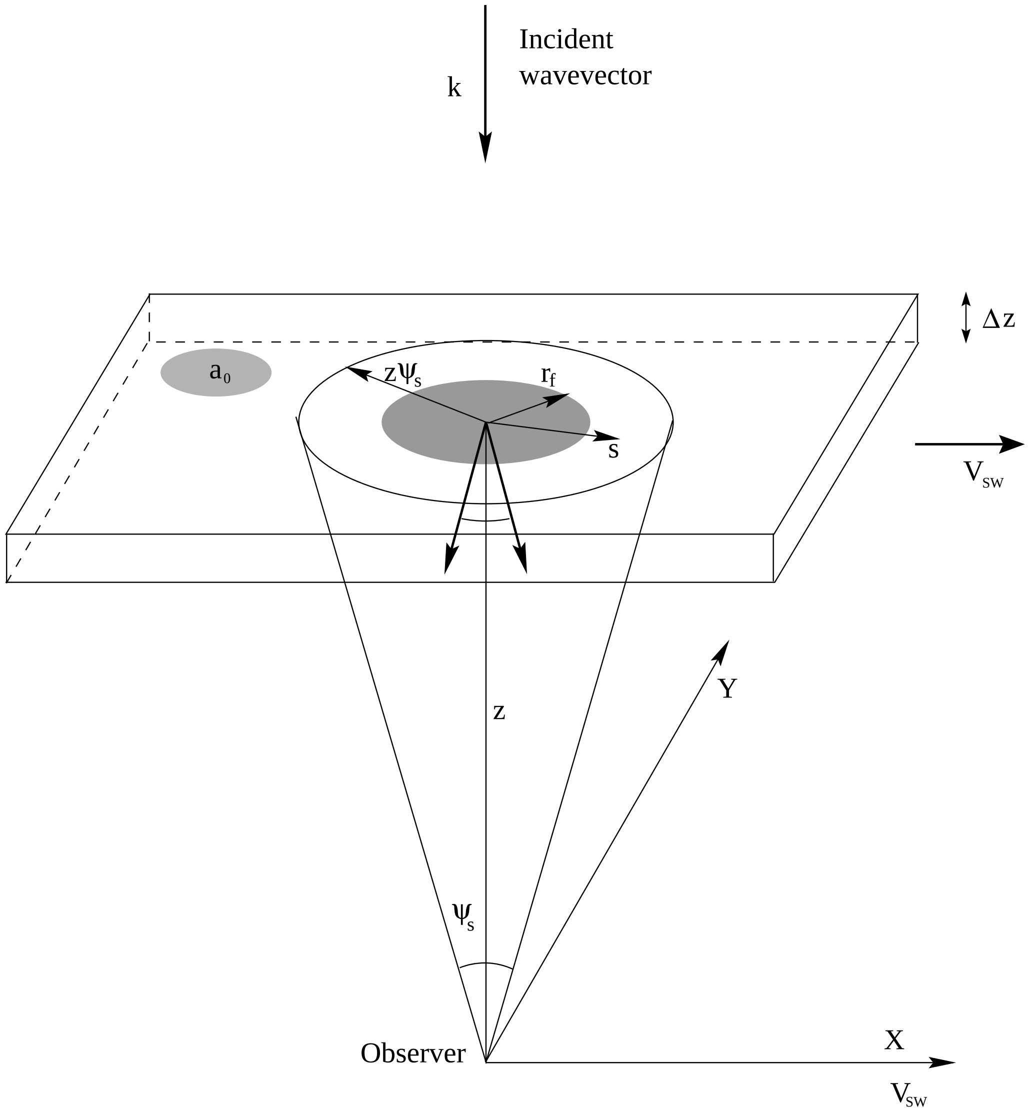

Figure 2.6: **The basic IPS geometry** – The figure shows an plane wave from a distant compact radio source incident on a scattering screen of thickness Δz, the wavevector of which is marked by a bold arrow. The emergent radiation has its wavevector distributed in an angular spectrum, ψ_s, the extrema of which are shown by the two bold arrows on the screen. A given point on the observing plane, at distance z from the screen, receives radiation from a circular patch of radius $z\psi_s$ on the screen. The first Fresnel zone is marked with as a dark patch of radius $\sqrt{z\lambda}$. A typical scale size of electron density fluctuations is marked by a light patch of size, a_0. The screen moves with the velocity of the Solar Wind, denoted by V_{SW} and the coordinate system is arranged such that the x axis is aligned with V_{SW}.

translates the spatial fluctuation of the interference pattern into the temporal intensity fluctuations seen by the stationary telescope. With no loss of generality, the coordinate system used can be so arranged that the X axis is aligned with the direction of the velocity of Solar Wind.

2.4 IPS assumptions

The framework of the theory of IPS is based on many standard assumptions, which have been used extensively by other researchers in the field. This section lists the various assumption made and discusses the manner in which they simplify the problem and their respective domains of validity. The requirements for additional assumptions shall become clear in the following section where the formalism for the power spectra of intensity fluctuations due to IPS is presented.

1. **Thin screen approximation** – We assume that the scattering medium which gives rise to the observed scintillations can be represented by a *thin* screen or an *ideal phase screen* on which the plane wave is incident. An ideal phase screen is mathematical construct which has 0 thickness and imposes purely phase fluctuations (no amplitude fluctuations) on the emergent wavefront. Though the thin screen approximation is unable to accommodate a scattering medium extended along the *l.o.s.*, it is conceptually a useful model and allows a mental picture to be developed. It also has the advantage that theoretical formalism exists for scintillations of any strength due to thin screens, while one is limited to weak scattering regimes while dealing with extended scattering medium. This assumption is relaxed later when a formalism is presented to treat the extended medium as collection of thin screens (Section 2.5.2).

2. **Weak scattering** – On passing though a scattering medium, the emergent wavefront has phase fluctuations imposed on it. In the weak scattering domain these fluctuation are assumed to be small, i.e.

   $$\sigma_{\phi} << 1\ rad \tag{2.14}$$

   where σ_{ϕ} is the rms phase fluctuation on the emergent wavefront. It can be shown that the phase deviation due to a screen of thickness Δz is given by :

   $$\phi(\mathbf{r}) = k \int_{\Delta z} \Delta\mu(\mathbf{r})\ dz \tag{2.15}$$

   where $\Delta\mu$ is the deviation of the refractive index, μ, from its mean value. $\Delta\mu$ can be related to the fluctuations in the electron number density, Δn_e, the physical property of the Solar Wind of interest, in the following manner. In the regime where plasma frequency, ω_p, is much smaller than the frequency of observation, $\omega_0 = 2\pi\ \nu_0$, μ is related to electron number density in the interplanetary medium, n_e, in the following manner :

$$\mu^2 = 1 - \frac{n_e\ e^2}{\epsilon_0\ m_e\ \omega_0^2} \tag{2.16}$$

where e and m_e are the charge and the mass of electron respectively and ϵ_0 is the permitivity of the medium. $\Delta\mu$ can then be expressed in terms of Δn_e as follows :

$$\Delta\mu^2 = \Delta n_e^2 \left(\frac{r_e\ \lambda_0^2}{2\pi}\right)^2 \tag{2.17}$$

where $r_e = e^2/(4\pi\epsilon_0 m_e c^2) = 2.82 \times 10^{-15} m$ is the classical electron radius and λ_0 the wavelength of observation. Δn_e and $\Delta\mu$, therefore, differ only by a constant. Using equations 2.17 and 2.15, $\phi(\mathbf{r})$ can be expressed in terms of Δn_e in the following manner :

$$\phi(\mathbf{r}) = r_e\ \lambda_0 \int_{\Delta z} \Delta n_e(\mathbf{r})\ dz \tag{2.18}$$

For the interplanetary medium, the values of n_e lie in the range $10^3 - 10^9\ m^{-3}$. Assuming $\Delta n_e \sim n_e$ is valid for our observing wavelength of 0.92 m and the given range of Δn_e, equation 2.14 is valid if Δz is much less than $10^2 - 10^8\ km$. This assumption begins to get violated as the *l.o.s.* to the source comes close to the Sun, where the $\Delta\mu$ is much larger. Figure 2.7 shows the variation of the scintillation index, m, with distance from the Sun. Weak scattering assumption is believed to be valid beyond an elongation of $\sim 14°$ for 327 MHz. In the weak scattering regime, m and p are related by :

$$m = m_0\ p^{-b} \tag{2.19}$$

where m_0 is the scintillation index at $p = 1$. The steady decline of m with p, in the weak scattering regime, is a consequence of the n_e (and hence Δn_e) falling off as $\sim R^{-2}$. For a featureless Solar Wind moving at a constant radial velocity, b can be shown to have a value of 1.6.

3. **Small angular spread assumption** – The plane wave incident on a random scattering medium emerges with a spread in its angular spectrum, ψ_s. Any point on the observing plane, therefore, receives contributions from a solid angle within ψ_s of the angle of incidence. If a_0 is a characteristic length scale of the medium, ψ_s is related to it in the following manner :

$$\psi_s \approx \frac{\lambda}{2\pi a_0} = \frac{1}{k a_0} \tag{2.20}$$

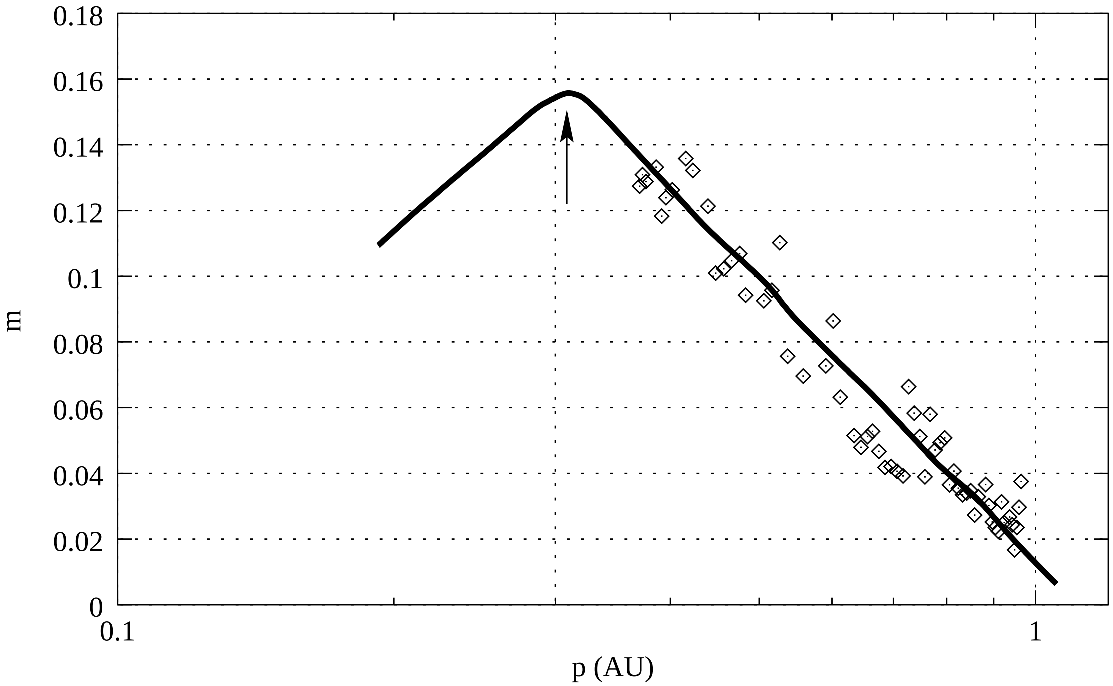

Figure 2.7: **The m-p curve** – The figure shows the variation of the scintillation index, m, with p, the distance of the P-point from the Sun. The bold line shows the expected curve, the data are the observed values of m for 0134+329 from our dataset. One is said to be in the *weak* scattering regime when m increases monotonically with decreasing $\log(p)$. The peak of the m-p curve, marked by the arrow, occurs close to an elongation of $\sim 14°$ at 327 MHz. At smaller p values, m decreases with p and this region lies in the *strong* scattering regime.

For the interplanetary medium, a_0 is $\sim 100\ km$. For a power law spectrum of density fluctuations, the medium itself has no unique scale size associated with it (Section 2.4) and the characteristic length scale is given by the *Fresnel scale size*, discussed in Section 2.5.1. For our wavelength of observation of ($\lambda = 0.92\ m$, $\nu = 327\ MHz$), ψ_s is typically $\sim 10^{-6}\ rad$ and this assumption holds very well. As $\lambda << a_0$, this assumption amounts to *Geometric Optics* approximation. An upper limit on the Δz, within which the phase differences are not sufficient to produce interference can easily be arrived at. The path difference between two rays traversing a distance z travelling at an angle $z\psi_s$ to each other is $z\psi_s^2/2$. The condition for this path difference to be small is given by :

$$\frac{z\psi_s^2}{2} \ll \frac{\lambda}{2} \tag{2.21}$$

Substituting for ψ_s from equation 2.20 in the above relation yields $z \ll ka_0^2$. Therefore, if the thickness of the screen is much less than ka_0^2, interference effects within the screen are negligible and it is equivalent to an ideal phase screen. As the radiation travels to the observer, the phase differences corresponding to the path differences between various wavefronts comprising the angular spectrum become significant and produce interference.

4. **Spectrum of electron density fluctuations** –

   As the fluctuations in electron density are stochastic in nature it is desirable to quantify them using a stable statistical measure. The spectrum of density fluctuations is used most often to quantify the electron density fluctuations. In the early days (before 1970), a gaussian form for this spectrum was used, it has since been shown that the spectrum is better represented by power law forms :

$$\Phi_{\Delta n_e}(\mathbf{q}) = C_n^2 \left(\frac{q^2}{q_o^2}\right)^{-\frac{1}{2}\alpha} exp\left(-\frac{q^2}{q_i^2}\right) \tag{2.22}$$

   where $\mathbf{q} = (q_x, q_y)$ is the two dimensional spatial frequency, $q^2 = (q_x^2 + q_y^2)$ and C_n^2 is the constant of proportionality. The above expression assumes circular symmetry in the density fluctuations. The power law of electron density fluctuations is expected to remain valid between the two characteristic spatial wavenumbers, the inner scale, q_i, and the outer scale, q_o. The spectral index of the power law, α, is referred to as the *index of electron density fluctuations* or simply the index. A detailed discussion on the observational verification of this assumption and the value of q_i and α is presented in Section 2.6.

5. **Time stationarity** – It is assumed that the statistical properties of the interplanetary medium sampled by a given *l.o.s.* do not change significantly during the course of the observation. This assumption is very reasonable as the time

scales of the observations are of the order of tens of minutes. It is necessary to make this assumption as it is required to observe for durations long enough to reduce the noise on the data to acceptable levels.

6. **Frozen screen** – This assumption is a manifestation of the belief that the temporal variation in the observed intensity of a scintillating source is mainly due to the bulk motion of the Solar Wind across the *l.o.s.*. If the refractive index of the medium be represented by $\mu(\lambda, \mathbf{r}, t) = \mu_0 + \Delta\mu(\lambda, \mathbf{r}, t)$, the temporal variations of $\Delta\mu(\lambda, \mathbf{r}, t)$ are assumed to be much slower than $\tau \sim a_0/V$, the time it takes for an irregularity pattern of typical scale size a_0 to pass through the *l.o.s.*. This can be expressed mathematically as :

$$\Delta\mu(\mathbf{r}, t) = \Delta\mu(\mathbf{r} - \mathbf{v}t, 0) \tag{2.23}$$

The refractive index fluctuations are essentially *frozen* in the medium as it is swept past the *l.o.s.*. This assumption is referred to as Taylor's hypothesis and simplifies the theory by reducing the problem to that of wave propagation through a medium with only spatial refractive index fluctuations. This assumption is made use of in multi-station IPS observations where the time series of intensity fluctuations observed at different stations separated by a few hundred *km* are correlated. This assumption establishes the following relation between the frequency of temporal fluctuations and the spatial wavenumber q_x :

$$q_x = \frac{2\pi\ \nu}{|V_\perp(z)|} \tag{2.24}$$

where $V_\perp(z)$ is the component of the velocity of Solar Wind along the X axis. Very close to the Sun($\epsilon < 10^\circ$), this assumption breaks down because of the large random motion components in the velocity of the Solar Wind.

2.5 Power spectrum of intensity fluctuations

Under the assumptions discussed in the previous section, the power spectrum of intensity fluctuations measured at the observing plane can be related to the physical parameters of the Solar Wind like the velocity, strength of scattering, spectral index and inner scale of the power law of electron density fluctuations and axial ratio of the irregularity patterns. In this section, we present the formalism which relates the observed power spectrum to the physical properties of the Solar Wind just mentioned.

2.5.1 Power spectrum of intensity fluctuations for a thin screen

In the geometry shown in Figure 2.6, a plane wave is incident on a weakly scattering thin screen. A given point on the observing plane receives contribution from a circular patch on the scattering screen of radius $z\psi_s$ where z is distance between the observing plane and the scattering screen and ψ_s the maximum angle of scattering. As z increases, the path differences for the various rays travelling within the angular spectrum of spread ψ_s become large enough for these rays to interfere at the observing plane. This is the primary cause of intensity fluctuations. Using equation 2.18 the spectrum of two dimensional spatial phase fluctuation can be related to the three dimensional spectrum of spatial n_e fluctuations in the following manner :

$$\Phi_\phi(\mathbf{q}, z) = 2\pi\ (r_e\lambda_0)^2\ \Delta z\ \Phi_{\Delta n_e}(q_x, q_y, q_z = 0, z) \tag{2.25}$$

The Fourier transform of the auto-correlation function of the intensity fluctuations on the observing plane, which is same as the spatial spectrum of intensity fluctuations on the plane is given by :

$$\Phi_{\Delta I}(\mathbf{q}) = \frac{1}{(2\pi)^2}\int\int \langle (I(\mathbf{r_0}) - \langle I\rangle_t)\ (I(\mathbf{r_0}+\mathbf{r}) - \langle I\rangle_t)\rangle_t\ \exp(i\mathbf{q}.\mathbf{r})\ d\mathbf{r} \tag{2.26}$$

where $\mathbf{q} = (q_x, q_y)$ is two dimensional wave number and $\langle\rangle_t$ denotes ensemble average. This can be written as :

$$\Phi_{\Delta I}(\mathbf{q}) = \frac{1}{(2\pi)^2}\int\int \left(\langle I(\mathbf{r_0})\ I(\mathbf{r_0}+\mathbf{r})\rangle_t - \langle I\rangle_t^2\right) \exp(i\mathbf{q}.\mathbf{r})\ d\mathbf{r} \tag{2.27}$$

where $\langle I\rangle$ is the mean intensity of the radiation on the observing plane. Under the assumptions discussed in Section 2.4, the wave equation has a solution of the form :

$$F(\mathbf{q}, z) = F(\mathbf{q}, 0)\exp\left(\frac{-iq^2z}{2k}\right) \tag{2.28}$$

where $F(\mathbf{q}, 0)$ is the electromagnetic field at $z = 0$ and $F(\mathbf{q}, z)$ the field at any later z. Using this solution for the wave equation and equation 2.27 it can be shown that :

$$\Phi_{\Delta I}(\mathbf{q}, z) = 4\sin^2\left(\frac{q^2z}{2k}\right)\ \Phi_\phi(\mathbf{q}) \tag{2.29}$$

Using equation 2.25, the above equation can be expressed in terms of $\Phi_{\Delta n_e}(\mathbf{q})$ as :

$$\Phi_{\Delta I}(\mathbf{q}, z) = 4\sin^2\left(\frac{q^2z}{2k}\right)\ 2\pi(r_e\lambda)^2\Phi_{\Delta n_e}(\mathbf{q}) \tag{2.30}$$

The above equation gives the two dimensional spectrum of spatial intensity fluctuations seen on a observing plane at a distance z from the scattering screen. As the interference pattern moves across the observing plane with the velocity, v, of the Solar Wind, the stationary observer on the observing plane samples a strip in the interference pattern (Figure 2.6). The part of the intensity fluctuation pattern sampled by the telescope can be represented as :

$$\Delta I_{obs,z}(\mathbf{r}) = \Delta I(vt) = \Delta I_z(\mathbf{r}) S(\mathbf{r}) \tag{2.31}$$

where $\Delta I_z(\mathbf{r})$ is the intensity fluctuation pattern on the observing plane at a distance z from the screen, $\Delta I_{obs,z}(\mathbf{r})$ is the strip across the interference pattern which is sampled by the telescope and $S(\mathbf{r})$ represents the sampling function with which the pattern has been sampled. $S(\mathbf{r})$ can be thought of as a function which is unity in a strip of infinitesimal width along the X axis ($y = 0$) and 0 elsewhere in the observing plane. The empirically measured auto-correlation function, $\rho(vt)$, from the time varying intensity measured at a single station is related to the true 2D auto-correlation function as :

$$\rho(vt) = \rho_{obs}(x, y = 0) = \rho_{true}(\mathbf{r}) S(\mathbf{r}) \tag{2.32}$$

Using the convolution theorem, the Fourier transform of ρ_{obs} can be expressed as a convolution of the power spectra of $\Delta I_z(\mathbf{r})$ and Fourier transform $S(\mathbf{r})$. The Fourier transform of $S(\mathbf{r})$ is a constant along the q_y axis and has infinitesimal width along q_x. The power spectrum of spatial fluctuations sampled by the observer can therefore be written as :

$$P_z(\mathbf{q}) = \int d\mathbf{q}\ \Phi_{\Delta I}(\mathbf{q}, z)\ \delta(q_x) \tag{2.33}$$

where $\delta(q_x)$ is the Fourier transform of $S(\mathbf{r})$. The above equation can be reduced to the following form :

$$P_z(q_x) = \int dq_y\ \Phi_{\Delta I}(\mathbf{q}, z) \tag{2.34}$$

The observed power spectrum of temporal intensity fluctuations can be related to the spectrum of spatial intensity fluctuations on the observing plane using equation 2.24.

$$P_z(\nu) = \frac{2\pi}{|V_\perp|} \int dq_y\ \Phi_{\Delta I}(\mathbf{q}, z) \tag{2.35}$$

where $V_\perp(z)$ is the component of the velocity of the Solar Wind perpendicular to the *l.o.s.* at a distance z along the *l.o.s.*. The power spectrum of intensity fluctuations observed at the Earth is thus a strip scan across the two dimensional spatial intensity fluctuation power spectrum, transverse to the velocity of the Solar Wind.

The Fresnel Propagation Filter

The $\sin^2$ term in equation 2.30 is referred to as the *Fresnel propagation filter* or simply the Fresnel filter.

$$F_f = \sin^2\left(\frac{q^2 \lambda z}{4\pi}\right) \tag{2.36}$$

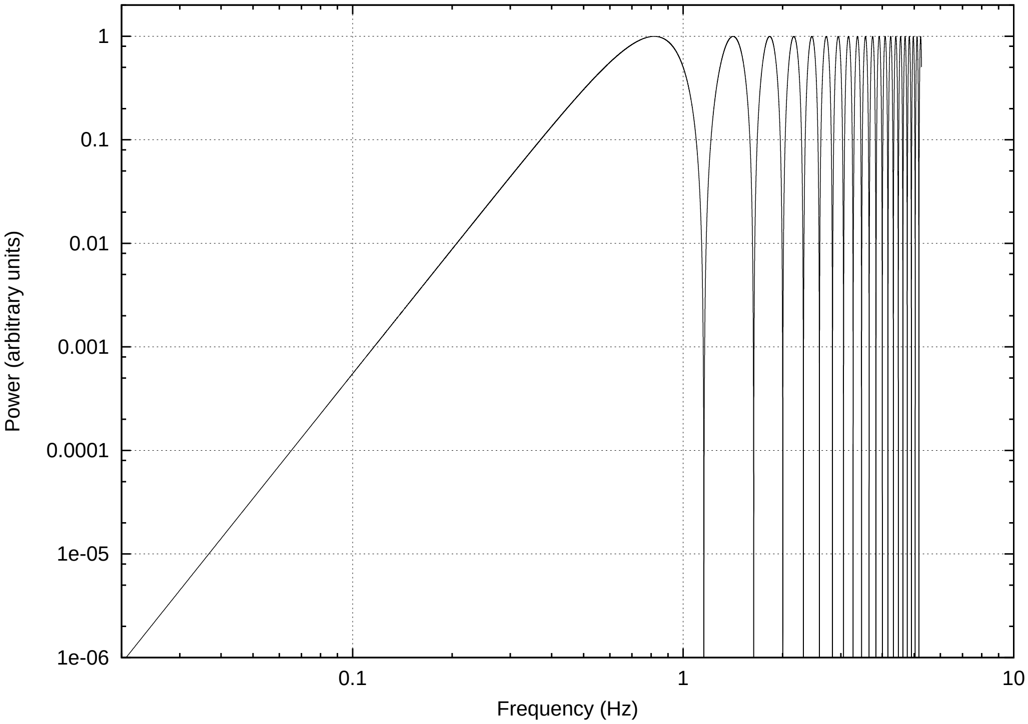

Figure 2.8: **The Fresnel filter** – The figure shows the Fresnel filter function, $sin^2(q^2 z/2k)$, on a log–log scale. A z corresponding to the P-point distance for a $l.o.s.$ at $\epsilon = 30°$ and $\lambda = 0.92\ m$ were used to compute the Fresnel filter along with a Solar Wind velocity of 400 $km\ sec^{-1}$.

It relates the spectrum of electron density fluctuations in the thin screen to the spectrum of intensity fluctuations seen on the observing plane (equation 2.30). The Fresnel filter represents the interference effects which lead to intensity scintillation.

Figure 2.8 shows the Fresnel propagation filter at 327 MHz for typical parameters for IPS geometry (z corresponding to the P-point distance for a $l.o.s.$ at $\epsilon = 30°$, $\lambda = 0.92\ m$). The original spatial frequency spectrum has been converted to a temporal frequency one using the equation 2.24 and a Solar Wind velocity of 400 $km\ sec^{-1}$. From the figure it is apparent that the Fresnel filter severely attenuates the power spectrum at low spatial frequencies. A characteristic frequency in the spatial frequency domain, q_f, the spectrum at larger spatial scales than which is significantly attenuated can be defined as :

$$q_f = \sqrt{\frac{4\pi}{\lambda z}} \tag{2.37}$$

q_f can be approximately related to the radius of the first Fresnel zone, $r_f = \sqrt{z\lambda}$. The phase difference incurred due to path difference for a ray coming from an arbitrary point $\mathbf{s}$ on the screen is given by :

$$\phi = \frac{|\mathbf{s}|^2}{2z}\frac{2\pi}{\lambda} \tag{2.38}$$

and the rate of change of ϕ with change in $|\mathbf{s}|$ by :

$$\frac{d\phi}{d|\mathbf{s}|} = \frac{|\mathbf{s}|}{z}\frac{2\pi}{\lambda} \tag{2.39}$$

The phase difference, therefore, oscillates faster and faster as $|\mathbf{s}|$ increases. The characteristic scale size beyond which the phase oscillations become so fast that the interference pattern is averaged out can be estimated by :

$$|\mathbf{s}| \gg \sqrt{z\lambda} = r_f \tag{2.40}$$

Thus even though a given point on the observing plane may receive radiation from a large patch on the scattering screen (of radius $z\psi_s$), as shown in Figure 2.6, it is the region contained in the radius of r_f which dominates the interference pattern observed. IPS, therefore, is less sensitive to spatial scales much larger than r_f and cannot be used to estimate q_0, the outer scale of the power law of electron density fluctuations (Section 2.4).

Though the distribution of electron density fluctuations on the scattering screen is governed by a power law and there is no unique scale size which can be associated with the screen, it is worth remarking that the fluctuations at a scale close to r_f dominate the observed interference pattern because of steep slope of the power law index.

As is evident from Figure 2.8, the F_f oscillates rapidly for large q (large ν). F_f can therefore be replaced by its average value of 1/2 when $q \gg q_f$ while evaluating the integral in equation 2.35.

An examination of the dependence of the Fresnel filter on z shows that interference effects are absent at the thin screen itself ($z = 0$) and they develop slowly with increase in z. A characteristic distance, beyond which scintillations are said to be fully developed, can be obtained by equating the argument of the sin to $\pi/2$, which leads to :

$$z_f(q) = \frac{2\pi^2}{q^2\lambda} \tag{2.41}$$

The distance at which the fluctuations develop is a strong function of q and is smaller for larger q or smaller spatial scales.

The Fresnel filter shows a sharp drop in the intensity after the first maxima, this shape is referred to as the *Fresnel knee.*

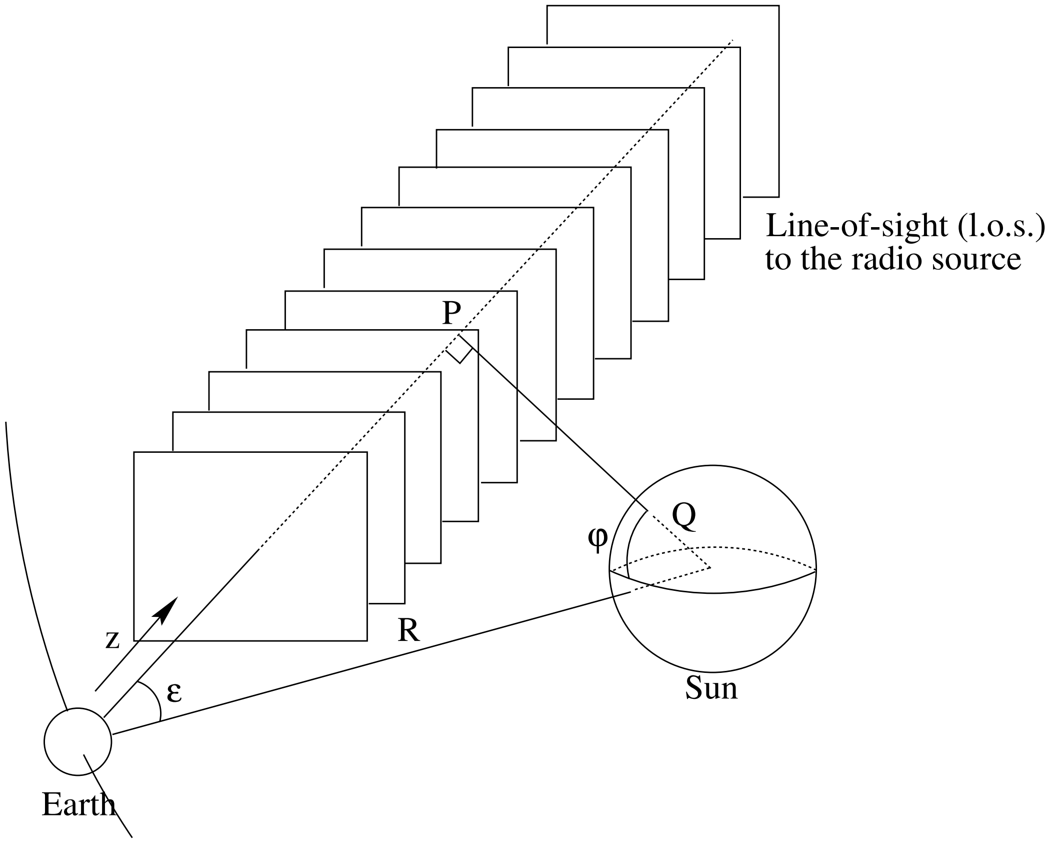

Figure 2.9: **The thin screens along a *l.o.s.*** – Solar Wind is modelled as a set of thin screens stacked along the *l.o.s.*. A representative few are shown in the schematic. The properties of each of the thin screens are independent of one another.

2.5.2 The extended medium

The above formalism is valid for a scattering medium confined to a thin screen. As the spectrum of density fluctuation of electrons in the Solar Wind has a $R^{-\beta}$ dependence (Section 2.4), a considerable portion of the *l.o.s.* often has enough strength of scattering (C_n^2) to introduce phase fluctuations which lead to intensity fluctuation at the observing plane. A single thin screen is, therefore, an inadequate description of the Solar Wind.

In the weak scattering approximation (Section 2.4), the formalism presented can be generalised to include extended scattering medium by replacing the extended medium with a stack of independent thin screens as shown in Figure 2.9. The final intensity pattern seen on the observing plane can then be regarded as the sum of the individual patterns produced by each of the thin screens.

$$P(\nu) = 2\pi \int \frac{dz}{|V_\perp(z)|} \int dq_y \; 4\sin^2\left(\frac{q^2 \lambda z}{4\pi}\right) \; \Phi_{\Delta n_e}(\mathbf{q}, R) \tag{2.42}$$

Physically, this is same as assuming that each thin screen has the same plane wave front incident on it, i.e. the fraction of radiation scattered by earlier thin screens is negligible, and that the radiation once scattered is not scattered again or *Born approximation* holds. This is the primary reason for the weak scattering assumption introduced in the previous section. In the strong scattering regime, multiple scatterings can no longer be ignored. The radiation incident on any thin screen comprises of the sum of the part of plane wave from the distant radio source which has passed unscattered through the earlier thin screens and the part which has been scattered by them. Each thin screen, therefore, has a different set of incident plane wavefronts.

The strength of scattering of a given thin screen is given by the local level of turbulence and is quantified by C_n^2. C_n^2 is assumed to be proportional to $R^{-\beta}$ where R is the heliocentric distance to the thin screen under consideration. The turbulence spectrum therefore has the following dependence on the radial distance from the Sun :

$$\Phi_{\Delta n_e}(R) \propto R^{-\beta} \tag{2.43}$$

This assumption forms the basis for the simple featureless models of the Solar Wind presented in Section 3.2.1. For Solar Wind moving radially with uniform velocity, $\beta = 4$ under the assumption that $\delta n_e \sim n_e$.

2.5.3 Effect of finite source size

The formalism presented till now considers a plane wavefront to be incident on each of the thin screens. This can be produced only by a geometric point source, infinite distance away from the scattering screen. In practice, every source has a finite size and therefore subtends a finite angle at the scattering screen. The incident radiation on the scattering screen therefore has a finite *angular spectrum* rather than a unique well defined direction of propagation. The wavefront incident on the scattering screen is a superposition of the plane wavefronts which comprise the angular spectrum. An extended source can be treated as a collection of independent point sources and it results in reducing the coherence of the radiation incident on the scattering screen. Consider a source with structure given by the *Brightness distribution*, $B(\theta, \phi)$, in the plane of the sky. Its Fourier transform is referred to as the *Visibility function*

$$V(u,v) = \int\int d\theta \; d\phi \exp\left(-2\pi i(u\theta + v\phi)\right) B(\theta,\phi) \tag{2.44}$$

and is the spatial *Autocorrelation function* of the incident electric field with distance in units of wavelength. From equation 2.44 it follows that the visibility is a constant for a point source, i.e. the radiation always remains correlated all over the scattering screen. Consider a source with a Gaussian brightness distribution with a half width of $\theta_\circ$, the visibility function for it has a width of $1/2\pi\theta_\circ$:

$$V(u,v) = \exp\left(-(2\pi\theta_\circ)^2\frac{(u^2+v^2)}{2}\right) \tag{2.45}$$

Thus the radiation from an extended source incident on the scattering screen is correlated only over finite length scales. If the radiation remain correlated over regions much larger than the size of the region which contributes to the interference pattern on the observing plane, the scintillations shall not be effected significantly. Thus in the regime

$$z\psi_s \ll \frac{\lambda}{2\pi\theta_\circ} \tag{2.46}$$

the interference pattern on the observing plane shall not be effected significantly by the extended source structure. Using a z of 1 AU and a ψ_s of 10^{-6} rad gives a $\theta_\circ$ limit of $\sim 0.2''$ for a λ of 0.92 m by when the source size effects have become significantly important.

The power spectrum of intensity fluctuations due to an extended source can be expressed as the product of that due a point source and the visibility function corresponding to the brightness distribution of the extended source.

$$\Phi_{I\ ext}(q,z,\theta_\circ) = \Phi_{I\ point}(q,z)|V(qz\theta_\circ)|^2 \tag{2.47}$$

where the visibility, $V(qz\theta_\circ)$, has been expressed in variables natural to the problem at hand. The presence of the visibility function in the expression for power spectrum of intensity fluctuations acts as a *low-pass* filter for the power spectrum, attenuating the high q and hence high ν part of the spectrum. This attenuation becomes more severe for screens at larger distance from the Earth. More details of the effect of $\theta_\circ$ on the observed power spectrum are presented in Section 2.6.

2.5.4 Effect of receiver bandwidth

The formalism presented above deals with quasi-monochromatic waves. In practice every observing instrument has a finite bandwidth over which it receives the signal. As scintillations are a frequency dependent phenomena, with a finite coherence frequency scale, observations over bandwidths larger than the coherence scales leads to averaging of the scintillations. The effect of receiver bandwidth on the observed scintillations has been discussed by various workers. Little (Little, 1968) discussed the effect of receiver bandwidth on the scintillations due to a point source. Salpeter (Salpeter, 1967) and Budden and Uscinski (Budden and Uscinski, 1970) showed that increasing the bandwidth decreased the scintillation in a manner similar to increase in source size. Cronyn (Cronyn, 1970) presented a clear picture of the effects of finite bandwidth on the observation of scintillating sources.

The effect of bandwidth on the observed scintillations can be estimated by the following argument. Most observations are made in the small bandwidth limit, which is given by the relation :

$$\frac{\Delta\nu}{\nu_0} << 1 \tag{2.48}$$

where ν_0 is the observing frequency and $\Delta\nu$ the bandwidth of observation. For such *quasi monochromatic* radiation, a *coherence* time scale, τ_{PB}, within which the phase fluctuations of the electric field remain correlated, is given by $1/\Delta\nu$. The electric field at the receiver is the sum of contributions from different parts of the phase screen. If the propagation time from different parts of the thin screen to the receiver differs by more than the τ_{PB}, the coherence of the electric field is lost and the scintillations are quenched. The contribution coming from an elemental area element at $\mathbf{s}$ on the screen has to travel an additional distance $\delta r = s^2/(2z)$, in the small angle approximation (Figure 2.6). This corresponds to a time delay of $s^2/(2zc)$. If this delay is larger than τ_{PB}, the electric field from this region will not be coherent with the field from the region $\mathbf{s} = 0$. The largest value of $\mathbf{s}$ of interest to us is given by $\mathbf{s_{max}} = z\psi_s$. Thus for the decoherence due to finite bandwidth to be negligible, the following must hold :

$$\frac{z\psi_s^2}{2c} \ll \tau_{PB} \tag{2.49}$$

In the weak scattering approximation, equation 2.20 can be used to relate ψ_s to the scale size of intensity fluctuations on ground and the above equation can be written as :

$$\frac{z\lambda_0^2}{8\pi^2 a_0^2 c} \ll \tau_{PB} \tag{2.50}$$

The above equation can be expressed in the following manner to give a limit on the scale size, a_0, beyond which effects of finite bandwidth necessarily need to be incorporated :

$$a_0^2 \ll \frac{z\lambda^2\Delta\nu}{8\pi^2 c} \tag{2.51}$$

For a bandwidth of 4 MHz at a λ of 0.92 m and a z of 1 AU, the a_0 below which bandwidth effects become important is $\sim$ 4.6 km. The temporal frequency, ν, this scale size corresponds to was computed using equation 2.24, assuming a typical velocity of 400 $km\ sec^{-1}$ for the Solar Wind and it turns out to be $\sim$ 87 Hz. As the measured power spectrum of intensity fluctuations usually cutoff by $\sim$ 6 Hz due to dominance of system noise, the effects of finite bandwidth are negligible. Previous workers at the Ooty Radio Telescope have explicitly verified this by comparing observations made using a $\Delta\nu$ of 1 and 4 MHz. No discernible differences were found in the power spectra observed using the two bandwidths.

2.5.5 The final expression

On the basis of the discussion presented in the earlier part of this section, the power spectrum of intensity fluctuations in terms of the physical properties of the Solar Wind can be expressed as :

$$P(\nu) = (2\pi r_e \lambda)^2 \int \frac{C_n^2(z)dz}{|V_\perp(z)|} \int dq_y \sin^2\left(\frac{q^2\lambda z}{4\pi}\right) |V(q,z,\theta_\circ)|^2 q^{-\alpha} exp\left(-\frac{q^2}{q_i^2}\right) \ R^{-\beta} \tag{2.52}$$

This formulation takes into the effects of the extended scattering medium and finite source size. The effects of finite bandwidth have been shown to be small enough to be ignored (Section 2.5.4). As IPS is not sensitive to q_o (Section 2.5.1), it has not been incorporated in the model for the power spectra.

2.6 Effects of variation of model parameters on the power spectra

This section discusses the form of the expression for the power spectrum of intensity fluctuations due to IPS and the effects of variations of individual properties of the Solar Wind on the observed power spectra. The figures presented in this section have been obtained by numerically integrating equation 2.52.

Effect of velocity variations

From equations 2.55 and 2.24 it can be seen that velocity of the Solar Wind scales the power spectrum along the ν axis. The entire power spectrum stretches or contracts along the ν axis with increase or decrease in the velocity of the Solar Wind. The scintillation index observed towards a *l.o.s.*, which is measured by the area under the power spectrum, remains unaffected by the changes in velocity of the Solar Wind. Figure 2.10 shows power spectra for v ranging from 200 – 1000 $km\ sec^{-1}$ keeping all other parameters of the Solar Wind model the same. The Fresnel knee (Section 2.5.1) is clearly visible in these power spectra and forms a convenient feature which can be used to estimate the velocity of the Solar Wind as the temporal frequency of the spectrum is proportional to the velocity of the Solar Wind. The power spectra are rather sensitive to the variations in the velocity of the Solar Wind. This property of the power spectra makes them an efficient and reliable diagnostic for studying the velocity of the Solar Wind.

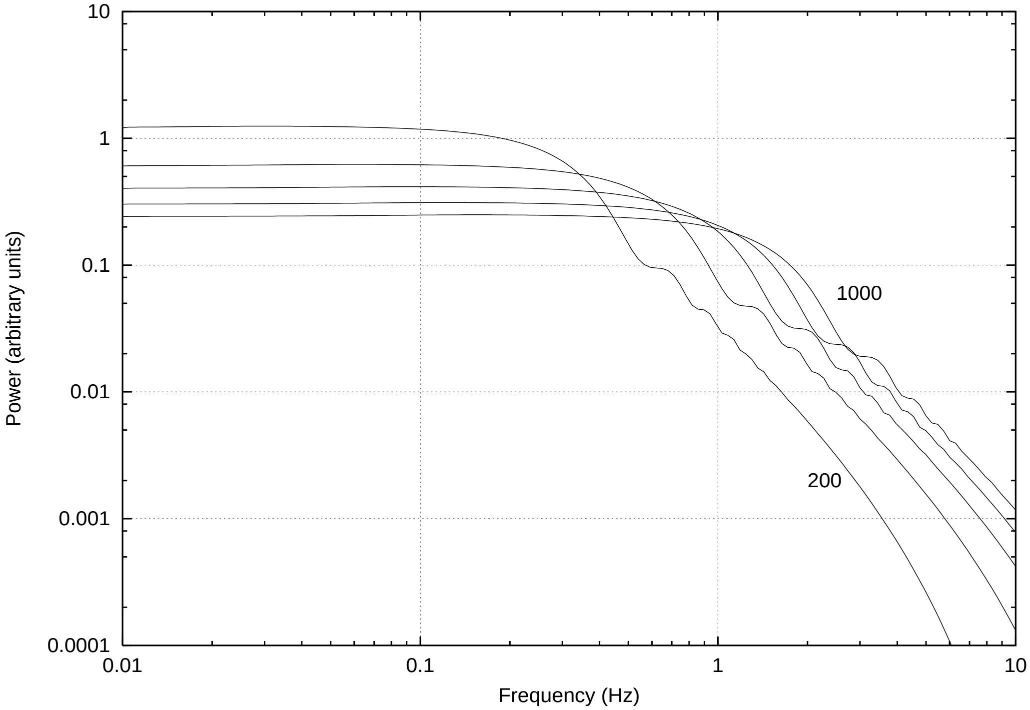

Figure 2.10: **Effect of v of the Solar Wind on the power spectrum** – Power spectra for velocities of the Solar Wind ranging from 200 – 1000 $km\ sec^{-1}$, in steps of 200 $km\ sec^{-1}$, are shown. The spectra with velocities of 200 and 1000 $km\ sec^{-1}$ have been labelled. The spectra have been generated using $AR = 1.0$, $\alpha = 3.0$ and $q_i = 3.3\ km^{-1}$ for a $\theta_\circ$ of $0''$ at 30° ϵ.

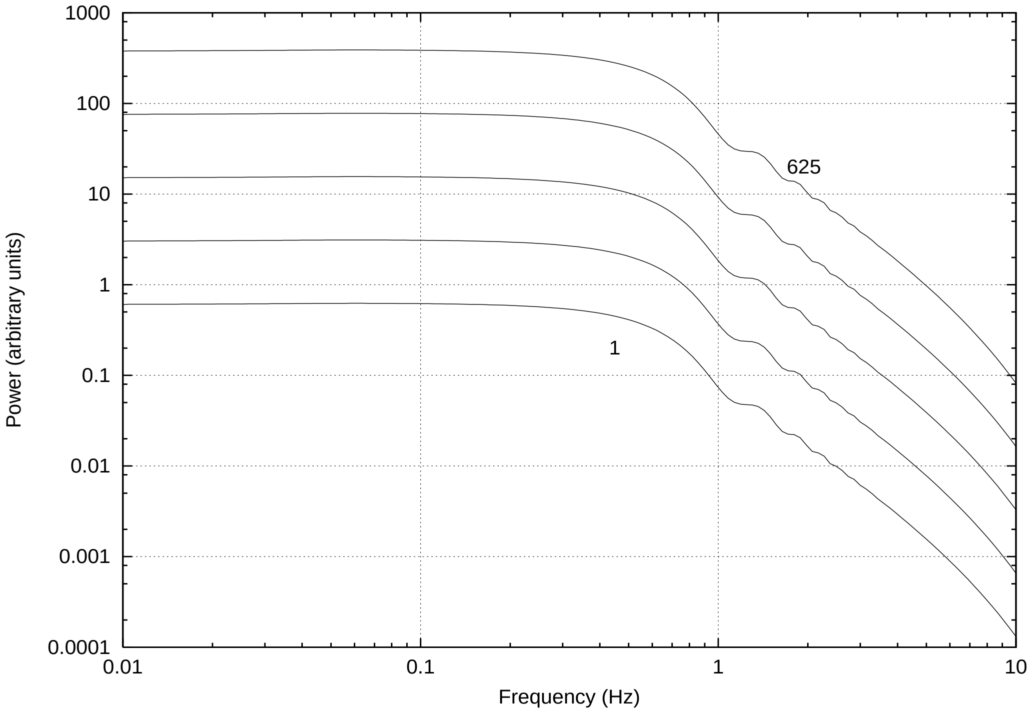

Figure 2.11: **Effect of variation in C_n^2 on the power spectrum** – The figure shows power spectra for values of C_n^2 $1, 5, 25, 125$ and 625 in arbitrary units. The spectra with C_n^2 of 1 and 625 have been labelled. The spectra have been generated using $V = 400\ km\ sec^-1$, $AR = 1.0$, $\alpha = 3.0$ and $q_i = 3.3\ km^{-1}$ for a $\theta_\circ$ of $0''$ at 30° ϵ.

Effect of variations of strength of scattering

Equation 2.52 shows that the strength of scattering, C_n^2, is a constant multiplying the entire power spectrum. Increase or decrease in C_n^2 has the effect of bodily moving the power spectrum up or down, as seen on a log scale. Figure 2.11 shows the power spectra for a wide range of C_n^2 values while keeping all the other parameters of the Solar Wind model constant. As the area under the power spectrum, which is proportional to m, is a direct measure of the strength of scattering along the $l.o.s.$, IPS provides a sensitive means to estimate the C_n^2 along the $l.o.s.$.

Effect of source size variations

The source size, $\theta_\circ$, effects the power spectrum through the source visibility function in the integrand of eqution 2.52. The visibility function takes the form :

$$V(q, z, \theta_\circ) = exp(-q^2 z^2 \theta_\circ^2) \tag{2.53}$$

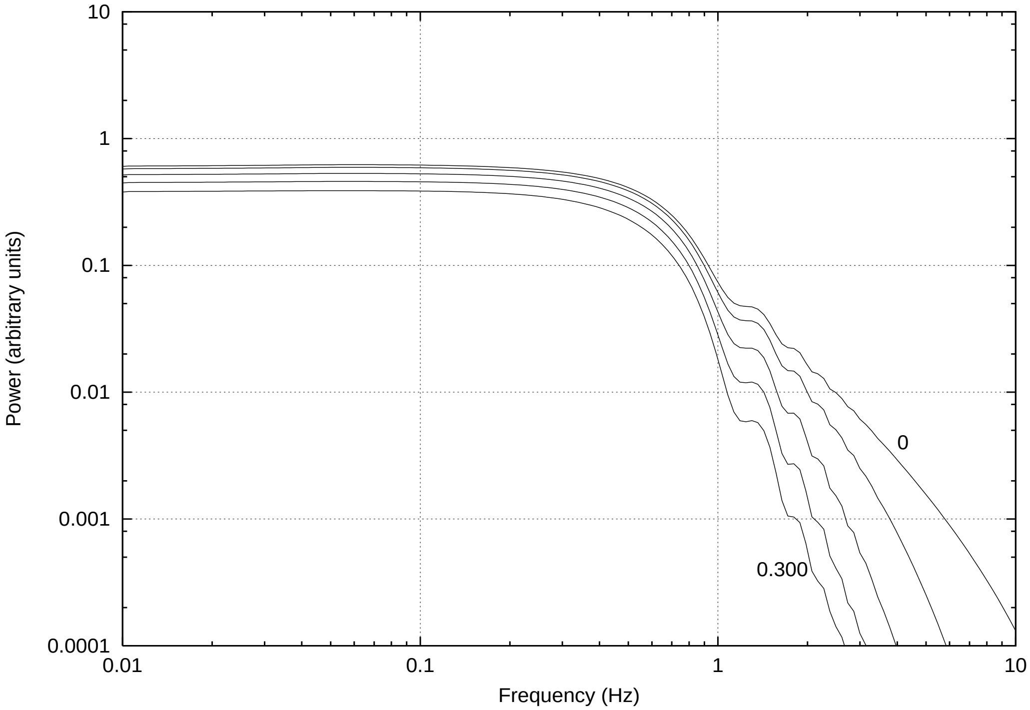

Figure 2.12: **Effect of variation in $\theta_\circ$ on the power spectrum** – Power spectra for $\theta_\circ$ values ranging from $0''$ to $0.300''$, in steps of $0.075''$, are plotted. The spectra with $\theta_\circ$ of $0''$ and $0.300''$ have been labelled. The spectra have been generated using $V = 400\ km\ sec^{-1}, AR = 1.0$, $\alpha = 3.0$ and $q_i = 3.3\ km^{-1}$ at 30° ϵ.

for a symmetric Gaussian *Brightness* distribution. The $\theta_\circ$ therefore acts like a *low pass* filter, attenuating the part of the spectrum at $q > 1/z\theta_\circ$. Figure 2.12 shows the power spectra for a $\theta_\circ$ range of $0''$ – $0.300''$, in steps of $0.075''$, while keeping all the other parameters of the Solar Wind model constant. As expected, more extended sources show a steeper fall in the power at high ν part of the spectrum. Larger sources tend to have smaller values of m because the area under the power spectrum decreases with increase in $\theta_\circ$.

If the source Brightness distribution is not represented well by a symmetric Gaussian, the source visibility function used above is not valid. This can lead to systematic errors in estimation of size of the scintillating component of the source using the symmetric Gaussian visibility function. For instance, the $\theta_\circ$ estimated for an elongated source shall depend upon the angular extent of the source projected along the direction of motion of Solar Wind. As the angular size projected along the Solar Wind velocity changes with elongation of the source, the estimated $\theta_\circ$ undergoes systematic variations. In order to uses sources with more complicated structure, like a multicomponent source, more detailed information of the source structure is required so that an appropriate visibility function can be used. However, no serious attempts of modelling the IPS data using a detailed model for the structure of the source have been made.

Effect of axial ratio variations

The irregularity pattern in the Solar Wind has been known to be anisotropic since early 1970s when it was discovered that irregularities tend to be elongated along the direction of the interplanetary magnetic field lines (Blessing and Dennison, 1972). The spatial structure of the density irregularity can then be represented by an ellipse. Axial ratio, AR, is defined as the ratio of the length scale along the direction of velocity of the Solar Wind to the direction perpendicular to it. An $AR > 1$, therefore, corresponds to an irregularity pattern elongated along the direction of velocity of Solar Wind, $AR < 1$ to pattern elongated perpendicular to the direction of velocity of the Solar Wind and an $AR = 1$ to an isotropic irregularity pattern. The effect of AR has been included in the power spectrum of intensity fluctuations by using the following form for $\Phi_{\Delta n_e}(\mathbf{q})$:

$$\Phi_{\Delta n_e}(\mathbf{q}) \propto \left(q_x^2 + \frac{q_y^2}{AR^2}\right)^{-\alpha/2} \tag{2.54}$$

Figure 2.13 shows power spectra with AR ranging from 0.5 to 1.5. Incorporating this in the equation 2.52 leads to :

$$\begin{aligned} P(\nu) \;=\; & (2\pi r_e\lambda)^2 \int \frac{C_n^2(z)dz}{|V_\perp(z)|} \int dq_y \sin^2\left(\frac{q^2\lambda z}{4\pi}\right) |V(q,z,\theta_\circ)|^2 \\ & \left(q_x^2 + \frac{q_y^2}{AR^2}\right)^{-\alpha/2} exp\left(-\frac{q^2}{q_i^2}\right) R^{-\beta} \end{aligned} \tag{2.55}$$

The effect of AR is seen most prominently in the low q_x (low ν, equation 2.24) part of the power spectrum. An increase in AR results in an increasingly rounded Fresnel knee and smoothed oscillations.

There is observational evidence for the Axial Ratio to be close to unity by the time the Solar Wind traverses out to 0.3 AU. Coles and Kaufman (Coles and Kaufman, 1978) obtained a reliable upper limit of 1.3 on the mean AR in the weak scattering regime using multi-station IPS observations. More recent investigations by Yamauchi et. al (Yamauchi et al., 1996; Yamauchi et al., 1998) arrive at the conclusion that the AR of the Solar Wind settles down to a value close to unity by $\epsilon = 15°$ (60 $R_\odot$) both in the ecliptic and at high latitudes. Previous workers have used values of AR varying between $\sim$ 1.0 and 1.3 (Manoharan, 1991; Gothoskar, 1994), but usually close to unity. In this work we use a value of unity for AR.

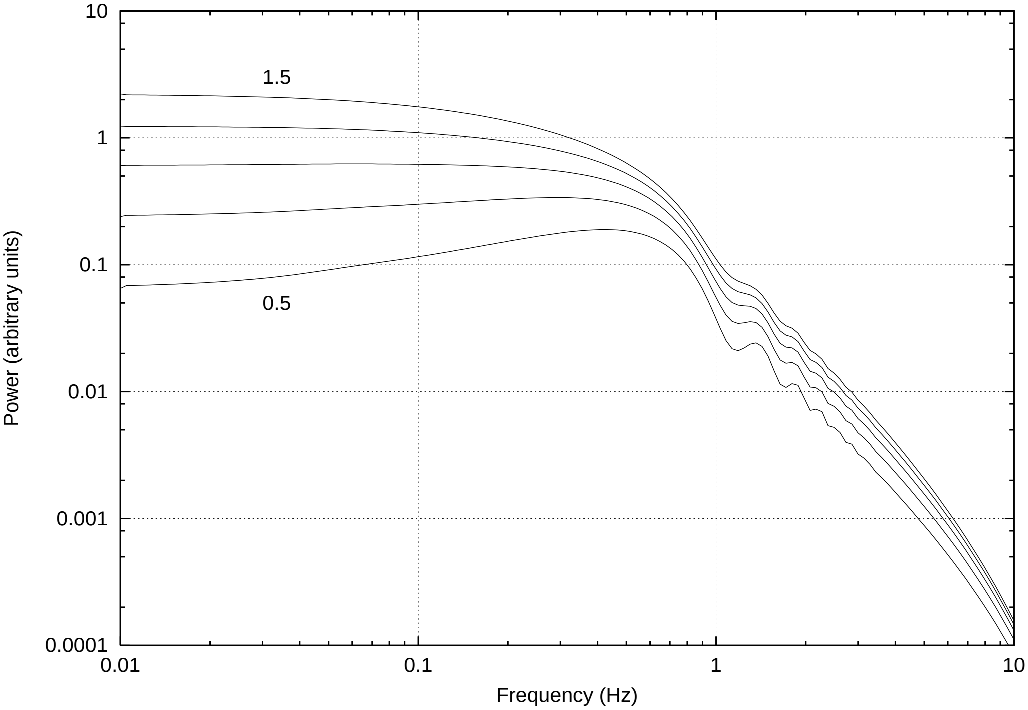

Figure 2.13: **Effect of variation in AR on the power spectrum** – The figure shows power spectra for AR ranging from 0.5 to 1.5, in steps of 0.25. The spectra with AR of 0.5 and 1.5 have been labelled. The spectra have been generated using $V = 400\ km\ sec^{-1}$, $\alpha = 3.0$ and $q_i = 3.3\ km^{-1}$ for a $\theta_\circ$ of $0''$ at $30^\circ\ \epsilon$.

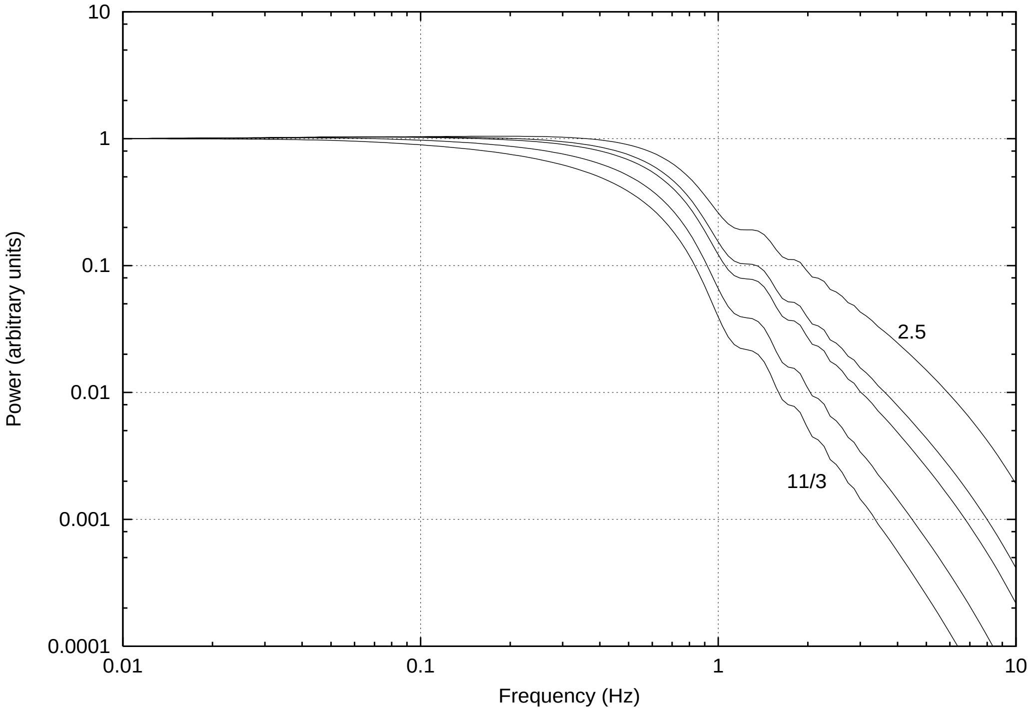

Figure 2.14: **Effect of variation in α on the power spectrum** – The figure shows power spectra for α of $2.5, 2.8, 3.0, 3.2$ and $11/3$. The spectra with α of 2.5 and 11/3 have been labelled. The spectra have been generated using $V = 400\ km\ sec^{-1}$, $AR = 1.0$ and $q_i = 3.3\ km^{-1}$ for a $\theta_\circ$ of $0''$ at $30°\ \epsilon$.

Effect of spectral index variations

The spectral index of electron density fluctuations, α, affects the slope of the power spectrum beyond the first Fresnel maxima. The slope becomes steeper with increase in α leading to a reduction in the strength of scintillation. For $\nu > \nu_f$, the power spectrum is a straight line on a *log–log* plot with a slope of $(-\alpha + 1)$, in absence of any other effect. The increase in the slope by unity is due to the strip integration performed over the coordinate q_y. Power spectra with α values ranging from 2.5 to 11/3 are shown in Figure 2.14. The position of the first Fresnel maxima is however not effected by change in α. IPS provides information about the power law index of spectrum of electron density fluctuations in the ν range of ~ 0.01 to $5.0\ Hz$. This corresponds to a spatial wavenumber range of $\sim 10^{-7}$ to $8 \times 10^{-5}\ m^{-1}$ for a Solar Wind velocity of $400\ km\ sec^{-1}$.

The power laws with different values of α are normalised to have the same power at $q = 1$. As IPS investigates a range of q between $\sim 10^{-8}$ and $10^{-4}\ m^{-1}$, a small change in α leads to a very large change in C_n^2, due to the *lever arm* kind of effect. The spectra shown in the Figure 2.14 have been normalised to have the same numerical values at $0.01\ Hz$. These spectra are, therefore, only pictorial representations of the change in the shape with variation in α.

Most of the work in the pre-1970 period was done assuming a Gaussian spectrum of electron density while a power law form for the spectrum has been favoured after that. Inrtiligator and Wolfe (Intriligator and Wolfe, 1970) used spacecraft observations to estimate the power spectrum of proton density fluctuations. Lovelace et al. (Lovelace et al., 1970) used IPS observations to investigate the same. Cronyn (Cronyn, 1972) pointed out that the observations mentioned above were consistent with a single continuous power law with a correlation length of 10^6 km or larger. Unti et al. (Unti et al., 1973) measured an average α of 2.6 in the range 4.8×10^{-3} to 13.3 Hz, using OGO-5 data, and placed Cronyn's suggestion on a firmer footing. Woo and Armstrong (Woo and Armstrong, 1979) report an α of 3.0 ± 0.1 in the frequency range 0.1 to 10.0 Hz between 2.2 and 31 $R_\odot$ using Viking, Helios and Pioneer spacecraft data. Celnikier et al. (Celnikier et al., 1983) presented evidence for a break in the power law spectrum of electron density fluctuations at 6.0×10^{-2} Hz with an α of 2.7 before the break and of 1.9 after the break. Their conclusions were based on ISEE propagation experiment and were free from systematics though the duration of observations was only 3 hours.

Manoharan et al. found a correlation between the velocity of the Solar Wind and its α (Manoharan et al., 1994). Near the Solar Minima, the phase of the solar cycle of interest to us, they find α to increase from ~ 2.7 to ~ 3.8 as the velocity increases from 250 to 550 $km\ sec^{-1}$, beyond which α remained practically a constant. This data also yielded a correlation between α and $\theta_\odot$ of the P-point of the *l.o.s.*, a consequence of the latitudinal velocity profile of the Solar Wind. They found α to be almost a constant at ~ 3.0 within $\pm 20^\circ$ $\theta_\odot$ beyond which it increased to ~ 4.0 by $\pm 70^\circ$ $\theta_\odot$. They report absence of any *noticeable* dependence of α on elongation which is in agreement with earlier investigations (Coles and Harmon, 1978; Woo and Armstrong, 1979; Yakovlev et al., 1980). Yamauchi et al. (Yamauchi et al., 1998) also find an α close to 3.0 for the equatorial Solar Wind in the 40 $R_\odot$ to 80 $R_\odot$ region investigated by them.

Thus there is insufficient agreement in the observations on the value of α and different datasets and techniques have yielded different results. We have chosen to use a value of 3.0 for α.

Effect of inner scale variations

As q_i and $\theta_\circ$ have similar functional form, they have a similar effect on the power spectrum of intensity fluctuations. The effects of the two on the power spectra can be studied if the $\theta_\circ$ is known *a priori*. While the source size filter has a z dependence (equation 2.53), the q_i effect is independent of it. This property can be exploited to investigate the effect of q_i under circumstances when $\theta_\circ$ is not known.

The effect of q_i becomes distinguishable from that of $\theta_\circ$ when the power spectrum is dominated by the contribution to *l.o.s.* from small z, where the source size filter is not as effective. Observations of sources at large elongations are, therefore, useful in studying q_i without contamination from the $\theta_\circ$ effects. When the source size is large ($> 100mas$), the source size filter tends to dominate the power spectrum and the effects of q_i become difficult to discern in the IPS spectra.

A linearly increasing q_i at distances $> 50\ R_\odot$ has been reported by previous workers (Yakovlev et al., 1980; Scott et al., 1983; Coles and Harmon, 1989). Manoharan used the following form for inner scale in the range $15^\circ < \epsilon < 30^\circ$ ($60 < R_\odot < 120$) (Manoharan, 1991) :

$$s_i \approx \left(\frac{R}{R_0}\right)^{1.0\pm0.1} km \tag{2.56}$$

where $s_i = 3/q_i$ and q_i is the spatial wavenumber at which the spectrum cuts off. The linear increase in s_i begins to flatten by $\sim 100\ R_\odot$ (Manoharan, 1991). Yamauchi et al. also find similar trends in their more recent studies in the range $5R_\odot < R < 76R_\odot$ (Yamauchi et al., 1996; Yamauchi et al., 1998).

In order to estimate the significance of changes in q_i in the elongation range of interest to us ($20^\circ \leq \epsilon \leq 80^\circ$ or $80R_\odot < R < 320R_\odot$), we used a Solar Wind model with no q_i to model the data and looked for variations in the $\theta_\circ$ with elongation. No significant trend was seen for $\theta_\circ$ to vary with elongation. We conclude that the variation of q_i is, therefore, not important in the range of elongations to which our observations are confined ($20^\circ \leq \epsilon \leq 80^\circ$) and use a q_i close to 0 in this work since source size effects are dominant.

Random velocities

The turbulent interplanetary medium is expected to have a complex velocity field. The turbulent motion in the Solar Wind adds to the bulk motion of the Solar Wind giving rise to a dispersion in the velocity. In addition, structure in the Solar Wind may lead to substantially different velocities along different parts of the *l.o.s.*. Multi-station IPS observations by previous workers have shown that the random velocities decrease with distance from the Sun and become insignificant by an elongation of about 10° (40 $R_\odot$) (Vitkevich and Vlasov, 1970; Ekers and Little, 1971; Armstrong and Woo, 1981; Scott et al., 1983). The present study assumes the random velocities to be negligible as we limit ourselves to observations at $\epsilon \geq 20^\circ$.

Chapter 3

Motivation for Tomographic Analysis

3.1 Introduction

Many imaging instruments routinely observe the solar corona out to distances of few tens of $R_\odot$ and many satellites provide *in-situ* sampling of the Solar Wind plasma close to 1 AU. In order to be able to relate the studies close to the Sun to the measurements at 1 AU, it is important to study the Solar Wind in the region of the heliosphere from 0.1–1.0 AU. IPS is the most useful remote sensing technique which can be used to study the Solar Wind in this region. While IPS data is useful for studying the three dimensional structure of the Solar Wind, such studies have been few in number. This is because of the considerable inherent complexity of the problem and the fact that it is observationally very demanding to obtain data-sets suitable for such a task. In this chapter we discuss the uniform Solar Wind models commonly in use and point out their drawbacks. We argue that IPS data is well suited for a tomographic reconstruction of the inner heliosphere and discuss the feasibility of such a study.

3.2 Modelling Solar Wind using IPS observations

Detailed modelling of the observed power spectrum requires knowledge of the properties of Solar Wind all along the *l.o.s.*. This information is usually not available and deriving it from Earth based observation is often the primary motive for IPS studies. As has been discussed in Section 2.5.2, the power spectrum observed towards a *l.o.s.* is a sum of the power spectra due to the individual thin screens along the *l.o.s.*. The power spectra due to individual thin screens depend upon the physical properties of the Solar Wind which constitutes the thin screen (Section 2.5.1).

In principle, the physical properties of a given thin screens are independent of the physical properties of other thin screens. Thus the number of the free parameters involved in the computing power spectrum observed towards a $l.o.s.$ can be quite large. The constraints available, from the point of view of modelling $P(\nu)$ in terms of thin screen spectra, usually come from the power spectrum observed itself and are much smaller in number. It is, therefore, necessary to reduce drastically the number of free parameters in the model by introducing some reasonable assumptions. Traditionally, this has been achieved in one of the following two ways.

3.2.1 Featureless Solar Wind models

In these models the Solar Wind is assumed to be an isotropic and steady flow of magnetised plasma devoid of any structure. These models substantially reduce the number of free parameters as the physical properties of individual thin screens no longer remain independent quantities. In fact, a single number can specify a given physical parameter of the Solar Wind for all the thin screens. This leads to the number of free parameters being reduced to the number of physical parameter of the Solar Wind which one wishes to model.

Lack of structure and the consequent uniformity of velocity imply that there is no interaction between the Solar Wind originating from different parts of the solar surface. The acceleration of the Solar Wind to the velocities observed in the interplanetary medium and by the Earth orbiting satellites is believed to be complete by the time it traverses out to $0.1AU$ (Grall et al., 1996). The Solar Wind plasma, originating from a given part of the solar surface, *free-streams* along Archimedean spirals with a constant and purely radial velocity at all points on the trajectory (Figure 1.3) beyond this distance. The structure-less Solar Wind, therefore, traverses the region of the heliosphere sampled by IPS ($\sim 0.35 - 1AU$ at $327MHz$) with no change in it's velocity. In these models, $V_\perp(z)$ can be computed from the relative locations of the Sun, the Earth and the orientation of the $l.o.s.$ (Figure 2.1). It has a well defined maxima at the point on the $l.o.s.$ closest to the Sun, referred to as the P-point in the literature, and is a function of the elongation. $V_\perp(z)$ is plotted for a few elongations in Figure 3.1. From Figure 3.1 and equation 2.24 it follows that power spectra due to the thin screens near the P-point have the highest frequency content. Thus the high frequency part of the observed power spectrum receives contributions dominantly from the P-point.

The constant radial velocity of Solar Wind requires n_e to drop as squared of the distance from the Sun in order to ensure conservation of mass. The strength of scintillations, quantified by C_n^2, is proportional to δn_e^2. Assuming $\delta n_e \propto n_e$, C_n^2 drops as R^{-4}, where R is the heliocentric distance. The contribution of each of the thin screens along the $l.o.s.$ to the observed power spectrum can thus be thought of as

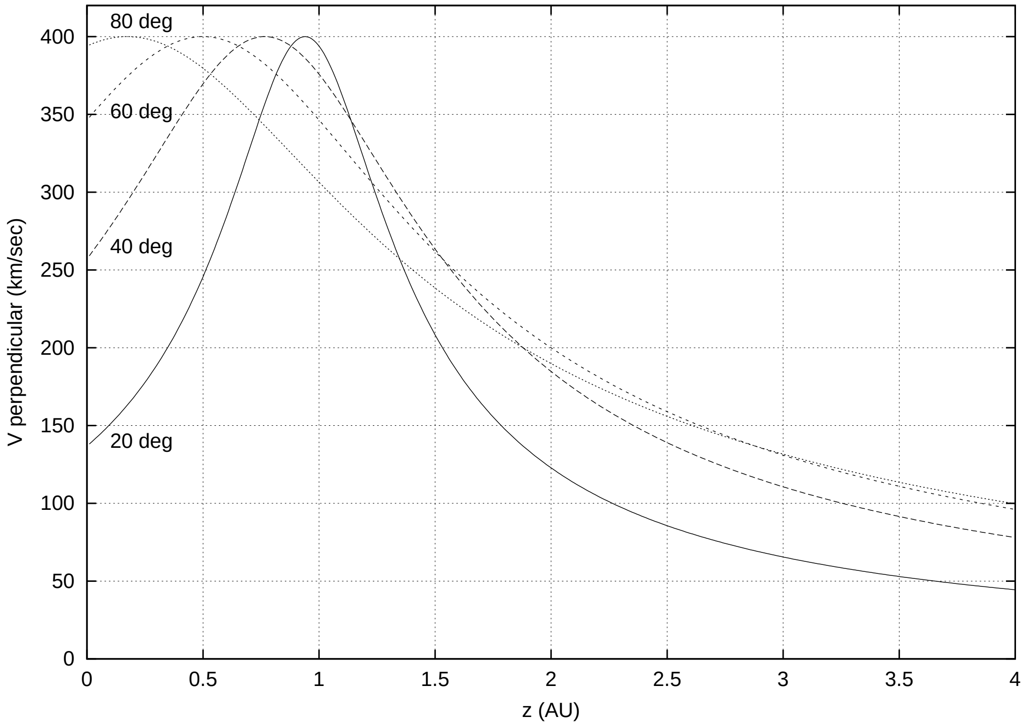

Figure 3.1: **The component of velocity of the Solar Wind $\perp$ to the *l.o.s.*** – This figure plots $V_{\perp}(z)$ along the length of the $l.o.s.$. Plots for $\epsilon = 20°, 40°, 60°$ and $80°$ are presented. All the curves have a well defined peak at the z corresponding to the P-point $(z = \cos(\epsilon))$. The width of the peak in $V_{\perp}(z)$ increases considerably with elongation. A feature-less Solar Wind model with a purely radial velocity of $400\ km\ s^{-1}$ was used to generate these curves.

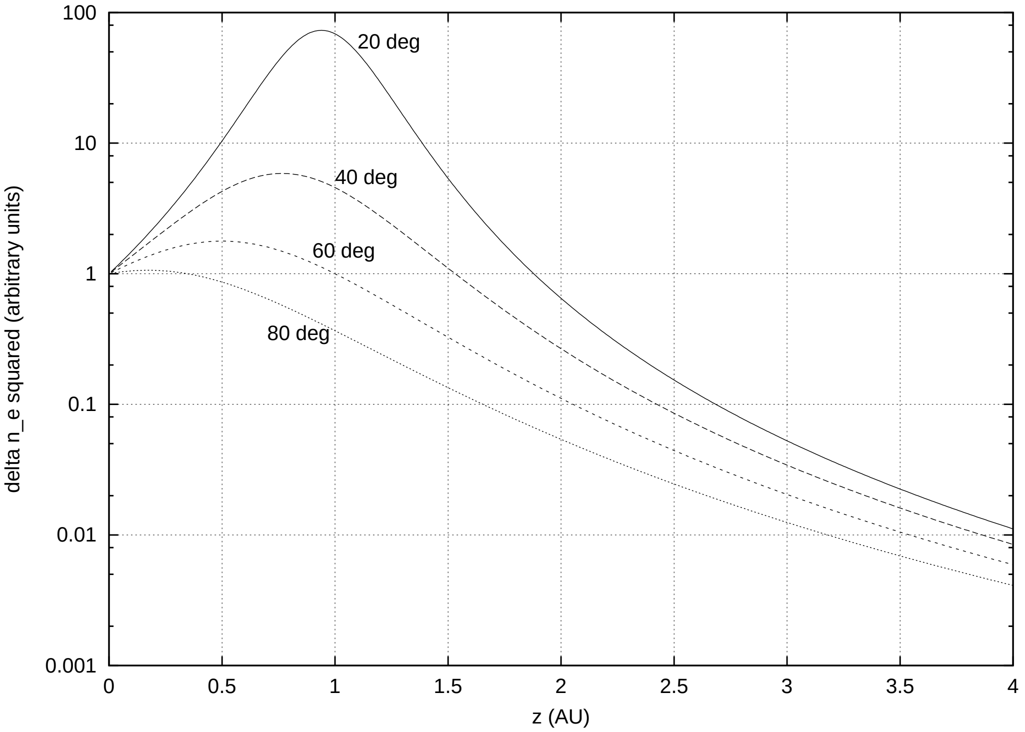

Figure 3.2: **Variation of $(\delta n_e^2)^2$ along the *l.o.s.*** – This figure shows $(\delta n_e^2)^2$ along the *l.o.s.*. Plots for $\epsilon = 20°, 40°, 60°$ and $80°$ are presented. Note the steep fall in $(\delta n_e^2)^2$ and the broadening of the maxima with increase in elongation. A featureless Solar Wind model with R^{-2} fall off for δn_e was used to generate these curves.

being weighted by a factor which varies as R^{-4}. Figure 3.2 clearly shows that most of the contribution to the power spectrum of intensity fluctuations comes from the part of the *l.o.s.* closest to the Sun. At elongations greater than 60°, the maximum contribution to the observed IPS moves farther away from P-point because of the *Fresnel filter* term (2.36) in the equation 2.35.

The other Solar Wind parameters, namely *Axial Ratio*, α and q_i are usually not varied in these models from one thin screen to the next and are set to appropriate values.

These models are most often used to describe the ambient or the quiescent part of the Solar Wind(Section 1.6. They have also been used for studying the departure of the Solar Wind from the expected ambient behaviour by comparing the observed properties of the Solar Wind to the expectations from these models.

3.2.2 The 'P' point approximation

As mentioned earlier, a small part of the *l.o.s.* contributes significantly to the power spectrum. The P-point approximation constitutes the extreme case of this approximation where the Solar Wind at the P-point of the *l.o.s.* is assumed to dominate the power spectrum of intensity fluctuations (Figure 2.1). Contributions to the power spectrum from all other parts of the *l.o.s.* are considered negligible in comparison. This approximation finds justification in the steep fall off of δn_e as a function of the heliocentric distance, R, and the consequent maxima of C_n^2 at the P-point (Section 3.2.1 and Figure 3.2). It becomes less and less valid with increase in elongation as the maxima of δn_e broadens considerably with elongation. Also, the contribution to the power spectrum from parts of the *l.o.s.* close to the Earth gets reduced because of the *Fresnel filter* term in equation 2.35, hence the point of dominant contribution to the power spectrum shifts slightly away from the P-point.

The P-point approximation is often used to associate the properties of the Solar Wind seen in the interplanetary medium to the sites of their origin on the solar surface. This is achieved by tracing back the path of the Solar Wind from the P-point to the solar surface (or some fiducial spherical surface at some fixed radial distance from the Sun) along the Archimedean spiral defined by the velocity of the Solar Wind. The P-point approximation is better suited for studying the transients like Interplanetary Disturbances (IPDs) or investigating the behaviour of the disturbed Solar Wind, where the featureless Solar Wind models are poorly suited.

3.3 Earlier attempts

Though most of the IPS studies of the Solar Wind have made use of uniform Solar Wind models, they have none-the-less been used to study the structures in the Solar Wind. In spite of the apparent inconsistency in the approach, it had been adopted because of lack of better options as IPS is the only remote sensing tool available to invesitgate the interplanetary medium in a large part of the inner heliosphere. There have been numerous attempts to study the Solar Wind using the assumptions discussed in the Section 3.2. Some of these are discussed below. Only a representative few references have been included here and they are meant to give a flavour of the nature of the work done, no attempts have been made to provide a complete set of references.

Velocity estimates

IPS has been used to estimate the velocity of the Solar Wind. The early attempts were by Armstrong and Coles (Armstrong and Coles, 1972) at 74 MHz and Kakinuma et. al. (Kakinuma et al., 1973) at 69.3 MHz in early 1970s and used the multi-station observations. Bourgois et. al. (Bourgois et al., 1985) used the EISCAT facilities to estimate the Solar Wind velocity at 933.5 MHz in 1985 which had significantly longer baselines and hence were able to provide more accurate determination of properties of the drifting interference pattern. Single station estimates of Solar Wind velocity were first reported by Manoharan and Ananthakrishnan in 1990, where they estimate the velocity of the Solar Wind by fitting the observed power spectra with uniform Solar Wind models (Manoharan and Ananthakrishnan, 1990). Both single station and multi station velocity estimates have been in use ever since and have proved their usefulness over the years.

‘g’ maps

There have been attempts to map properties of Solar Wind using the P-point approximation, by the Cambridge group (Gapper et al., 1982) since early 1980s. These attempts concerned themselves with mainly looking for deviations from the *normal* Solar Wind conditions and used a parameter, g, to quantify the departure from the normal Solar Wind conditions. g was defined as :

$$g = \frac{m_\epsilon}{\langle g(\epsilon)\rangle} \tag{3.1}$$

where m_ϵ was the scintillation index observed on particular source at an elongation ϵ and $\langle m(\epsilon)\rangle$ the average of a large number of observations of scintillation indices of the same source at the same elongation. A survey was undertaken by Purvis et. al. using the Cambridge 81.5 MHz array, to catalogue the sources suitable for IPS observations in an attempt to improve the sampling of the heliosphere by increasing the number of sources available (Purvis et al., 1987). A large number of sources were observed and the g maps were examined for presence of large scale correlated features. These sources were observed everyday at transit and a g map was obtained daily. These g maps were used to track Interplanetary Disturbances (Tappin et al., 1983) and Co-rotating Streams (Tappin et al., 1984) in the Interplanetary Medium. They were also considered as a tool for forecasting geomagnetic activity, but met with rather limited success (Leinbach et al., 1994).

There have been attempts at real time forecasting the Interplanetary Disturbances on the basis of solar activity. IPS observations were used to test the predictions and also obtain more information in order to make a well constrained model for the event (Manoharan et al., 1995).

Turbulence parameters

IPS has been a very useful technique to study the turbulence parameters of the Solar Wind over a large range of heliocentric distances and latitudes. Various studies which investigate the Solar Wind parameters like α, *Axial Ratio* and q_i and their radial evolution have been undertaken both for the ambient Solar Wind and the IPDs (Coles and Harmon, 1978; Yamauchi et al., 1996; Yamauchi et al., 1998, 1999; Manoharan et al., 2000).

Solar cycle dependence of Solar Wind properties

IPS data has also been used to study the changes in the properties of the ambient Solar Wind with the progression of the solar activity cycle. A review of the subject is provided by Kojima and Kakinuma (Kojima and Kakinuma, 1990). The dependence of Interplanetary Disturbances on the solar activity cycle has also been investigated using IPS data (Manoharan, 1996).

Studies of transients

IPS observations have routinely been used to study the transient phenomena observed in the Interplanetary Medium (Ananthakrishnan et al., 1999). Another use to which IPS data has been put is to try to associate the Interplanetary Disturbances with the event and structures seen on the Sun (Manoharan, 1997b). There have also been attempts at comparatively detailed modelling of the IPDs using IPS data (Gothoskar and Rao, 1999).

Two component model for Solar Wind

There have been attempts to model the Solar Wind as a *two fluid* system (Grall et al., 1995; Rao et al., 1995). This approach used the cross correlation function of the time series of intensity fluctuations observed at two (or more) different observing stations to estimate the velocity of the Solar Wind and demonstrated convincingly the presence of two velocity streams. This approximation is one step better than the featureless models and yielded better fits to the observed data. Additional inputs from white light synoptic observations were also used to constrain the free parameters of the model which are more than twice in number than those required by the featureless Solar Wind models.

3.4 Deviations from uniform Solar Wind models

The presence of considerable structure in the Solar Wind has been well known since the early studies of the Solar Wind. The assumptions of uniform Solar Wind are no longer valid under such situations. A few instances where this happens are discussed below.

3.4.1 Latitudinal structure of the Solar Wind

It is now well established that the Solar Wind, at least during the epochs close to solar minima, has a well defined latitudinal structure (Section 1.6). The velocity of the Solar Wind in the equatorial regions is about $\sim 400\ km\ s^{-1}$. It increases to about $\sim 700\ km\ s^{-1}$ by mid-latitude regions and continues to remain at similar values right up-to the poles. There have also been some claims of there being a north-south asymmetry in the velocity profiles. All $l.o.s.$s to sources away from the ecliptic plane sample the Solar Wind arising from both the equatorial regions and regions outside the equatorial belt. Hence the assumption of a featureless Solar Wind is not well suited for non-ecliptic sources.

3.4.2 Radial evolution of Solar Wind

The ambient Solar Wind is also endowed with considerable structure, referred to as stream structure. This has been discussed in some detail in Section 1.6. The non-uniform velocity of the Solar Wind arising from different parts of the Sun cause the slower Solar Wind and the faster moving plasma behind it to interact. This interaction develops as the Solar Wind traverses radially outwards and leads to a non-uniform radial profile of physical properties of the Solar Wind. In particular, Co-rotating Interaction Regions (CIRs) are formed when the fast Solar Wind, usually arising from coronal holes, pushes against the slower moving Solar Wind ahead of it. They have an accumulation of matter at their leading edge and leave an under dense region in their wake. CIRs undergo gradual steepening in their density and velocity profiles and often develop into shocks beyond $\sim 2AU$ and are discussed in a little more detail in Section 1.6. Around the Solar minima they often form stable structures which may live for a few solar rotations. As this leads to presence of structures evolving in both, space and time, in the Solar Wind, the assumptions made in Section 3.2 are violated.

3.4.3 Solar activity and IPDs

The Sun is the site of many interesting, complex and violent phenomenon. Some of these phenomenon give rise to mass ejections which travel in the Interplanetary Medium to a few *AU* before they merge in the ambient Solar Wind. The physical properties of the Solar Wind which constitutes the IPDs are significantly different from those of the ambient Solar Wind. IPS power spectrum is sensitive to some of these physical properties like velocity, C_n^2, α and *Axial Ratio*. Presence of IPDs also renders the assumptions and approximations described in Section 3.2 invalid.

Another shortcoming of the P-point approximation which should be highlighted is that it is of limited use for locating the sites of the Solar Wind sampled by a *l.o.s.*. This ambiguity arises because the angle subtended by the part of the *l.o.s.* within the half-width of the *l.o.s.* weight function on the Sun is substantial. This effect is practically independent of the ϵ because the weight function has a broader maxima at higher values of ϵ, and hence larger half-widths, which subtend similar angles at the Sun. The site location often have ambiguities of as much as 45°.

3.5 Tomography

In view of above discussion, it is clear that a study of the Solar Wind must take the inherent 3D structures in the Solar Wind into account. Tomography, which, deals with the subject of reconstructing a 3D model of an object by using a set of 2D projections of the object also has similar objectives. The most familiar examples of tomography come from medical imaging where it has proven to be a very useful non-invasive investigation tool. We explore the relevance and utility of tomographic reconstruction methods for obtaining 3D models for the Solar Wind.

The basic idea behind tomography or a tomographic reconstruction is fairly simple. Consider an optically thin source of emission occupying a finite volume. Each pixel in an image of such a source represents the *l.o.s.* integration of the volumetric emissivity of the source integrated over the bandwidth of observation. By obtaining images of the emission source from several different observing angles, the underlying 3D structure of the emission can be deduced. The optically thin source can be replaced by an optically thin absorbing medium, in which case the image is, in some sense, a shadow. The basic requirement is that of an observable which retains additive information of the entire path traversed in the medium. Emissivity and optical depth both fulfil this requirement. Much of the following discussion is based on a very readable article by Swindell and Barrett (Swindell and Barrett, 1977).

3.5.1 Formulation of the problem

The problem of tomographic reconstruction for the simple case of a monochromatic beam passing through a 2D optically thin absorbing medium can be formulated as follows. The attenuation suffered by a monochromatic pencil beam of incident intensity, I_0, on passing through a uniform absorbing medium is given by the expression :

$$I = I_0 \exp\left(-\mu x\right) \tag{3.2}$$

where μ is the linear absorption coefficient of the medium and x is the path length traversed in the medium. For a inhomogeneous medium, the expression takes the form :

$$I_\phi(x') = I_0 \exp\left\{ - \int_{Source}^{Detector} \mu(x,y)\ dy' \right\} \tag{3.3}$$

where ϕ the orientation of the projection with respect to the reference coordinate system shown in figure 3.3. In order to linearise the formulation, the above equation is expressed as :

$$f_\phi(x') \ = \ -\ln(I_\phi/I_0) \ = \ \int_{Source}^{Detector} \mu(x,y)\ dy' \tag{3.4}$$

The goal is to obtain an estimate of $\mu(x,y)$ from a sufficiently large set of projection data, $f_\phi(x')$s.

3.5.2 Reconstruction

The mathematical basis for performing a tomographic reconstruction has been known at least since 1917 (Radon, 1917). The most crucial ingredient of the reconstruction is the *central slice theorem*, also referred to as the *projection-slice theorem.* This theorem states that the 1D Fourier transform of a 1D projection of a 2D object is mathematically identical to a slice through the 2D Fourier transform of the object itself. This result can be proved as follows:

Let the object distribution be denoted by $\mu(\vec{r})$, where $\vec{r} = (x,y)$. Consider a projection along the y' axis given by :

$$f_\phi(x') = \int_{-\infty}^{\infty} \mu(\vec{r})\ dy' \tag{3.5}$$

where (x',y') axes are rotated by an angle ϕ with respect to the fixed (x,y) coordinates (Figure 3.3). The 1D Fourier transform of the projection is :

$$F_1\{f_\phi(x')\} = \int_{-\infty}^{\infty} f_\phi(x')\ \exp(i2\pi\ k'x')\ dx' \tag{3.6}$$

where k' is the spatial frequency variable conjugate to x'. Substituting from equation 3.5, we get :

$$F_1\{f_\phi(x')\} = \int_{-\infty}^{\infty} dx' \int_{-\infty}^{\infty} \mu(\vec{r})\ \exp(i2\pi\ k'x')\ dy' \tag{3.7}$$

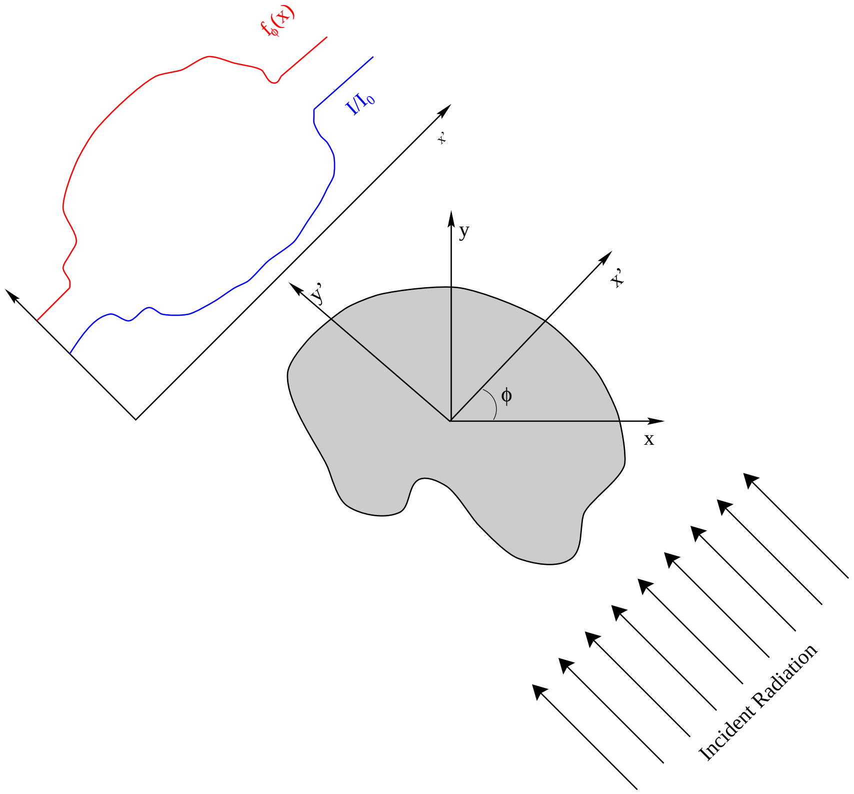

Figure 3.3: **Obtaining projection data for a tomographic reconstruction** – A 2D optically thin medium is fixed with respect to the (x, y) frame. The direction of the illuminating beam is specified by the y' axis and takes various values as it rotates. The projection data is gathered along the x' axis for each angle of rotation, ϕ. The projection function, $f_\phi(x')$, and the fraction of emergent intensity, I/I_0, are plotted schematically.

which can be expressed as :

$$F_1\{f_\phi(x')\} = \left[\int_{-\infty}^{\infty} dx' \int_{-\infty}^{\infty} \mu(\vec{r}) \ \exp\{i2\pi \ (k'x' + l'y')\} \ dy'\right]_{l'=0} \tag{3.8}$$

where l' is the spatial frequency variable conjugate to y'. The equation just obtained is the 2D Fourier transform, $F_2(\mu)$, evaluated along the line $l' = 0$, a slice in the 2D frequency plane. This completes the proof of the theorem.

As k' and l' are always conjugate to x' and y' respectively, the line $l' = 0$ rotates as the projection angle is changed. A set of projections over a 180° range in ϕ is sufficient to determine $F_2(\mu)$ at all points. The 2D Fourier transform of the object readily yields the object itself by an inverse Fourier transform.

The Central Slice theorem can be generalised to state that the N dimensional Fourier transform of a N dimensional projection of a $(N+1)$ dimensional object is mathematically identical to a slice through the N dimensional Fourier transform of the object itself. Arguments similar to those presented above, allow for reconstruction of a 3D object from a set of its 2D projections.

The spatial resolution of the reconstructed image is of the order of the resolution of the individual observations. If the resolution of all the projections used are not the same, the reconstructed image is not expected to have to resolution better than the lowest resolution observation. The reconstruction process becomes better constrained as the number of observed projections increases. The fidelity of the reconstruction increases till a limit, due to Nyquist sampling, is reached. With Nyquist sampling the reconstruction process becomes a formal mathematical inversion and exact reconstruction of the original source can be achieved.

The detector noise in the projection observed is often a significant source of error in the reconstruction process. Presence of noise leads to inconsistencies in the data, i.e., there exists no solution which satisfies all the constraints imposed by the projection data. In practice, therefore, the reconstruction from the data is always some *best-fit* solution, $\hat{\mu}(x, y)$, because of finite sampling and the inherent noise in the data.

Apart from the Fourier transforms based algorithms, some other image reconstruction algorithms have also been used. Among the popular ones are *back projection* and *algebraic reconstruction technique* (ART) and their variants.

3.5.3 Applications

The first practical applications of tomography began to appear in early 1960s (Cormack, 1964) and were in the field of medical imaging. These applications used X-rays to render visible thin slices through any section of a living human body. The reconstructions obtained had achieved a phenomenal resolution of 2 mm and noise levels corresponding to a 0.5% change in optical depth by late 1970s. The applications now span a wide range ranging from Astronomy, non-destructive testing of materials and mapping of temperature field in a gas using the associated change in the refractive index of the gas. A search in NASA's Astrophysics Data System Abstract Service using tomography as a key word and with a time range from 1995 to 1999 returned a list with 141 entries. The titles of a small selection of references from the list are mentioned below to illustrate the variety of subjects dealt with: Neutrino absorption tomography of Earth's interior (Jain et al., 1999), Explosion-seismic tomography of a magmatic body beneath Mount Etna (Laigle and Hirn, 1999), Application of Computer Tomography (CT) for Search of Life in Extreme Environments (Tsapin et al., 1999), Coronal structure of the Whole Sun Month: A tomographic reconstruction (Zidowitz, 1999), Ionospheric calibration of radar altimeters using GPS tomography (Ruffini et al., 1998), Next generation tomography: Accretion Disks as they "really" are (Vrielmann and et al., 1998), Tomographic Method for Meteor-Flux Determination from Radar Observations (Belkovich et al., 1997) and 21 Centimetre Tomography of the Intergalactic Medium at High Redshift (Madau et al., 1997).

There have been attempts to apply the technique of tomography to the solar corona. The first attempt to explore the feasibility of such an exercise, known to us, was in 1994 (Davila, 1994). The availability of good quality data from satellite missions like SOHO and Earth based coronographs has kindled the interest in exploring this technique (Zidowitz, 1999; Panasyuk, 1999).

3.6 Tomography and IPS

The primary observable of IPS, the power spectrum of intensity fluctuations, is a measure of the weighted sum of the properties of the Solar Wind along the $l.o.s.$ (equation 2.42). As the power spectrum carries additive information of the entire path length traversed in the Interplanetary Medium, it satisfies one of the necessary conditions for being useful for tomographic reconstruction. In addition, tomography requires a set of projections of the medium along different directions or planes. A projection, by definition, involves an integration along one of the axes and hence has one less dimension than the projected object. A 3D object is projected on 2D planes and a 2D object along 1D lines. While the medium of our interest, the inner heliosphere, is a 3D object, IPS provides only integration along individual $l.o.s.$s, which are essentially directions in space and may be thought of as individual pixels of a 2D image. Thus, though the observable of IPS is well suited for a tomographic reconstruction, IPS data cannot be used directly for tomography as it is not in the form of projections of the medium. If the problem can be posed in terms tomographic reconstruction of a 2D medium, the IPS data can be used as an input to the reconstruction process. Assuming that it is possible to model the radial propagation of the Solar Wind in an acceptable manner, individual IPS measurements along different directions can be backproject on a fiducial spherical surface centred on the Sun. The properties of the Solar Wind, as projected on this 2D surface, can be reconstructed from individual IPS measurements using tomographic techniques. A model for radial propagation of Solar Wind can then be used to propagate this fiducial surface to fill the entire inner heliosphere and generate the 3D model of Solar Wind.

It is essential for a tomographic reconstruction that the entire medium being reconstructed should be projected along many different directions. The reconstruction process is well constrained only if each of the projections sample the entire medium. If a significant contribution to the projection comes from a part of the volume not sampled by many different *l.o.s.*s, it leads to non-unique tomographic reconstructions. All the *l.o.s.*s available to IPS, at any given time, lie in a volume enclosed between the two cones obtained by rotating the *l.o.s.*s at the smallest and the largest ϵ, respectively, about the Sun–Earth line, as explained in Figure 3.4. The part of the heliosphere at $R < \sin(\epsilon_{min})$ is never accessible to IPS as the weak scattering assumption breaks down close to the Sun. As the S/N of IPS measurements decreases with elongation, observations at elongations larger than ϵ_{max} are not very useful for studying the Solar Wind. The contribution to IPS from the regions at larger heliocentric distances, in the accessible volume, reduces because of $1/R^4$ decrease in δn_e and that from the near field regions of the Earth get weighted down as the phase fluctuations imposed by the thin screens in this region do not develop into intensity scintillation for an Earth based observer. Thus, in the available volume of solid angle, the sensitivity of IPS observations to Solar Wind is not constant and varies considerably.

The rotation of the Sun allows a large number of perspectives to be presented to Earth based observers. Ecliptic cuts across the regions of inner heliosphere covered at 3 different phases in the rotation of the Sun are shown in Figure 3.5. Thus IPS *l.o.s.*s can sample a large fraction the inner heliosphere with many different perspectives as seen from the ecliptic. It takes the period of a solar rotation to sample the medium with a complete set of projections.

3.7 Tomography assumptions

A tomographic reconstruction of the inner heliosphere using IPS data bases itself on the following key assumptions.

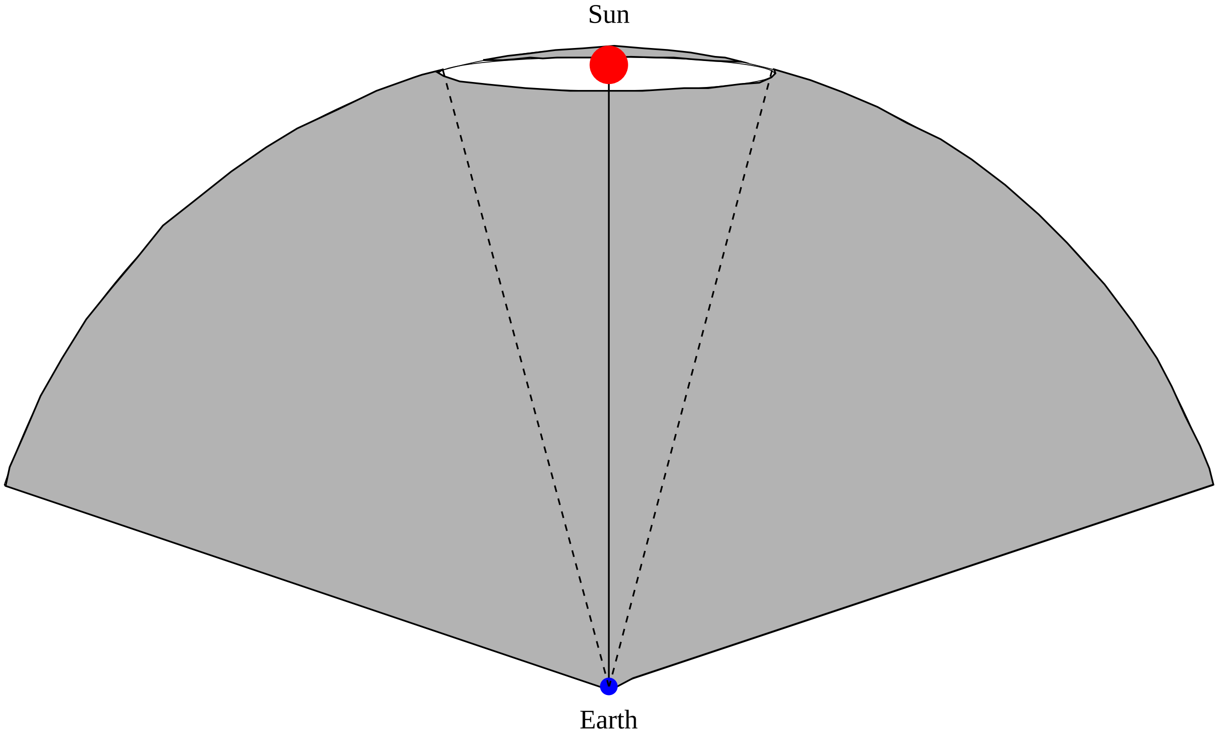

Figure 3.4: **Heliospheric coverage of IPS observations** – IPS *l.o.s.*s can sample a large fraction of the heliosphere at any given time. Consider the solid angle enclosed by the cone corresponding to maximum elongation at which IPS observations are made and remove from it a much smaller cone centred on the Sun defined by the minimum elongation closer than which IPS assumptions break down. The solid angle enclosed between these two cones is the part of inner heliosphere suitable for IPS observations.

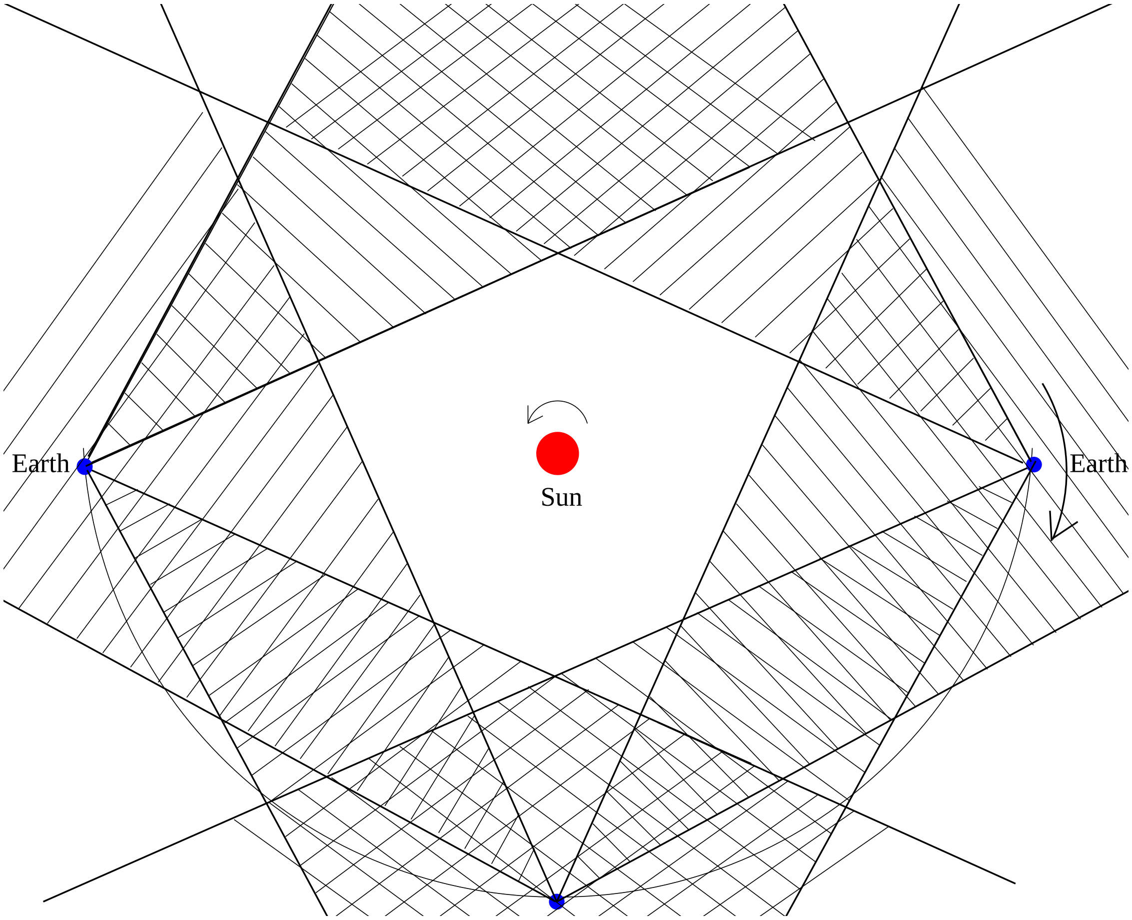

Figure 3.5: **Overlap of regions sampled by IPS *l.o.s.*s** – As the Sun rotates, stable features in the Solar Wind co-rotate along with it, much like the twirling skirt of a ballerina, and different perspectives of the inner heliosphere are presented to an Earth based observer. In order to demonstrate the overlap of the regions of the heliosphere sampled, the regions accessible to IPS from three different locations of the Earth spread over half the rotation period of the Sun are shown in the Sun's reference frame. The overlap of hashed regions represents the overlap in sampling of the same physical region by different *l.o.s.*s. The view presented is a schematic cut across the ecliptic plane.

1. **Time stationarity** – A true tomographic reconstruction requires the entire inner heliosphere to be sampled using a large number of *l.o.s.* and good spatial coverage on time scales smaller than the time scales of variation of the physical properties of the interplanetary medium in the inner heliosphere. This requires observations of a large number of the distant compact radio sources simultaneously from many different vantage points which offer different perspectives, say at different angular positions along the ecliptic. All Earth based observations are necessarily limited to only one perspective at any given time. The perspective available changes slowly due to the rotation of the Sun with a small additional component due to revolution the Earth around the Sun. As it takes one solar rotation period for the entire inner heliosphere to be sampled using IPS, it is necessary to assume that Solar Wind undergoes little time evolution during this period. A significant time evolution of the Solar Wind in this period leads to inconsistencies in the data-set and render the data unsuitable for a tomographic reconstruction.

2. **Radial evolution** – As has been pointed out earlier, the Solar Wind may undergo significant change in some of its properties as it travels outwards from the Sun. The rigorous modelling of the radial evolution of Solar Wind requires solving 3D magneto-hydrodynamical equations with the right boundary conditions. In absence of a rigorous solution, one is forced to use some heuristic arguments to guess the approximate functional dependence of the physical properties of the Solar Wind which evolve with radial distance. A model for radial dependence therefore needs to be assumed in order to perform the tomographic inversion.

3. **Simple structure** – The large scale structure in the Solar Wind is assumed to described well using models with a few degrees of freedom. While the Solar Wind is known to have time variations at a range of time scale, it is hoped that the fast variations will get averaged out in the large bulk of the data spread over an entire Carrington rotation and stable long lived structures would be seen clearly. The studies of large scale average structure of the Sun, in the past, have not given any indications of it being very complex in nature.

3.8 Limitation of IPS tomography

Astrophysics is an observational, not experimental, science. The phenomenon studied are almost always inaccessible to direct manipulation and must, usually, be observed from large distances and often indirectly. The vantage point being usually confined to the Earth (or near Earth satellites), limits our view of the heavens to a single perspective of the 3D universe. These, rather severe constraints, lead to many limitations on a tomographic reconstruction, which are enumerated below.

1. **Sensitive only to long lived features** – As the data collected over the period of a solar is used to yield an average 3D structure of the Solar Wind for the entire period, this technique is sensitive to only long lived stable features. Short time variations tend to get averaged out and act as additional noise in the data. Systematic time evolution during the course of the observations will lead to inconsistencies in the data-set.

2. **Problems due to limited and non-uniform sampling** – At any given instant of time, a solid angle of $\sim 5.8 rad^2$ $(0.44\ 4\pi)$ [1] is accessible to IPS. There are, usually, many compact radio sources with sufficient flux densities in this large solid angle which can be used as IPS sources. The distribution of the sources in this solid angle is often not uniform, giving rise to a non-uniform coverage of the inner heliosphere. This leads to the reconstruction not being equally well constrained in all parts.

3. **Problems away from the ecliptic** – As one moves away from the ecliptic plane, the overlap of the regions being sampled by the *l.o.s.*s with significantly different perspectives reduces substantially. This is purely a geometrical effect. The reconstructed models of the Solar Wind, therefore, tend to become less constrained further away from the ecliptic.

3.9 Problems envisaged

In addition to the problems due to violations of assumption, an attempt at tomographic reconstruction also faces the following problems :

1. **Observationally intensive** – The observational effort required to acquire IPS data for the purpose of a tomographic reconstruction is quite demanding. It is necessary to sample a large number of *l.o.s.*s everyday, at least for the duration of one solar rotation. In order to cover the sources in the chosen ϵ range at least $12 hrs$ of observing time are needed everyday. In order to pick up the signature of structure in the Solar Wind being sampled by the *l.o.s.*, good S/N observations are necessary. This practically requires the availability of a dedicated telescope with good sensitivity and considerable declination coverage for long lengths of time. It is most unusual, if not outright impossible, for telescopes with good sensitivity and declination coverage to be available for many hundreds of hours of observing time for a given project.

---

[1] Using $\epsilon_{min} = 20°$ and $\epsilon_{max} = 80°$

2. **Computationally complex and intensive** – A rather voluminous data-set is necessary for a well constrained tomographic reconstruction. The software required to attempt tomographic reconstruction using IPS data would be of respectable complexity and the volume of the software would also be considerable, especially in view of the fact that the software would be required to be developed in-house single handedly. Apart from the software effort involved, the exercise would be computationally very intensive and the convergence of the reconstruction is not assured.

In view of the above, it is not surprising that there have been few attempts at tomographic reconstruction of the Solar Wind using IPS. The only other attempts have been by the groups at University of California, LaJolla, USA (Jackson et al., 1997; Jackson et al., 1998) and the Solar-Terrestrial Environment Laboratory group at Nagoya, Japan (Kojima et al., 1998; Asai et al., 1998). Both these attempts used data from dedicated IPS observatories at Cambridge (81.5 MHz IPS array) and Nagoya (327 MHz multi-station observations).

We had the advantage of having a sensitive telescope with a good declination coverage, the Ooty Radio Telescope, India available to us practically as a dedicated IPS instrument. The Ooty IPS measurements provide another significant advantage of measuring both the scintillation index, m, and the IPS velocity from the same data, unlike the Cambridge and Nagoya measurements. Being at a higher observing frequency of 327 MHz, the Ooty IPS observations suffer much less contamination from ionospheric scintillations as compared to the Cambridge observations. The higher observing frequency and sensitivity of the Ooty Radio Telescope allow the study of a larger region of heliosphere from $\sim$ 0.3–1.0 AU and thus provide the missing link between the measurements close to the Sun and at 1 AU. As our epoch of observation was close to the minima of the solar activity cycle and we considered it appropriate to attempt a more focussed study of the tomographic reconstruction of the equatorial Solar Wind.

3.10 Other attempts at obtaining the 3D structure of Solar Wind

The reasons detailed in Section 3.4 demonstrate that uniform Solar Wind models provide unrealistic descriptions of the Solar Wind. Any realistic attempt at studying the Solar Wind must take into account its inherent 3D structure. There have been attempts involving varying degrees of complexity and finesse which have met with varying degrees of success. The attempts have mainly been reconstructions of the 3D structure of the Solar Corona, a few $R_\odot$ away from the solar surface. A representative few are discussed here.

3.10.1 Solar Corona

Since the feasibility study by Davila (Davila, 1994) in 1994, there have been a few attempts to tomographically reconstruct the 3D structure of the solar corona. The most recent efforts have been by Zidowitz (Zidowitz, 1999) and Panasyuk (Panasyuk, 1999). The former attempt used polarised brightness images of the corona from 1.122 to 2.446 R_{Sun}, from the Mark-III K-coronometer at Hawaii. The latter used the UV Coronograph Spectrometer on SOHO, where each exposure was an array of photon counts for a given slit position in the plane of the sky. Both these attempts have used observations from an epoch close to the solar minima, during the *Whole Sun Month* (August 10 to September, 1996) and conclude that tomography is a useful technique for studying the large scale long lived features during the solar minima.

Hick et. al (Hick and Jackson, 1998) have used white light Thomson scattering data for a tomographic reconstruction of the electron density distribution in the inner heliosphere. They have used images from the photometer instrumentation on board the spacecrafts HELIOS 1 and HELIOS 2 and their prime motivation was to developed a technique for use with Solar Mass Ejection Imager (SMEI) data, once it became available.

Chapter 4

Observations and Data analysis

4.1 Introduction

The two essential requisites for tomography are

1. An observable sensitive to an integral along the the path of propagation in the medium being studied.
2. Ability to sample the same physical part of the medium with many different perspectives.

The plan of observing was optimised to suit these demands of tomographic reconstruction. The various aspects which were kept in mind were the epoch and duration of observations, the selection of sources, the heliographic latitude coverage, the elongation coverage and the observing strategy. This chapter describes the observational setup used for IPS observations at the Ooty Radio Telescope, the observing strategy and the data-set which was obtained as a part of the present work. The data processing done to obtain the power spectrum of intensity fluctuations from the observed time series and the computation of scintillation index, m, is discussed as well.

4.2 The Ooty Radio Telescope

The data used in this thesis was obtained from the Ooty Radio Telescope (ORT) (Swarup et al., 1971) which is operated by the Radio Astronomy Centre, Ooty, a part of the National Centre for Radio Astrophysics, Pune, India. The ORT is located in the state of Tamil Nadu in India at $+11°23'$ North, $76°40'$ East and at an altitude of 2150 m above the mean sea level. Figure 4.1 shows a views of the ORT and the control room building. It is an equatorially mounted parabolic

Figure 4.1: **The Ooty Radio Telescope** – The first picture is a view of the Ooty Radio Telescope looking southwards. A few of the parabolic frames which support the steel wires which form the reflecting surface are clearly seen. The feed system, held fixed at the focus of the parabola, is also clearly visible. The second picture is an early morning view of the ORT Control Room.

cylinder of length 530 m along the North-South direction, 30 m along the East-West direction, operates at a centre frequency of 327 MHz and the maximum bandwidth of the signal available is 12 MHz. The equatorial mounting of the telescope has been achieved by placing the telescope on a hill which has a natural North-South slope close to the value of the geographic latitude of the place. The half-power beamwidth of the ORT is 2° in hour angle and $3'$ in declination. The ORT has an effective collecting area of about $8,000\ m^2$, a system temperature (T_{sys}) of $150^\circ K$ and is sensitive to the part of the incident radiation linearly polarised along the North-South axis. The sensitivity of the telescope to linearly polarised radiation is a consequence of it's reflecting surface being made of stainless steel wires which run along the length of the telescope and the fact that the dipole arrays at the focus are also linearly polarised. The reflecting wires are $1,100$ in number and 0.38 mm in diameter. Tracking along hour angle is achieved by simply compensating for the rotation of the Earth by rotating the telescope along the North-South axis from East to West. A total of $9\frac{1}{2}$ hours of hour angle coverage is available, from 4 hours East to $5\frac{1}{2}$ hours West.

The feed system of the ORT comprises of a set of $1,056$ dipoles arranged along the focal line of the parabolic reflector. The dipoles are organised in 22 groups of 48 dipoles each, referred to as modules. After ORT feed system upgrade in 1991–1992, the telescope can now routinely achieve a signal-to-noise ratio (S/N) of 25 for 1 sec integration on a 1 Jy source for a bandwidth of 4 MHz. Beam forming along the declination axis is done by applying a phase gradient along the North-South direction. This is effected by introducing a phase shift between the signal from individual dipoles in a module and both an appropriate delay and a phase shift between the signal from different modules. The range of declination accessible from ORT is $\pm 60^\circ$.

The outputs from each of the modules are given to power dividers which produce 12 outputs. These outputs can be independently combined, with slightly different delay gradients across the modules, to form 12 beams in the sky, separated by $3'$ in declination, all of which can be used simultaneously. This allows a region of angular size $36'$ by 2° to be observed using the 12 different beams at any given time.

Each of the ORT beams can be in operated in either a *total power* mode or a *correlation* mode, also referred to as the *phase switched* mode. The signal from all the 22 modules of the ORT are added in phase in the total power mode. In the phase switched mode, the outputs from all the modules comprising the North and the South halves are separately added in phase. The final output is obtained by multiplying or cross-correlating the signal from the North and the South halves. The beams for the two modes differ in the North-South direction, they have half widths of $5'.5 \sec(\delta)$ and $3'.5 \sec(\delta)$ in the total power and phase switched modes respectively. Using the ORT in correlation mode offers the following advantages

1. It allows one to choose any arbitrary patch of the sky for use as an off-source region as the correlated signal is not sensitive to a change in uniform background. This is a very useful feature as IPS observations frequently require observations of off-source regions to estimate the deflection due to the source and to monitor the general health of the system.

2. The interference of local origin does not correlate between the North and the South halves of the ORT.

On the other hand, using the ORT in total power mode offers a $\sqrt{2}$ better sensitivity than the phase switched mode but it is more susceptible to interference and T_{sys} variations.

4.3 IPS Observations

Two of the 12 ORT beams were used in phase switched mode for the observations presented in this thesis, one to observe the source (beam 7) and the other to look at neighbouring patch of the sky, $12'$ South of the source, to monitor the interference environment (beam 4). The IPS data acquisition system used a bandwidth of 4 MHz. The signal from both these beams was simultaneously fed to a chart recorder for visual monitoring and for use later to flag the interference in the data. The signal was integrated with an RC time constant of 45 ms, sampled every 20 ms by a 12 bit ADC and recorded. The data was recorded in chunks of $2,600$ contiguous samples of the intensity time series, amounting to a duration of 52 sec, referred to as a record. The mean and variance of each record were computed and displayed in real time and were used as indicators of data quality and strength of scintillation.

Typically, a scan on a source has about $10-15$ data records. Off-source observations were taken every 90 min in order to determine the reference zero level. This reference level includes contribution of the sky background, noise temperature of the receiver system and any other systematics. Off-source observations were made by tracking a neighbouring region in the sky a few degrees away in declination.

4.4 The Data-set

4.4.1 Epoch

The observations for this thesis were conducted at the ORT from the 20 April 1997 to 31 August 1997. The period of observation commenced less than an year after the minimum of the solar cycle number 23 and spanned about 5 Carrington

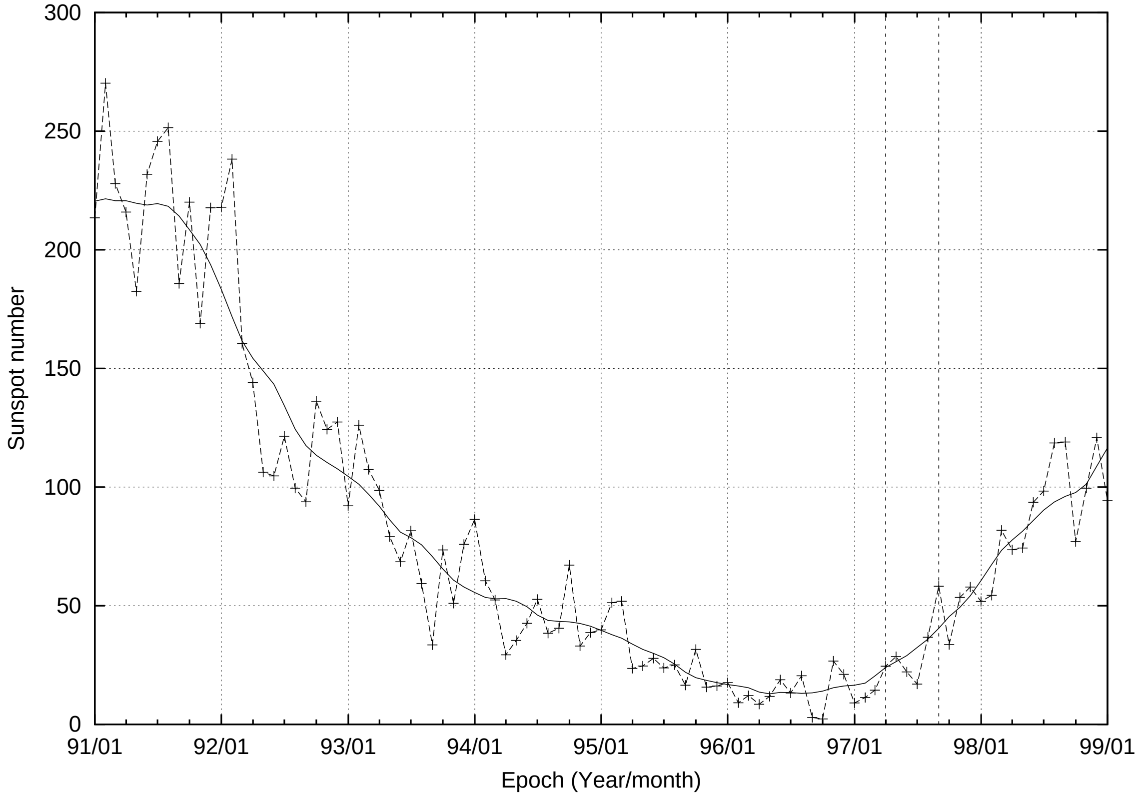

Figure 4.2: **Sunspot number progression for Solar cycle** 23 – The solid curve represents the smoothed sunspot number and the dashed curve the observed sunspot number. The epoch of observation presented in this thesis is marked by the vertical dashed lines. The sunspot data presented in this figure has been obtained from the Space Weather Operations group of Space Environment Centre, Boulder, Colorado.

rotations. The location of the epoch of observation with respect to the phase of the 23^{rd} solar cycle is shown in the Figure 4.2. The epoch of observations presented in thesis is marked by the vertical dashed lines. The data presented in this figure has been obtained from the Space Weather Operations group of Space Environment Centre, Boulder, Colorado. Our observations were in a period of reasonably low solar activity, though there were a few spectacular mass ejections and consequent Interplanetary Disturbances (IPDs).

4.4.2 Source Selection

The sources observed were selected from the catalogue of known scintillators which has been built up over the years at the ORT (Balasubramaniam, 1997; Manoharan, 1997a). This ensured that the sources selected had components compact enough to scintillate and that these components had a reasonable flux density. An angular size cutoff limit of $300mas$ was used and the mean angular size of the sources observed was $\sim 125mas$. A majority of the sources observed had flux densities $> 4\ Jy$ at $327\ MHz$. Only in situations where few sources above this flux density threshold were available, the criterion was relaxed to include sources with lower flux densities. Table 4.4.2 lists the sources which were observed at least 20 times during the period of observations along with the number of observations on the source. In addition to the 71 sources listed in this table, another 28 sources were observed at least 10 times during the observation period.

4.4.3 Considerations for Tomographic Reconstruction

For the purpose of a tomographic reconstruction, it is useful to observe different $l.o.s.$s, which, when projected back on the solar surface, have significant overlaps. The $l.o.s.$s to ecliptic sources map back to almost an equatorial belt on the Sun, a few tens of degrees in width (Section 2.1 and Figure 2.4). As the $l.o.s.$s to ecliptic sources at different elongations and observed at different phases of the solar rotation period all map back to an almost equatorial belt, they have large overlaps with one another. Therefore the $l.o.s.$s most suited for tomography are the ones which sample the equatorial region of the solar surface. The sources to be observed were, hence, chosen such that most of the $l.o.s.$s sample this region. A few sources sampling the mid and high/low latitude ranges were also included. Most of the sources were observed only once a day. Two sources close to the ecliptic plane, one on the East and the other on the West of the Sun were observed more frequently, often ~ 4 times a day. These sources formed a control sample for estimation of short time scale variations in the Solar Wind. Typically one source each for mid and high/low latitudes both on the East and the West of the Sun was chosen to be observed once a day. The heliographic latitude ($\theta_\odot$) distribution of the P-point of the $l.o.s.$ to the observed sources is shown in Figure 4.3. The daily coverage of the equatorial belt of the Sun is quite dense from the start of the observations on day number 110 to about day number 210, beyond which there are some breaks in the observations, mainly due to bad weather conditions. The distribution of $\theta_\odot$ is more clearly seen in the histogram, which shows the equatorial belt is most densely covered region of the solar surface and most of the observations lie in the $\theta_\odot$ range -20° to 10°.

4.4.4 ϵ coverage

The sources were observed over a large range of elongations ($20^\circ \geq \epsilon \geq 90^\circ$) in order to be able to have an opportunity to study the radial evolution of the Solar Wind. The distribution of elongation, ϵ, of the observed sources is presented in Figure 4.4. All through the course of the observations, a large range of ϵ was sampled. The

Table 4.1: **List of sources observed** – The names of the sources, in $B1950$ convention, along with the number of times each source was observed are listed. Only the 71 sources which were observed at least 20 times, during the observing period, have been listed.

No.	Source (B1950)	Flux (Jy) (327 MHz)	Scintillating Flux (Jy)	Angular Size (")
1	0003-003	11.0	4.90	0.050
2	0005-062	4.7	2.20	0.180
3	0056-001	4.9	4.20	0.050
4	0115+027	6.8	0.90	0.100
5	0115-016	4.4	3.80	0.200
6	0116+082	5.2	4.50	0.250
7	0128+040	5.2	3.40	0.080
8	0129-071	4.2	2.60	0.100
9	0134+329	43.3	4.10	0.050
10	0144-022	3.0	1.80	0.080
11	0202+149	6.1	3.80	0.100
12	0218+111	4.7	1.20	0.180
13	0240-002	11.2	1.20	0.220
14	0316+162	8.1	4.50	0.025
15	0316+413	16.1	4.00	0.050
16	0320+053	7.6	5.30	0.100
17	0333+128	5.2	4.20	0.050
18	0347+057	8.8	1.50	0.150
19	0349+063	3.7	2.20	0.050
20	0352+210	2.0	1.60	0.050
21	0402+160	2.5	2.30	0.050
22	0403-132	7.4	3.60	0.100
23	0409+229	3.8	1.10	0.150
24	0422+084	3.3	1.30	0.050
25	0425+214	3.3	2.80	0.060
26	0456+270	2.2	2.20	0.100
27	0459+252	16.8	1.10	0.180
28	0518+165	17.2	5.90	0.040
29	0531+194	15.3	6.30	0.050
30	0540+187	6.3	0.90	0.120
31	0548+165	4.4	3.70	0.050
32	0552+125	2.5	2.40	0.250
33	0600+219	6.5	1.60	0.070
34	0601+203	8.2	4.10	0.300
35	0610+260	16.9	1.10	0.050

No.	Source (B1950)	Flux (327 MHz)	Scintillating Flux (η)	Angular Size (")
36	0616+136	4.8	0.50	0.050
37	0618+145	9.0	1.60	0.050
38	0622+147	6.4	2.90	0.120
39	0624-058	48.0	4.70	0.200
40	0632+189	3.2	1.90	0.150
41	0645+147	2.5	1.10	0.200
42	0654-140	9.5	3.80	0.070
43	0656+213	2.3	1.90	0.050
44	0722-095	6.1	1.00	0.050
45	0725+147	8.2	2.90	0.140
46	0735+178	2.3	1.80	0.100
47	0741-063	12.9	5.00	0.070
48	0758+143	7.6	2.40	0.100
49	0802+163	2.0	1.20	0.030
50	0818+179	4.6	3.40	0.040
51	0820+225	4.2	1.80	0.020
52	0827+235	2.2	2.10	0.030
53	0831+171	6.0	3.00	0.160
54	0850+140	11.1	2.50	0.150
55	0855+143	7.0	1.90	0.120
56	0915+227	4.3	1.20	0.120
57	0939+139	10.9	4.70	0.200
58	1005+077	17.2	6.60	0.500
59	1019+222	7.7	3.80	0.030
60	1023+067	4.6	0.80	0.150
61	1025+154	2.4	2.20	0.220
62	1040+123	8.9	2.40	0.050
63	1105+148	3.0	2.20	0.030
64	1116+128	3.6	1.70	0.030
65	1136-135	12.5	0.80	0.200
66	1453-109	10.3	2.40	0.120
67	2308-109	3.9	3.30	0.050
68	2318-166	8.8	5.50	0.070
69	2322-052	5.4	1.10	0.100
70	2337-063	3.8	3.00	0.050
71	2347-026	5.7	4.30	0.040

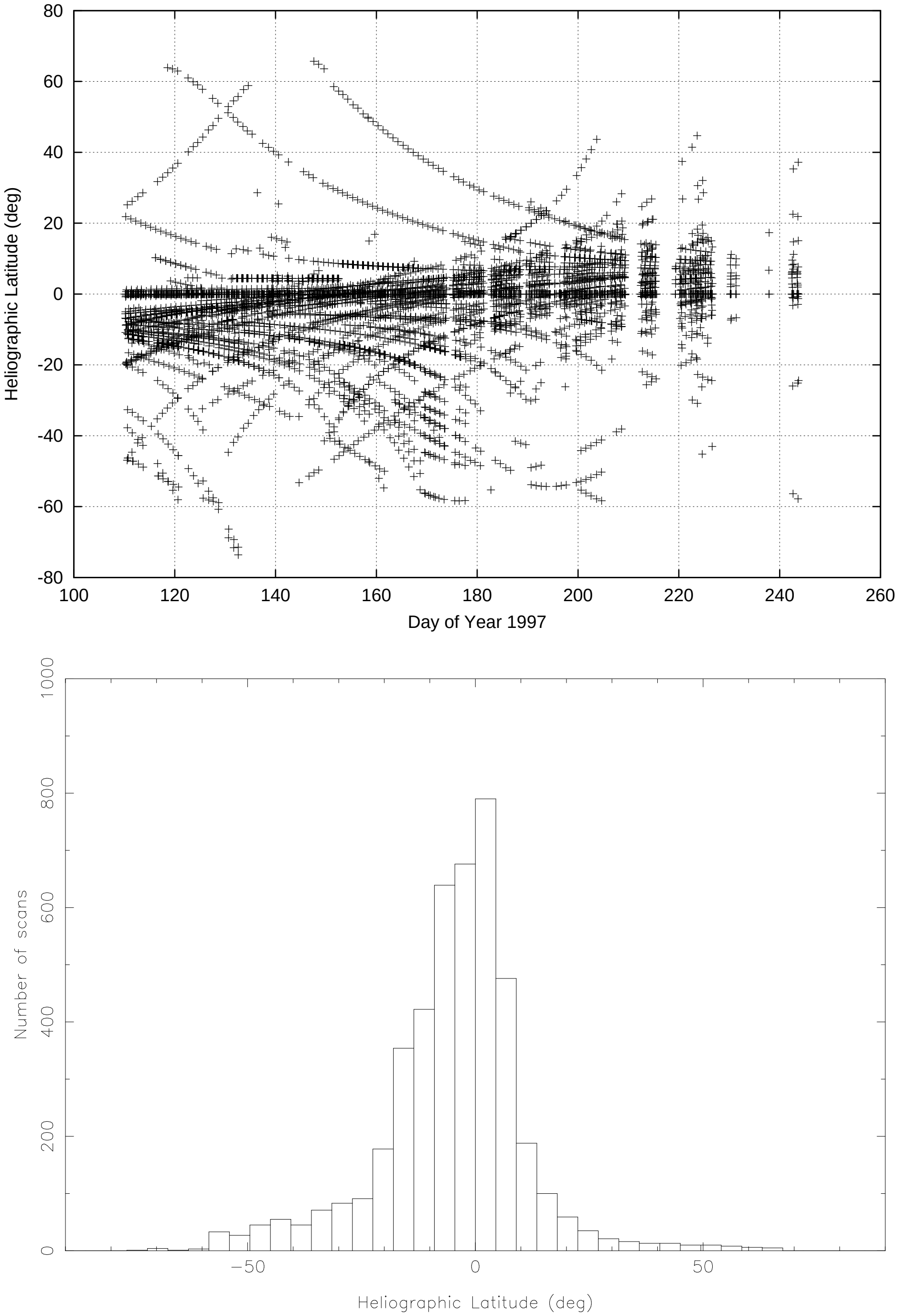

Figure 4.3: **Distribution of $\theta_\odot$ of observed sources** – The top panel shows $\theta_\odot$ for each of the scans on the scintillating source as a function of DOY 1997 while the bottom panel shows the $\theta_\odot$ distribution in the form of a histogram. The equatorial region is very well sampled on individual days from day number 110 to 210, beyond which there are some data gaps. The histogram of $\theta_\odot$ distribution shows that most of the observations lie in the $\theta_\odot$ range $-20°$ to $10°$.

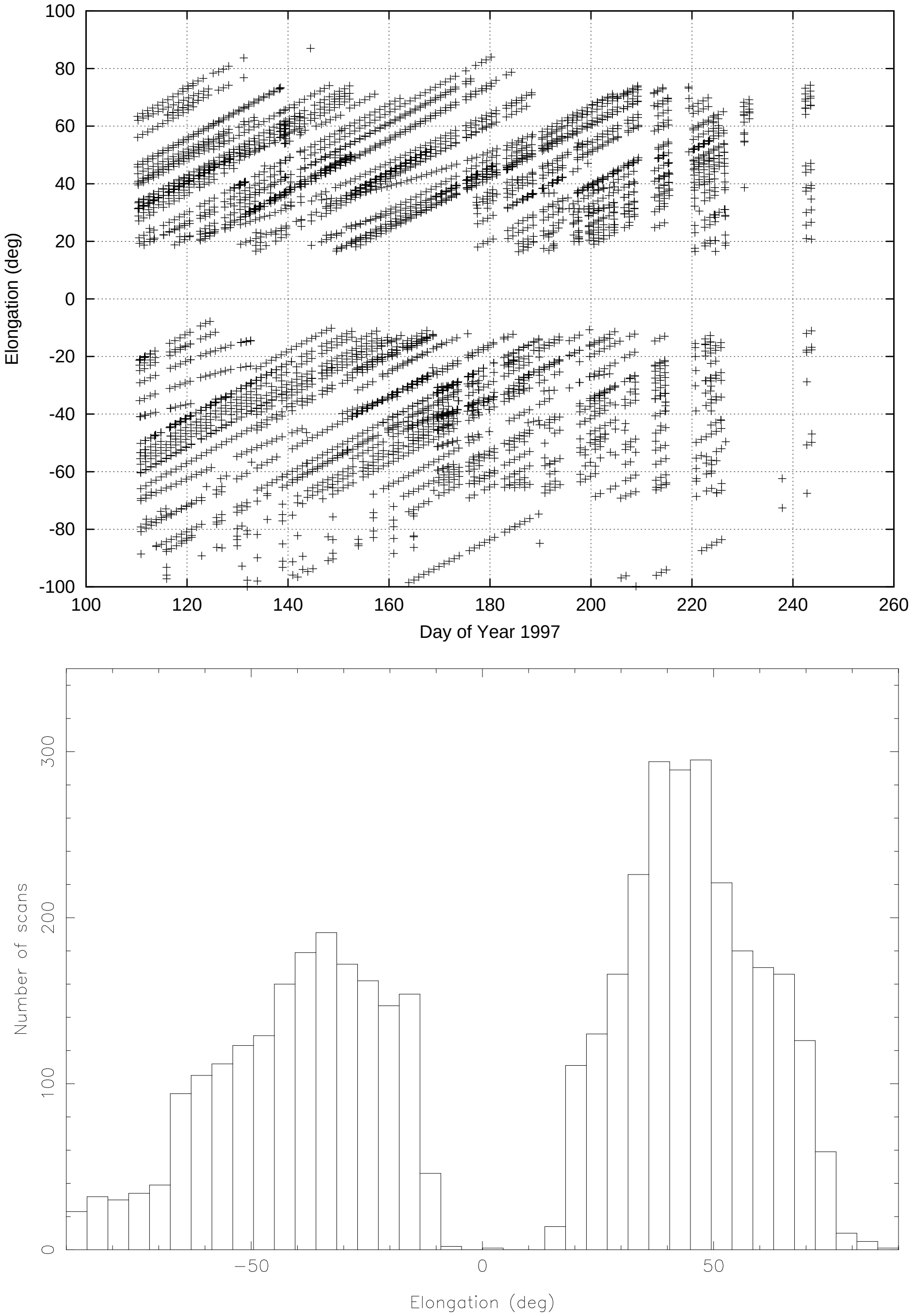

Figure 4.4: **Distribution of ϵ of observed sources** – The top panel shows ϵ for each of the scans on the scintillating source as a function of DOY 1997 while the bottom panel shows the ϵ distribution in the form of a histogram. A large range of ϵ was sampled all through the observations. The coverage on the East of the Sun is a little denser than that on the West of the Sun. Most of the observations lie in the range 20° to 80° on either side of the Sun.

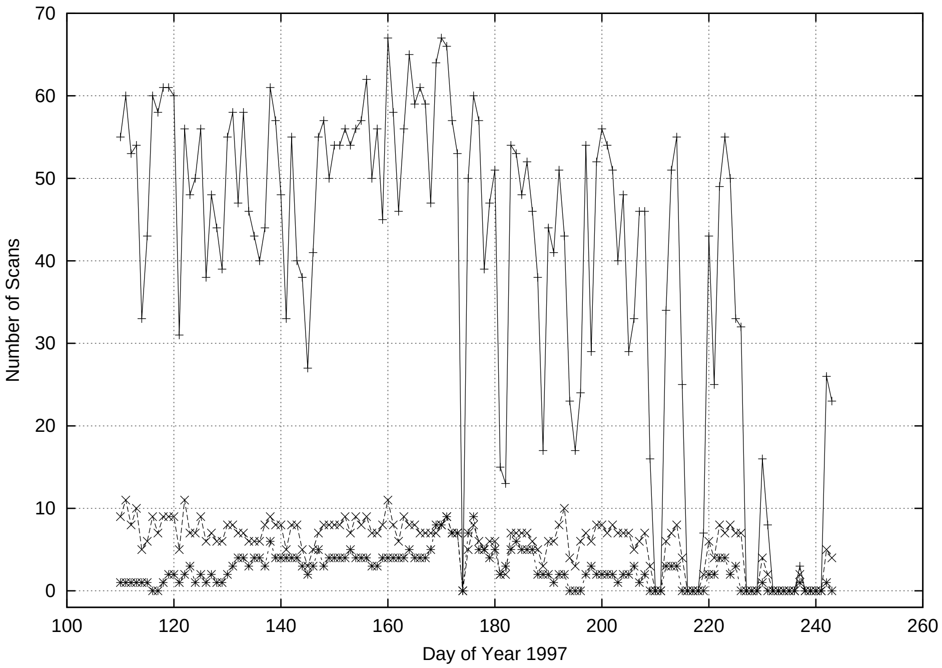

Figure 4.5: **Number of scans per day** – Total number of scans on a given observing day are represented by + symbols, number of scans on Calibrator sources by ⋆ symbols and number of off-source scans by × symbols. On an average 40 scans are available for a typical observing days among which there are 6 scans on off-source regions and 3 scans on calibrator sources.

number of observations on the East of the Sun are a somewhat more than that on the West of the Sun. The ϵ range 20° to 80° is very well covered on either side of the Sun.

The data-set comprises of a total of $5,418$ scans, including the calibrator and off-source scans, and totals upto about $1,500$ hrs of telescope time spread over $4\frac{1}{2}$ months. On a typical observing day, the observing session lasted about 15 hrs. The number of scans on scintillating sources, calibrators and off-source scans are presented in Figure 4.5. The average values of number of scans observed on a given observing day, the number of off-source scans and scans on calibrators are 39.6, 5.9 and 2.7 respectively. The large differences in the number of scans on different days arise mainly because of presence of interference in the early part of the observations and mainly bad weather towards the later part of the observations apart from power failures.

4.5 Data Analysis

4.5.1 Data Flagging

While the interference environment at the site of ORT is usually quite favourable, there are some intermittent sources of man made interference. Often the interference, when present, is too strong to escape notice. The mean and variance of all the data records in every scan were examined and the ones which deviated considerably from the rest were flagged. The chart recorder tracks of the on-source beam and the off-source beam were visually inspected to look for correlated intensity fluctuations. As a compact astronomical source cannot give rise to correlated fluctuations in both the beams (which look at different parts of the sky separated by $12'$), such features were attributed to terrestrial interfering sources and records showing such features were flagged.

4.5.2 Flux calibration

The number of flux calibrators observed in every observing session usually varied between 2–5. The counts per Jy, ξ_i, was determined by dividing the source deflection by the known flux of the calibrator at the frequency of observation, S_{327}. The deflection on the calibrator was estimated by taking the difference of counts observed on the calibrator, C_{CAL}, and 'cold sky', C_{OFF}. The cold sky observations are often referred to as 'off-source' scans.

$$\xi_i = \frac{C_{CALi} - C_{OFF}}{S_{327}} \tag{4.1}$$

The off-source counts, typically 5–10 per day, were usually obtained by observing a region of the sky separated by a few degrees in declination while continuing to track the current Right Ascension. This caused different estimates of off-source counts to be obtained by observing different patches in the sky. This is an acceptable practice because in the phase switched mode, the ORT acts like a two element interferometer and therefore is not sensitive to a uniform background flux, as explained in the Section 4.2. In order to increase stability and reduce the effect of confusion, the counts from all the off-source scans observed in a given calendar day were averaged to determine C_{OFF}. The value of ξ used for a given observing day was obtained by averaging the ξ_i for all the individual calibrator sources observed on that day.

$$\xi = \frac{1}{N}\sum_{i=1}^{N}\xi_i \tag{4.2}$$

The ξ so determined was used to estimate the flux of each of the sources observed. The flux corresponding to counts observed on each of the off-source scans was also

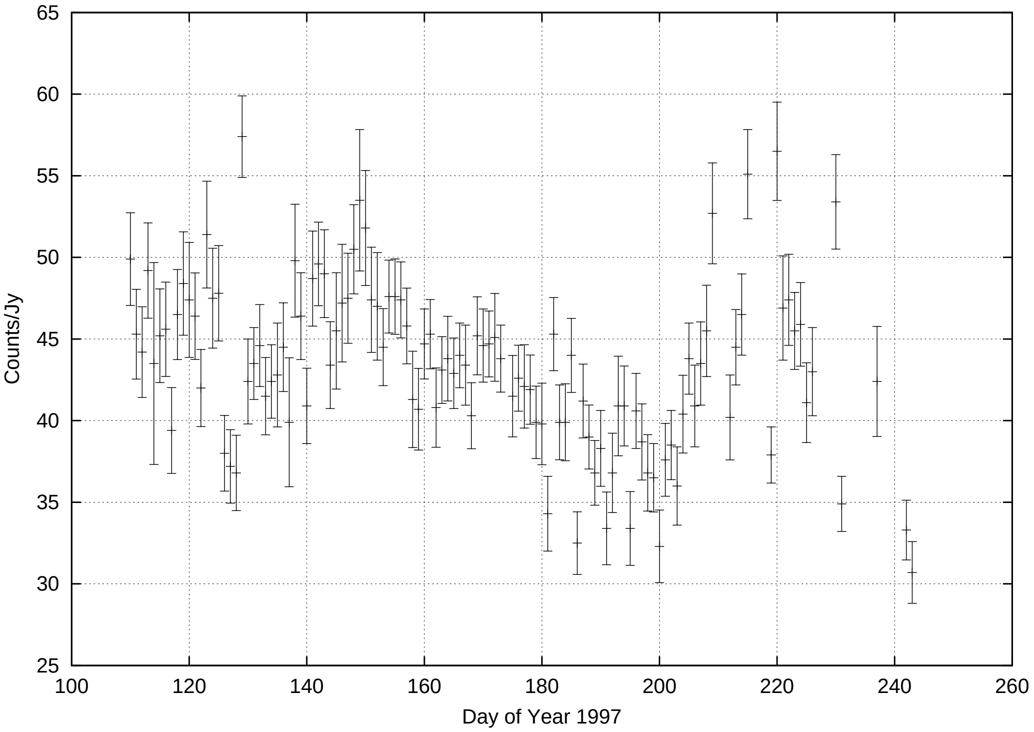

Figure 4.6: ξ **for the period of observations** – The Counts per Jy computed for the period of observations are shown as a function of observing day. The error bars represent the statistical uncertainty in the determination of ξ. ξ remained at a value close to 45 for a large part of the observing period. The correction for declination dependence has been incorporated in the Counts per Jy shown here.

estimated and all the off-source scans which yielded a flux $> 1/4$ Jy were discarded and the remaining were used to recompute C_{OFF}. This recomputed C_{OFF} was then used to compute ξ and the fluxes of sources observed were recomputed. The statistical uncertainty in ξ was determined from the rms uncertainty on the individual ξ_is which were averaged to obtain ξ. The values of ξ for the entire period of observation are shown in Figure 4.6. ξ remained between 40 and 50 for most of the observing period.

The ORT beam provides much higher resolution in declination as compared to that along the $HourAngle$. The flux received by the ORT beam therefore comes from an ellipsoidal patch in the sky with a large eccentricity $(2^\circ \times 3'.5 \sec(\delta))$. This causes the flux density of a source as measured at ORT to differ often from that measured at other observatories or obtained from interpolation of measured spectra because of the presence of confusing background sources. The *confusion flux* corresponding to the ORT beam, 1.5 Jy at 327 MHz, (Swarup et al., 1971) was considered significant and was taken into account by cross calibrating the flux density of one calibrator against another. The most frequently observed calibrator source, 2145+151, was chosen to be the reference calibrator and was assumed to have a flux of 8.1 Jy at 327 MHz. The corrected values of the calibrator flux densities were used for computation of ξ.

The effective collecting area of the ORT, A_{eff}, depends on the declination of the source being observed. This is a consequence of the fact that rather than moving the telescope along the declination axis to point to the source, an appropriate phase gradient is applied across the aperture of the telescope. This results in reducing the effective collecting area of the telescope because of projection and other effects. This declination dependence is found to be approximated quite well by a $\cos^2(\delta)$ functional form. As ξ depends on A_{eff}, it also has the functional dependence on declination which has been taken into account. Care was taken to choose the calibrators which were at elongations greater than 40° in order to avoid the systematic undulations in the baseline due to the Sun in the sidelobes of the telescope.

The flux densities of the observed sources were computed using the following relation :

$$S_{327} = \frac{C_{ON} - C_{OFF}}{\xi \ \cos^2(\delta)} \tag{4.3}$$

Most of the sources were observed a large number of times. Mean and variance of the the flux density measurements for sources observed more than 15 times were computed. The scans which yielded fluxes differing by more than 3σ from the mean were considered unreliable and were hence rejected.

4.5.3 Obtaining the power spectra

In order to obtain the power spectrum of the time series of intensity fluctuations, each record in a scan was subjected to the following procedure. A running mean, computed over 512 data points (10.24 *sec*), was subtracted from each record. This removed the low frequency (< 0.1 Hz) variations from the data which could have contaminations due to the Sun in the sidelobes of the beam and also from the low level ionospheric scintillation. Running mean subtraction left us with a time series of with $2,088$ data points in each record. The first $2,048$ of these data points were used to take a 2^{11} point complex FFT. A cosine taper was applied to the leading and the trailing 512 data points in the time series in order to reduce the edge effects. The power spectrum was obtained by squaring and adding the real and imaginary parts of the FFT output. The power spectrum at this point has a frequency resolution of 2.44×10^{-2} Hz ($50/2048$ Hz) and extends from 0 to 25 Hz. The application of a cosine taper caused a decrease in the amplitudes towards the 'edges' of the time series and a consequent decline in the spectral power. This was corrected for by multiplying the power spectrum obtained with the ratio of variances of the time series of intensity fluctuations computed before and after the application of cosine

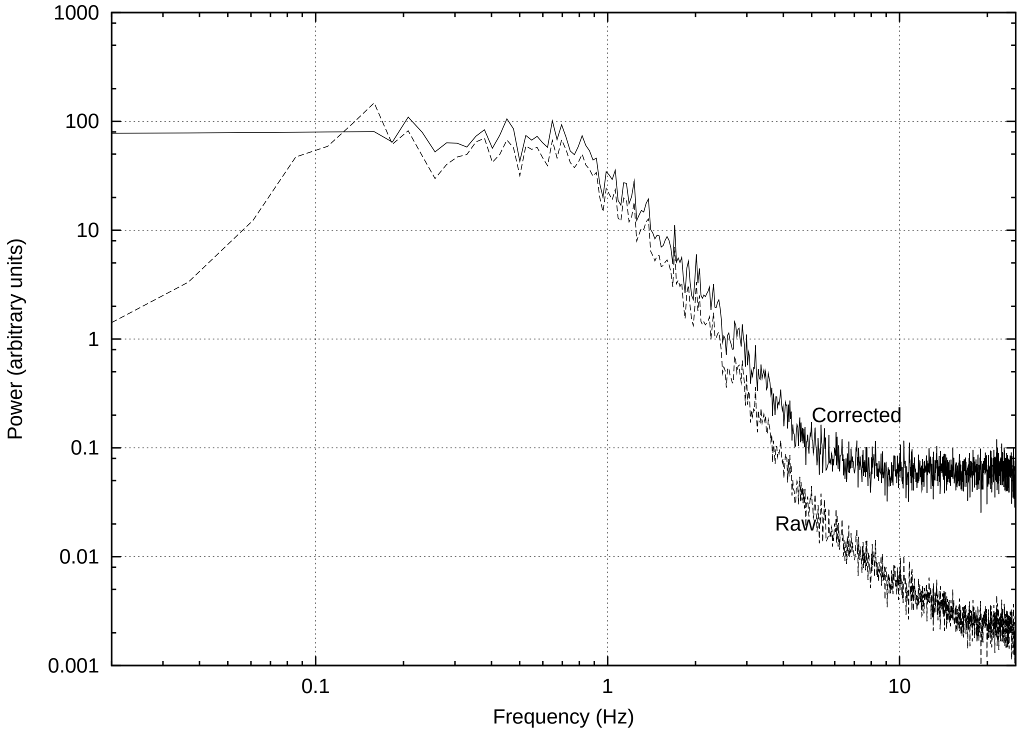

Figure 4.7: **The power spectrum before and after correction for τ and running mean subtraction** – The power spectrum labelled *Raw* was obtained on taking FFT of the mean subtracted time series. The power spectrum obtained after correcting for the τ of the detector, the effects of mean subtraction and cosine taper is labelled as *Corrected*. The mean subtraction gave rise to the low frequency dip, the τ of the detector the high frequency drop and the cosine taper an overall decrease in the power in the raw power spectrum.

taper.

The IPS data acquisition system had a RC time constant, τ, of 0.045 *sec.* A detector with a finite τ acts like a low pass filter as it limits the agility with which the system can respond. This effect was corrected for by dividing the power spectra by the Fourier transform of the RC response function. The effect of running mean subtraction, which acts as a high pass filter, was also corrected for in a similar manner. Spectra from individual records in a scan were averaged to produce the final power spectrum for the scan which was used for subsequent analysis. The low frequency part of the spectrum ($< 0.3\ Hz$) was obtained by extrapolating from the curve obtained by fitting a second order polynomial to the next 40 points. Figure 4.7 shows the raw power spectrum as obtained on taking the FFT of mean subtracted time series and the power spectrum after correcting for τ and running mean subtraction.

A sample ‘on-source’ and ‘off-source’ power spectrum, after correction for the effects mentioned above, is presented in the Figures 4.8 and 4.9. The power spectra are shown on both *log–log* and *log-linear* scales. Note that the on-source power spectrum hits the noise level by $\sim 6\ Hz$ and that the off-source power spectrum is flat for the entire frequency range.

The observed power spectra, $P(\nu)_{obs}$, receives contributions from two independent sources – $P(\nu)_{IPS}$ due to scintillations and $P(\nu)_{sys}$ due to the thermal noise from the receiver.

$$P(\nu)_{obs} = P(\nu)_{IPS} + P(\nu)_{sys} \tag{4.4}$$

The IPS power spectrum does not extend beyond about $5 - 6\ Hz$ in weak scattering regime (Figure 4.8) and beyond $10\ Hz$ in the strong scattering regime. Since the receiver noise is a white noise, its power spectrum is expected and found to be constant, independent of the frequency (Figure 4.9). The power spectra observed had a frequency content from $0 - 25\ Hz$ and more than half of it lies beyond the IPS cut-off frequency. We estimated the average power level due to the system noise by averaging the on-source spectrum in the frequency range $8 - 20\ Hz$. This part of the spectrum also served as a monitor for interference and the general health of the system. The mean power due to the receiver noise was subtracted from the observed power spectrum to estimate the true spectrum of IPS. The same power spectrum as shown in Figure 4.8 is presented in Figure 4.10 after subtracting the contribution of the system noise. The subtraction makes no discernible difference in the part of the power spectrum below $\sim 2\ Hz$. The *broken* appearance of the power spectrum with the system noise subtracted out is an artifact of plotting the spectrum on a *log* scale along the Y axis.

The area under the power spectrum, $A_{P(\nu)}$, was computed using the trapezoidal rule for integration of discreet data as expressed by the following expression :

$$A_{P(\nu)} = \sum_{i=1}^{N-1} \left(P_i\ d\nu_i + \frac{1}{2}\ (P_{i+1} - P_i)\ d\nu_i \right) \tag{4.5}$$

where N is the number of spectral points available. $A_{P(\nu)}$ is a measure of the strength of scintillations due to IPS, σ_{IPS}, which is used to define the scintillation index (equation 2.4).

4.5.4 Estimating the uncertainty in the power spectrum

The statistical uncertainty in the measurement of power spectra is given by the equation :

$$\delta P(\nu) = K P(\nu) \tag{4.6}$$

where K is a constant of proportionality and is of order unity. We regard the power spectra obtained from different records in a scan as independent realisations of the

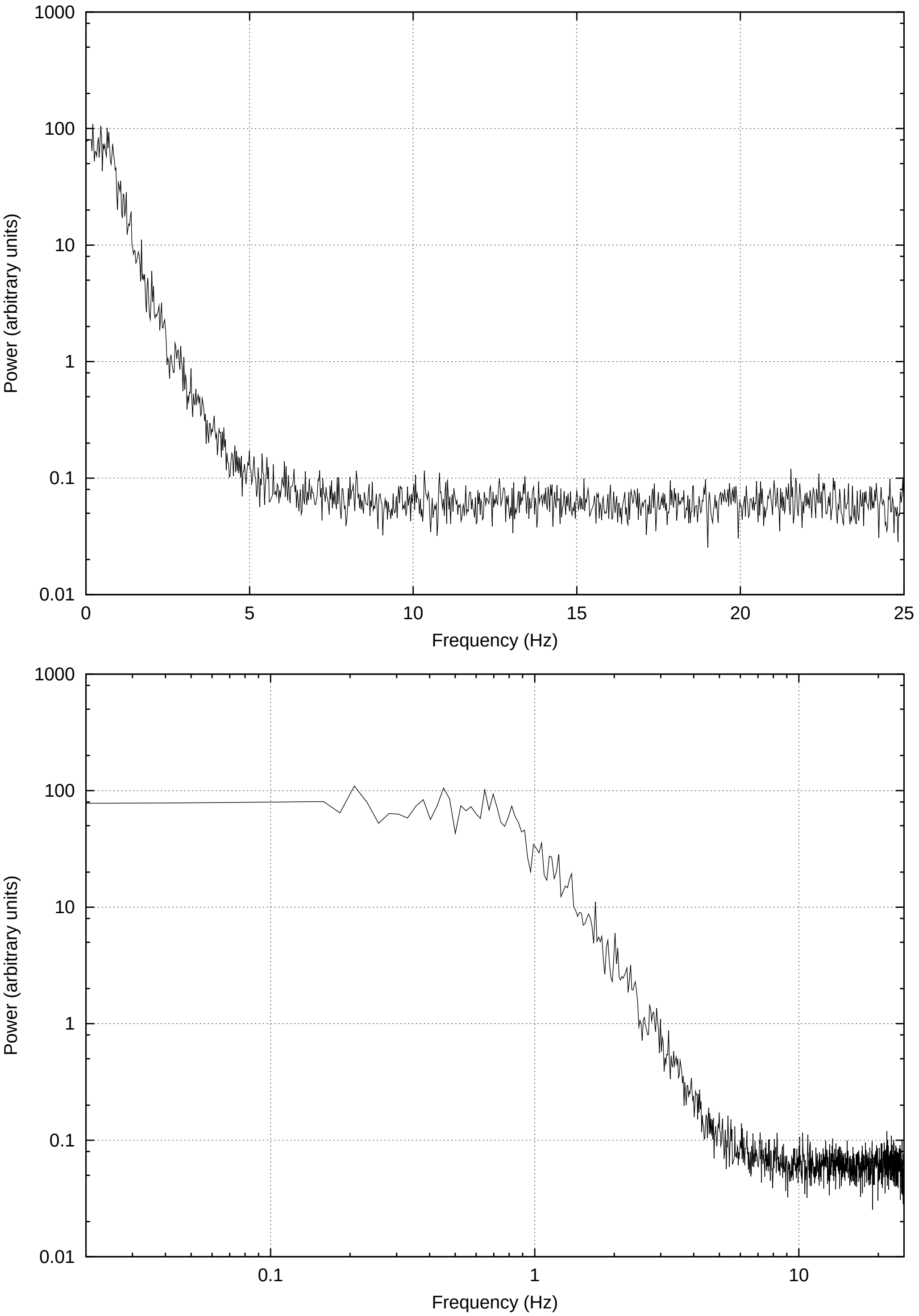

Figure 4.8: **An 'On-source' power spectrum** – The first panel shows a typical 'on-source' power spectrum in a log-linear scale while the second panel presents the same data in a log-log scale. Note that the power spectrum drops to flat noise floor by about 6 Hz.

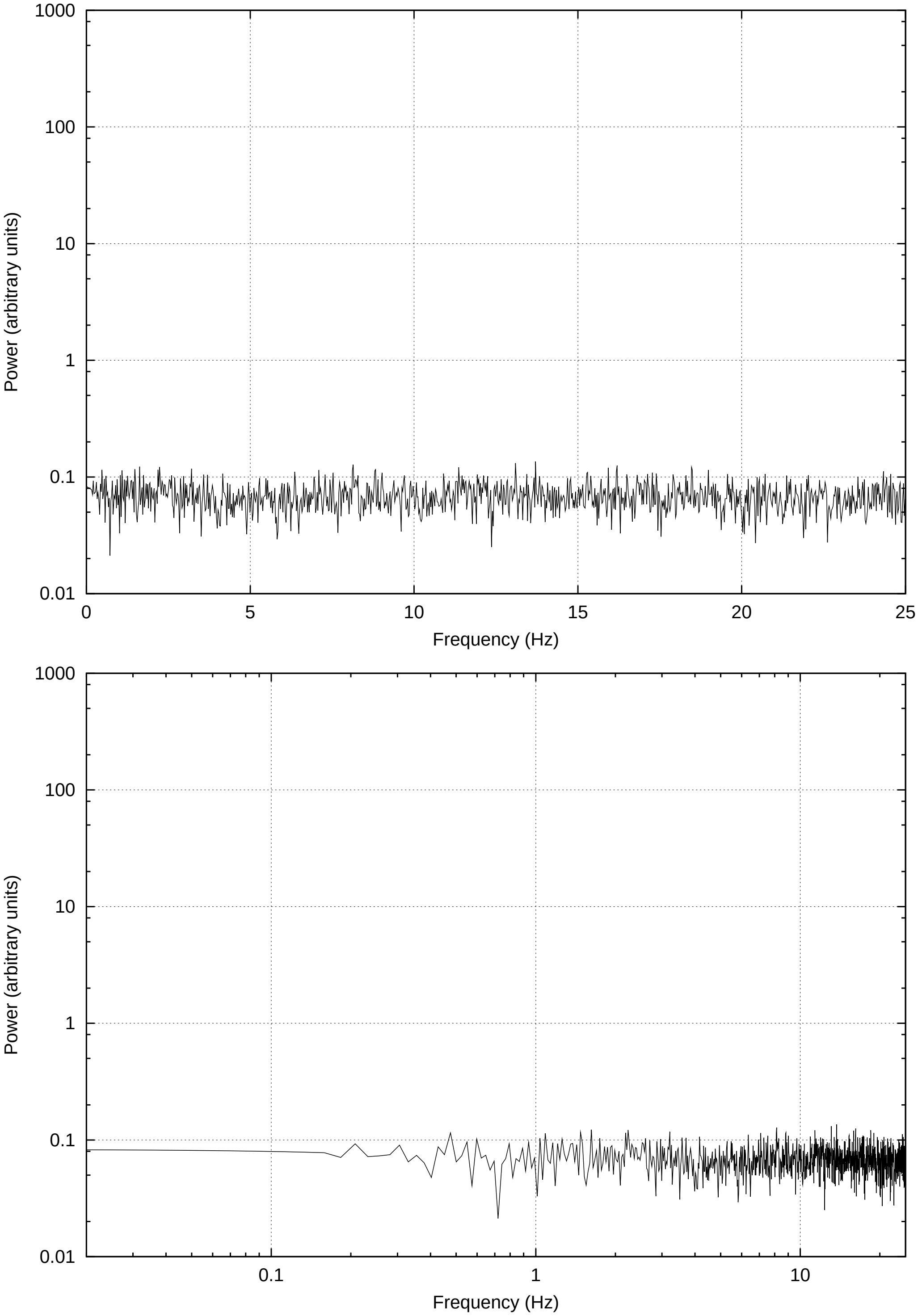

Figure 4.9: **An 'Off-source' power spectrum** – The first panel shows a typical 'off-source' power spectrum in a log-linear scale while the second panel presents the same data in a log-log scale. The power spectrum remains featureless in its entire range.

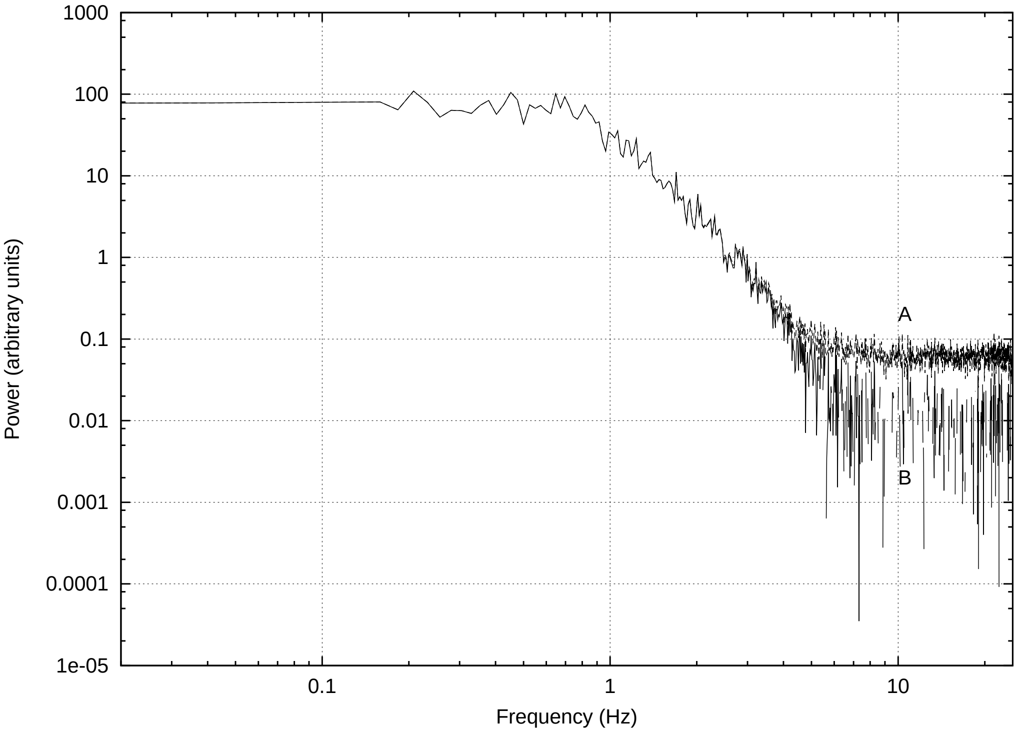

Figure 4.10: **Subtraction of the system noise from the power spectrum** – The power spectrum before and after the subtraction of the system noise, labelled **A** and **B** respectively, are shown. The system noise is estimated from the part of the power spectrum which does not receive contribution from IPS. The power spectrum after system noise subtraction becomes zero mean above 8 Hz and hence must necessarily become $-$ve on occasions. The *broken* appearance of the noise subtracted spectra in the high frequency region is because $-$ve values of the spectrum cannot be represented on a log scale.

same statistical process. The fractional uncertainty in the power spectrum for a given scan would therefore be :

$$\frac{\delta P(\nu)_{obs}}{P(\nu)_{obs}} = (N_{records})^{-\frac{1}{2}} \tag{4.7}$$

where $N_{records}$ is the number of records available in the scan. $N_{records}$ was typically between 10 and 18 for the present data-set. As different spectral points are also independent measurements, fractional uncertainty in $P(\nu)_{obs}$ can further be reduced, at the cost of spectral resolution, by averaging adjacent spectral points. The fractional uncertainty would then be given by :

$$\frac{\delta P(\nu)_{obs}}{P(\nu)_{obs}} = (N_{records} \times N_{avg})^{-\frac{1}{2}} \tag{4.8}$$

where N_{avg} is the number of spectral points averaged to produce a single point in the final power spectrum. An N_{avg} of 4 has been used in the power spectra shown in Figures 4.8 and 4.9. Strictly speaking, the above equation holds when no taper is used. On using a taper, the effective N_{avg} is smaller than the number of spectral points averaged over. The quantity of interest, the ratio of uncertainty in $\delta P(\nu)_{IPS}$ to $P(\nu)_{IPS}$, is given by the following equation :

$$\frac{\delta P(\nu)_{IPS}}{P(\nu)_{IPS}} = \frac{\delta P(\nu)_{obs}}{P(\nu)_{obs} - P(\nu)_{sys}} \tag{4.9}$$

The frequency dependence of equation 4.9 can be seen more clearly if it is expressed as :

$$\frac{\delta P(\nu)_{IPS}}{P(\nu)_{IPS}} = \frac{\delta P(\nu)_{obs}}{P(\nu)_{obs}} \left(\frac{1}{1 - P(\nu)_{sys}/P(\nu)_{obs}} \right) \tag{4.10}$$

In the regime where $P(\nu)_{obs} \gg P(\nu)_{sys}$, the RHS of equation 4.10 is practically a constant independent of frequency (Equation 4.8). When $P(\nu)_{obs}$ becomes comparable to $P(\nu)_{sys}$, the denominator approaches 0, increasing the fractional uncertainty in $P(\nu)_{IPS}$ to very large values.

Uncertainty in $A_{P(\nu)}$ was computed using rules of propagation of errors and equation 4.5, which yielded the following expression :

$$(\delta A_{P(\nu)})^2 = \left(\frac{d\nu_1}{2}\right)^2 (\delta P_1)^2 + \sum_{i=2}^{N-1} \left(\frac{d\nu_{i-1} + d\nu_i}{2}\right)^2 (\delta P_i)^2 + \left(\frac{d\nu_N}{2}\right)^2 (\delta P_N)^2 \tag{4.11}$$

with δP_i given by equation 4.9. The first and the last terms on the RHS of the Equation 4.11 take care of the lowest and the highest ends of the spectrum. Figure 4.11 shows the percentage uncertainty in $A_{P(\nu)}$ for all the scintillating sources observed in a log-log plot. The percentage uncertainty decreased rapidly as $A_{P(\nu)}$ increased. Figure 4.12 presents the histogram of distribution of the uncertainty

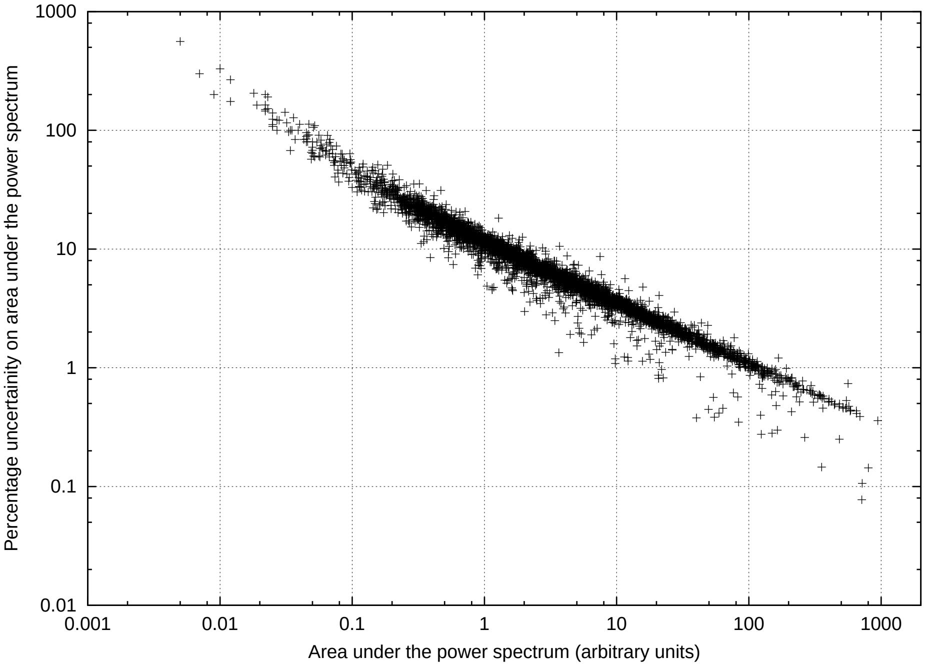

Figure 4.11: **Percentage uncertainty in $A_{P(\nu)}$** – The graph shows percentage uncertainty in $A_{P(\nu)}$ as a function of $A_{P(\nu)}$ on a *log–log* plot. There is a very well defined trend for the uncertainty to decrease with increase in $A_{P(\nu)}$.

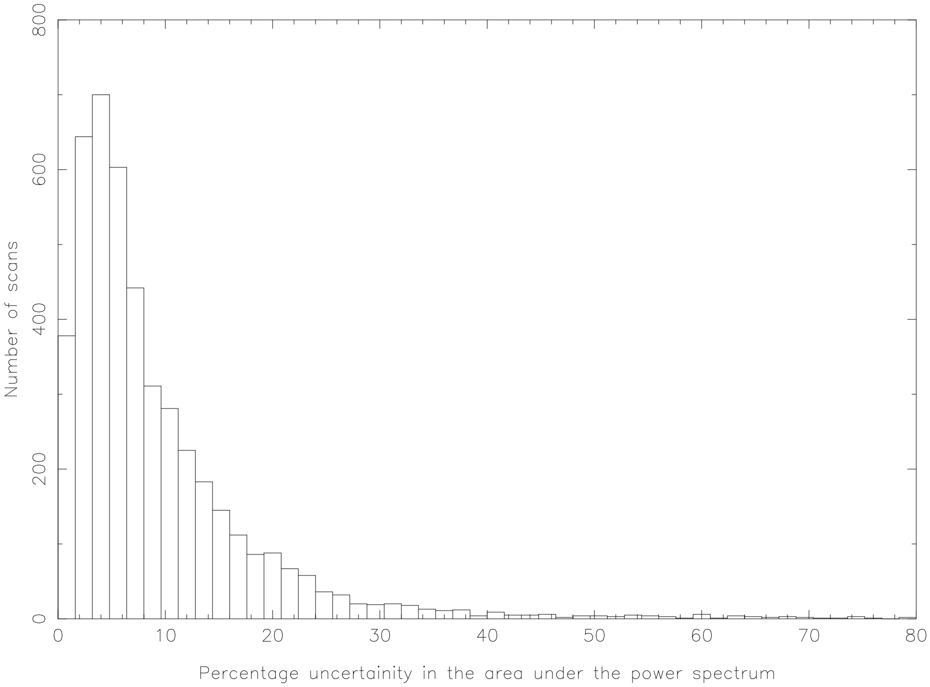

Figure 4.12: $\delta A_{P(\nu)}$ **distribution** – The figure shows the distribution of percentage uncertainty in $A_{P(\nu)}$. Most of the observations have uncertainties less than 20%.

in $A_{P(\nu)}$. While Figure 4.12 shows the distribution for the observations of only scintillating sources, Figure 4.11 shows the entire data-set including off-source and calibrator observations. Typically, the data points at values lower than 0.25 on the X axis in Figure 4.11 come from off-source observations. The observations constitute a data-set with rather good S/N as most of the observations have uncertainties less than 20%.

4.5.5 Uniform statistical averaging of the power spectra

The analysis procedure detailed in the Section 4.5.3 provides power spectra with the system noise subtracted and spectral points spaced uniformly along the ν axis and a progressively decreasing S/N with increase in frequency. However, for fitting spectra it is desirable to have a power spectrum with constant fractional uncertainty across the entire frequency range. The variation of fractional uncertainty across the power spectrum can be made acceptably small by averaging an increasing number of spectral points with increase in frequency. This averaging procedure is referred to as *uniform statistical* averaging, in the following text and has also been used by previous workers in the field (Manoharan, 1991; Gothoskar, 1994). The number of spectral points to be averaged follow form the relation :

$$N_{avg} = k\ \nu \tag{4.12}$$

where k is a constant which was chosen to be 4. An additional constraint that a minimum of 4 spectral points be averaged was also enforced. This leads to an increasingly coarser resolution with frequency. While only 4 spectral points need to be averaged at 1.0 Hz yielding a frequency resolution of $\sim$ 0.1 Hz, 40 spectral points need to be averaged at 10.0 Hz, limiting the frequency resolution to $\sim$ 1.0 Hz. The final power spectrum thus obtained has 45 spectral points. The spectral points are equispaced in $log(\nu)$ scale beyond $\sim$ 1.0 Hz. Figure 4.13 shows the same power spectrum as shown in Figure 4.10 after uniform statistical averaging. Error bars shown correspond to 1σ. The dashed horizontal line marks the system noise level which has been subtracted out from the power spectrum. The size of the error bar remains practically the same over the entire frequency range, when plotted on a *log* scale, till the power spectrum drops below the system noise level. This implies that the fractional error on the power spectrum is almost constant across the entire frequency range of interest. Uniform statistically averaged power spectra were used for the entire analysis procedure detailed in this thesis and all the spectra presented now on have been so averaged. Such averaging schemes are particularly useful for fitting power law spectra where the need for frequency resolution decreases at high frequencies.

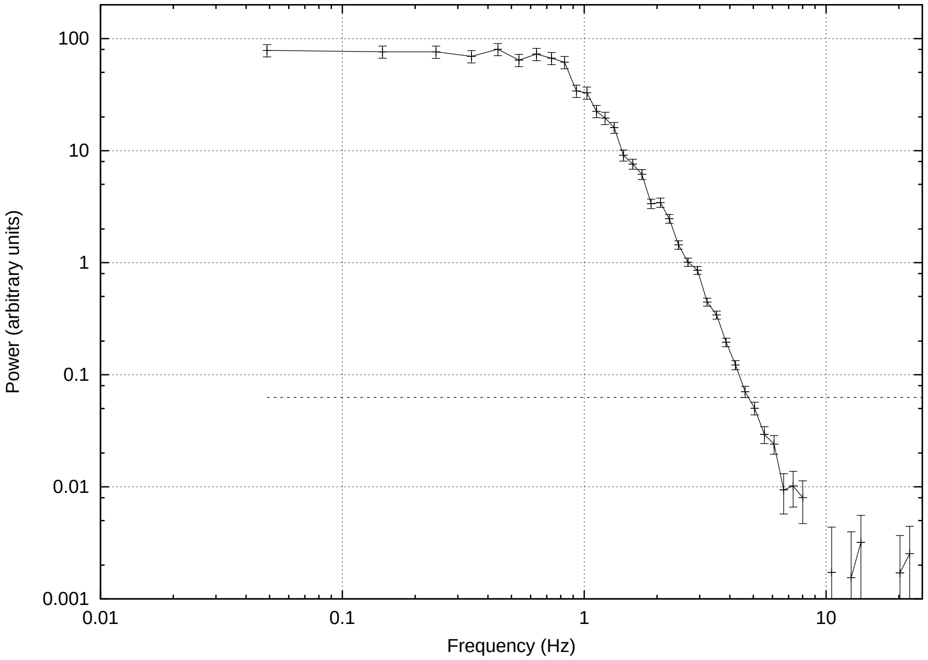

Figure 4.13: **Uniform statistically averaged power spectrum** – The same power spectrum as presented in figure 4.10 is shown after uniform statistical averaging. Little change in the size of 1σ error bars across the power spectrum, on a *log* scale, imply that the fractional uncertainty remains practically a constant. The horizontal dashed line marks the system noise level which has been subtracted from the power spectrum.

4.5.6 Computing the scintillation index

The primary definition of scintillation index, m, is given by equation 2.4 (Section 2.2) for noise free data. The operational definition needs to be modified due to the presence of the receiver noise in the data. In practice, because of the receiver noise, σ_{IPS} is not a direct observable. The intensity fluctuations observed for a scintillating source, have contributions both from the scintillating source and the receiver noise. Since the two are independent, we can write :

$$\sigma^2_{ON} = \sigma^2_{IPS} + \sigma^2_{Reciever} \tag{4.13}$$

If we assume that the measured σ_{OFF} is the same as the $\sigma_{Reciever}$, we can then express m as :

$$m = \frac{\sqrt{\sigma^2_{ON} - \sigma^2_{OFF}}}{C_{ON} - C_{OFF}} \tag{4.14}$$

where C_{ON} and C_{OFF} are the on-source and the off-source counts respectively and σ^2_{ON} and σ^2_{OFF} the on-source and the off-source variances respectively. This definition of m, apart from its ease of implementation, offers the advantage that it does not depend on flux calibration and is hence free of the errors associated with it. However, these advantages get offset by the following disadvantages of using this definition for m :

1. The detector used has a finite RC time constant, τ, which tends to smoothen the input signal and thus leads to an underestimate of the rms of intensity fluctuations. It is not possible to correct the data for the this effect from the time series alone.

2. An independent estimate of the system noise, C_{OFF}, obtained by looking at a different direction in the sky is required. This may not be strictly correct in some cases, due to the changes in the temperature of the sky background.

The area under the power spectrum, $A_{P(\nu)}$, is a measure of σ_{IPS} and can therefore be used to compute m using equation 2.13. This approach does not suffer from the above disadvantages since the correction for the RC time constant can be applied in the spectral domain and the contribution from the system noise can easily be estimated from the on source spectrum itself and removed from $A_{P(\nu)}$ (Section 4.5.3). The expression used to compute m is given by the equation :

$$m^2_{raw} = \frac{1}{I^2_{\circ}} \int_{\nu=0}^{\nu_c} \left(P(\nu)_{obs} - P(\nu)_{sys}\right) d\nu \tag{4.15}$$

where $P(\nu)_{obs}$ is the observed power spectrum and $P(\nu)_{sys}$ is the contribution due to system noise, estimated as described in Section 4.5.3. As the contribution of IPS to the $P(\nu)_{obs}$ drops below $P(\nu)_{sys}$ by about $\sim 6\ Hz$, it is not meaningful to include the part of the power spectrum beyond this range for the computation of m. ν_c represents the cut-off frequency the power spectrum beyond which was not included in computing m and represents the frequency where $P(\nu)_{IPS}$ becomes comparable to $P(\nu)_{sys}$.

Equation 4.15 uses the total flux of the source to compute the scintillation index. For sources which have both compact and extended components, the flux from only the compact component contributes to the scintillations but sum of the flux from both the compact and the extended components figures in the denominator. While this leads to a useful estimate of the fraction of flux coming from the compact components if one is studying the sources themselves, our motivation here is to study the Solar Wind. It is more useful, for our purpose, to have scintillation indices which correspond to an effective scintillating source rather than retain the information of the fraction of flux in the scintillating component of the source. We have, therefore, chosen to normalise the observed scintillation index with, η, the fraction of the flux from the scintillating component of the source. The effective scintillation index which we use is given by :

$$m^2 = m^2_{point} = \frac{m^2_{raw}}{\eta^2} = \frac{1}{(\xi\ S_{327}\ \eta)^2} \int_{\nu=0}^{\nu_c} (P(\nu)_{obs} - P(\nu)_{sys})\, d\nu \tag{4.16}$$

where ξ is the conversion factor from raw counts to Jy. Using equation 4.5, m as expressed by the above equation, was functionally computed using the following expression :

$$m^2 = \frac{A_{P(\nu)}}{(\xi\ S_{327}\ \eta)^2} \tag{4.17}$$

As the sources chosen to be observed were taken from the catalogue of scintillating sources built up over the years, η for them was already available (Balasubramaniam, 1997; Manoharan, 1997a).

4.5.7 Estimating the uncertainty in scintillation index

The statistical uncertainty in m was estimated using the standard prescription for error propagation on equation 4.17. In order to compute the statistical uncertainty in m, the contribution of the uncertainty in the measurement of $A_{P(\nu)}$ and that in the estimation of ξ was taken into account. δm was then obtained using the following two equations :

$$(\delta m^2)^2 = \left(\frac{\delta A_{P(\nu)}}{A_{P(\nu)}}\right)^2 m^4 \ +\ 4\left(\frac{\delta\xi}{\xi}\right)^2 m^4 \tag{4.18}$$

$$\delta(m) = 2m\ \delta(m^2) \tag{4.19}$$

The errors in the values of η and S_{327} for a given source also add to the uncertainty in m. These errors are systematic in nature and are more difficult to estimate. Such errors lead to an over or under estimation of the numerical value of m by a constant multiplicative factor. Estimates of m for the same source can, therefore, still be compared with one another without being affected by these errors. The mean and median values for percentage uncertainty on m in the data-set were computed to be 12.4% and 12.5%, respectively.

4.5.8 Computing g values

While the m values provide a measure of the strength of scintillations, they depend on the angular size, $\theta_\circ$, of the source observed and elongation, as discussed in Section 2 and illustrated in Figure 2.7. Note that the dependence on the fractional flux of the scintillating component has been removed in our formulation.

These attributes of m seriously limit its utility when there is a need to compare observations on different sources or even observations on the same source at different epochs. A quantity which is independent of the parameters of the source observed and the known functional dependence on elongation is needed to be able to meaningfully compare the observations across sources and epochs. The parameter g, which can be obtained from m by removing its dependence on the $\theta_\circ$ and elongation is used for such purposes.

The elongation dependence of m is represented by a power law of the form :

$$m \propto \sin(\epsilon)^{-b} \tag{4.20}$$

where b has a value of 1.66 for uniform isotropic Solar Wind with a constant radial velocity. Dividing m by this functional dependence removes the elongation dependent effects of the uniform isotropic Solar Wind. In order to remove the effect of the angular size of the source, $\theta_\circ$, a ratio of m, computed theoretically, for a source of angular size $\theta_\circ$ to that for a true point source ($\theta_\circ = 0$) :

$$\Theta_{\theta_\circ}(\epsilon) = \frac{m_{\theta_\circ}(\epsilon)}{m_0(\epsilon)} \tag{4.21}$$

was constructed as a function of elongation. A uniform isotropic Solar Wind model was used for computation of m. This ratio was used to correct for the drop in m with increase in $\theta_\circ$ by dividing m by $\Theta_{\theta_\circ}(\epsilon)$. The expression for g after correction for the various effects mentioned above acquired the following form :

$$g' = \frac{m}{\sin(\epsilon)^{-b}\ S_{327}\ \Theta_{\theta_\circ}(\epsilon)} \tag{4.22}$$

Traditionally, g is normalised such that it's value is unity for normal Solar Wind conditions and it's deviation from unity is a measure of departure of the Solar Wind from normal quiet isotropic conditions.

Previous workers, especially the Cambridge group, have chosen to compute g by using the average $m-p$ curves for the source constructed using numerous observations of the same source at different elongations spread over many years. The value of g is the ratio of m observed for a given source at a specific elongation to the prediction from the best fit $m-p$ curve for the same source at the same elongation. g values computed in this manner are assured to be close to unity for quite Solar Wind conditions and the departures from unity can be can be used as indicators of disturbed Solar Wind conditions. We used the values of scintillating flux, η, determined using the Ooty Radio Telescope IPS observations over many years. In order to remove normalise out the proportionality constant in equation 4.20, we have chosen to normalise the individual g' values, computed as above, by the average value of g' for our observations.

$$g_i = \frac{g'_i}{\frac{1}{N}\sum_{j=1}^{N} g'_j} \tag{4.23}$$

Chapter 5

Single station IPS modelling

As discussed in Chapter 2, there exists an elaborate theoretical framework to model the power spectrum of intensity fluctuations observed towards a compact radio source, when the *l.o.s.* to it passes close to the Sun. The parameters of the model are the physical properties of the Solar Wind along the *l.o.s.*. Section 3.2.1 discussed the featureless model for Solar Wind, the most widely used model to arrive at the distribution of the properties of the Solar Wind along the *l.o.s.*. In the present chapter we discuss the details of the fitting procedure used to estimate the velocity and C_n^2 from the power spectra and describe the automated fitting procedure we developed to reduce the drudgery of manually fitting a large number of spectra.

5.1 Need for automated estimation of the best fit IPS model

Traditionally, the best fit Solar Wind model for the observed power spectra have been estimated by manually varying the parameters of the Solar Wind model and visually estimating the *goodness* of the fit (Manoharan and Ananthakrishnan, 1990; Manoharan, 1991; Gothoskar, 1994). If the data volumes are large, this is a very tedious task and is prone to human errors, besides being inherently subjective. The absence of an objective criterion for the goodness of the fit allows personal biases of the person fitting the IPS model to creep in.

Given the large volume of the data-set, for which the best fit IPS models was required, it was thought useful to automate this process. Apart from reducing the tedium and the possibility of human errors, this offers the significant advantage that the best fit IPS models estimated have been arrived at using an objective mathematical criterion.

5.2 Criterion for χ^2 definition

The most crucial element in the automated estimation of the best fit IPS model is the prescription for quantifying the departures of the observed power spectrum from the spectrum computed using a model of the Solar Wind. We refer to this quantitative measure as the χ^2 of the observed spectrum with respect to the model power spectrum. The χ^2 must mimic the criterion used by an intelligent human being to estimate the best fit model. The closer the χ^2 definition captures the criterion of visual fit (relied upon by human beings) closer will be the best fits determined by the automated procedure to the best fits to which the human being would have converged. Once the useful χ^2 definition has been arrived at, there are several algorithms available to perform the actual task of multidimensional χ^2 minimisation.

The power spectrum of intensity fluctuations often spans more than two orders of magnitude along the ordinate. In order to discern the effects of variations of physical properties of the Solar Wind on the power spectra and to accommodate the large span along the ordinate, it is necessary to visualise the power spectra on log – log scales. An example of the power spectrum for which the IPS best fit model needs to be estimated is shown in Figure 4.10. To be useful as a criterion for the goodness of fit, the χ^2 should be defined keeping the following considerations in view :

1. While trying to arrive at a good visual fit, the eye tries to ensure that the deviations between the model power spectrum and the observed power spectrum remain comparable all through the relevant frequency range as seen on a *log – log* scale. This leads to the following considerations:

   (a) As the power spectrum spans a very large range in power, it is important to ensure that the χ^2 is not dominated by contributions from the low frequency part of the power spectrum which has the highest power. Trying to achieve a reasonable fit all through the relevant frequency range is, mathematically, same as trying to ensure that the χ^2 be sensitive to fractional deviations between the model and the data rather than the magnitude of the deviations. In order to ensure that equal fractional deviations get weighted equally, χ^2 should be computed using $log(P(\nu))$ rather than $P(\nu)$.

   (b) The available power spectrum has spectral points uniformly distributed along the frequency axis. On a $log(\nu)$ scale, this leads to a sparely populated power spectrum at the low ν end and a crowding of points at the high ν end. Most of the contribution to χ^2 comes from the high ν part of the power spectrum as most of the points populate that part of the spectrum. To arrive at a reasonable fit along the entire frequency range on a *log* scale, it must be ensured that χ^2 receives equal contributions from equal intervals in $log(\nu)$.

2. The contribution of each spectral point to the χ^2 should be weighted by the inverse of the statistical uncertainty on the power corresponding to the spectral point. As has been shown in Figure 4.10 and explained in Section 4.5.4, the S/N deteriorates with increase in frequency. This causes the χ^2 to be dominated by the contributions from low ν good S/N part of the power spectrum, leading to a better fit in the low ν part as compared to the high ν part of the spectrum. In order to ensure a uniform quality of the model fit along the entire frequency range, the fractional uncertainty on the power spectrum should not change significantly across the power spectrum.

Both these requirements are met by the uniform statistically averaged power spectra described in Section 4.5.5.

5.3 Automated IPS model fitting

5.3.1 The Philosophy

Considering the above points, a prescription for quantifying the departures of a model power spectrum from the observed data should be arrived at. With a quantitative definition for χ^2 in place, automating the procedure of obtaining best fit IPS models is comparatively straightforward. The task can be thought of as a multidimensional χ^2 minimisation problem with the parameters of the IPS model forming the χ^2 degrees of freedom. The spectral points available in the power spectrum form the constraints and the error bars on them the weights of each of the constraints.

5.3.2 Definition of χ^2

Based on the discussion in Sections 5.2 and 4.5.5, the following definition was adopted to compute the normalised χ^2 between the IPS model and the observed power spectrum :

$$\chi^2 = \frac{1}{(N_D - N_{model})} \sum_{i=1}^{N_D} \left\{ \frac{log_{10}(P_{D\ i}) - log_{10}(P_{M\ i})}{\sigma_{P_{D}\ i}} \right\}^2 \tag{5.1}$$

where P_D and P_M are the observed and the model *uniform statistically averaged* power spectra respectively, with the index i running over the N_D spectral points available for computing χ^2, $\sigma_{P_D\ i}$ the inverse of the weight with which a given spectral point in the spectrum contributes to the χ^2, N_{model} the number of free parameters used in the χ^2 minimisation procedure and $N_D - N_{model}$ the number of χ^2 degrees of freedom.

The number of spectral points per octave is not a constant in the uniform statistically averaged spectra. While 9 spectral points lie in the range 0.1 – 1.0 Hz, there lie 25 spectral points in the octave from 1.0 – 10.0 Hz. To ensure that equal intervals in $log(\nu)$ contribute equally to the χ^2, the entire ν range of the power spectrum was divided in 10 equal bins. The $\sigma_{P_D\ i}$ for each spectral point of the power spectrum was made proportional to the number of spectral points which fall in the bin to which it belongs, $N_{\nu\ i}$, as is given by the following expression :

$$\sigma_{P_D\ i} = \frac{\delta P_{D\ i}}{P_{D\ i}}\ N_{\nu\ i} \tag{5.2}$$

where $\delta P_{D\ i}/P_{D\ i}$ is the uncertainty in the estimation of the uniform statistically averaged spectra. This ensured that equal bins in $log(\nu)$ contribute equally to the χ^2.

The IPS power spectrum usually cuts off by about $\sim$ 6 Hz and the spectrum beyond that is dominated by the system noise. The entire spectrum should therefore not be used for computing the χ^2 of the fit. We defined a cutoff frequency, ν_c, the spectrum beyond which was not used for computing the χ^2. ν_c is expected to separate the part of the power spectrum which receives significant contribution from IPS from the part which is dominated by the system noise. The system noise is estimated for each spectrum as explained in Section 4.5.3. Functionally, the second dip of the observed power spectrum to a level below the estimated system noise was used to mark the ν_c.

In addition to the statistical uncertainties, there is a possibility of systematic errors making significant contributions to the $\chi^2$and hence dominating the fit. In order to avoid such possibilities, the contribution to χ^2 from the parts of the spectrum most susceptible to systematic errors were weighted down. The power spectrum is susceptible to contamination from ionospheric scintillations at low ν (< 0.35 Hz). The $\sigma_{P_D\ i}$ for this part of the spectrum was increased by a factor of 2. The part of the power spectrum where the power level falls to the system noise level is most susceptible to systematic errors in the system noise level estimation and the break down of the assumption of system noise floor being flat. The $\sigma_{P_D\ i}$ for this part of the spectrum was increased by a factor of 3.

It is desirable to have a normalised χ^2 estimate where a numerical value significantly larger than unity indicates a poor fit to the data. In order to achieve this, the $\sigma_{P_D\ i}$ values need to be renormalised appropriately as their values have been modified. We choose the following normalisation, which ensures that the sum of the

$\sigma_{P_D\ i}$s does not change :

$$C = \frac{\sum_{i=1}^{N_D} \sigma'_{P_D\ i}}{\sum_{i=1}^{N_D} (\sigma'_{P_D\ i}\ N_{\nu\ i})} \tag{5.3}$$

where

$$\sigma'_{P_D\ i} = \frac{\delta P_{D\ i}}{P_{D\ i}}\ W_i \tag{5.4}$$

and W_i is the weight factor which is suitably modified to reduce the contribution from the low and high frequency parts of the spectrum, which are most susceptible to systematic errors. The final form for $\sigma_{P_D\ i}$ which was used in equation 5.1 is given by the following expression :

$$\sigma_{P_D\ i} = C\ \frac{\delta P_{D\ i}}{P_{D\ i}}\ W_i\ N_{\nu\ i} \tag{5.5}$$

5.3.3 The algorithm

A few different algorithms were considered for χ^2 minimisation and the non linear, un-bounded χ^2 minimisation algorithm due to Nelder and Mead (Nelder and Mead, 1965), the *Downhill simplex method*, was found to be most suitable for the task. This algorithm offers the advantage that it makes no special assumptions about the function being minimised and does not require the computation of the local gradients of the χ^2 in the multidimensional parameter phase space. This algorithm, being an unguided search, is not very efficient in terms of the number of function evaluations required but its robustness, in the present application, is an ample compensation and the computing time involved is not large enough to be of significant concern. The reader is referred to an illuminating discussion of this and other algorithms for multidimensional χ^2 minimisation by Press et al. (Press et al., 1992) from which this work has benefited substantially.

5.3.4 The Thin Screen power spectrum database

Finding the best fit IPS model for an observed power spectrum requires a large number of computations of power spectra along the given *l.o.s.* varying the model parameters of the Solar Wind. This, in turn, requires computation of the power spectra due to each of the thin screens along the *l.o.s.* with their properties specified by the Solar Wind model. A *l.o.s.* typically receives contributions from $\sim$ 200 thin screens. Computing every spectral point for a given thin screen spectrum involves an integration over q_y with an oscillating integrand (equation 2.35) and is computationally expensive. The repeated computation of the power spectra due to individual thin screens, therefore, forms the most computing intensive part of the exercise.

Table 5.1: **IPS model parameters available in the thin screen power spectra database** – This table gives the ranges of different IPS model parameters spanned by the thin screen power spectra database. The maximum and minimum values of the parameters, the increment and number of values of each of the model parameters available in the database are also provided. s_i is defined to be $3/q_i$. The database has $400 \times 14 \times 6 \times 5 \times 4 = 6.72 \times 10^5$ power spectra.

Parameter	Minimum value	Maximum value	Increment	No. of values
$z\ AU$	0.001	4.0	0.010	400
$\theta_\circ\ (mas)$	0	325	25	14
α	2.5	4.0	~ 0.3	6
AR	0.5	1.5	0.25	5
$s_i\ (km)$	0.0	50.0	12.5	4

An examination of the structure of the expression for the power spectrum (equation 2.55) shows that the two most important model parameters, v and C_n^2, can be brought outside the thin screen integral. C_n^2 is a constant which multiplies the thin screen power spectrum. An increase or decrease in the value of C_n^2 has the effect of sliding the entire spectrum up or down the ordinate without changing its shape, when seen on a log scale. v has the effect of a scaling on the ν axis and leads to *stretching* or *contracting* along the ν axis as it increases or decreases. All the other models parameters, namely $AR, \theta_\circ, \alpha$ and q_i $(= 3/s_i)$ occur in the integrand in a manner that they cannot be brought out of the integral. This presents the possibility that the thin screen power spectra corresponding to the expected values of Solar Wind and source parameters can be computed once and tabulated. When required, they can be read off from the table and can be scaled as required by the Solar Wind model.

A database of thin screen power spectra was computed spanning adequate ranges of the IPS model parameters with sufficiently small step sizes. The range and step sizes of the model parameters were decided on the basis of the discussion in Section 2.6 and are presented in Table 5.1. The database contains the power spectra as a function of $z, \theta_\circ, \alpha, AR$ and s_i. The following equation used to generate the power spectra for the database :

$$P_{q_x} = \int_{q_y=0}^{q_y\ max} dq_y\ sin^2\left(\frac{q^2 z}{2k}\right)\ exp(-qz\theta_\circ)^2\ \left(q_x^2 + \frac{q_y^2}{AR^2}\right)^{-\alpha/2}\ exp(-q/q_i)^2 \qquad (5.6)$$

Each of the thin screen power spectra in the database comprises of 200 spectral points. The q_x range covered by the computed spectrum was from 1.0×10^{-7} to $3.5 \times 10^{-4}\ m^{-1}$. For each q_x, the q_y range over which the integral was performed was from 0.0 to 2.5×10^{-3} m^{-1}. Various innovations were used in computing and organising the database. The presence of the Fresnel filter term in the integrand makes it oscillatory function with numerous nulls. Such a function demands exercise of caution while integration. The amplitude of the oscillations decreases rapidly with increasing q_x and so does the spacing between the successive nulls. This fact was exploited in carrying out the integration. The first 10 nulls of the Fresnel filter were located and the q_y range between consecutive nulls was individually integrated over. The Fresnel filter term was replaced by its average value of 0.5 beyond the 10^{th} null. In order to cover the large q_x range using a small number of spectral points while retaining a good spectral resolution in the q_x range of interest, the q_x range was divided into two parts. The q_x range between 1.0×10^{-7} and 8.0×10^{-5} was represented by 165 spectral points with a δq_x of 4.9×10^{-7} so that the oscillations due to the Fresnel filter are adequately sampled. Such fine resolution in q_x is not required in the region where the Fresnel filter has been replaced by its average value. This q_x range from 8.0×10^{-5} to 3.5×10^{-4}, had spectral points spaced uniformly in $log(q_x)$ scale and had only 35 spectral points.

The database can be thought of as a 6 dimensional array with $s_i, AR, \alpha, \theta_\circ, z$ and q_x being the six dimensions. The database itself took ~ 150 hrs to compute (using a single CPU of a Silicon Graphics Origin 200), is ~ 540 MB in size and contains 6.72×10^5 power spectra. The database is much too large for a thin screen spectrum of interest to be located by simply reading through it. The time taken for locating a spectrum significantly offsets the gains due to not having to compute it because of the limitations of the disk I/O speed. An efficient mechanism to locate the thin screen spectrum corresponding to the given values of the Solar Wind and geometry parameters was necessary. This was achieved by constructing a 5 dimensional array of pointers, whose indices corresponded to the values of the Solar Wind and the geometry parameters of the required thin screen spectrum and the pointer value to its location in the database.

The use of this database of thin screen power spectra reduced the time required to compute the power spectra along a $l.o.s.$ by almost 3 orders of magnitude. This phenomenal reduction in the run time was of crucial importance in making the exercise of automated best fit IPS model estimation viable. The estimation of best fit IPS models is only the first step towards the final aim of this work which is the reconstruction of the structure of the Solar Wind in the inner heliosphere. This task, which is much more demanding in terms of computing power requirements and is orders of magnitude more complex than finding the best fit IPS models, came into the realm of the possible only because of the massive reduction in run time achieved by the use of a database of thin screen power spectra.

5.3.5 Model parameters

The effects of variations of various IPS model parameters on the power spectrum have been discussed in the Section 2.6. The most important parameters for the present study are v and C_n^2 on a reference surface and they were always treated as free parameters of the IPS model. Given their values on this surface, $v_\perp(z)$ and $C_n^2(z)$ were geometrically computed using a featureless Solar Wind model. s_i and $\theta_\circ$ both effect the power spectrum in a similar manner. Both of them should, therefore, not be treated as free parameters simultaneously. To investigate the effects of variation of s_i with radial distance, we chose to freeze s_i to value close to 0 km and allowed $\theta_\circ$ to be a free parameter. Evolution of s_i with radial distance from the Sun should appear as a trend in the $\theta_\circ$ as a function of P-point distance of the $l.o.s.$. No evidence for such a trend was seen. The effects due to change in s_i were therefore not considered important and have been ignored in the IPS model. The value of s_i has been set to close to 0.0 km and the contribution from its constant value has been absorbed in the $\theta_\circ$ estimate. Based on the justification presented in Section 2.6, AR was held fixed at a value of 1.0. The $l.o.s.$ was modelled out to a distance of 3 AU. The contribution from the part of the $l.o.s.$ beyond this are $\sim 1.0\%$ even for the largest ϵ observed (Section 3.2.1).

A prudent choice was made for the initial guess which started the minimisation not too far from the expected minima. This helped in converging to the minima in a smaller number of iterations and reduced the possibility of wandering down some pathological local minima. The initial guess for v was arrived at using the second moment of the power spectrum, f_2, as a crude indicator of the average v of the Solar Wind sampled by the $l.o.s.$. The observed m was used to generate an initial guess for the C_n^2.

The $\theta_\circ$ known from earlier IPS observations (V. Balasubramanian, personal communication) were used as the starting guess. Average best fit $\theta_\circ$ was computed using all the observations of the given source. There was, usually, small scatter in the values of the $\theta_\circ$ estimated from different observations of the same source. No evidence for a discernible trend in $\theta_\circ$ as a function of ϵ emerged. This is not unexpected as the mean angular source size for our data-set is $122 mas$, large enough for the power spectrum to be dominated by the source size filter and the effects of s_i are much smaller in comparison (Section 2.6). Hence change in s_i with ϵ was not considered important. In subsequent runs of the best fit IPS model estimation, the $\theta_\circ$ was frozen to the average value arrived at in the earlier run.

5.3.6 Correction for the Earth's velocity

As IPS measures the apparent velocity of the Solar Wind perpendicular to the *l.o.s.*, the motion of the Earth around the Sun also contributes to it. Assuming a circular orbit for the Earth, the component of Earth's velocity perpendicular to the *l.o.s.* observed is given by the following equation :

$$v_{E,\perp} = v_E \; sin(\epsilon) \; cos(\theta) \tag{5.7}$$

where v_E is the average speed of the Earth in its orbit and is equal to 29.7 $km \; sec^{-1}$, ϵ the elongation of the source being observed and θ its ecliptic latitude. This leads to a significant systematic bias in the velocity estimates. This effect is most pronounced in the plane of the ecliptic, where $\cos(\theta) \sim 1$, to which most of the present observations are confined. This bias was corrected for by subtracting the contribution of the motion of the Earth around the Sun from the velocity estimates arrived at using IPS modelling.

The maximum bias introduced by ignoring the eccentricity of the Earths orbit is $\sim$ 0.5 $km \; sec^{-1}$, which is much smaller than the uncertainty in the best fit v estimated for a power spectrum.

5.3.7 Generality of the formalism

In the discussion in this chapter, the featureless Solar Wind model has been used to determine the IPS model parameters to be assigned to the thin screens along the *l.o.s.*, since this is the only reasonable choice available in absence of any other information about the Solar Wind along the *l.o.s.*. However the formalism we have developed treats the IPS model parameters assigned to each of the thin screens as independent quantities and imposes no such restriction. This feature of the formalism was exploited later to compute power spectra corresponding to an arbitrary distribution of Solar Wind properties along the *l.o.s.*and has been discussed in Section 7.5.

5.4 The simulations

The accuracy and precision of the automated IPS model estimation procedure was estimated by synthesising power spectra using a featureless Solar Wind model with known parameters and subjecting them to the automated best fit estimation procedure. v and C_n^2 were treated as free parameters of the χ^2 fit. Simulations were done with both *noiseless* power spectra and with spectra with appropriate noise added. The statistical uncertainty on the power spectrum can be computed given the power

Table 5.2: **Results of automated IPS model estimation simulations** – The first column specifies if the simulations had noise added to them, the second column gives the ratio of the mean best fit velocity to the true velocity used and the third column gives the ratio of *rms* of the best fit velocities to the true velocity in percentage. Columns four and five present the same information for C_n^2 as columns two and three for velocity.

Noise Added	$\overline{v_M}/v_D$	σ_{v_M}/v_D %	$\overline{C^2_{n\ M}}/C^2_{n\ D}$	$\sigma_{C^2_{n\ M}}/C^2_{n\ D}$ %
No	0.9989	0.17	0.9999	0.03
Yes	1.0011	2.19	1.0025	5.52

spectrum itself and has been computed using the equation 4.9. The geometry parameters of the actual observations were used to compute the power spectra. About 4000 power spectra were computed and the best fit models to them estimated. The parameters of the IPS model were accepted as the best fits when further iterations of the minimisation algorithm decreased the fractional χ^2 by amounts smaller than 10^{-4}. It should be pointed out that the criterion for terminating the minimisation process depends on the fractional change in the χ^2 value as the minimisation proceeds and is independent of the magnitude of the χ^2.

The results of the simulations are presented in Table 5.2. The results are presented as a ratio of the mean best fit velocity estimate, $\overline{v_M}$, to the value of velocity which was used to generate the data, v_D. The ratio of *rms* variation of σ_{v_M} to v_D is also presented. σ_{v_M} is defined as :

$$\sigma_{v_M} = \sqrt{\frac{\sum_{i=1}^{N}(v_M - \overline{v_M})^2}{N}} \tag{5.8}$$

where N is the number of power spectra used in this study. The results for C_n^2 are presented in a similar manner.

The distribution of χ^2 values obtained, for both noise free and noise added simulations, is presented in Figure 5.1. The χ^2 distribution for the noiseless simulations has a median value of 1.90×10^{-5} and a mean of 8.80×10^{-4}. The largest value of χ^2 obtained is 2.14×10^{-1}. For the noise added simulations, the median value of the χ^2 distribution is 6.38×10^{-2} and its mean is 6.94×10^{-2}. The largest value of χ^2 obtained is 2.43×10^{-1}. The automated fitting procedure typically converged in about 30–70 iterations and took, on an average, 0.95 sec to estimate the best fit model for one spectrum.

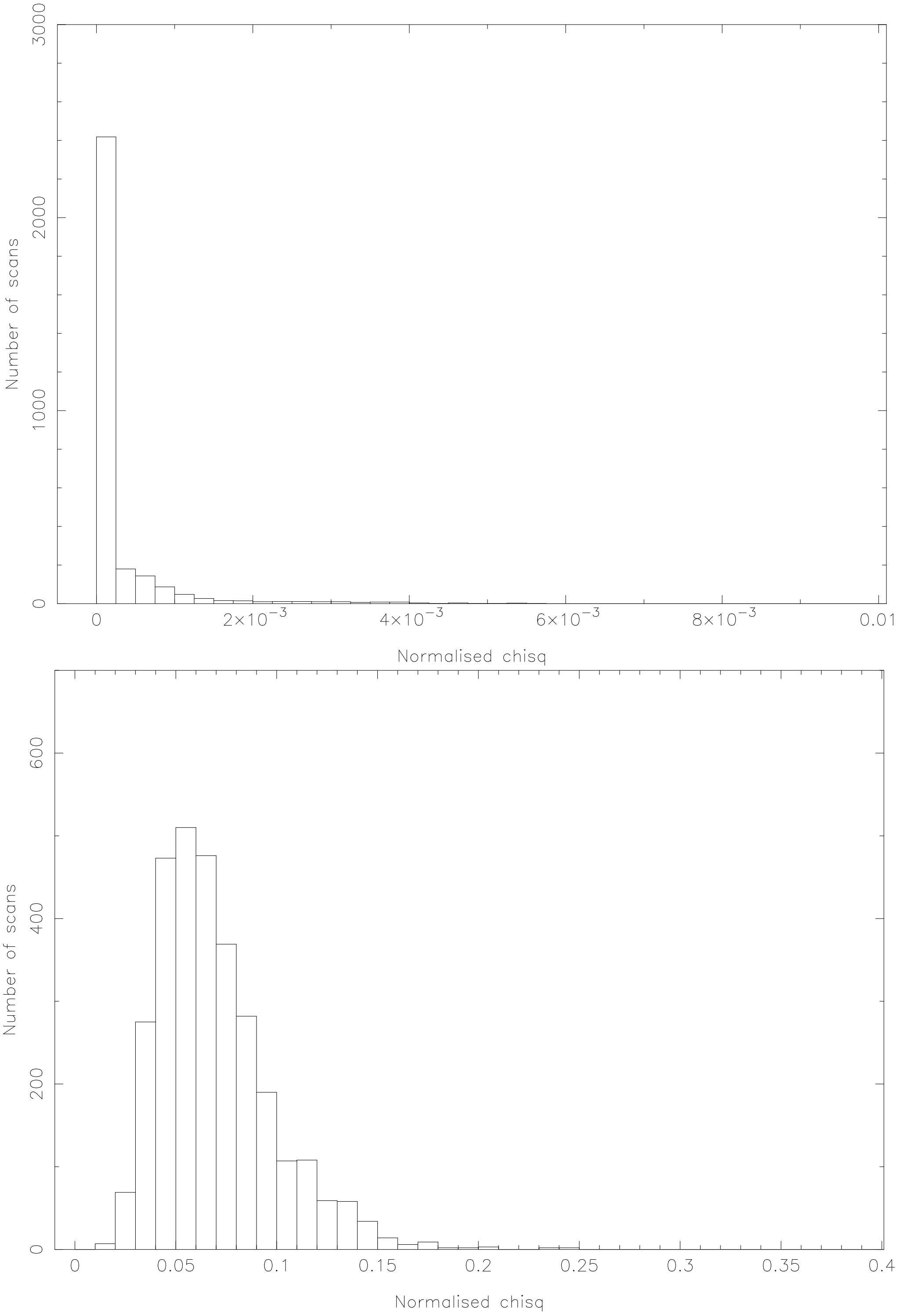

Figure 5.1: **Distribution of χ^2 for simulated data** – The χ^2 distributions for the noise-free simulations is shown in the first panel and that for the noise added simulations in the second panel. The median and mean for the noise-free simulations are 1.90×10^{-5} and 8.80×10^{-4} respectively. The same numbers for the noise added simulations are 6.38×10^{-2} and 6.94×10^{-2}. Note that the ranges of the χ^2 on the two plots are very different.

For the noise-free simulations, where the minimum achievable value of χ^2 is 0.0 and the automated procedure performs very well by giving a median value of 1.90×10^{-5}. It should be noted that the automated procedure achieved a median χ^2 which differs from the minimum achievable value by about the same amount as criterion specified for terminating the minimisation procedure ($\Delta\chi^2/\chi^2 < 1.0 \times 10^{-4}$) This implies that the χ^2 has a well defined minima in the parameter space with a sufficiently large gradient in its vicinity for the minimisation process to climb down right to the bottom of the valley. The χ^2 is, therefore, sensitive to changes in the values of the parameters of the model. In the case of noise added simulations, the minimum achievable value of χ^2 is related to the statistics of the added noise and is necessarily a positive definite quantity greater than 0.0. In addition, the gradient of χ^2 as a function of model parameters would be noisier close to the minima because the χ^2 itself would no longer be a smoothly varying function of the model parameters. The median value of the χ^2 distribution for the noise added simulations is therefore larger than that for the noise-free case but is still small enough to represent a remarkably good fit in the χ^2 sense. As mentioned in the Table 5.2, the values of fit parameters obtained differ only by a few % from the true values. The automated best fit IPS model estimation procedure was thus established to work reliably.

5.5 The results

The automated spectral fitting procedure was then applied to the observed power spectra. The distribution of χ^2 obtained for the observed power spectra, using the automated fitting procedure, is shown in Figure 5.2. The χ^2 distribution has a pronounced peak at ~ 0.2, a median value of 0.32 and a mean of 0.52. From equation 5.1 it can be seen that a small value for χ^2 can be obtained only if the differences between the model and the data are small as compared to the uncertainty in the data. For a given spectrum, a lower χ^2 for the same model can be obtained by assigning a larger uncertainty to the data. The χ^2 is thus a measure of the *significance* of the deviations of the model from the data. A value of normalised χ^2 of the order of unity is considered to represent a reasonable fit to the data. The data used in this study has good S/N, as discussed in Section 4.5.4 and shown in Figure 4.11. The median value of the χ^2 distribution (0.32) therefore implies that the model truly represents the data well in most cases. The featureless IPS model therefore offers an adequate description for the Solar Wind for most of the observed spectra. The estimates of $\theta_\circ$ from the automated fitting procedure matched the estimates arrived at by conventional manual best fit estimation very well.

Figure 5.3 presents the χ^2 obtained as a function of the error on the area under the power spectrum, $\delta A_{P(\nu)}$, which is a good indicator of the Signal to Noise (S/N) of the observed power spectrum. A trend is seen for χ^2 to decrease as $\delta A_{P(\nu)}$ increases,

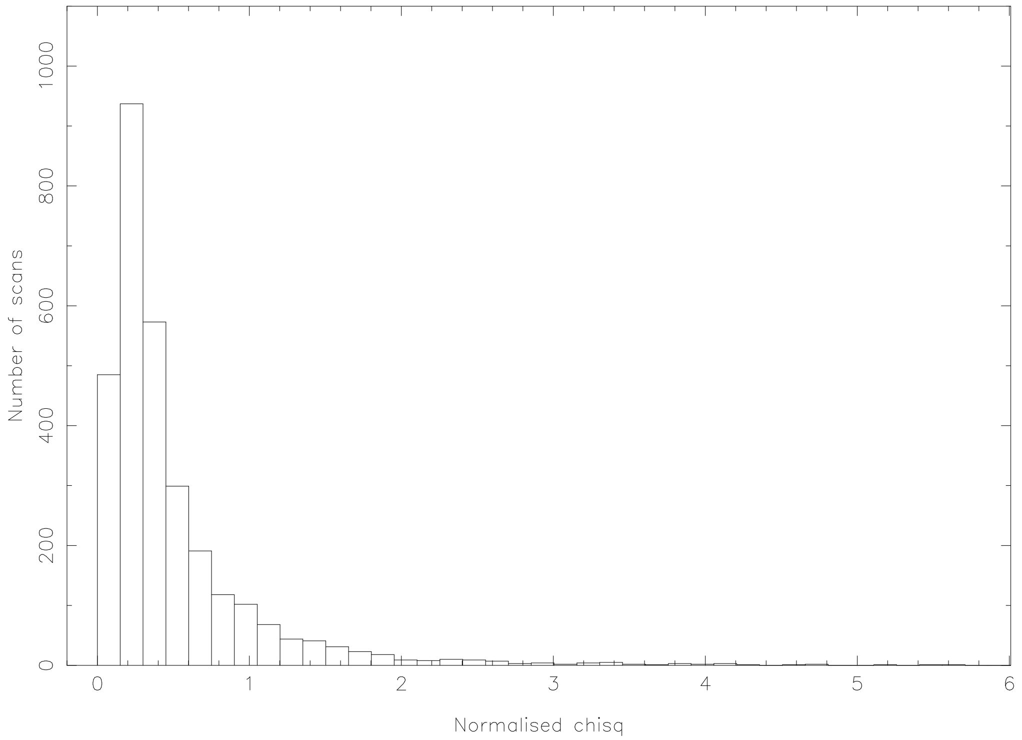

Figure 5.2: **Distribution of** χ^2 – The histogram shows the distribution of χ^2 for the IPS best fit models arrived at using the automated procedure. The distribution has a pronounced peak at ~ 0.2, a median of 0.32 and a mean of 0.52. The fact that the median and the mean values of the χ^2 distribution are significantly less than unity implies that the model chosen represents the data very well in a vast majority of cases. Of the about 4000 spectra fitted, 11.2% had χ^2 greater than 1.0.

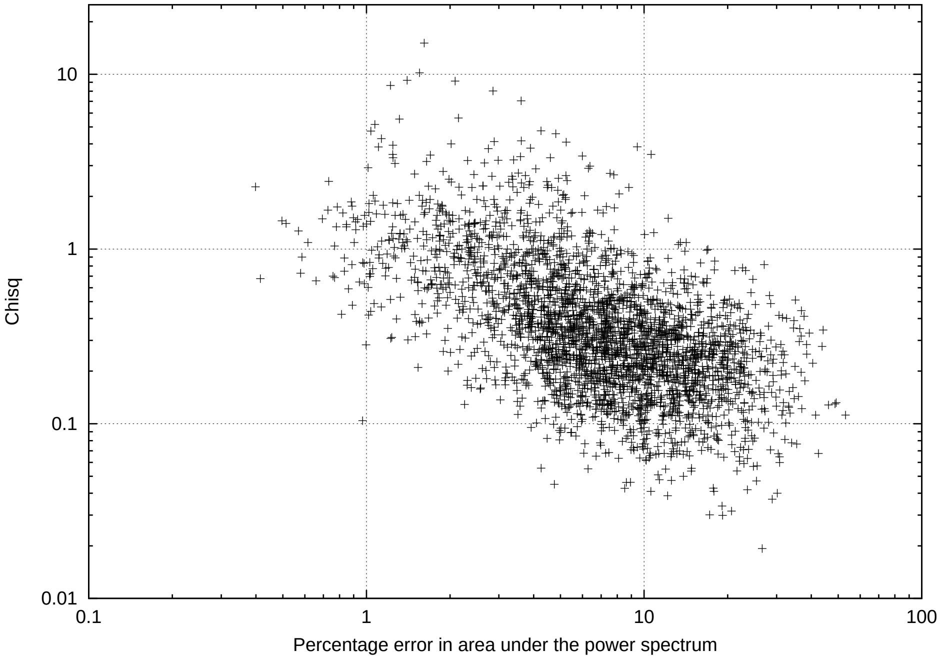

Figure 5.3: χ^2 **as a function of percentage error on area under the power spectrum** – There is a clear trend for the χ^2 to increase as the percentage $\delta A_{P(\nu)}$ decreases.

which can be explained as follows. As the S/N increases, the χ^2 becomes more sensitive to smaller differences between the model and the data. At poorer S/N the χ^2 is not sensitive to these small differences as they are smaller than or comparable to the uncertainty on the power spectrum itself. Thus the deviations from the simple featureless model become increasingly significant as the S/N increases and cause the χ^2 to increase with decrease in $\delta A_{P(\nu)}$. This implies that while the power spectra observed do carry the signatures of structure in the Solar Wind, in most cases these signatures are small enough to remain indiscernible due to the noise on the power spectrum. Only when the S/N is good, these signatures become apparent as deviations from the featureless Solar Wind model. The fact that a featureless Solar Wind model offers an *adequate* description of the observed power spectrum, in the χ^2 sense, is a consequence of the S/N of the observed spectra and not a merit of the model itself. Few power spectra with good S/N are represented well by a featureless Solar Wind model. Usually, even with good S/N power spectrum, a more realistic modelling of the distribution of the properties of the Solar Wind along the *l.o.s.* introduces a large number of free parameters in the problem. With little additional information available to serve as constraints, the only recourse is to use the almost unreasonably simplistic but reasonably constrained model to describe the Solar Wind.

In order to present a fair sampling of the of results of the automated best fit

IPS model estimation, we divide the data into three bins based on value of χ^2 of the model fit and the S/N of the observed power spectrum. The three bins in the χ^2 axis are defined as $\chi^2 < 0.1$, $0.1 \leq \chi^2 < 1.0$ and $\chi^2 \geq 1.0$ and those in $A_{P(\nu)}$ as $A_{P(\nu)} < 1$, $1 \leq A_{P(\nu)} < 10.0$ and $A_{P(\nu)} \geq 10.0$. Figure 5.3 can be divided into 9 parts on the basis of the bins just defined. Figures 5.4 – 5.11 present a few representative automated best fits IPS models along with the data from each of these parts. The curve with error bars is the observed power spectrum after uniform statistical averaging and the error bars represent 1σ statistical uncertainty estimated as explained in Section 4.5.4. The thick smooth curve is the best fit IPS model estimated by the automated procedure. A host of other information about the IPS fit parameters, the geometry of observation and the goodness of the model fit is also provided. The horizontal dashed-dotted line marks the system noise level and the vertical dashed-dotted line marks ν_c, the frequency where the power in the spectrum drops to system noise level. The first line on top of the power spectrum plot gives the IAU name of the source (B1950), epoch of observation (Day of year 1997, Indian Standard Time), s_i (m) and C_n^2 (arbitrary units) respectively. The second line gives the scan number of the observation, $\theta_\circ$ $(')$, AR, α and v $(km\ sec^{-1})$ respectively. The χ^2 of the IPS model is given in the top left hand corner of the panel. The coordinates of the P-point, R (AU), $\theta_\odot(^\circ)$ and $\phi_\odot(^\circ)$, are given in the top right hand corner. The ϵ $(^\circ)$ of the source is given in the second row of text in the panel.

5.6 Reliability of the best fit IPS models

As has been pointed out in Section 5.2, the automated determination of the best fit IPS model ensures only that the model arrived at corresponds to a local χ^2 minima. It is the responsibility of the definition of χ^2 to ensure that the best fit model arrived at is the one which a human being would also have converged to. The best fit model arrived at by an algorithm may differ from the one which a human being with all his intelligence and additional information available to him/her would have chosen. The most important reason why this may happen is that the best fit IPS model used is not adequate to describe the observed power spectrum, i.e. the Solar Wind sampled by the $l.o.s.$ is not described well by a featureless model. Figure 5.12 presents the power spectra which have the poorest fits, according to the χ^2 criterion. It is clear that no featureless Solar Wind model can provide an adequate fit to these power spectra, even on changing model parameters which we have held constant, namely AR, α and s_i. In these cases, large χ^2 values reflect the inadequacy of the model to represent the data, not the inability of the χ^2 minimisation procedure to provide good fits.

Another reason which can lead to such behaviour is poor S/N, where the fit is

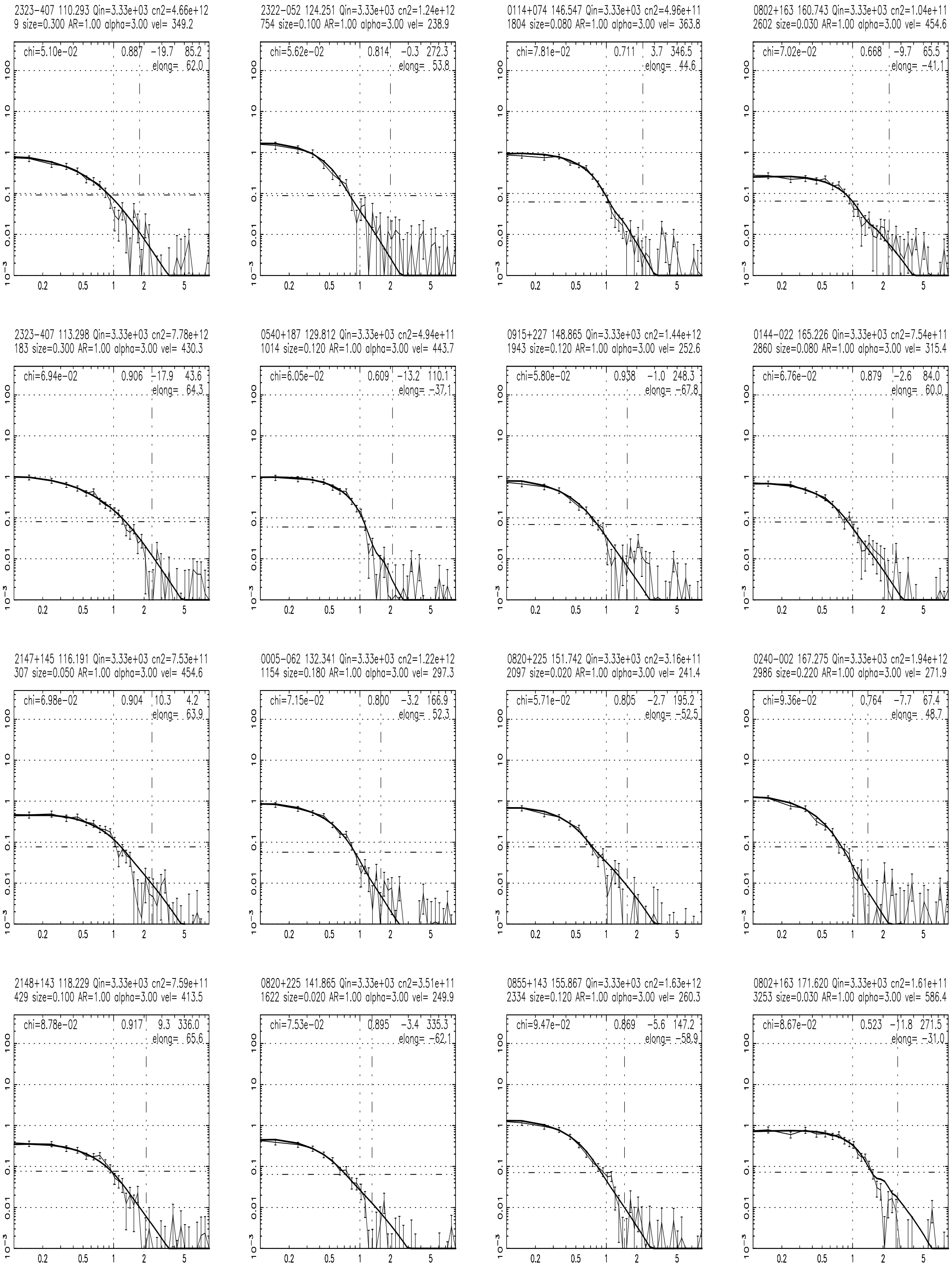

Figure 5.4: **IPS best fit models for $\chi^2 < 0.1$ and $A_{P(\nu)} < 1.0$** – The X axis has ν (Hz) plotted on it and the Y axis Power (arbitrary units). Both the axes are plotted in log scales. The observed uniform statistically averaged power spectrum is plotted with 1σ error bars and the thick smooth curve is best fit IPS model estimated. Additional information presented is explained in the text.

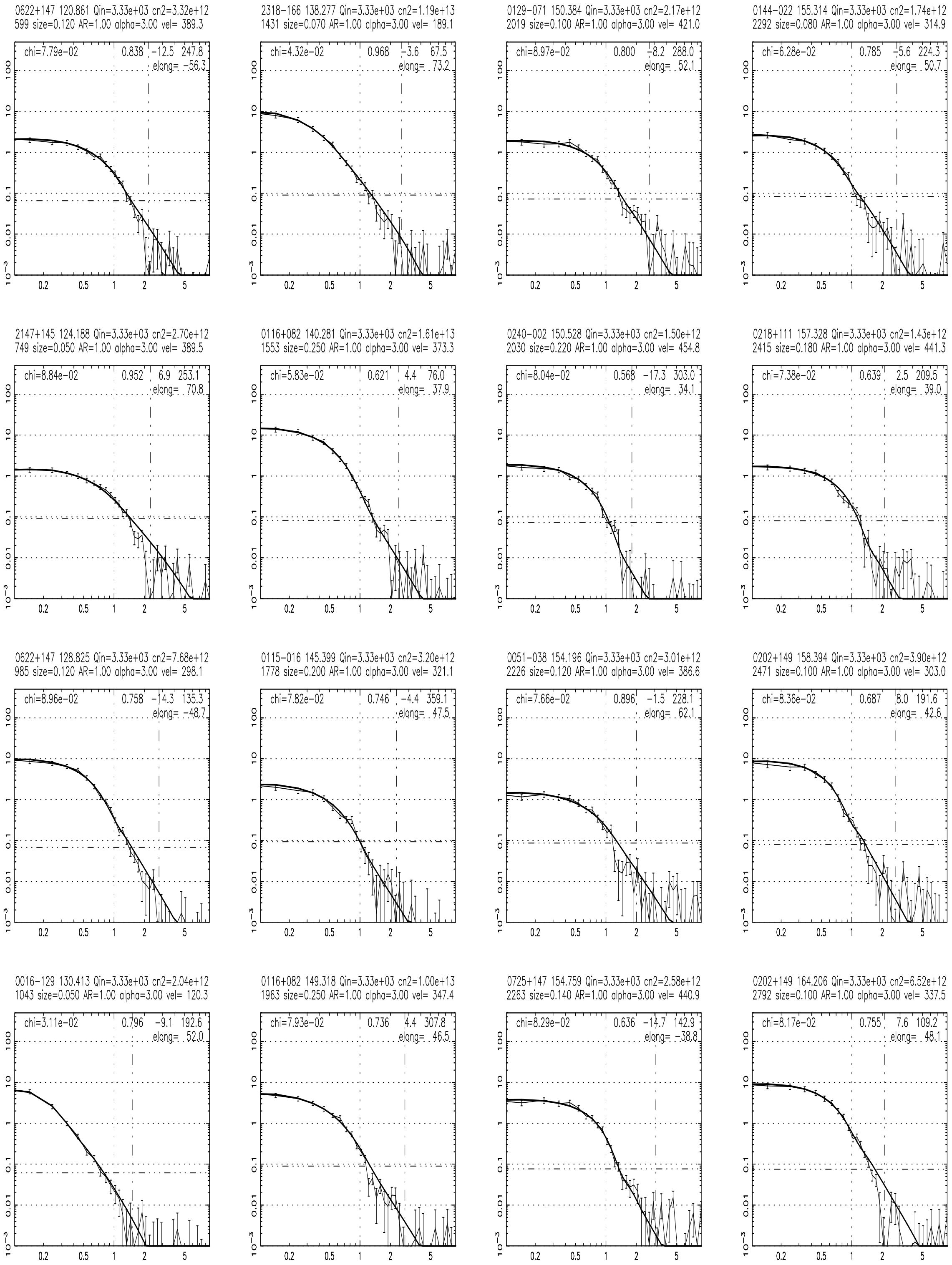

Figure 5.5: **IPS best fit models for $\chi^2 \ < 0.1$ and $0.1 \leq A_{P(\nu)} < 10.0$** – The power spectra are presented in the same format as Figure 5.4.

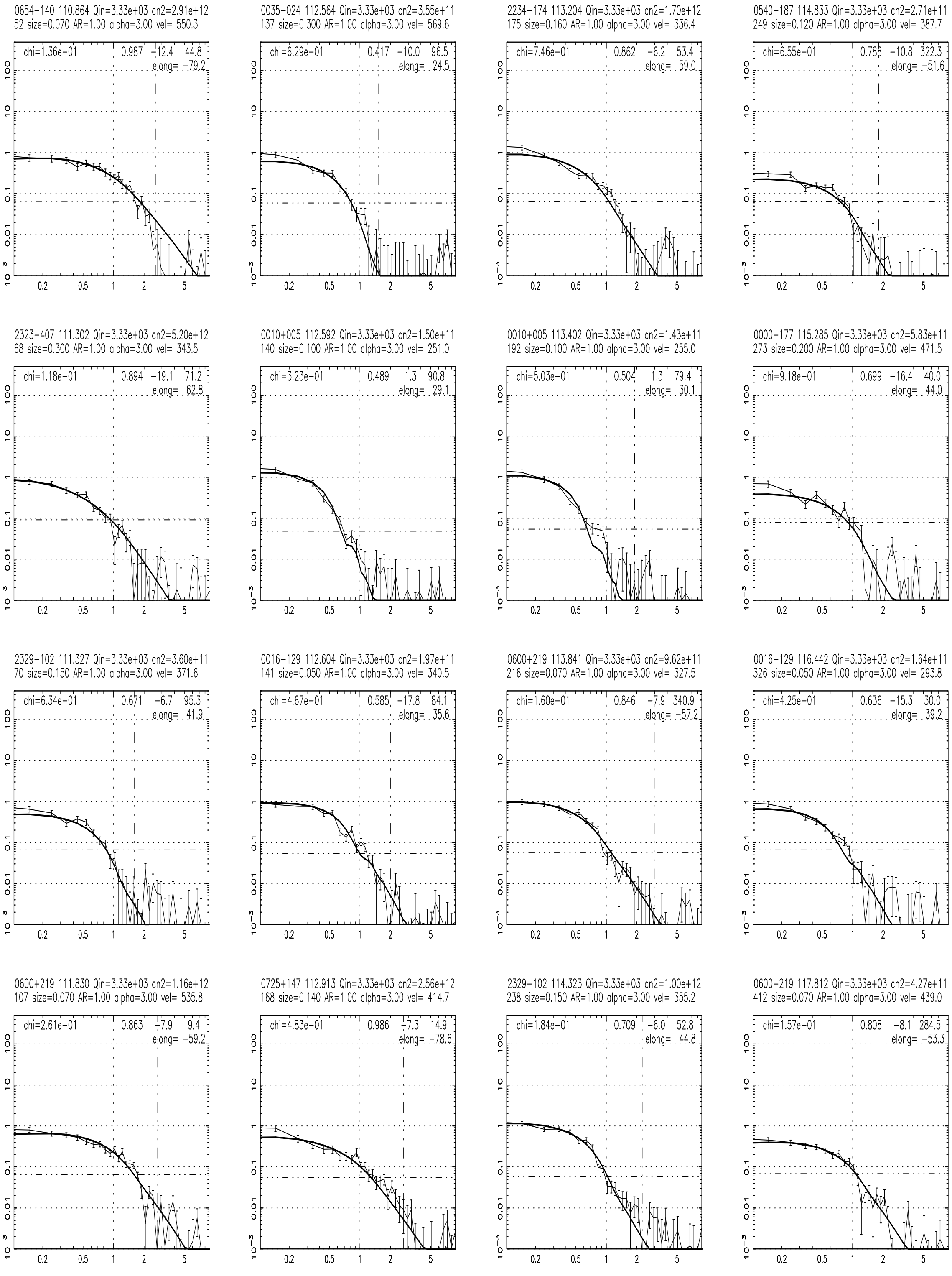

Figure 5.6: **IPS best fit models for** $0.1 \leq \chi^2 < 1.0$ **and** $A_{P(\nu)} < 1.0$ – The power spectra are presented in the same format as Figure 5.4.

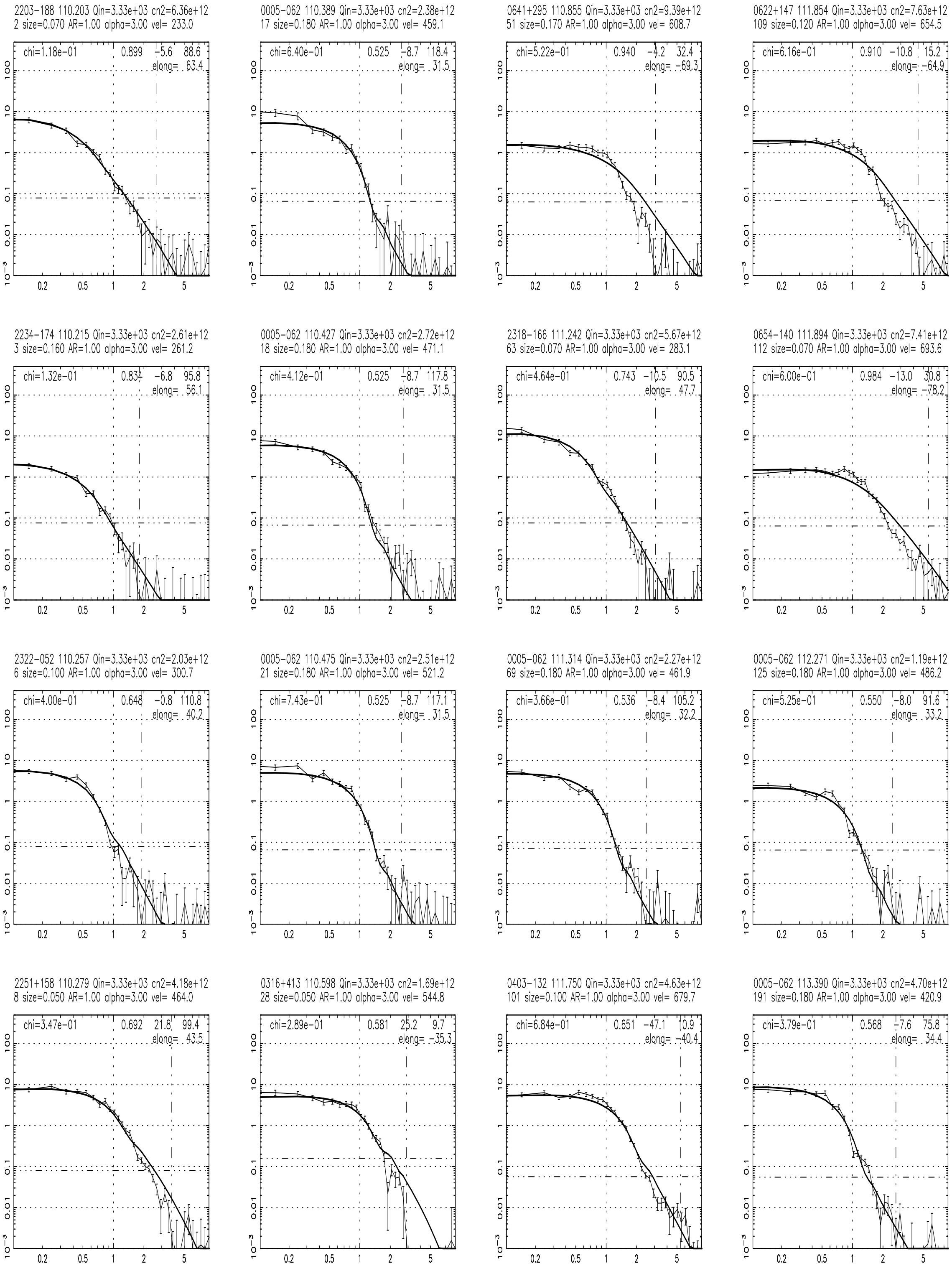

Figure 5.7: **IPS best fit models for** $0.1 \leq \chi^2 < 1.0$ **and** $0.1 \leq A_{P(\nu)} < 10.0$ – The power spectra are presented in the same format as Figure 5.4.

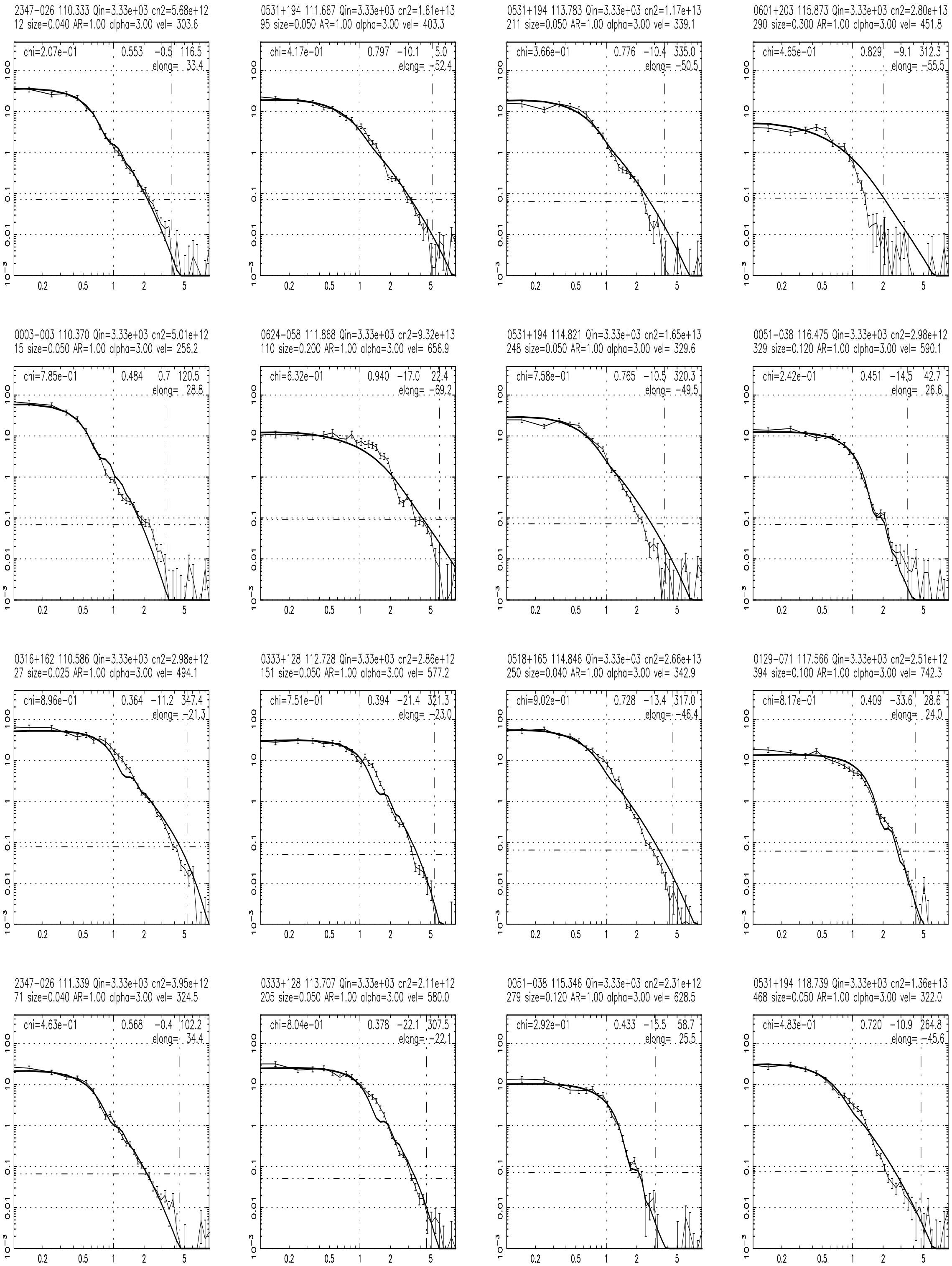

Figure 5.8: **IPS best fit models for** $0.1 \leq \chi^2 < 1.0$ **and** $A_{P(\nu)} > 10.0$ – The power spectra are presented in the same format as Figure 5.4.

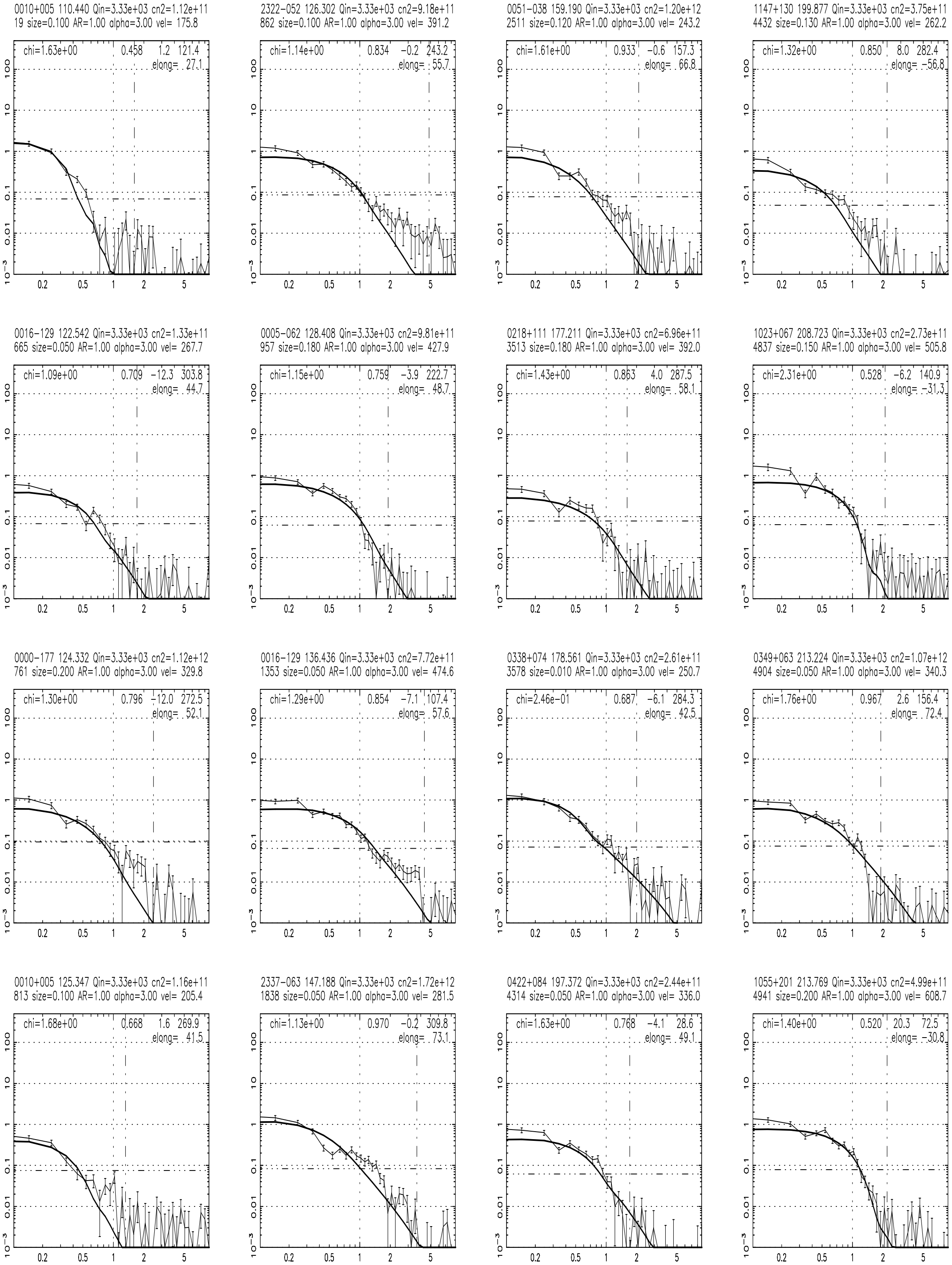

Figure 5.9: **IPS best fit models for $\chi^2 > 1.0$ and $A_{P(\nu)} < 1.0$** – The power spectra are presented in the same format as Figure 5.4. The third spectrum in the third column of panels (source name 0338+074) has χ^2 lower than 1.0 and has been included in the figure by oversight.

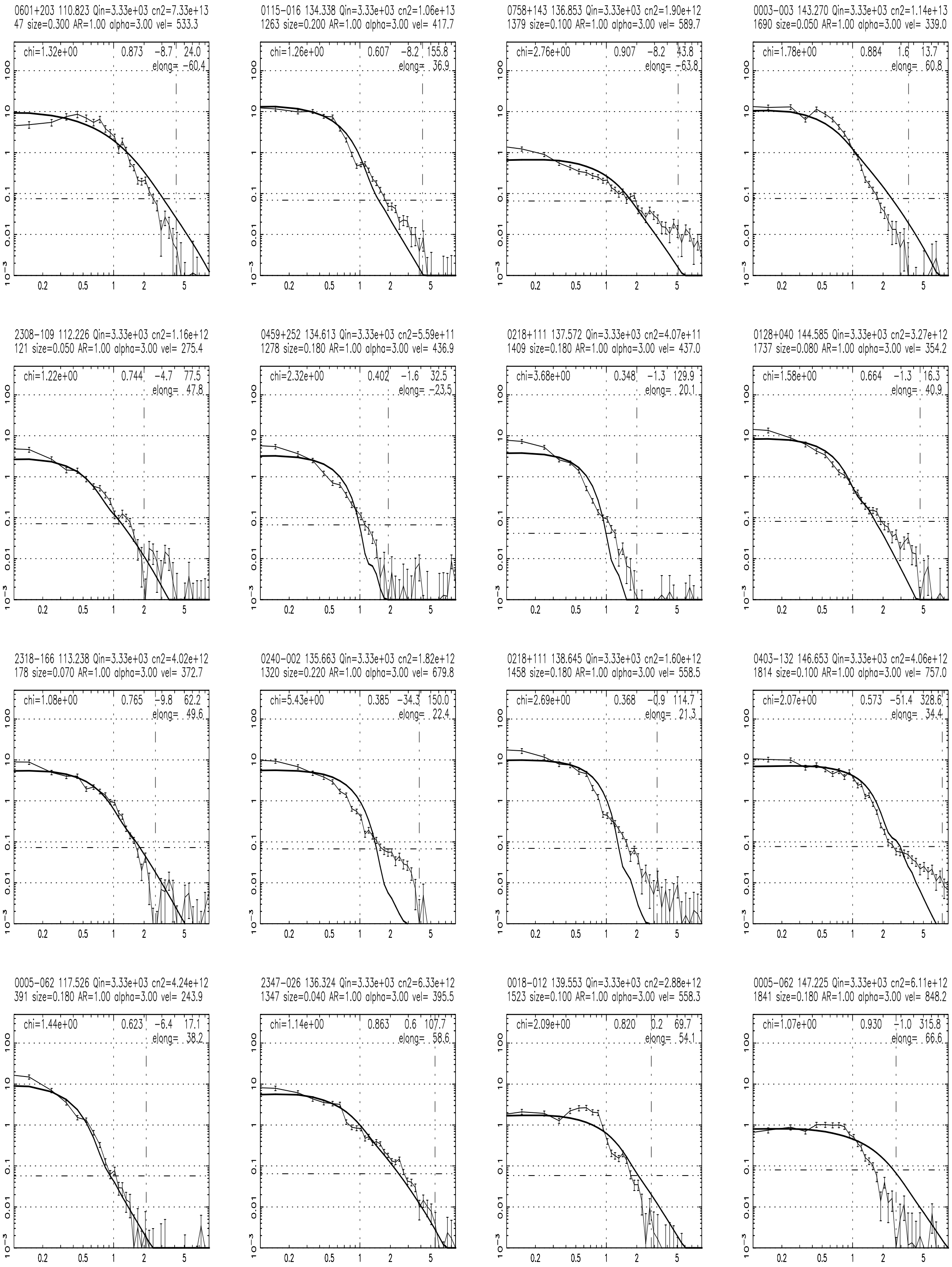

Figure 5.10: **IPS best fit models for** $\chi^2 > 1.0$ **and** $0.1 \leq A_{P(\nu)} < 10.0$ – The power spectra are presented in the same format as Figure 5.4.

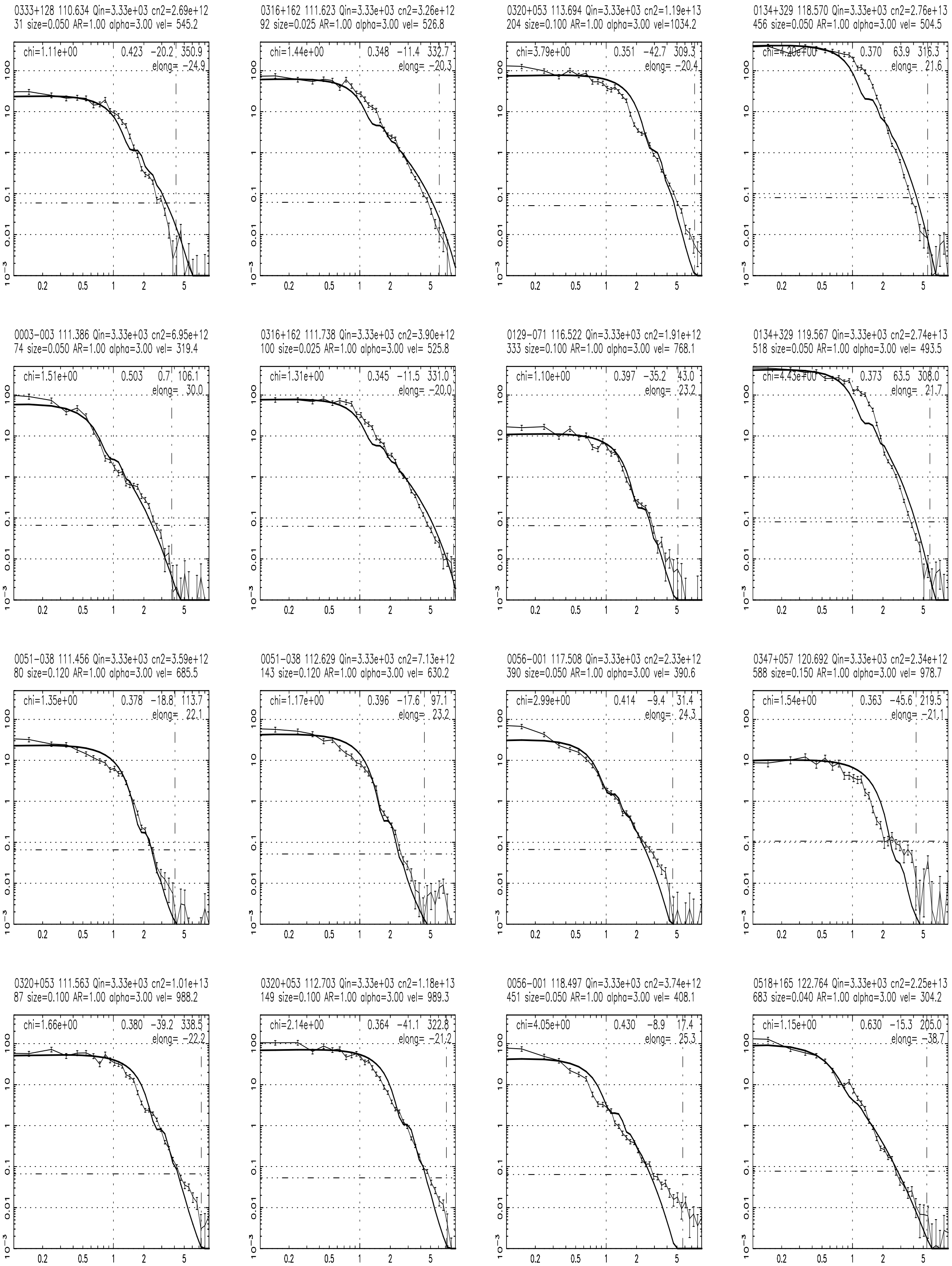
0333+128 110.634 Qin=3.33e+03 cn2=2.69e+12
31 size=0.050 AR=1.00 alpha=3.00 vel= 545.2

0316+162 111.623 Qin=3.33e+03 cn2=3.26e+12
92 size=0.025 AR=1.00 alpha=3.00 vel= 526.8

0320+053 113.694 Qin=3.33e+03 cn2=1.19e+13
204 size=0.100 AR=1.00 alpha=3.00 vel=1034.2

0134+329 118.570 Qin=3.33e+03 cn2=2.76e+13
456 size=0.050 AR=1.00 alpha=3.00 vel= 504.5

0003−003 111.386 Qin=3.33e+03 cn2=6.95e+12
74 size=0.050 AR=1.00 alpha=3.00 vel= 319.4

0316+162 111.738 Qin=3.33e+03 cn2=3.90e+12
100 size=0.025 AR=1.00 alpha=3.00 vel= 525.8

0129−071 116.522 Qin=3.33e+03 cn2=1.91e+12
333 size=0.100 AR=1.00 alpha=3.00 vel= 768.1

0134+329 119.567 Qin=3.33e+03 cn2=2.74e+13
518 size=0.050 AR=1.00 alpha=3.00 vel= 493.5

0051−038 111.456 Qin=3.33e+03 cn2=3.59e+12
80 size=0.120 AR=1.00 alpha=3.00 vel= 685.5

0051−038 112.629 Qin=3.33e+03 cn2=7.13e+12
143 size=0.120 AR=1.00 alpha=3.00 vel= 630.2

0056−001 117.508 Qin=3.33e+03 cn2=2.33e+12
390 size=0.050 AR=1.00 alpha=3.00 vel= 390.6

0347+057 120.692 Qin=3.33e+03 cn2=2.34e+12
588 size=0.150 AR=1.00 alpha=3.00 vel= 978.7

0320+053 111.563 Qin=3.33e+03 cn2=1.01e+13
87 size=0.100 AR=1.00 alpha=3.00 vel= 988.2

0320+053 112.703 Qin=3.33e+03 cn2=1.18e+13
149 size=0.100 AR=1.00 alpha=3.00 vel= 989.3

0056−001 118.497 Qin=3.33e+03 cn2=3.74e+12
451 size=0.050 AR=1.00 alpha=3.00 vel= 408.1

0518+165 122.764 Qin=3.33e+03 cn2=2.25e+13
683 size=0.040 AR=1.00 alpha=3.00 vel= 304.2

Figure 5.11: **IPS best fit models for** $\chi^2 > 1.0$ **and** $A_{P(\nu)} > 10.0$ – The power spectra are presented in the same format as Figure 5.4.

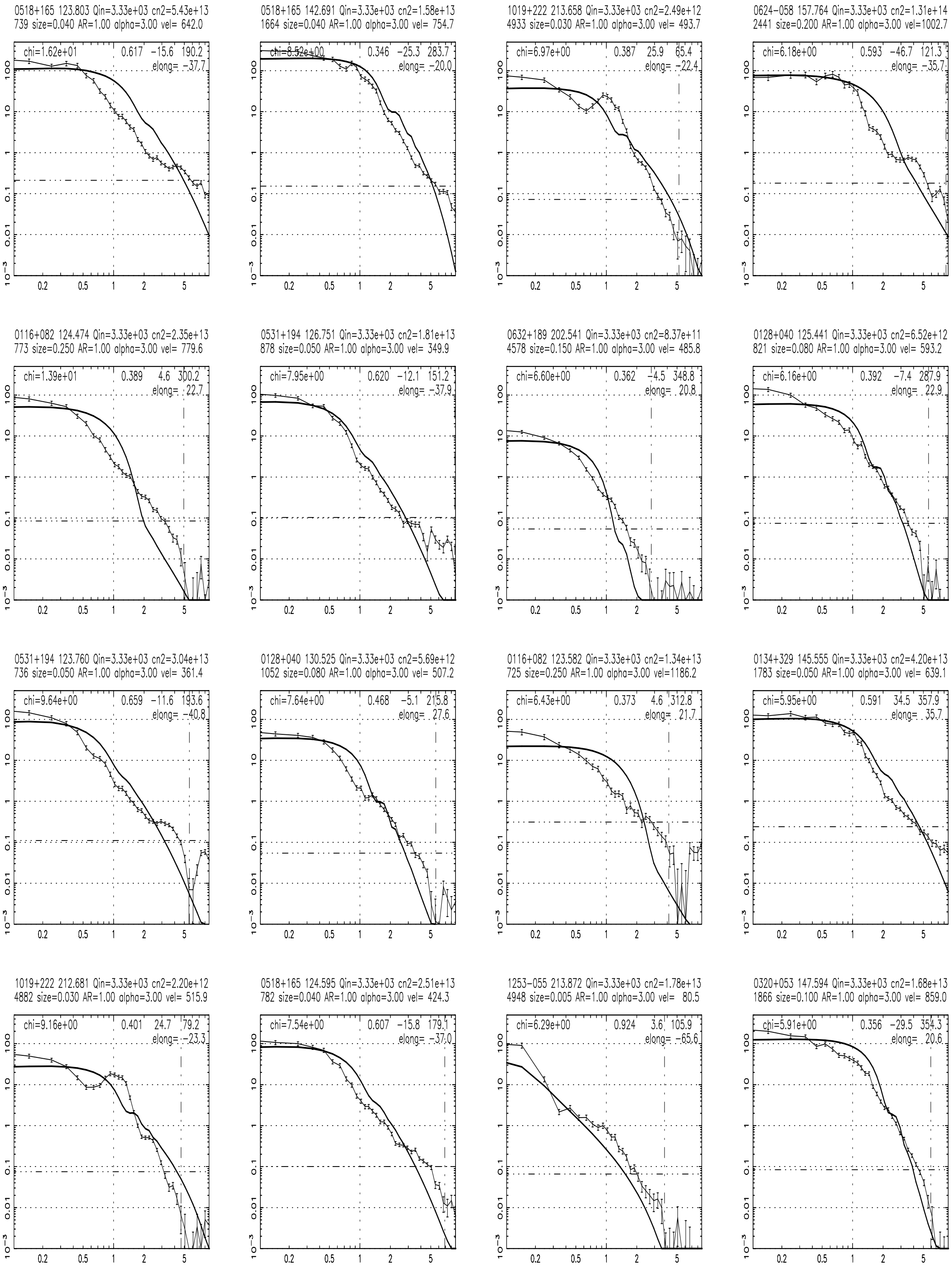

Figure 5.12: **Power spectra with the largest** χ^2 – The power spectra are presented in the same format as figure 5.4.

dominated by the noise on the power spectrum. The present dataset had few cases of such poor S/N power spectra all of which have been carefully weaned out. Poor data quality due to reasons ranging from man-made interference to thunder storms can also lead to a situation where a human may arrive at different fit parameters for the IPS model. Power spectra with poor data quality due to interference have also been flagged. There are some isolated cases when the results of the automated fit are clearly far from the appropriate Solar Wind model, these are the cases where the χ^2 minimisation algorithm travelled down an inappropriate local minima and was not able to climb out of it. Typically, $2-3$ such cases were encountered in each run of estimating the best fit IPS models for greater than 4000 power spectra. In these cases, a change in the initial guess for the fit parameters allowed to the χ^2 minimisation to proceed to the desired model without any problem.

The power spectra with extreme values of best fit IPS model parameters were examined individually to look for power spectra with poor S/N, interference, problems in system noise level estimation etc. which may have escaped the earlier rounds of data flagging. Figures 5.13 and 5.14 presents the power spectra with the largest and the smallest values of the best fit v respectively. Figure 5.15 and 5.16 present the power spectra the best fit models to which have the highest and the lowest g values respectively. The best fit IPS model parameters are found to be quite reasonable, given the constraint that a featureless Solar Wind model was used to represent the data. The model fits corresponding to the largest and the smallest $A_{P(\nu)}$ were also examined individually to access the quality of the best fit models and ensure that no power spectra with poor data quality remain unflagged.

We conclude that the automated procedure for estimating the featureless IPS model parameters for the observed power spectra works well. It relieves the astronomer of the drudgery of having to estimate the IPS model parameters for each of the observed power spectra individually. This makes possible an objective analysis of large databases of spectra and leaves the astronomer free to devote herself/himself to more interesting issues. Prominent departures from featureless Solar Wind model are caused by presence of significant structure in the Solar Wind being sampled by the *l.o.s.*. These can be caused, either by some transient phenomenon, like an Interplanetary Disturbance (IPD) crossing the *l.o.s.*, or the *l.o.s.* passing through a long lived structure in the Solar Wind, like a co-rotating interaction region (CIR). Such power spectra can easily be identified by their large χ^2 values. Since such events are usually not frequent, only a small fraction of the total number of observed power spectra sample such phenomena. This small subset of power spectra are often the most interesting ones to pursue. The automated estimation of the featureless IPS model parameters provides a very efficient way of locating such spectra in a large set of observations, without manually wading through thousands of power spectra.

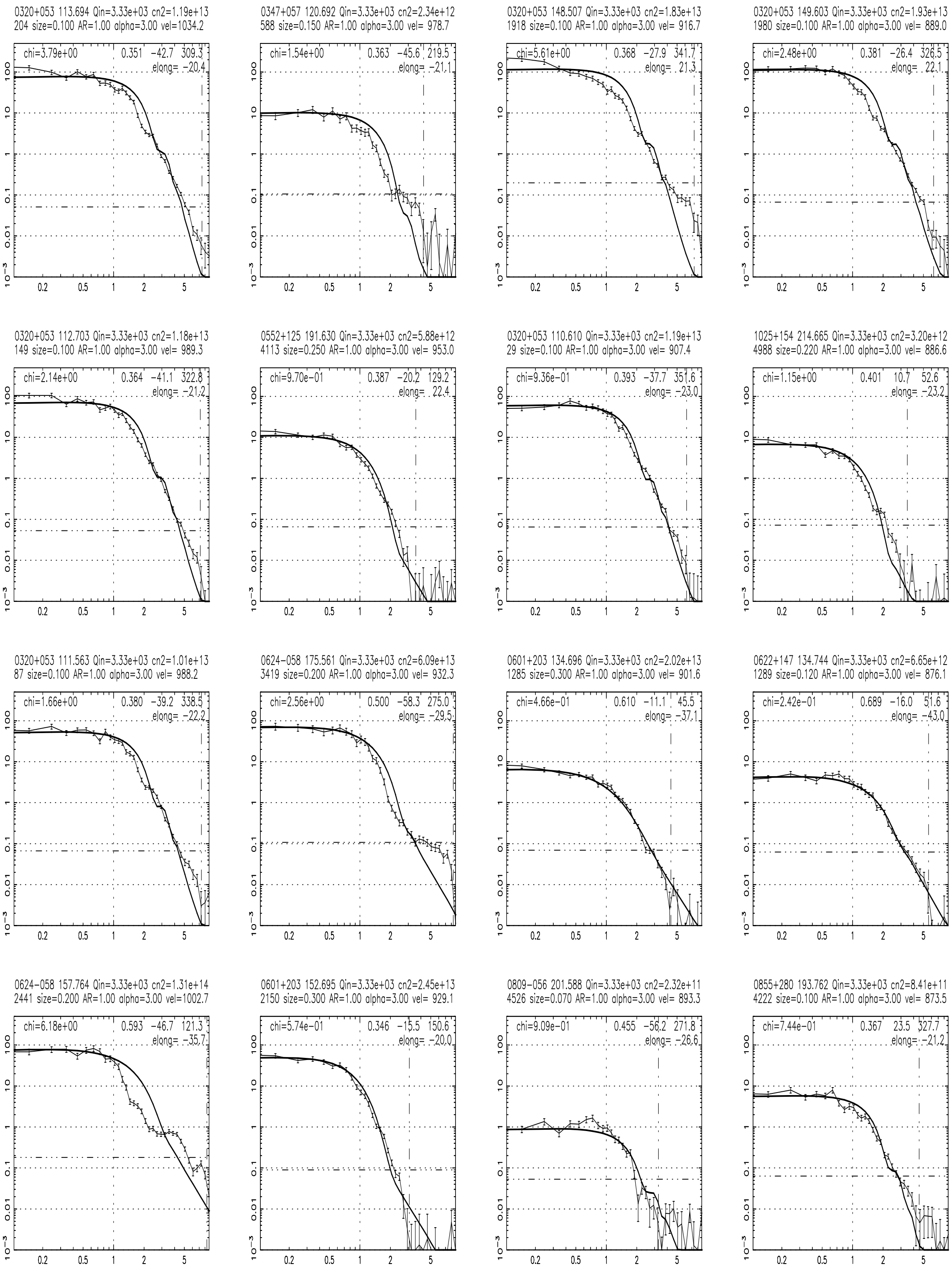

Figure 5.13: **Power spectra with the largest velocities** – The power spectra are presented in the same format as Figure 5.4.

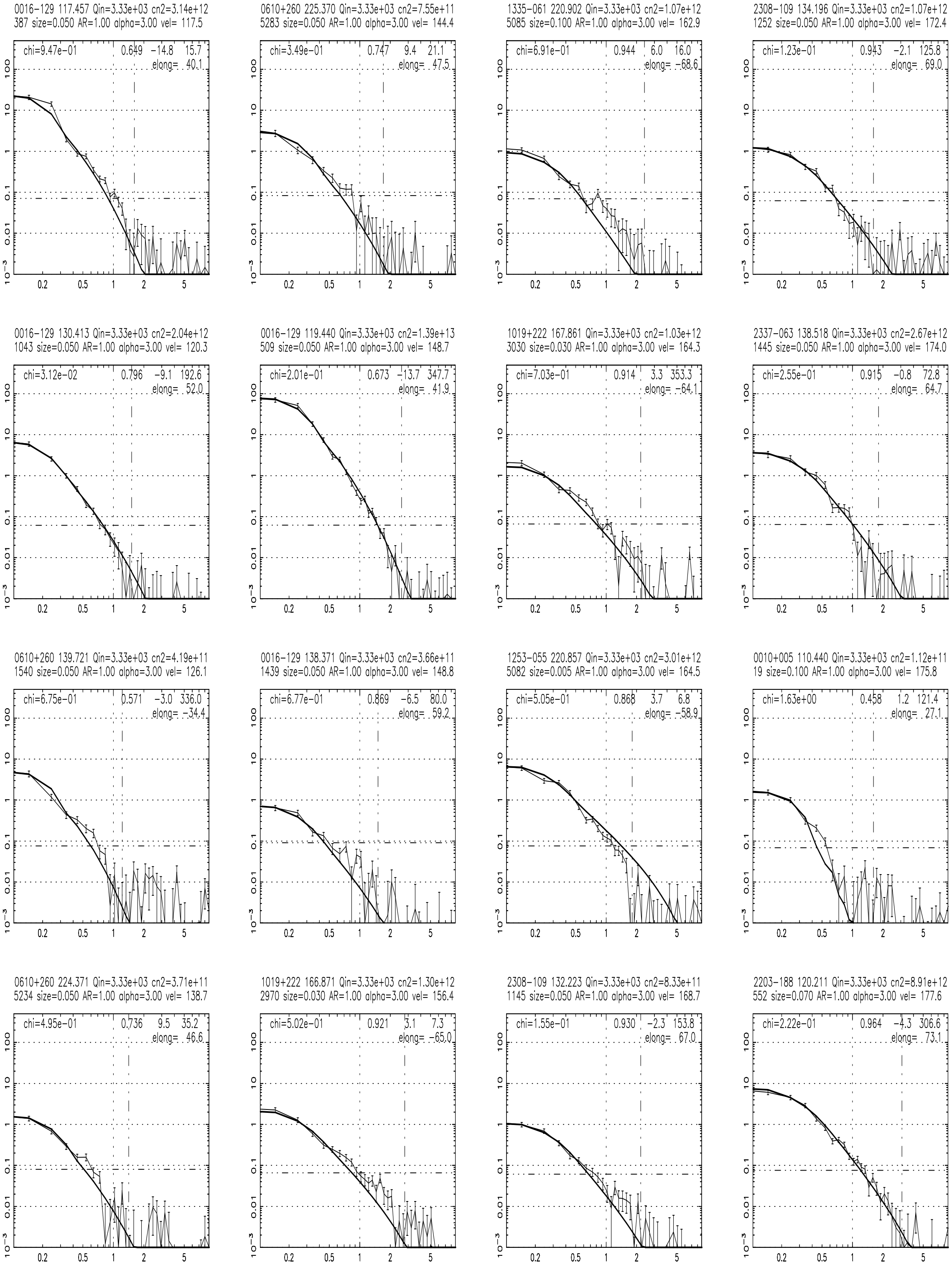

Figure 5.14: **Power spectra with the smallest velocities** – The power spectra are presented in the same format as Figure 5.4. The velocities obtained for these power spectra are unusually low and the possibility of their being effected by ionospheric scintillation is considered in Section 5.7.

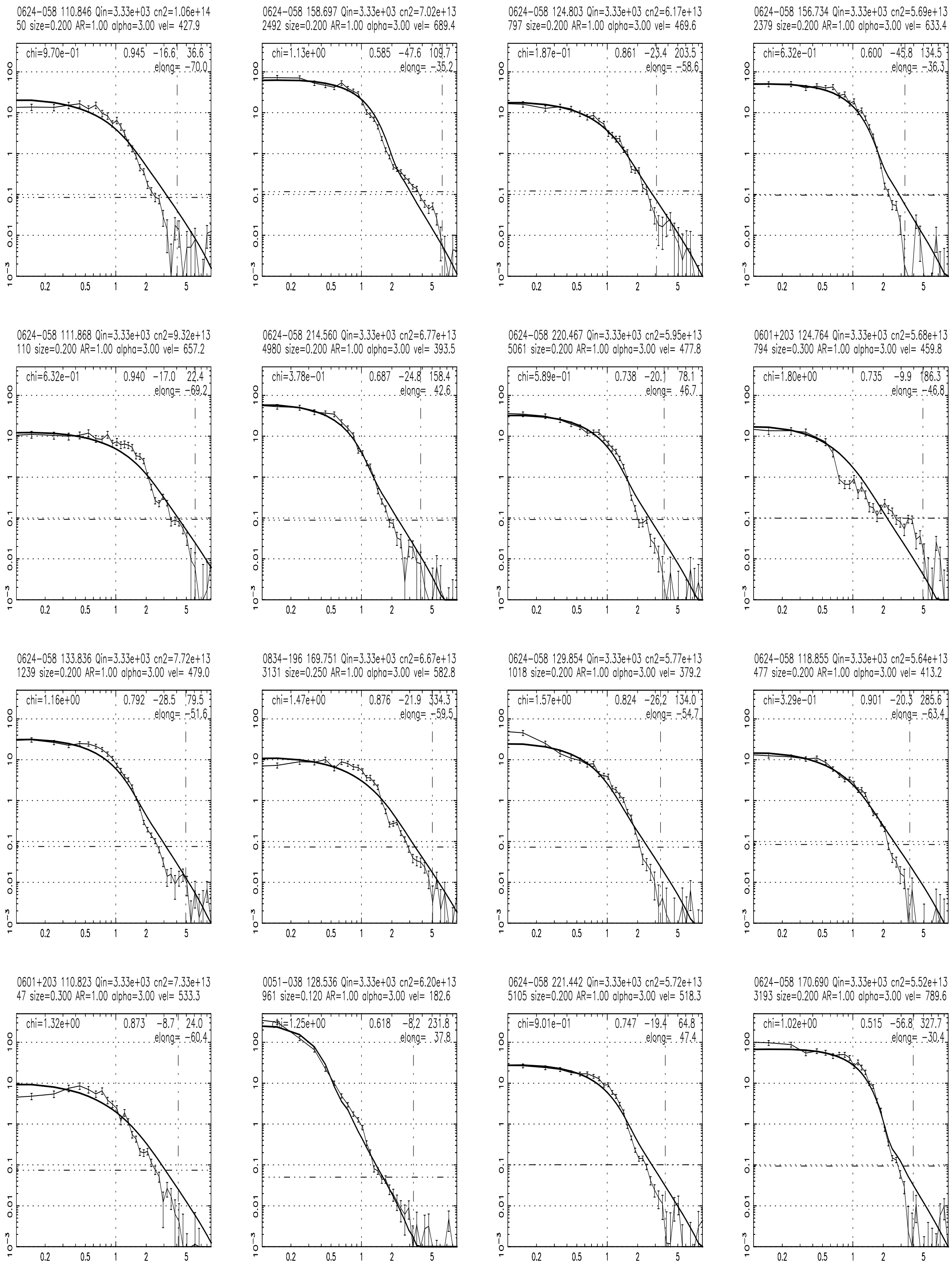

Figure 5.15: **Power spectra with the highest g values** – The power spectra are presented in the same format as Figure 5.4.

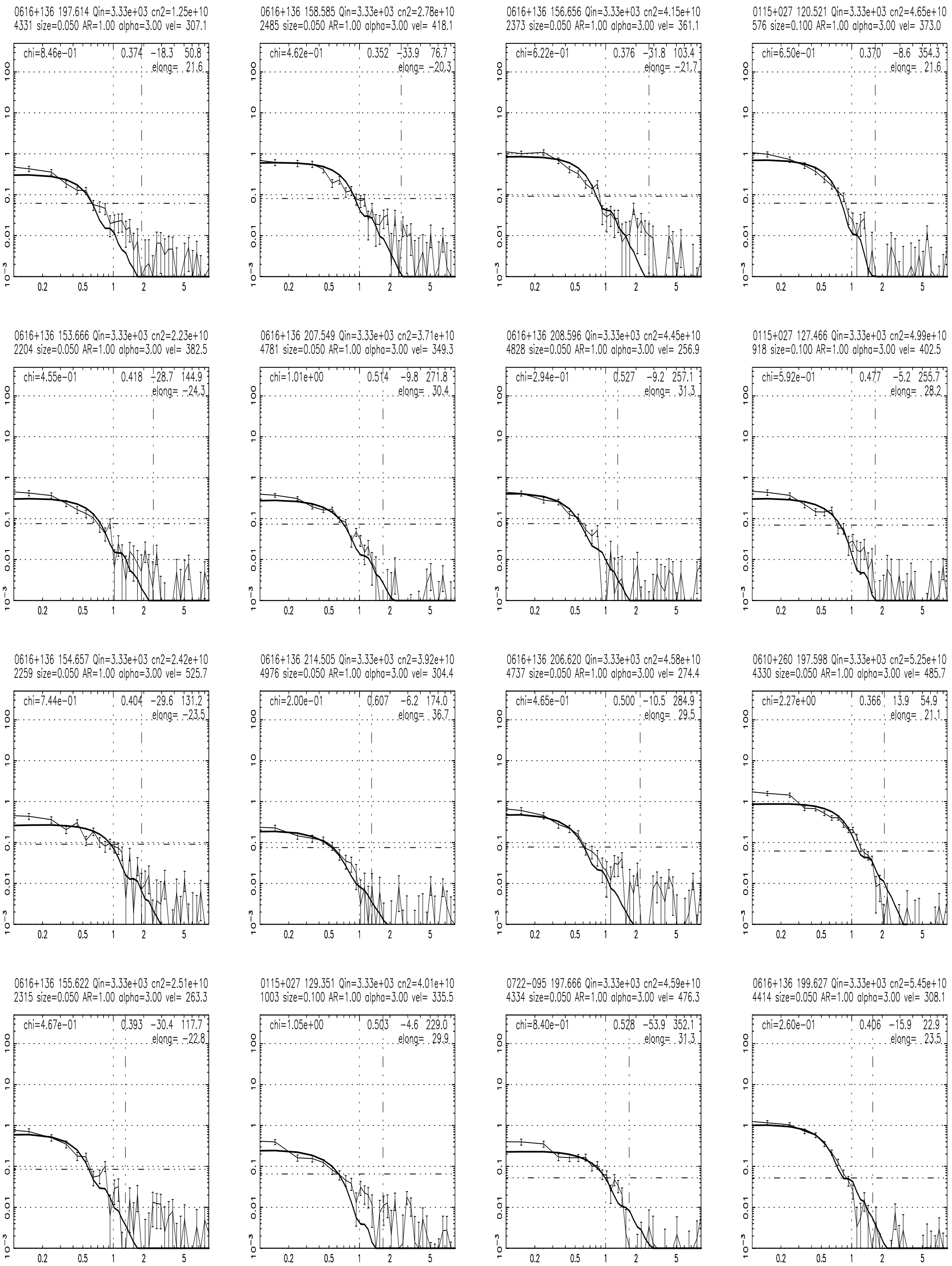

Figure 5.16: **Power spectra with the lowest g values** – The power spectra are presented in the same format as Figure 5.4.

5.7 A sample of the data

In order to get a feeling for the dataset obtained, the time series of best fit IPS model parameters for some of the sources which have been observed most frequently are shown in Figures 5.17 – 5.28. Observations towards some other sources which show interesting features are also shown.

The g values and the geometry parameters for the observations have also been presented. The g values have been computed for observations in the range $20^\circ \leq |\epsilon| \leq 80^\circ$. A host of interesting features are seen in these plots. Some of them are pointed out below :

1. The average latitudinal structure of the Solar Wind is clearly seen in the data (Section 6.3). The best fit IPS model velocity increases as the P-point moves away from the equatorial regions. A correlation between increase in the IPS velocity with decrease in elongation of observation can also be seen. Such a trend is seen only for non-ecliptic source and not for ecliptic sources. This is a manifestation of the P-point to the *l.o.s.*s of non-ecliptic sources moving to higher heliographic latitudes with decrease in elongation.

2. The most interesting transient event which took place during the epoch of observations is also clearly seen. This transient was detected in the Interplanetary Medium on the day number 134 (May 14, 1997) and is best sampled by the time series of IPS observations of 0116+082. This event was identified to be an Earth directed CME which was launched from the Sun on the May 12, 1997 (Plunkett et al., 1998; Thompson et al., 1998) and it influenced the Solar Wind in the Interplanetary Medium for next 3–4 days. There are many interesting things worth noticing about this IPD. The locations of the peaks in velocity and C_n^2 (or g) time series are displaced with respect to each other, the velocity peak seems to come about a day after the C_n^2 peak. This event is seen by *l.o.s.* to many other sources as well. Of the sources for which data is presented here it is seen by 0518+165, 0725+147, 0005-062, 0531+194, 0758+143, 0316+413 and 0548+165. The opening angle of the event in the heliosphere can be ascertained by finding out the distribution of the *l.o.s.*s which sample the event and has been estimated to be $> 110^\circ$.

3. It should be noted that there are hardly any periods where are fluctuations in the values of velocity and C_n^2 are less than 10%. The fluctuation in the Solar Wind from higher (or lower) heliographic latitudes seems to be less than as compared to the fluctuations in the Solar Wind from the equatorial belt.

4. Many different kinds of variations are seen in the velocity and C_n^2 time series, a few of them are mentioned below. There are instances where velocity and

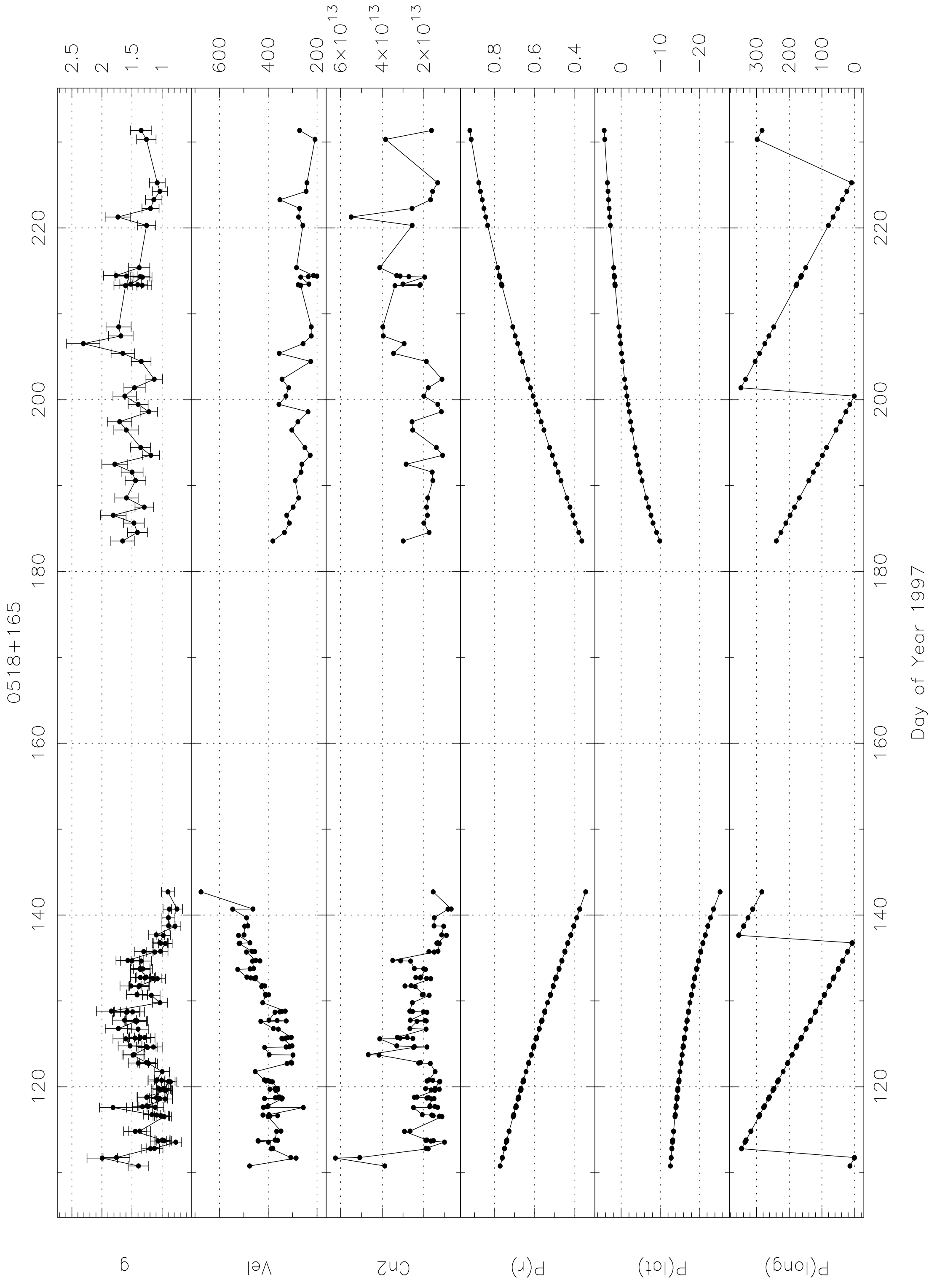

Figure 5.17: **Observations of** 0518+165 – The g value, the IPS best fit model and geometry parameters are presented as a function of the time of observation. The abscissa is the day number of year 1997. The parameters plotted are g, v ($km\ sec^{-1}$), C_n^2 (arbitrary units), radial distance of the P-point of the $l.o.s.$ (AU), $\theta_\odot$ of the P-point (°) and $\phi_\odot$ of the P-point (°) respectively. Observations at $|\epsilon| < 20°$ were not used in the present work and have not been plotted.

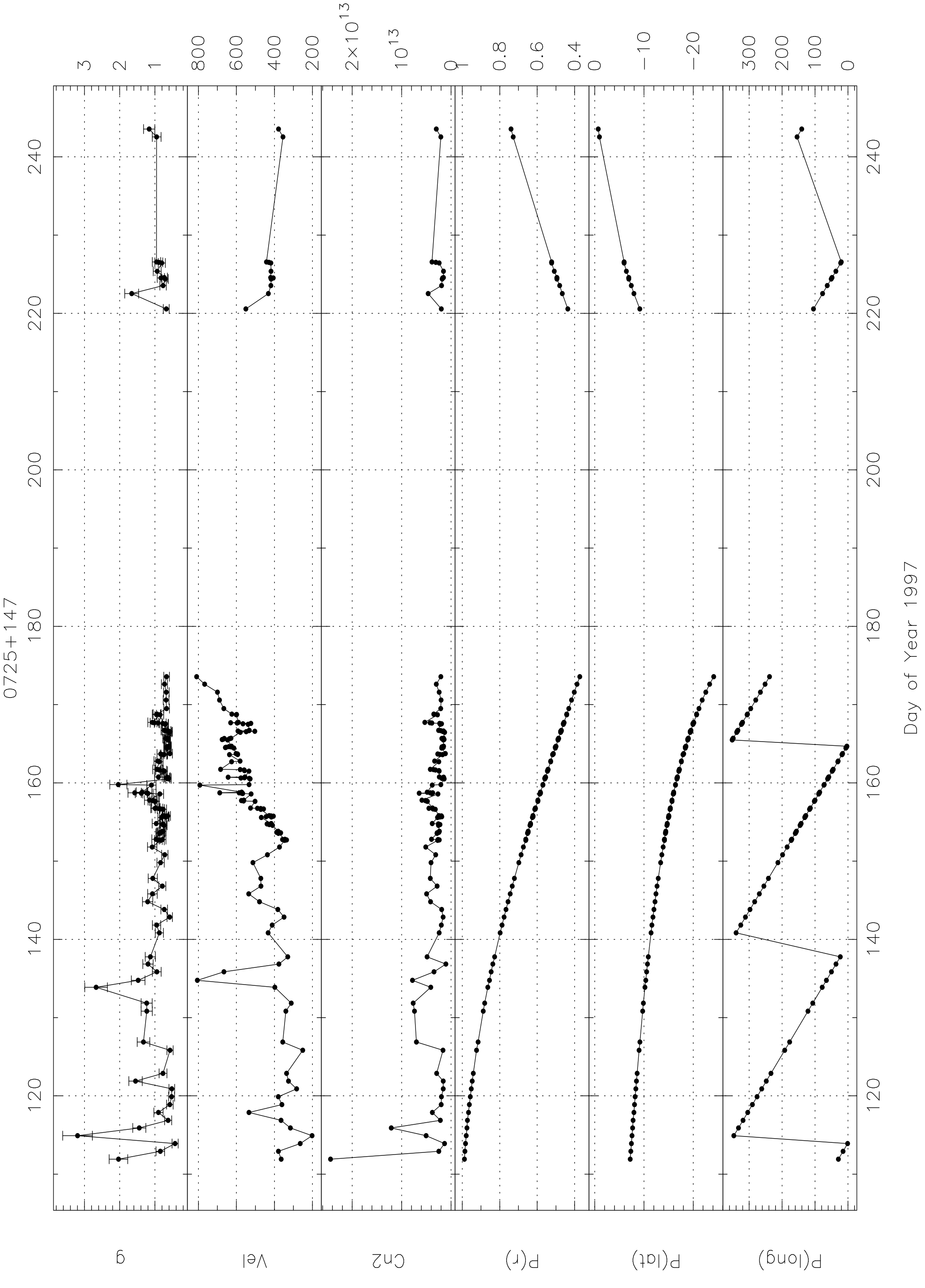

Figure 5.18: **Observations of** 0725+147 – The observations for the source 0725+147 are presented in the same format as for Figure 5.17.

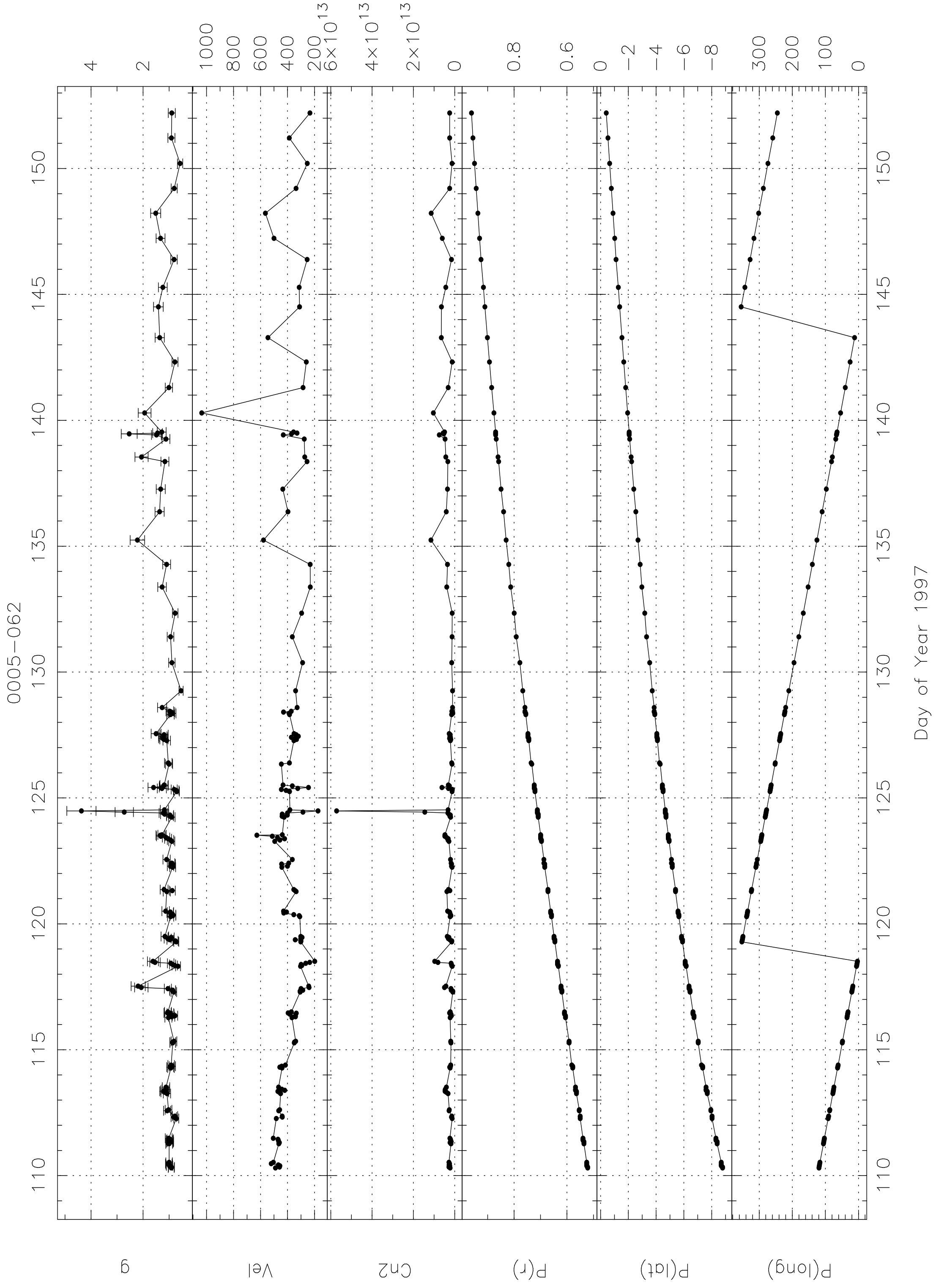

Figure 5.19: **Observations of** 0005-062 – The observations for the source 0005-062 are presented in the same format as for Figure 5.17.

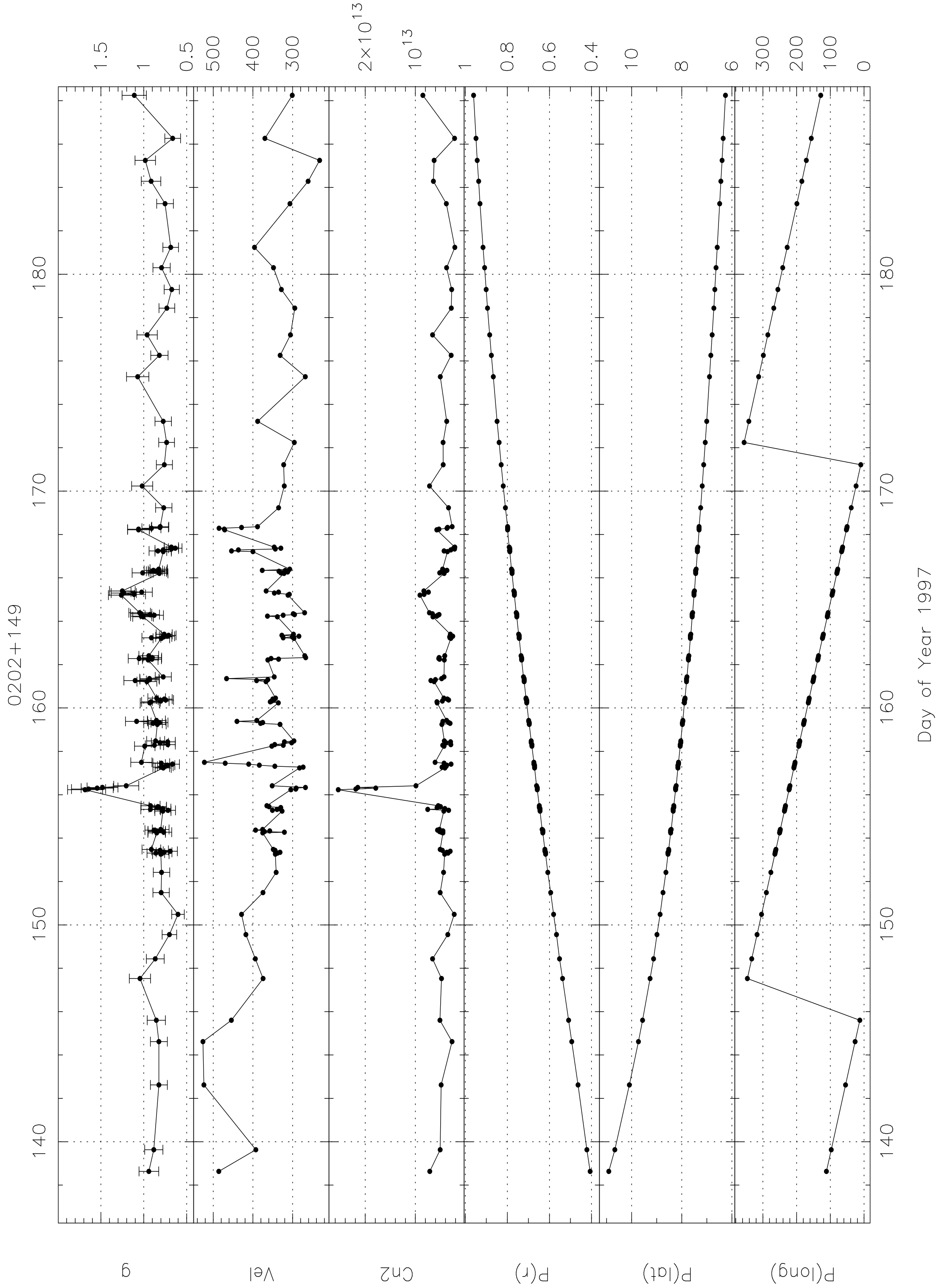

Figure 5.20: **Observations of** 0202+149 – The observations for the source 0202+149 are presented in the same format as for Figure 5.17.

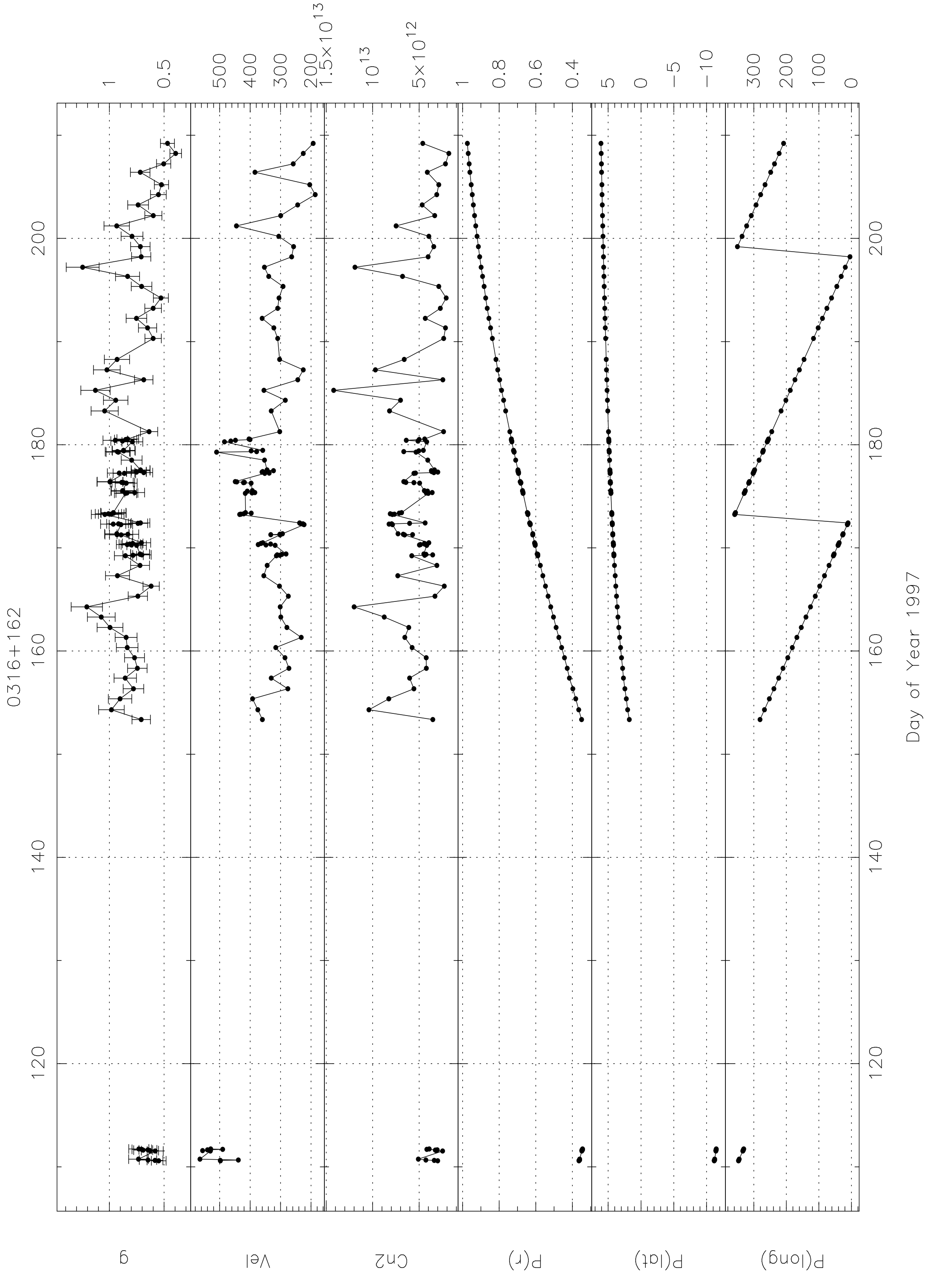

Figure 5.21: **Observations of** 0316+162 – The observations for the source 0316+162 are presented in the same format as for Figure 5.17.

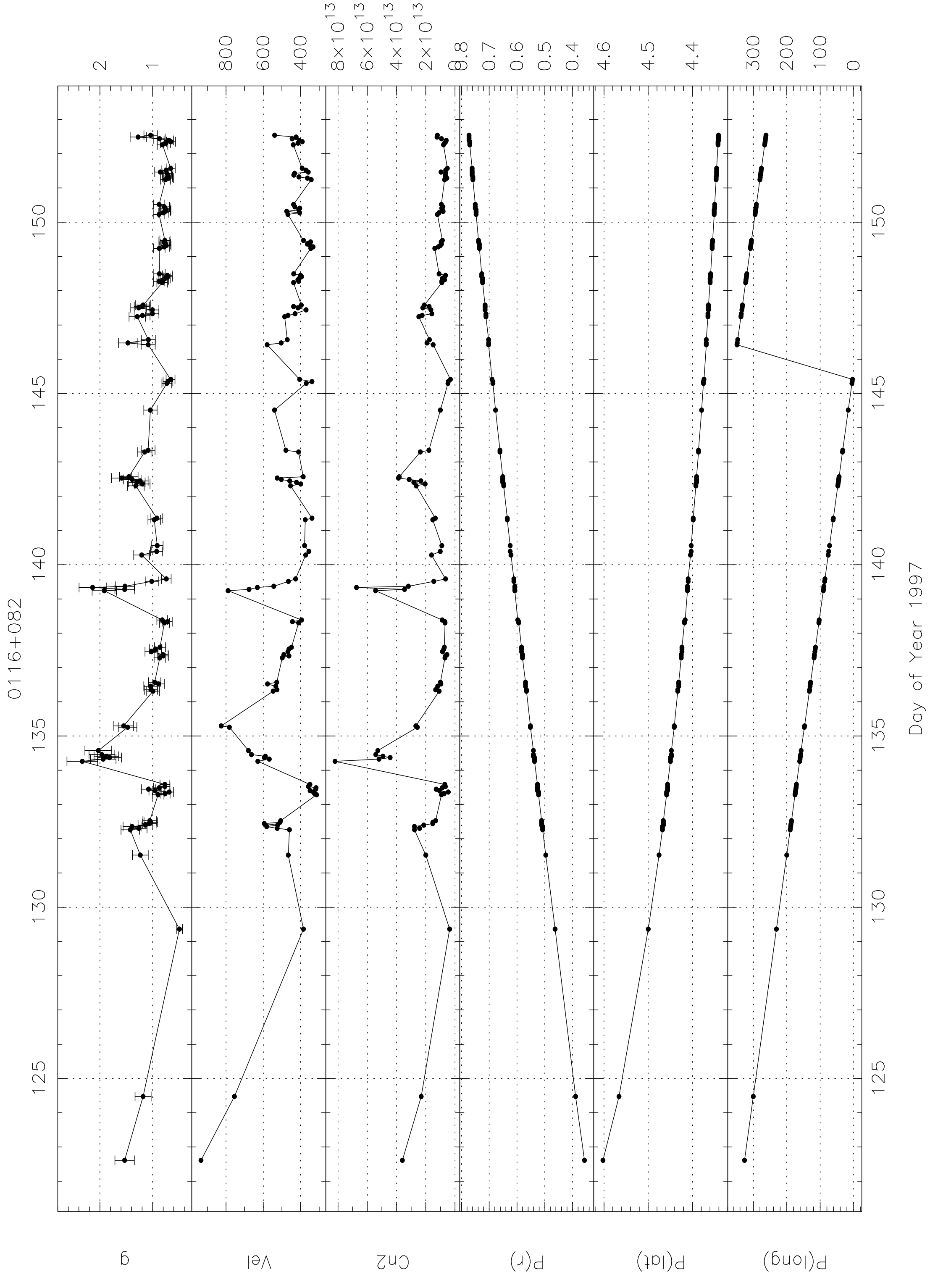

Figure 5.22: **Observations of** 0116+082 – The observations for the source 0116+082 are presented in the same format as for Figure 5.17.

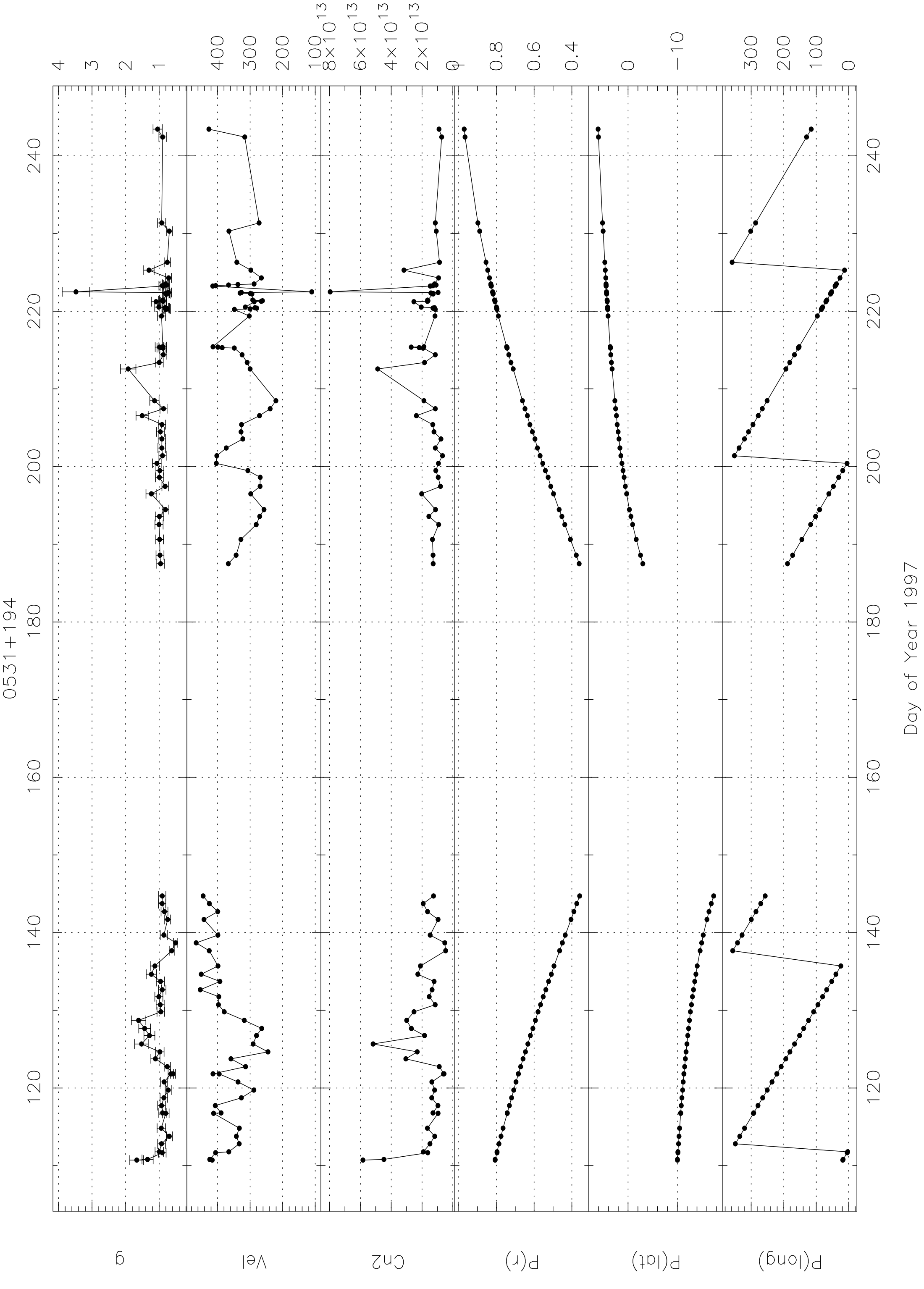

Figure 5.23: **Observations of** 0531+194 – The observations for the source 0531+194 are presented in the same format as for Figure 5.17.

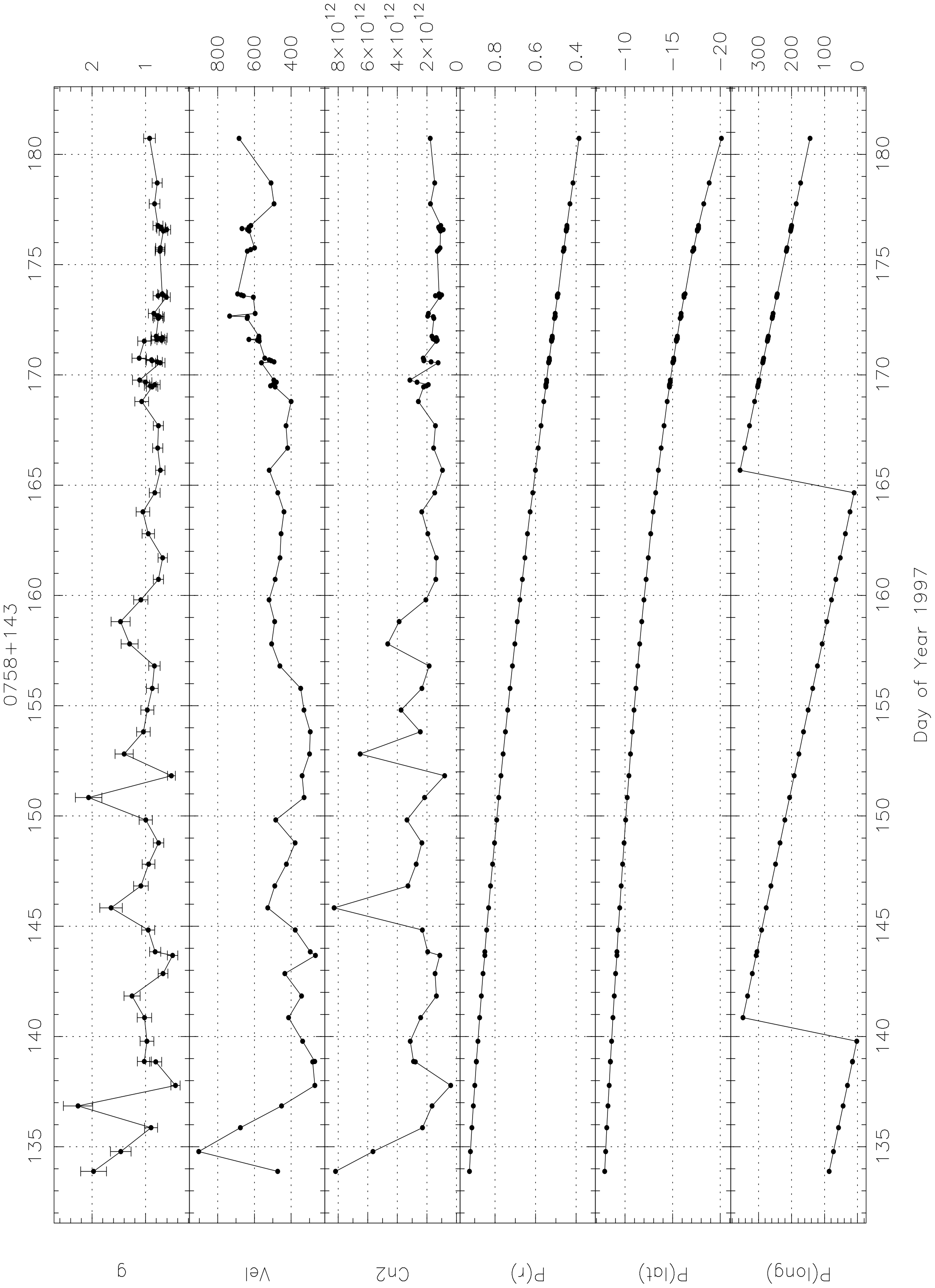

Figure 5.24: **Observations of** 0758+143 – The observations for the source 0758+143 are presented in the same format as for Figure 5.17.

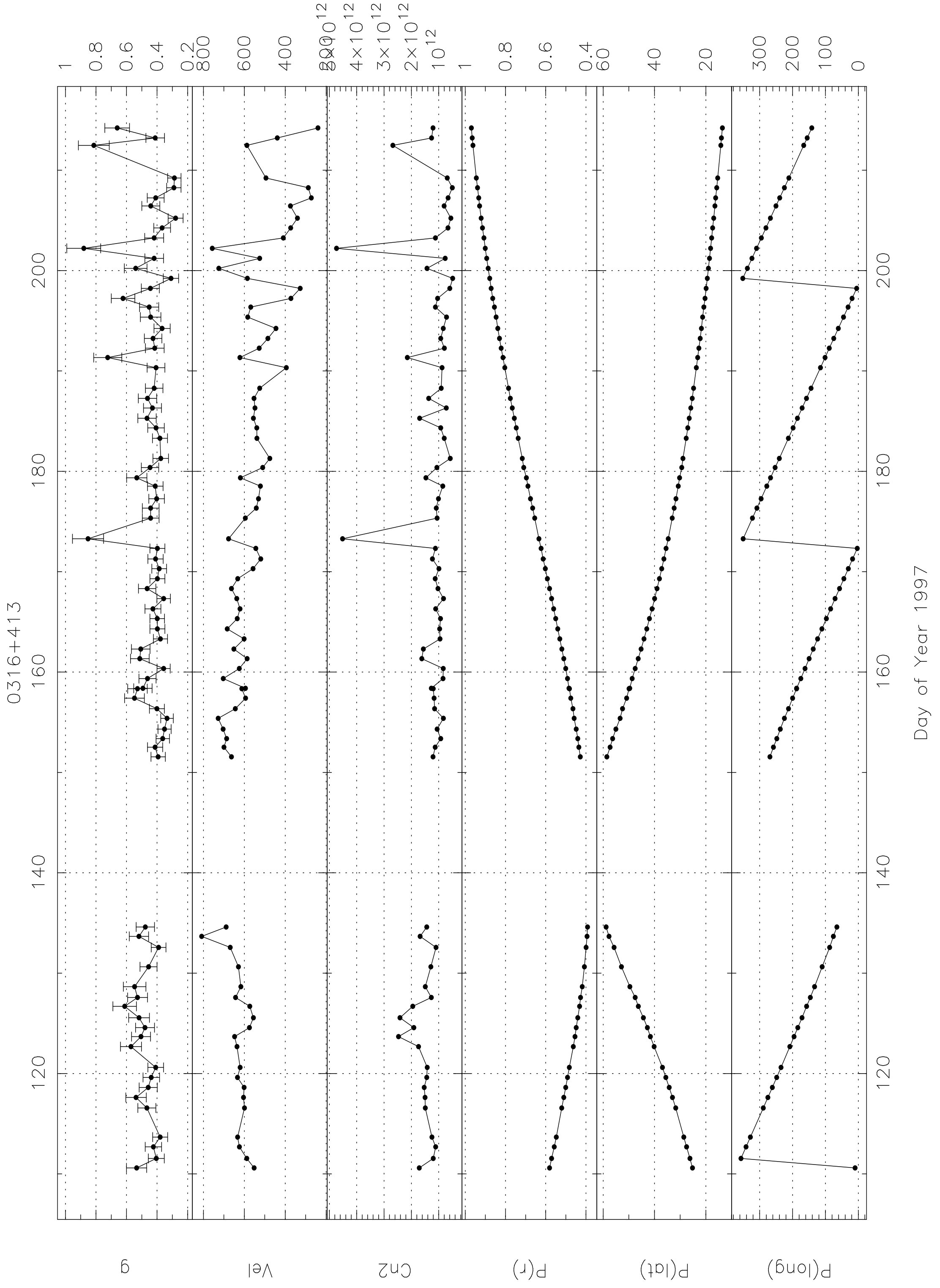

Figure 5.25: **Observations of** 0316+413 – The observations for the source 0316+413 are presented in the same format as for Figure 5.17.

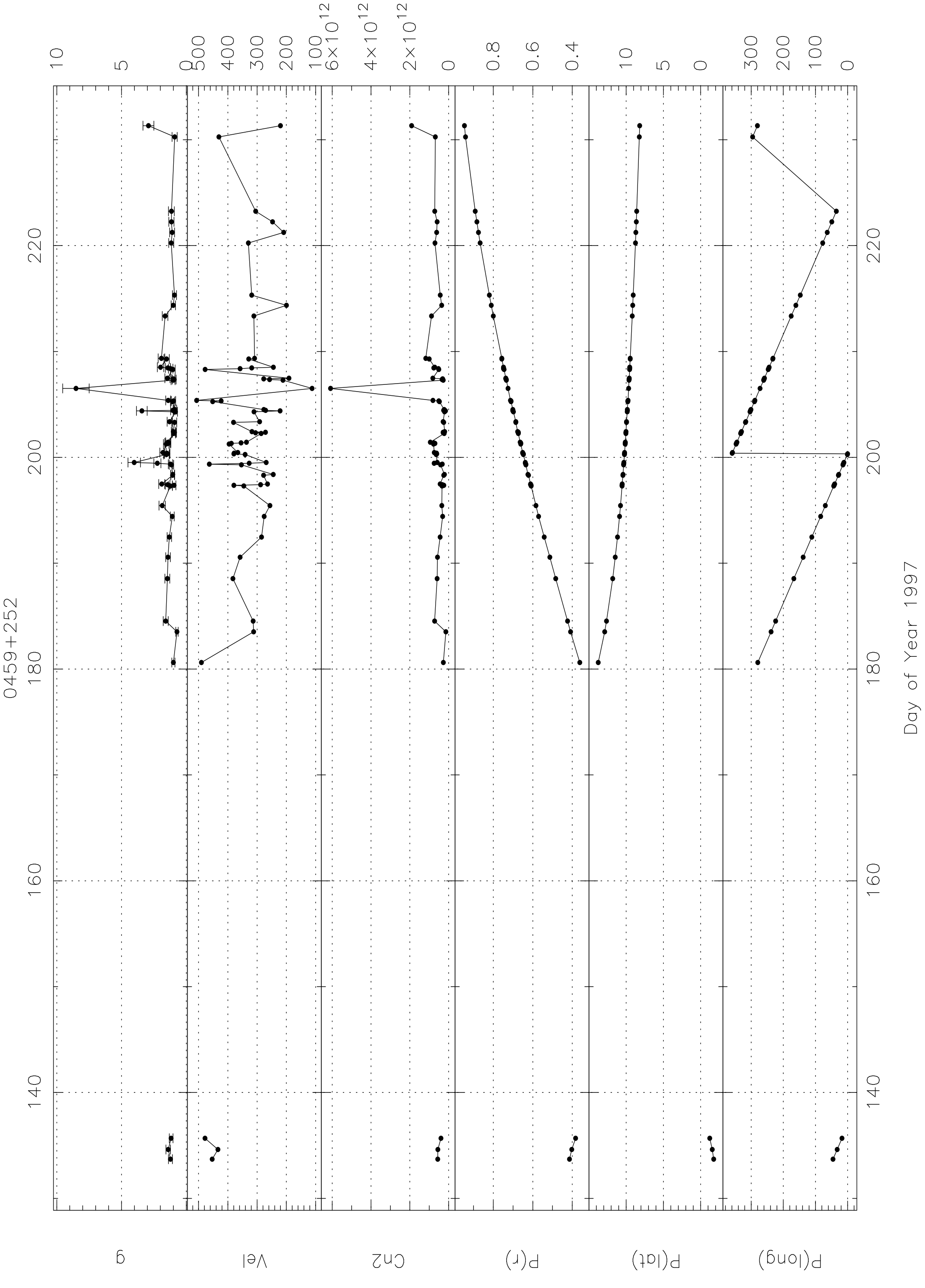

Figure 5.26: **Observations of** 0459+252 – The observations for the source 0459+252 are presented in the same format as for Figure 5.17.

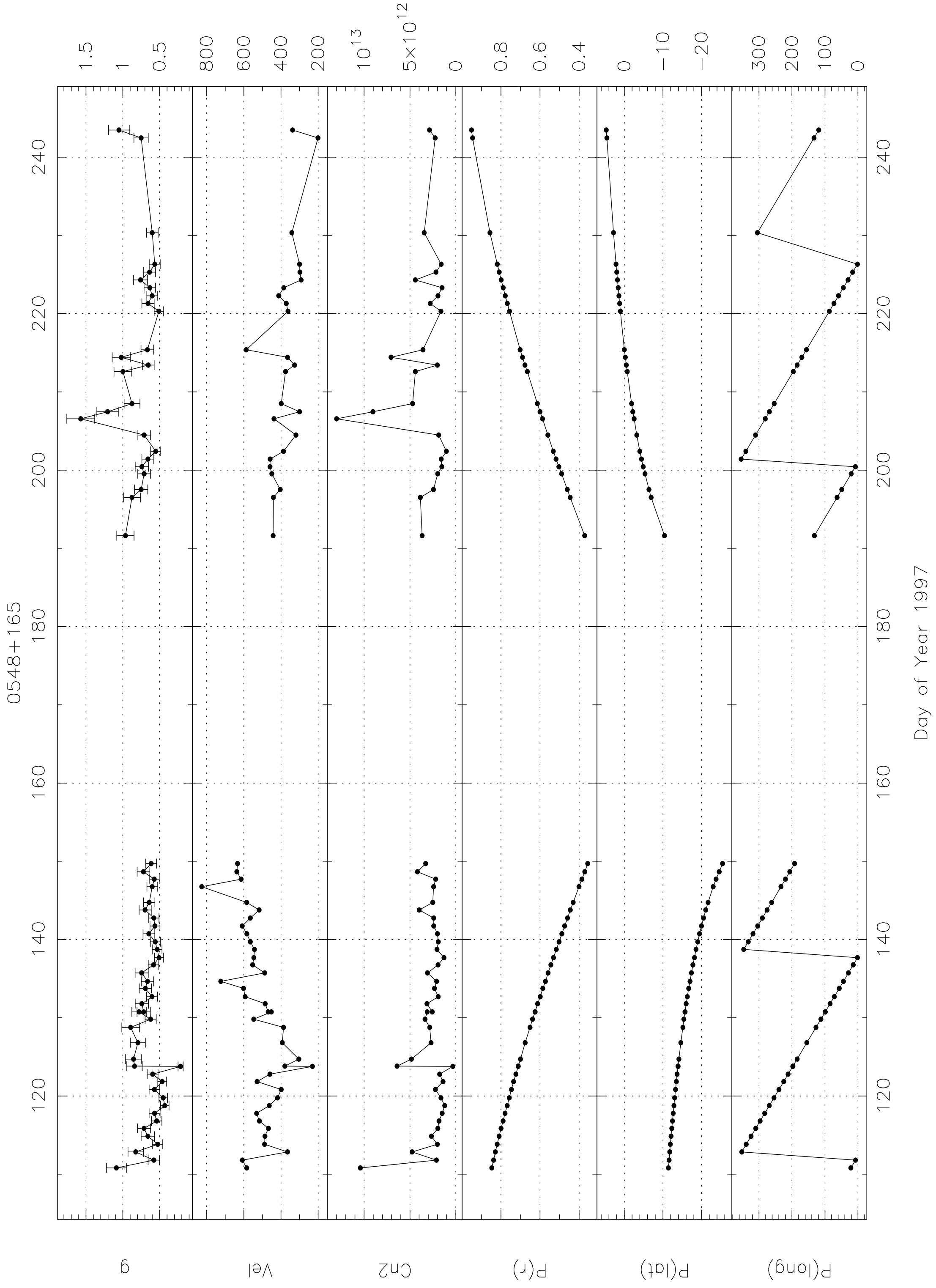

Figure 5.27: **Observations of** 0548+165 – The observations for the source 0548+165 are presented in the same format as for Figure 5.17.

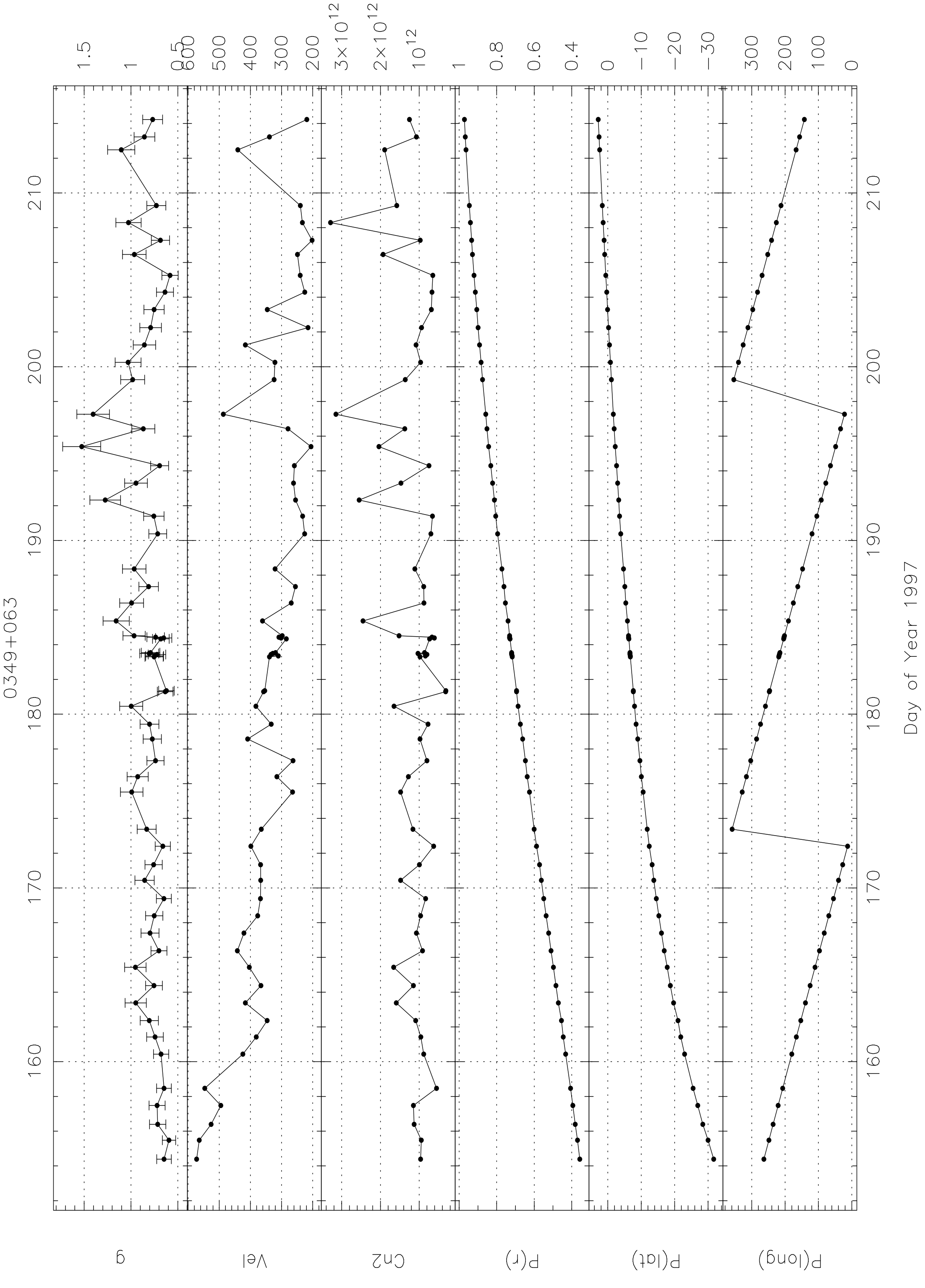

Figure 5.28: **Observations of** 0349+063 – The observations for the source 0349+063 are presented in the same format as for Figure 5.17.

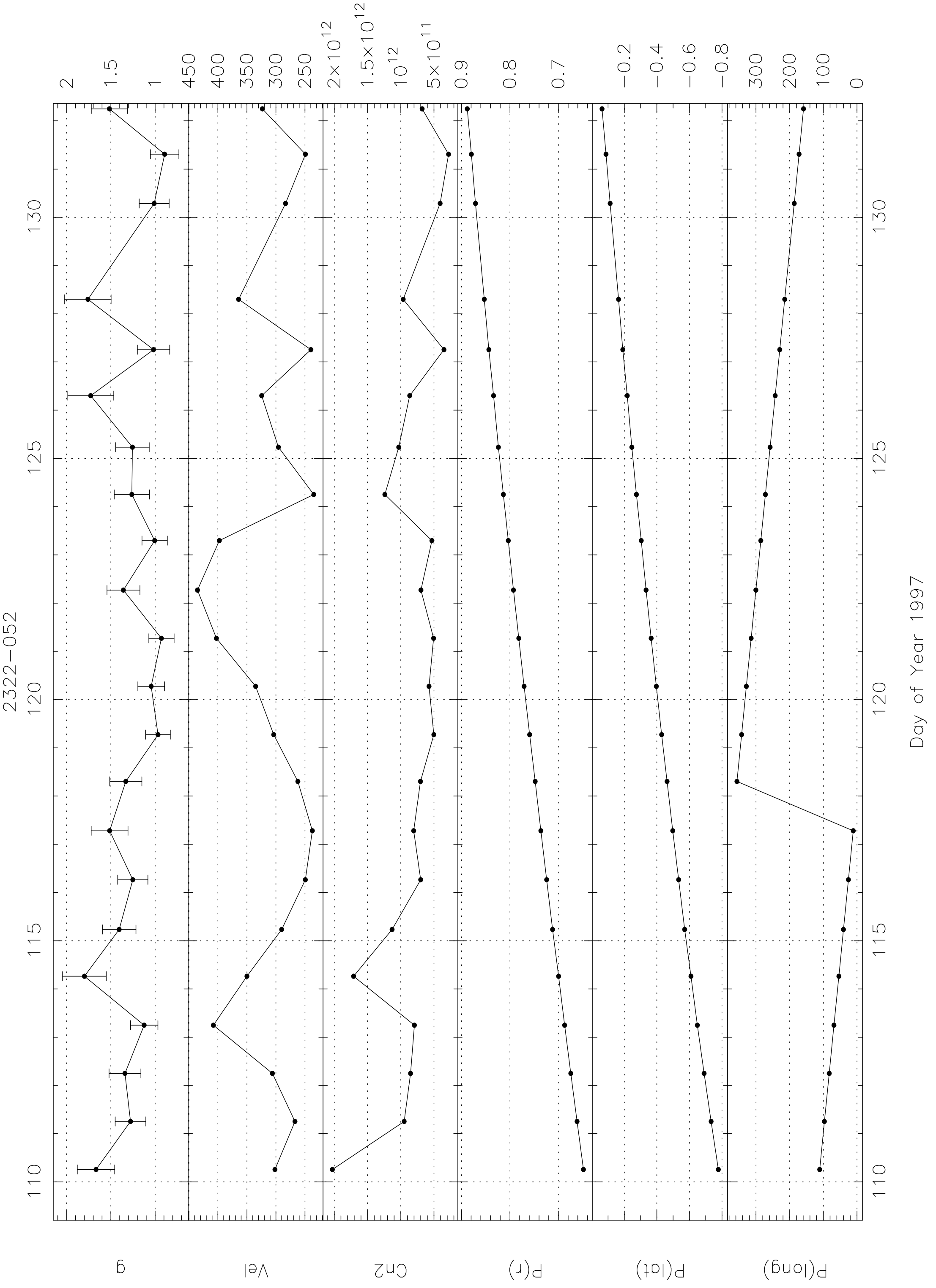

Figure 5.29: **Observations of** 2322-052 – The observations for the source 2322-052 are presented in the same format as for Figure 5.17.

C_n^2 vary in tandem, for instance the features seen towards 0116+082 on day number 139, 0758+143 on day number 146 and 0316+413 on day number 174. In some cases the peak values in the velocity and C_n^2 times series are not coincident, for example the C_n^2 peak comes earlier than the peak in velocity time series in the features seen towards 0202+149 on day number 157 and towards 0725+147 around day number 112. At times distinct features in the velocity time series have no corresponding feature in the C_n^2 time series, for instances the features seen towards 0531+194 around day number 200. Some distinct C_n^2 features also have no corresponding features in the velocity time series, for instance the features seen towards 0548+165 on day number 206 and towards 0316+162 from day numbers 155 to 165. There are also instances when the velocity and C_n^2 variations seem to be anti-correlated.

5. There are large amplitude *spikes* in in g and C_n^2 which take place over time scales of a few hours. A few of these are seen the accompanying figures - the feature on day number 124 seen towards 0005-062, on day number 222 towards 0531+194, on day numbers 173 towards 0316+413 and on day number 206 towards 0459+252. All these power spectra are poorly represented by the featureless Solar Wind models. None the less, the values of velocity and C_n^2 obtained from these models is probably representative of the average properties of the Solar Wind along the *l.o.s.*. This data is indicative of a very dense plasma blob with a small velocity component perpendicular to the *l.o.s.* passing through. The spatial extent of these blobs is expected to be small as the time scale associated with these events is of the order of a few hours.

6. In contrast to the short time scale variations mentioned above, correlated velocity and C_n^2 variations on time scale of many days are also seen. A few of these are the features seen towards 0316+162 from day numbers $\sim$ 155 to $\sim$ 165 and towards 2322-052 from day numbers $\sim$ 113 to $\sim$ 124.

7. The IPS velocities estimated for some of the power spectra turn out to be unusually low (115–175 $km\ sec^{-1}$). The spectra fitted with the lowest velocities are shown in Figure 5.14. The presence of ionospheric scintillation has the effect of enhancing the power in the low frequency part of the power spectrum, which would result in a low IPS velocity on fitting uniform Solar Wind models. While an examination of the raw observed power spectra did not indicate the clear presence of ionospheric scintillation, the possibility of a contamination due to low level ionospheric scintillation cannot be ruled out. We examined a few power spectra observed just before and after the ones with low velocities. In some of the cases we do find a tendency for the consecutive power spectra to have a low frequency excess but it is usually much less pronounced as compared to that in the spectra shown in Figure 5.14. Often the consecutive observations

are towards sources are close to one another in angular distance and sample nearby regions of the heliosphere. It is, therefore, not easy to discern the effects of ionospheric scintillation from those due to some high C_n^2 features in the Solar Wind away from the P-point. Some of these power spectra are isolated cases of low velocities, with the neighbouring spectra showing no such tendency. All these power spectra, except two, have g values close to unity, while ionospheric scintillation is expected to boost them to higher values. Though we cannot rule out the presence of ionospheric scintillation, we do not expect the low velocities from all these power spectra to be because of ionospheric scintillation.

One may suspect the IPS velocities for low S/N spectra to have been underestimated but not all of these spectra have a low S/N. We investigated the possibility of a tendency for the best fit IPS velocities to decrease as a function of S/N and no such trend could be discerned in the data-set.

The fact that 13 of the 16 highest velocity spectra come from observations at elongations less than 30° deserves a comment (Figure 5.13). In contrast, 75% of the lowest velocity measurements shown come from observations at elongations larger than 45°.

5.8 Possible studies of the Solar Wind using the data-set

The high S/N data-set with a dense coverage of the equatorial Solar Wind obtained for this thesis can yield a wealth of information about the Solar Wind. Data-sets with such extensive coverage are hard to obtain as they require a dedicated stable and sensitive telescope for long durations (many months) and are observationally very intensive to carry out. While the emphasis of this work has been a tomographic reconstruction of the Solar Wind in the inner heliosphere (Chapter 7), there are other studies as well for which this data-set is well suited. These include :

1. **Analysis and modelling of transients** – As has been mentioned in the previous section, the most prominent transient during the course of the observations was detected in the solar corona on the 12th May 1997, it occurred close to the central meridian and is believed to be an Earth directed CME (Plunkett et al., 1998; Thompson et al., 1998). Due to the dense coverage of the equatorial Solar Wind this Earth directed CME has been sampled very well by our data-set. The event has been sampled well by *l.o.s.*s to 27 different sources, with many observations both before and after the disturbance has passed through. Lines-of-sight to another 11 sources provide less extensive but useful constraints. This extensive sampling can constrain the spatial extent

and the radial velocity profile of the CME in a more robust manner than is usually possible. This data can also be used to study the properties of the disturbed Solar Wind plasma like turbulence characteristics and to estimate the mass of the CME as has been done earlier (Gothoskar and Rao, 1999; Manoharan et al., 2000). Using this information in conjunction with the data available from a variety of other sources ranging from radio heliographs and white light coronographs to Solar Wind plasma measurements by Earth orbiting satellites allow one to study this event in considerable detail and follow its evolution from close to the Sun to 1 AU. Preliminary studies have established the self consistency of the data-set and lead to a model consistent with observations at 1 AU from Solar and Heliospheric Observatory (SOHO) and WIND (Section 6.6) spacecrafts.

Large Angle and Spectrometric Coronograph (LASCO) coronograph onboard SOHO saw on an average 0.8 CMEs per day during our epoch of observations, most of which took place in the equatorial belt (St. Cyr et al., 2000). The dense coverage of the equatorial belt in our data-set implies that most of these CMEs would have been sampled by the observed $l.o.s.$s. As the coronograph data measures only projections on the plane of the sky, it cannot constrain the heliographic longitude of origin of the CMEs to better than $\pm 90°$. Our data-set and the SOHO-LASCO data together can be used to locate the sites of origin of CMEs in a better constrained manner. LASCO measurements extend upto $\sim 30\ R_\odot$ and provide radial velocity profiles of the CMEs (projected on the sky plane) while our IPS data provides measurements from 80 $R_\odot$ onwards, this can be used to study the radial velocity profiles of the CMEs over a large range of heliocentric distance.

The large variety of correlated velocity and C_n^2 variations which were mentioned in the previous section merit individual attention. The details of the time variations observed would depend on the geometry of the $l.o.s.$ and that of the Solar Wind structure being sampled. We plan to undertake detailed investigations for a few of the interesting cases.

2. **Radial evolution of Solar Wind properties** – The dense elongation coverage of the equatorial Solar Wind makes this data-set very useful for studying the radial evolution of properties of the Solar Wind to which IPS is sensitive. These properties are velocity, C_n^2, α, $AxialRatio$ and q_i. Of these, we consider the variation of velocity in considerable detail in Chapter 6.

   Though in the final analysis presented in this thesis, the values of AR, α and q_i have been kept fixed and only velocity and C_n^2 form the free parameters of the model, we did some experimenting allowing AR to be a free parameter as well. A trend for the average value of best fit AR to increase with heliocentric distance was noticed in these experiments. The AR of Solar Wind plasma is known to tend to a value close to 1.0 by about 0.3 AU starting from much higher values close to the Sun and there is little reason to expect its value to increase at larger heliocentric distances. We suspect that the apparent increase in the best fit value of AR is a reflection of the increasing departures of the observed power spectra from the uniform Solar Wind models. As the Solar Wind propagates outwards, the interaction between the slow and the fast moving plasma causes the structures to be increasingly prominent. The presence of structure in the Solar Wind cause the *knee* of the power spectrum to be more rounded and this is indistinguishable from an increase in AR to the uniform Solar Wind models. A more detailed simulation which incorporates the interaction of the Solar Wind, at least in some approximate manner, would help in understanding this behaviour and testing the conjecture presented above.

While our data-set is not be very sensitive to variations in q_i in equatorial Solar Wind with heliocentric distance because most of the power spectra are dominated by the source size filter rather than the q_i filter (Equation 2.52), it would be a useful database to study the variations in α. It may also be possible to look for latitudinal dependences of α in the equatorial belt of the Sun.

3. **Comparison of spacecraft and IPS velocity measurements** – Given the density of coverage of the equatorial regions, it would be possible to build a IPS velocity model, use this data-set, which can predict the velocity time series observed by the Earth orbiting satellites. While IPS velocity measurement are a weighted average along the entire *l.o.s.*, with the weighting factor being proportional to strength of fluctuations in the electron density spectrum, satellite *in-situ* measurements are local in nature and have no such weighting factor associated with them. A comparison of the velocity measurements obtained from these two methods, which differ in their basic nature, would help in understanding and rationalising the biases associated with them and the differences which they lead to.

As in this work, we concentrate on the tomographic reconstruction of Solar Wind in the inner heliosphere, the above mentioned studies will not be elaborated on any further. They will be presented separately and do not form a part of this thesis.

Chapter 6

Radial Evolution of the Solar Wind

6.1 Introduction

Historically, the early attempts to study the dependence of velocity of the Solar Wind on the radial distance from the Sun covered the distance range of about 0.5 – 1.0 AU. Intriligator and Neugebauer reported absence of statistically significant changes in the average velocity of the Solar Wind in range 0.7 – 1.0 AU using the Pioneer 9 and OGO 5 data from late 1968 and early 1969 (Intriligator and Neugebauer, 1975). Coles and Rickett also reported, from IPS observations, lack of evidence for significant variation in the average velocity of the Solar Wind near the ecliptic plane between 0.4 and 1.1 AU (Coles and Rickett, 1976). It is worth pointing out that in the database of IPS observations available to Coles and Rickett, the daily *rms* on the *mean* estimate of velocity was $\sim$ 100 $km\ sec^{-1}$, a point which they clearly make. Coles has summarised the pre 1978 observational status in a review (Coles, 1978). Schwenn et al. found that the average velocity of the Solar Wind increases by 52 ± 11 $km\ sec^{-1}\ AU^{-1}$ over a distance range of 0.3 – 1.0 AU, in the *slow* Solar Wind (Schwenn et al., 1981). They also found that the *fast* Solar Wind continued to propagate with nearly the same velocity. This study was based on the data from Helios 1 and Helios 2 satellites at epochs when the two spacecrafts were radially aligned with the Sun in 1976 and 1977.

There have been many recent attempts to study the velocity of the Solar Wind close to the Sun, in the acceleration region, both in the equatorial and the polar regions. These attempts have used remote sensing techniques like IPS at high radio frequencies ($\sim$ 2 – 8 GHz), which allows one to sample the regions in the range from $\sim$ 5 – 80 $R_\odot$, (Yamauchi et al., 1998; Grall et al., 1996; Yamauchi et al., 1996; Tokumaru et al., 1994). These and other similar studies limit the acceleration region of the Solar Wind to $\sim 60 - 80\ R_\odot$ ($0.25 - 0.35\ AU$).

Few attempts have been made, in the recent past, to investigate the radial evolution of the Solar Wind velocity in the $0.35 - 1.0\ AU$ range, the range accessible to IPS in the meterwave range of the electromagnetic spectrum. This chapter discusses our attempts to study the radial evolution of Solar Wind in this distance range. The entire data-set obtained has been included in this study. As our dataset was optimised to study the equatorial regions of the Sun, the regions outside a heliographic latitude range of $+15°N$ to $-15°S$ are poorly sampled. The sampling of the higher latitudes is much sparser as compared to the ecliptic and large fractions of the foot-points of *l.o.s.*s to these sources lie outside the ecliptic place. Their presence is not expected to cause any significant contamination from the non-equatorial Solar Wind to the equatorial Solar Wind but stabilises the solution at high latitude by putting constraints. Though the entire data-set obtained has been included in this study, the conclusions drawn from this analysis pertain only to the equatorial belt of the Sun ($+15°N$ to $-15°S$).

The original motivation for this piece of work was to construct an *initial guess* which could be used as an input to the tomographic reconstruction of the 3D structure of the Solar Wind. Some of the results which this exercise yielded were interesting enough to merit independent follow up.

6.2 Single station velocity determination

All power spectra in the dataset were modelled using a featureless Solar Wind model. This model, referred to in the literature as *single-station IPS model*, is described in Section 3.2. The automated procedure described in Chapter 5 was used to estimate the best fit IPS models for each of the observed power spectra. In the first run of the automated procedure, velocity, C_n^2 and source size were treated as free parameters of the IPS model. The results of the best fit estimation procedure were used to compute an average source size for each of the observed sources. The best fit models were re-estimated, using the automated procedure, with the source size frozen to be the average value for the source and velocity and C_n^2 as free parameters. AR, was held fixed at values of 1.0 and α was frozen to a value of 3.0. The rationale behind this choice is discussed in Section 2.6. q_i and $\theta_\circ$ effect the power spectrum of intensity fluctuations in a similar manner and need to be carefully distinguished between. The effects of variation of q_i with radial distance from the Sun were looked for and were not found to be discernible (Section 5.3.5). The effects due to change in q_i were, therefore, not considered important and have been ignored in the IPS model. A value of s_i ($s_i = 3/qi$) close to 0.0 km was used and the contribution from its constant value have been absorbed in the $\theta_\circ$ estimate. The effect of random velocity

Table 6.1: ϵ **and** P**-point distance bins** – Columns 2 and 3 give the minimum and the maximum P-point distances to the *l.o.s.*s included in a given bin, column 4 the mean P-point distance of the *l.o.s.*s, columns 5 and 6 the ϵ corresponding to the minimum and the maximum P-point distances and column 7 the number of observations which have contributed to the bin.

Bin No.	P_{min} AU	P_{max} AU	$\overline{P}$ AU	ϵ°_{min}	ϵ°_{max}	No. of data points
1	0.34	0.55	0.44	20.0	33.4	925
2	0.55	0.76	0.67	33.4	49.5	1497
3	0.76	0.98	0.87	49.5	80.0	1373

on the power spectra is believed to be negligibly small beyond radial distances of ~ 0.30 AU and was hence ignored (Section 2.6).

6.3 The latitudinal profile of Solar Wind velocity

The dataset was divided into three equal bins in distance of the P-point from the Sun. The P-point distance and ϵ ranges spanned by each of the bins are given in Table 6.1. The average P-point distance corresponding to the three bins is 0.44, 0.67 and 0.87 AU respectively. All the three bins have a large number of observations contributing to them, $\sim$ 1000 or more each.

For observations in each of these bins, all the *l.o.s.*s were projected on a fiducial spherical surface of radius $\overline{P}$, concentric with the Sun. The velocity of the Solar Wind was assumed to be purely radial and it was further assumed that the Solar Wind travelled with a constant velocity within each of the bins. The best fit IPS model velocity, obtained using the structure-less Solar Wind model, was assumed to be the velocity of propagation of the Solar Wind all along the *l.o.s.*. Care was taken to remove the contamination in the IPS model velocity due to the Earth's motion around the Sun (Section 5.3.6). In order to project the *l.o.s.* on the fiducial surface, a geometric projection of the *l.o.s.* was first computed. Knowing the constant velocity of propagation of the Solar Wind for the particular observation from the IPS best fit model, the travel time from the fiducial surface to the *l.o.s.* was computed. Using the known angular rotation rate of the Sun, the change in the Carrington longitude of the geometrically projected *l.o.s.* to account for travel time was computed and corrected for. The track on the fiducial surface so obtained was assumed to represent the site of origin of the Solar Wind sampled by a given *l.o.s.*. For estimating the velocity distribution on the fiducial surface, the surface was broken up into discreet elements of size 20°(*longitude*) × 2°(*latitude*).

The power spectrum observed along a *l.o.s.* is a weighted sum of the contributions from the Solar Wind along the *l.o.s.* (Sections 2.5.2 and 3.2) The velocity estimated from the IPS best fit model was assigned to the track on the fiducial surface to which the *l.o.s.* was mapped, with a weight estimated as follows. The projected *l.o.s.* was represented by a set of discreet pixels adjacent to one another on the fiducial surface. The fraction of area under the model power spectrum (i.e. the fraction of m^2) contributed by the part of the *l.o.s.* represented by a pixel was used as the weight with which the *l.o.s.* contributed to a given pixel. This weight was normalised by the maximum contribution to the given *l.o.s.* by any pixel. The part of the *l.o.s.* which contribute significantly to the observed power spectrum does not extend much beyond 2 AU. In order to use an objective limit for the *l.o.s.*, a threshold value of 0.05 for the weight was used as the cut-off value. Each element on the *l.o.s.* contributes only to a point on the fiducial surface. Since the Solar Wind properties vary only slowly with position, we have assigned the estimated velocity at the point to a region 5° around it so that the projected *l.o.s.* instead of being a line on the fiducial surface is a band of width 5°. Thus each element of the *l.o.s.* could contribute to more than one resolution element (pixel) on the fiducial surface.

A weighted average of all the contributions to each of the pixels was taken to produce an average velocity map for each of the fiducial surfaces. Further, since the quantity of interest is time and longitude independent properties of the Solar Wind, a weighted averaging over heliographic longitude, $\phi_\odot$, was done to obtain the average velocity structure along $\theta_\odot$.

$$\overline{v_{\theta_\odot}} = \frac{\Sigma_{\phi_\odot=0^\circ}^{360^\circ} \overline{v_{\theta_\odot \ \phi_\odot}} \ w_{\theta_\odot \ \phi_\odot}}{\Sigma_{i=0^\circ}^{360^\circ} w_{\theta_\odot \ \phi_\odot}} \tag{6.1}$$

The error bars represent formal errors on the average latitudinal structure of velocity and have been obtained using the following standard expression :

$$\sigma_{v_{\theta_\odot}} = \sqrt{\frac{\Sigma_{\phi_\odot=0^\circ}^{360^\circ} (\overline{v_{\theta_\odot}} - \overline{v_{\theta_\odot \ \phi_\odot}})^2 \ w_{\theta_\odot \ \phi_\odot}}{\Sigma_{\phi_\odot=0^\circ}^{360^\circ} w_{\theta_\odot \ \phi_\odot}}} \tag{6.2}$$

The velocity dependences on latitude so obtained are shown in Figure 6.1 for each of the three radial bins. Each of the curves is labelled by the bin number to which it corresponds. The velocity increase by almost 200 $km \ sec^{-1}$ as one moves from the equatorial regions towards either of the poles in a short span about 20°. This structure of the Solar Wind is now well known and has been discussed by various researchers (Kojima and Kakinuma, 1990; Ananthkrishnan et al., 1995; Kojima et al., 1998) using IPS data and various empirical functional forms have been proposed to describe it. Spacecraft observations from ULYSSES out of the ecliptic

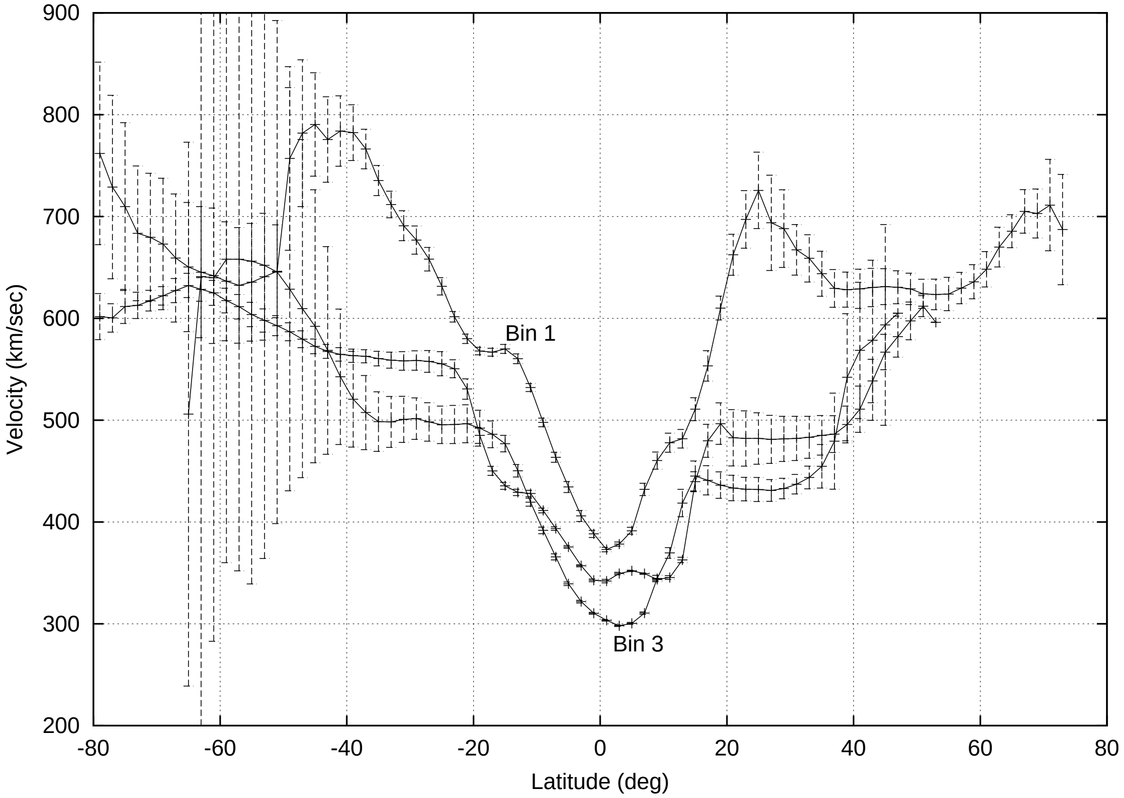

Figure 6.1: **Average velocity structure of the Solar Wind along $\theta_\odot$** – The three curves correspond to observations in each of the three P-point bins referred to in Table 6.1. The curves corresponding to the 1^{st} and the 3^{rd} bins have been labelled and the middle curve corresponds to the bin 2. The error bars on the data points represent 1σ uncertainties. They have been obtained by computing the *rms* of all the velocity contributions to a given latitude bin and dividing it by the root the number of contributions to the bin. The minimum value of velocity for bin 1 is 372.9 $km\ sec^{-1}$ and that for bins 2 and 3 are 342.0 and 298.1 $km\ sec^{-1}$, respectively. The mean value of velocity in the latitude range $\pm 10^\circ$ are 427 ± 43, 360 ± 23 and 332 ± 32 $km\ sec^{-1}$ for bins 1, 2 and 3 respectively.

plane provided the first *in-situ* measurements of the high latitude Solar Wind and confirmed this trend (Phillips et al., 1995).

From Figure 6.1 it is also evident that there is an distinct trend for the velocity of the Solar Wind to decrease with increase in the heliocentric distance. Thus there is a clear tendency for equatorial Solar Wind to decelerate as it flows outwards. This trend is different from the expected behaviour of the velocity of the Solar Wind. In order to convince ourselves of the authenticity of the trend, the analysis procedure and the data-set were critically examined to check for biases which could produce artifacts to mimic it. The next two sections discuss the various biases which have been considered.

6.4 The P-point approximation and its extension

In order to check if the observed radial dependence could be caused by the analysis procedure, the data was subjected to the conventional P-point analysis. The P-point analysis differs from the present analysis in asserting that the power spectrum observed along a $l.o.s.$ is so dominated by the part of the $l.o.s.$ close to the P-point that the contribution of the rest of the $l.o.s.$ is negligible (Section 3.2.1). A $l.o.s.$ is therefore believed to sample the Solar Wind from the small patch on the fiducial surface to which the Archimedean spiral from the P-point maps back. In contrast, the present analysis considers the $l.o.s.$ mapped to the fiducial surface to be band of considerable length and 5° in width. In the frame work of the present analysis the P-point analysis can be achieved by choosing the threshold value for the $l.o.s.$ weight to be so large that the the effective projected $l.o.s.$ is confined to a single pixel. In addition, the projected values were assigned only to the pixel which the Archimedean spiral mapped to and not to a patch 5° in width as in the above analysis. A value of 0.90 for the $l.o.s.$ weight was found to limit the effective projected $l.o.s.$ to a single pixel and was used to do the P-point analysis. The results of the exercise are shown in Figure 6.2. A trend for radial evolution of the velocity profile of the equatorial Solar Wind is still seen but its significance is compromised as the noise on the velocity profiles is large. The trend becomes significant if rather than the profiles, average values of the velocities for the three profiles, say in the latitude range $-10°$ to $+10°$, are compared. The average values are 424 ± 48, 361 ± 28 and 330 ± 33 $km\ sec^{-1}$ respectively in the order of increasing distance from the Sun, which are practically the same as obtained for the profiles obtained from our analysis (Figure 6.1). It should be noted that the 1σ error bars receive significant contribution from the systematic variations of velocity in the latitude range $\pm 10°$ and do not represent the random errors alone.

The only two parameters which differ between our analysis and the conventional

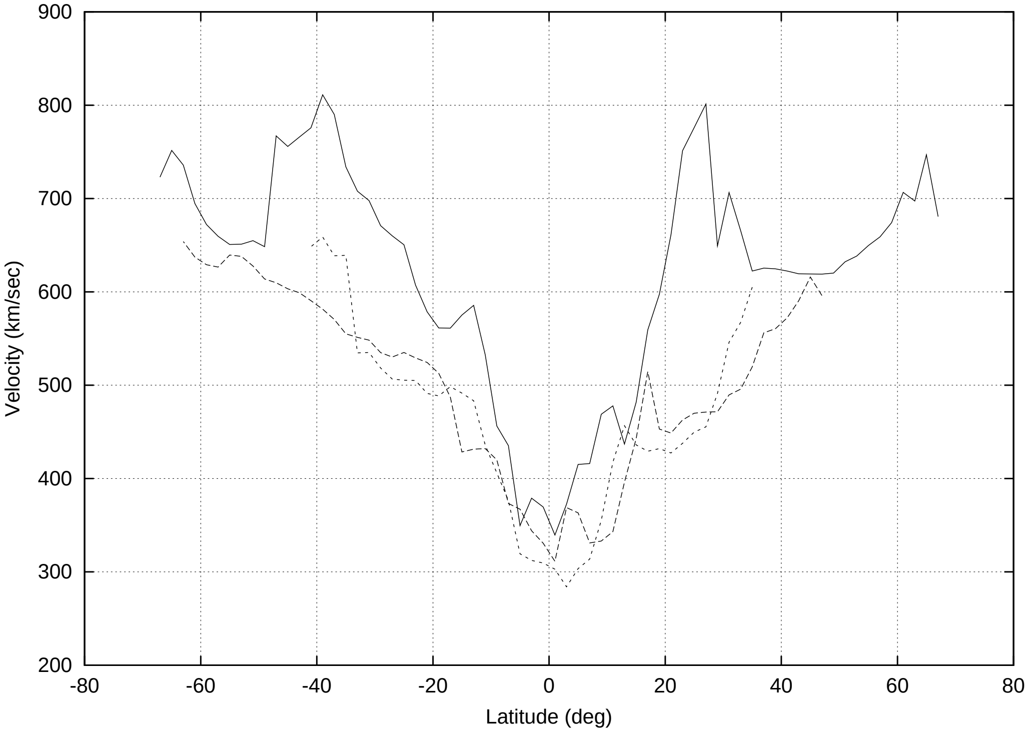

Figure 6.2: **The results of the P-point analysis** – The figure shows the results obtained on subjecting the same dataset as used in Figure 6.1 to the standard P-point analysis. A threshold value of 0.90 was used for the $l.o.s.$ weight and each $l.o.s.$ contributed to only one pixel on the fiducial surface. The solid curve corresponds to the first bin and the dashed and the dotted curves to the second and the third bin respectively.

P-point analysis are the choice of the threshold value of the $l.o.s.$ weight (to limit the effective extent of $l.o.s.$) and the width assigned to the $l.o.s.$. The noisiness of latitudinal profiles obtained using the P-point analysis and the clear presence of the decreasing trend in our analysis prompted us to do a systematic study by varying these two parameters. The results of the study are shown in Figures 6.2 – 6.5. These figures have all been made to the same scale and the error bars have not been plotted in order to aid comparison.

Figures 6.3 and 6.4 show the results of the analysis of the same data-set as in Figure 6.1 using a threshold for $l.o.s.$ weight of 0.50 and 0.05 respectively. The footpoints of the $l.o.s.$ on the fiducial surface were treated like a geometric line threading the pixels on the surface, no additional width was assigned to the projection of the $l.o.s.$. Figure 6.5 shows the results of the analysis using a threshold for $l.o.s.$ weight of 0.50 and assigning a width of 5° to the $l.o.s.$ projected on the fiducial surface. From Figures 6.2 – 6.5 it is evident that the trend for radial evolution of velocity profile becomes increasingly clear as the threshold value used for the $l.o.s.$ weight is

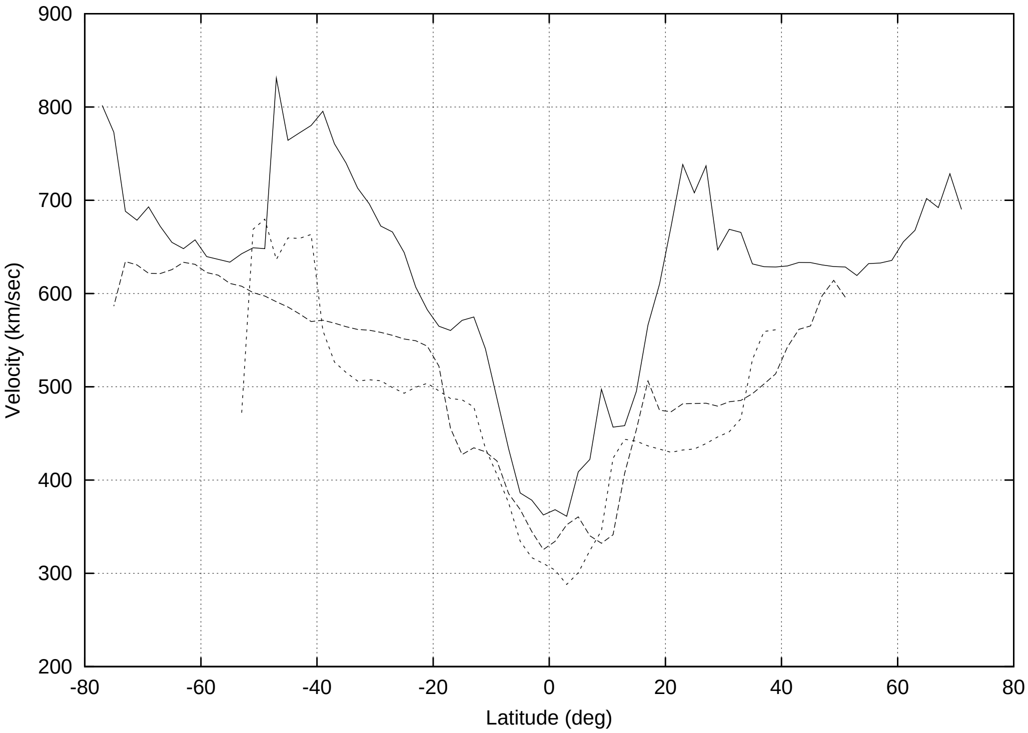

Figure 6.3: **Line-of-sight weight threshold of** 0.50 – A plot similar to figure 6.2 except that the *l.o.s.*s were projected back using a threshold value of 0.50 for *l.o.s.* weight. No width was assigned to the *l.o.s.*, in contrast to the analysis in Figure 6.1. The solid curve corresponds to the first bin and the dashed and the dotted curves to the second and the third bin respectively.

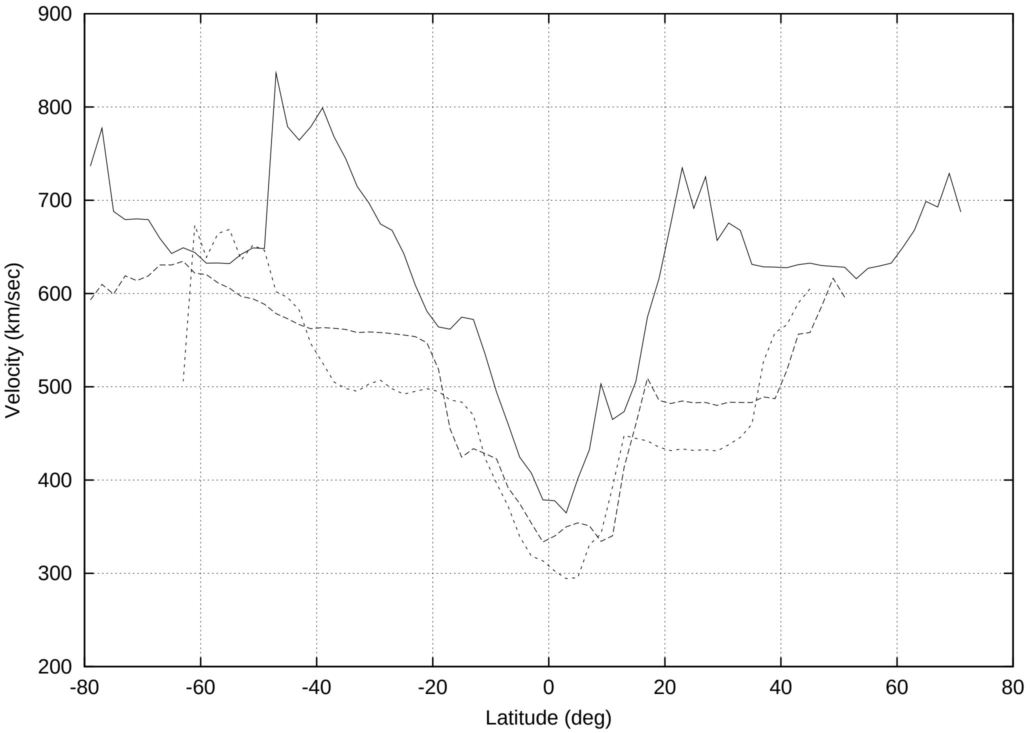

Figure 6.4: **Line-of-sight weight threshold of** 0.05 – A plot similar to Figure 6.2 except that the *l.o.s.*s were projected back using a threshold value of 0.05 for *l.o.s.* weight, same as that for Figure 6.1. No width was assigned to the *l.o.s.*, in contrast to the analysis in Figure 6.1. The solid curve corresponds to the first bin and the dashed and the dotted curves to the second and the third bin respectively.

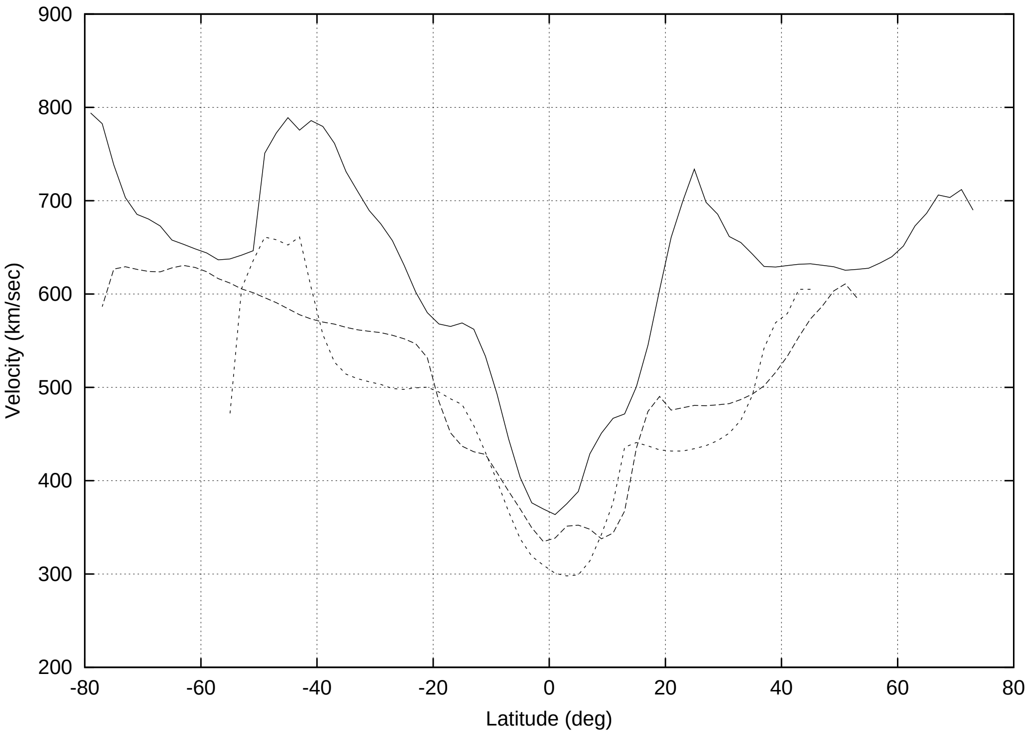

Figure 6.5: **Line-of-sight weight threshold of** 0.50 **and a width of** 5° – A plot similar to Figure 6.2 with the analysis differing in that the a threshold value of 0.50 for *l.o.s.*weight was used. In addition, instead of treating the projected *l.o.s.* like a geometric line, it was assumed to have a width of 5°. The solid curve corresponds to the first bin and the dashed and dotted curves to the second and the third bin respectively.

lowered.

The decrease in threshold of *l.o.s.* weight leads to an increase in the length of the track to which a given *l.o.s.* is mapped and allows a given observation to contribute to a larger number of pixels. It is worth pointing out that, as the velocity distribution on the fiducial surface is averaged over longitude, in order to obtain the average latitudinal velocity profile, the increase in the longitudinal extent of the *l.o.s.* is of no consequence. For most *l.o.s.*s, the latitudinal extent also increases with increase in the longitudinal extent of the *l.o.s.* and this increase in latitudinal extent grows as the P-point of the *l.o.s.* moves away from the heliographic equator. The trend becomes even clearer if a width, larger than the pixel dimensions, is assigned to the *l.o.s.*s, as the *l.o.s.* can then contribute to a the neighbouring pixels as well.

This effect of including larger and larger parts of the *l.o.s.* is a *convolution* of the velocity on the fiducial surface with a smoothing function which is the projection of the weighted patch on the solar surface to which a *l.o.s.* is mapped, on the latitude axis. The weights correspond to the strength with which given points on the *l.o.s.* (pixels in this case) contribute to the power spectrum. As the threshold weight used to delimit the *l.o.s.* is reduced or the width assigned to the *l.o.s.* is increased, this smoothing function increases in spatial extent. Smoothing with a function of progressively larger spatial extent removes the more and more of the higher frequency structure from the latitudinal velocity profile, resulting in smoother profiles. This effect is similar to that of passing a signal through a *low-pass* filter with a decreasing passband bandwidth or that of a convolution of an image by a progressively broader point spread function. The high frequency components act like noise in the velocity profile and reduce the significance of the differences between the velocity structure at different radial distances from the Sun.

The hypothesis that the difference between the conventional P-point analysis and the analysis described here is that of a convolution with a smoothing function was put to test. The velocity latitude profiles computed using the P-point approximation were convolved with a *box car* smoothing function of different spatial scale sizes and were compared with the results of our analysis. The P-point velocity profiles, smoothed to spatial scale sizes corresponding to 6°, 10° and 14°, are shown in Figure 6.6 for bin 1 and 2 and in Figure 6.7 for bin 3. A constant velocity of 200 $km\ sec^{-1}$ has been added to the profile smoothed to 6° and 100 $km\ sec^{-1}$ to the one smoothed to 10° in order to facilitate comparison. The velocity profiles obtained from our analysis (Figure 6.1) have been over-plotted on the profile smoothed to 14°. Though the the profiles do not match in detail, they are quite similar in the $\theta_\odot$ range of interest. The smoothing which takes place in our analysis procedure is a combined effect of the latitudinal extent of the individual *l.o.s.*s and differs in detail from the simple box car smoothing used above. Section 6.5.1 discusses the nature of smoothing in our analysis is more detail.

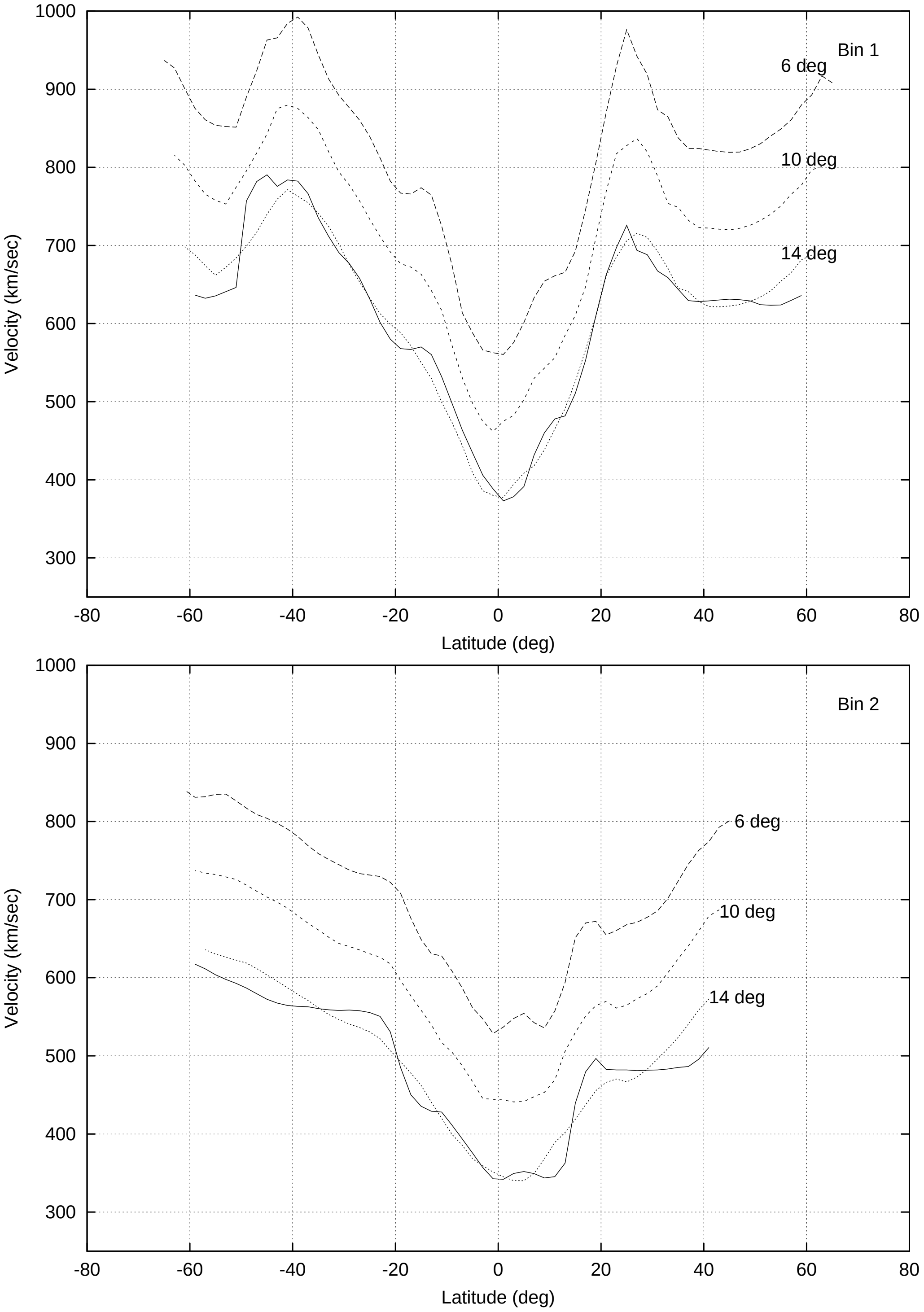

Figure 6.6: **Latitudinal velocity profiles from P-point analysis for Bin 1 and 2, smoothed to different spatial scales** – The figure shows the results of smoothing the velocity profile obtained form conventional P-point analysis over 6°, 10° and 14°. A constant velocity of 200 $km\ sec^{-1}$ has been added to the profile smoothed to 6° and 100 $km\ sec^{-1}$ to the one smoothed to 10° in order to facilitate comparison. The velocity profiles obtained from our analysis (Figure 6.1) have been over-plotted on the profile smoothed to 14°. The first panel shows the velocity profiles for bin 1 and the second panel those for bin 2.

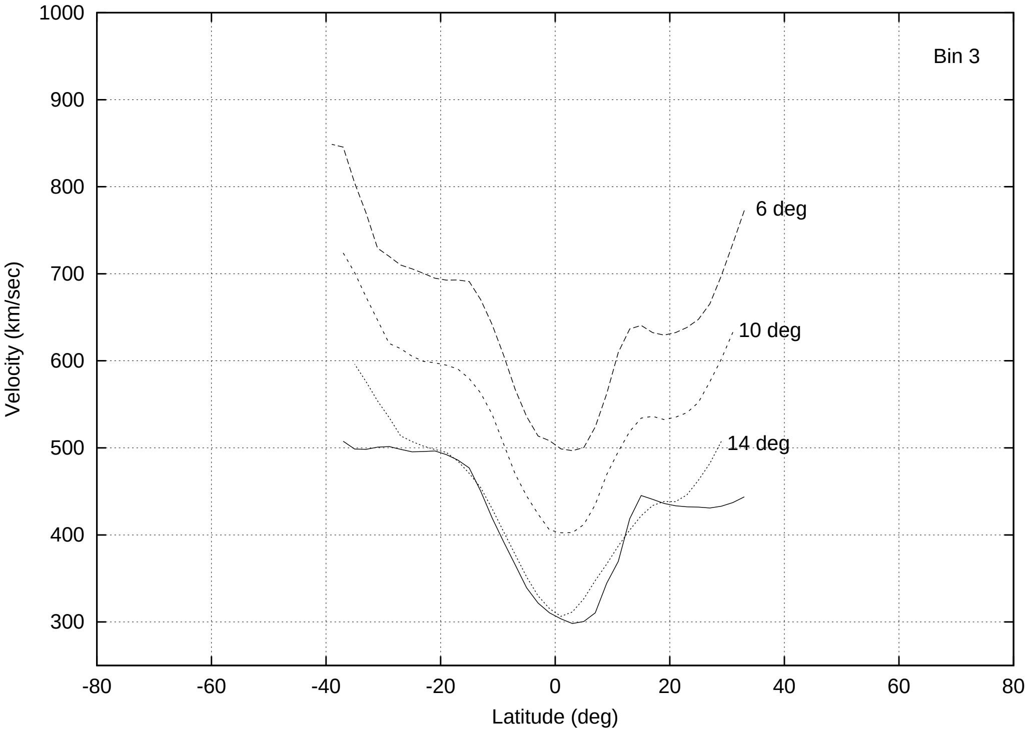

Figure 6.7: **Latitudinal velocity profiles from P-point analysis for Bin 3, smoothed to different spatial scales** – The latitudinal velocity profiles for bin 3 are shown in the same format as Figure 6.6.

In summary, the trend for deceleration of the average Solar Wind velocity is also seen on subjecting the data-set to the conventional P-point analysis but the significance of the trend is low because of the high frequency fluctuations in the latitudinal profiles. Our analysis, by assigning the velocities to bands on the fiducial surface rather than individual pixels, produces smoother profiles in which this trend stands out clearly. This method and the P-point analysis can be thought of as differing only in the latitudinal length scales over which the profiles are smoothed, as has been shown by the arguments presented above.

6.5 Discussion of possible artifacts and biases

In order to check if this trend for deceleration of Solar Wind was an artifact of the analysis procedure, the sampling of heliosphere or a bias introduced because of incorrect choice of parameters for IPS Solar Wind model, the following possibilities were considered.

6.5.1 Artifacts due to sampling of the inner heliosphere

The observed velocity along a *l.o.s.* depends on the velocity of the Solar Wind at every point on its track on the fiducial surface. As a source moves closer to the Sun, its P-point tends to move to higher heliographic latitudes and, therefore, the footpoints of the *l.o.s.* on the fiducial surface also extend to higher latitudes closer to the Sun (Section 2.1 and Figures 2.3 and 2.4). All *l.o.s.*s must originate from the Earth and, hence, must have a part of their track map back close to the heliographic equator. Given that the velocity varies steeply with heliographic latitude, the smoothening over a range of latitudes may lead to a contamination of the low latitude velocities by the high latitude velocities. If the distribution of P-point latitude of the observations, and the consequent sampling of the fiducial surface, is different in the three bins, the extent of this contamination and the length scales of smoothening in them might also be different. Smoothening over increasing length scales is expected to increase the value of the minima of the profiles. This contamination would produce a bias in the data which follows the observed trend of decrease in velocity with heliocentric distance. To look for the presence of this bias and estimate its severity, the following study was done.

The histograms of the P-point $\theta_\odot$ for the observations which contribute to each of the radial bins are shown in Figure 6.8. The effect of the P-point moving to progressively higher latitudes with decrease in elongations is clearly seen in the histograms. The histogram for bin 3 (bottom panel) is has a pronounced peak around median $\theta_\odot$ value of $-0^\circ.42$. Bin 2 (middle panel) has a broader distribution

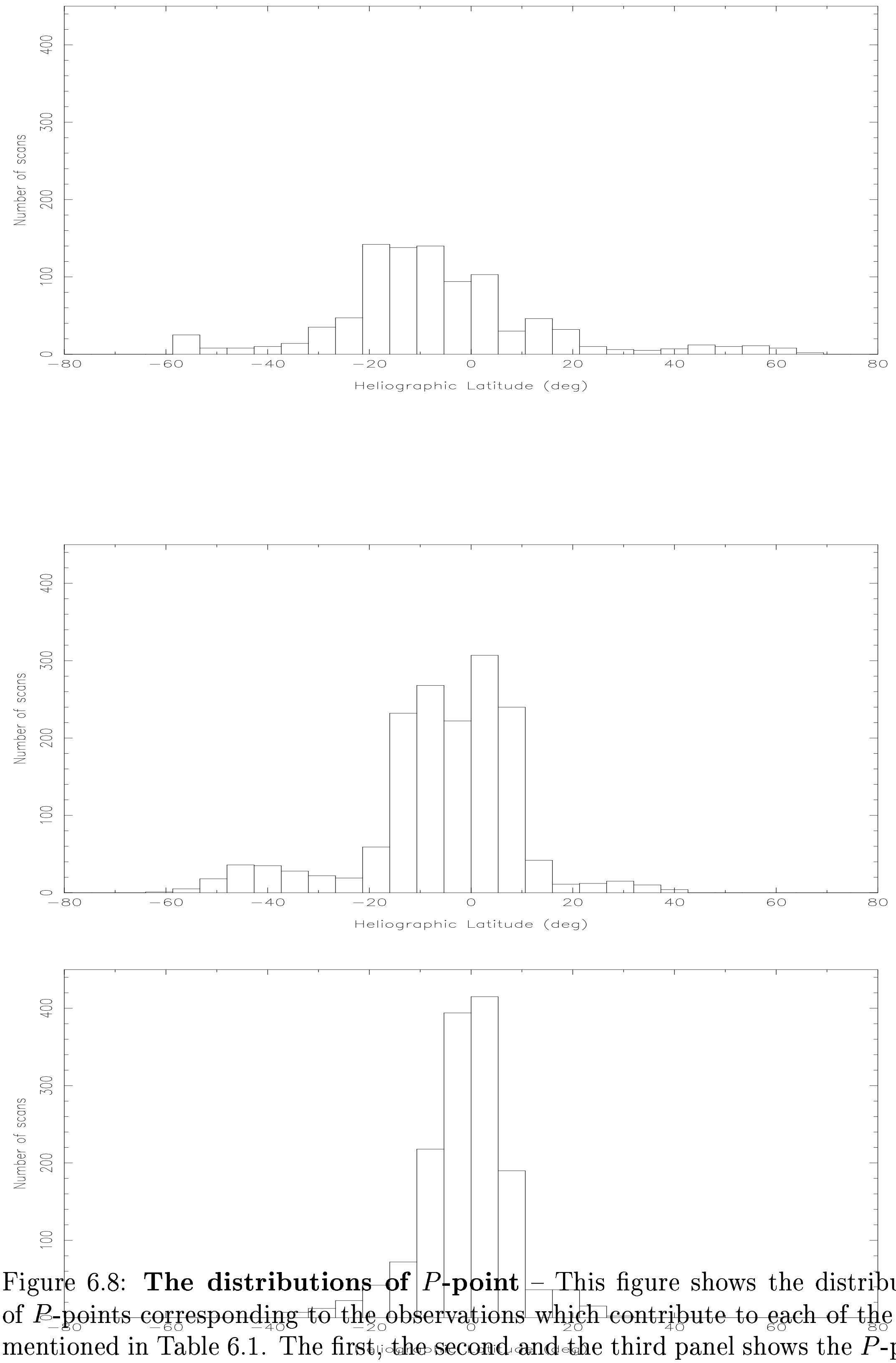

Figure 6.8: **The distributions of P-point** – This figure shows the distribution of P-points corresponding to the observations which contribute to each of the bins mentioned in Table 6.1. The first, the second and the third panel shows the P-point distribution for the first, the second and the third bin respectively.

as compared to bin 3 and the median $\theta_\odot$ value lies at $-4^\circ.1$. Bin 1 (top panel) has the broadest distribution and has a median $\theta_\odot$ value of $-8^\circ.8$. As bin 1 has the broadest distribution of P-points, the *l.o.s.*s contributing to it span the largest range in $\theta_\odot$. The steep rise in the velocity with latitude may lead to some contamination of the velocity profile in the low latitude region because the near Earth part of the *l.o.s.*s to even high latitude P-points map back close to the equator. On the other hand, the distribution of weight with which a part of *l.o.s.* contributes to the power spectrum is most sharply peaked for observations closest to the Sun, as discussed in Section 3.2.1. Also, the Fresnel filter term cuts down the contribution from the near Earth parts of the *l.o.s.*, which is the place from where one expects contaminations to creep in. These aspects allows the contributions from the higher P-point *l.o.s.*s to be mapped back to the proper place on the fiducial surface with minimal contamination to the low heliographic latitudes. The differences in the latitudinal spreads of the footpoints of *l.o.s.* in different bins, due to the differences in the P-point distribution, lead us suspect that the velocity latitude profiles for different bins may be smoothed over different spatial scales, with the bins closer to Sun smoothed over the largest spatial scales. Smoothing over increasing scale sizes is expected to increasingly raise the value of the minima of the profiles, a trend similar what is observed.

In order to estimate the extent of contamination in the velocity latitudinal profiles due to the bias introduced by the differences in P-point distribution for the three bins, the following simulation was carried out. Power spectra were generated assuming a latitudinal distribution of velocity of Solar Wind on a fiducial surface, similar to the observed distribution (Figure 6.9) and no radial velocity evolution. The best fit IPS model parameters for these power spectra were estimated using the automated procedure discussed in Chapter 5. This data was then subjected to the same analysis as described in Section 6.3 and latitude velocity profiles were estimated. The results of the exercise are shown in Figure 6.9. The model latitudinal velocity profile used to generate the power spectra and the profiles obtained for each of the three bins are marked. The figure is drawn to the same scale as Figure 6.1 to ease comparison. It is evident from the figure that the analysis is able to reproduce the model profile which was used to generate the data very well in the $\theta_\odot$ range -15° to 15°. The latitudinal profiles for the three bins are very close to one another in the $\theta_\odot$ range of interest. This clearly establishes that the differences in P-point sampling of different bins, and the consequent differences in sampling of the heliosphere and smoothing scales, do not produce any significant contaminations which may show up as biases mimicking average deceleration of the Solar Wind.

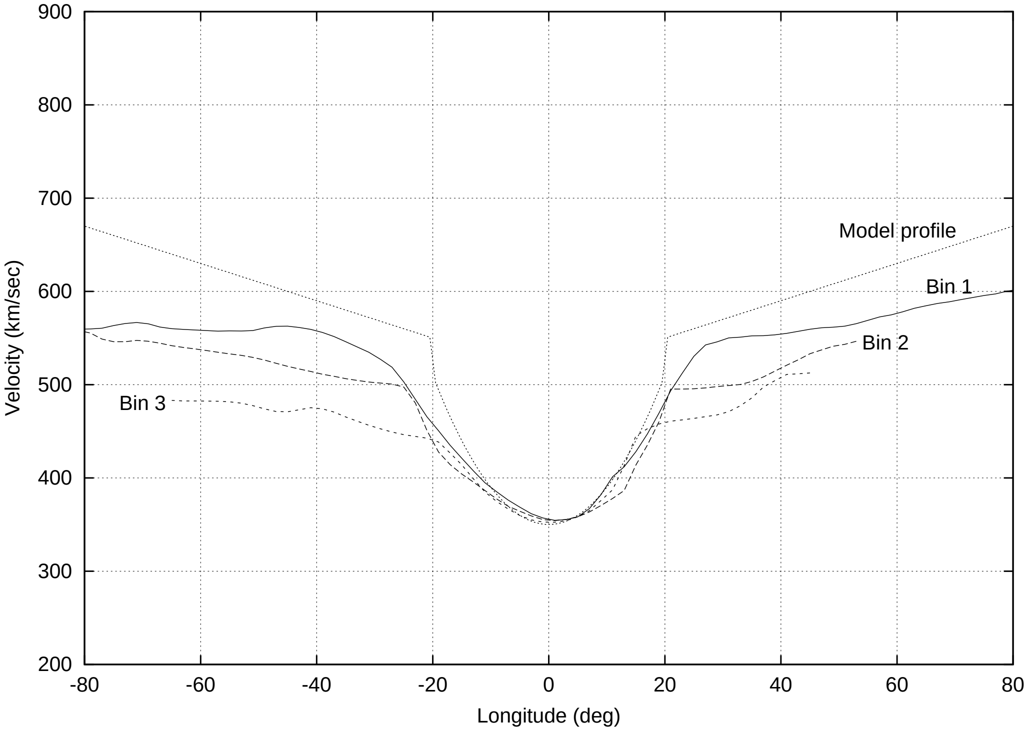

Figure 6.9: **Latitudinal Velocity profiles for simulated data** – This figure presents the results of the simulation done to estimate the artifacts in the observed latitudinal velocity profiles due to differences in sampling of the heliosphere and smoothing scale sizes. An input model with the shown velocity profile was used with no radial evolution. The velocity profiles profiles obtained for different bins have been labelled. All the three profiles stay close to the model profile used to generate the data in the $\theta_\odot$ range of interest (±15°). The differences in sampling of the heliosphere and smoothing scale sizes, hence, do not produce artifacts of magnitudes which may show up as the observed average deceleration of the Solar Wind with heliocentric distance.

6.5.2 Incorrect choices for Solar Wind model parameters

The Solar Wind model parameters which had been set to fixed values for the purpose of this study, were AR, α and q_i. We consider the possibility that the observed velocity trend arises due to these assumptions.

Axial Ratio biases

Since we have constrained Axial Ratio, AR, to be 1.0, in the entire range of observations from 0.34 – 0.98 AU, in our fitting procedure an intrinsic evolution of AR of Solar Wind along the radial direction from the Sun can manifest itself as evolution of velocity. For a power spectrum generated using a given AR, as the AR used in the IPS fitting procedure is increased, the velocity of the best fit IPS model also increases. The observed trend that the velocity of Solar Wind decrease with radial distance from the Sun can be explained by radial evolution of AR alone if the AR increases from about 1.0 to greater than 1.5 over the radial distance range of interest.

There is little justification to expect AR to increase as the Solar Wind travels away from the Sun. From values as high as 14 reported close to the Sun (Armstrong et al., 1990) the AR drops to a value of unity at about 0.3 AU and continues to be at unity for larger heliocentric distances (Bourgois et al., 1985; Yamauchi et al., 1998). Even if the assumption of AR being close to unity is in error for the innermost bin, it could only be larger than unity. In such a situation, the velocities of the Solar Wind estimated by the best fit IPS model assuming AR to be 1.0 would be less than the true value. If AR undergoes any radial evolution, it is expected only to decrease with radial distance and settle down to a value of unity. Under such circumstances, the IPS model velocity estimates would be underestimates closer to the Sun and the would approach the true value as AR approaches unity, thus showing an acceleration of Solar Wind with radial distance, which is contrary to the observed trend.

Biases due to spectral index

As the value of the spectral index, α, increase, the high frequency part of the power spectrum becomes steeper. If the IPS model used to obtain the best fit uses a larger value of α than appropriate, the velocity would tend to be overestimated and vice versa. As has been mentioned in Section 6.2 we have fixed the value of α to 3.0. If the velocity evolution seen is to be explained it terms of incorrect choice of α for the Solar Wind model, unaided by any other effects, α must increase with radial distance from the Sun to explain the decrease in velocity. Observations show that close to the Sun ($10 - 80\ R_\odot$) α shows a slight increase from ~ 2.75 to ~ 3.0 between

10 and 20 $R_\odot$ and then remains close to ~ 3.0 out till 80 R_{Sun} (Yamauchi et al., 1998).

Some evidence for α and the velocity of the Solar Wind to be correlated has been presented by Manoharan et al. (Manoharan et al., 1994) and has been discussed in Section 2.6. One of their conclusions is that close to a solar minimum, α increase both with velocity and $\theta_\odot$. The velocity range of interest for the present discussion is 300 – 500 $km\ sec^{-1}$. In this velocity range, α is reported to change from ~ 2.75 to ~ 3.2. Little change in the value of α is reported in the $\theta_\odot$ range of interest to the present discussion. An attempt to explain the observed decrease in velocity as a bias introduced because of a decrease in α with decrease in velocity, on the basis on $\alpha \propto v$ arguments, leads to an inconsistency in the argument. If the trend seen in velocity is solely due to an inappropriate use of a constant value of α, this trend should disappear on allowing α to vary appropriately. But the disappearance of the trend in velocity violates the $\alpha \propto v$ relationship, which was the basis for introducing the variation in α to explain the variation in velocity. To the best of our knowledge, no systematic trend for variation of α with radial distance in the range 0.3 – 1.0 AU has been reported in the literature. There is, hence, no reason to expect any biases because of improper choice of α causing the trend for average deceleration of the Solar Wind seen in our analysis.

Biases due to inner scale

An error in the choice of the value of inner scale, q_i, manifests itself as an error in the angular size of scintillating component of the source. We have assumed q_i effects to be unimportant for our analysis, as discussed in Section 6.2. The fact that q_i has no bearing on velocity estimates ensures that an error in the choice of its value or any evolution of its value cannot give rise to trends in velocity along the radial direction from the Sun.

Effects due to random velocity of Solar Wind

The IPS model used does not incorporate the effects of random velocity of the Solar Wind. The presence of random velocity is likely to lead to an over/under estimation of the bulk velocity of the Solar Wind. There is no evidence for the random velocity component to be significant in the range of heliocentric distance of interest. The random velocities are known to be small enough to be unimportant by $\sim 20\ R_\odot$ (Scott et al., 1983; Armstrong and Woo, 1981; Ekers and Little, 1971). No trends in the velocity of the Solar Wind are hence expected to arise because of the effects of the random velocities of the Solar Wind.

6.5.3 Inadequacies of the IPS Solar Wind model

This analysis relies crucially on the velocity of the Solar Wind estimated using the single station IPS Solar Wind model described in Chapter 5 and Section 6.2. In these models, Solar Wind is represented by a structure-less flow of plasma with purely radial velocity. The *real* Solar Wind is known to have structure, though its structure is not expected to be elaborate (Section 1.4). In view of the fact that the part of the *l.o.s.* close to the P-point dominates the contribution to the power spectrum observed along a *l.o.s.* (Section 3.2.1) and in the absence of any other information about the properties of the Solar Wind along the *l.o.s.*, the structure-less model is the most prudent choice available. The featureless Solar Wind model is expected to provide reasonable estimates of the average properties of the Solar Wind along the *l.o.s.*, especially close to the P-point. Though this model is too simplistic to offer a good description of the true Solar Wind, its use is not expected to produce any systematic effects along the radial direction. The analysis procedure used tends to smooth and obliterate any velocity structure of the Solar Wind, because of averaging effects. If some trends emerge even in presence of these smoothing effects, they are expected to be more pronounced in reality.

In oder to develop a more realistic model for the Solar Wind, information of the 3D distribution of the properties of Solar Wind is required. This is precisely the aim of the exercise of tomography towards which the present analysis is the first step. The present analysis has some advantages over tomography though, it depends much less crucially on the various assumptions necessary for tomography (Section 3.7) and the number of free parameters it involves is much smaller.

6.5.4 Biases due to Signal to Noise problems

The Signal to Noise ratio, S/N, of the measured power spectrum, the basic observable of IPS, decreases with radial distance from the Sun. If there is a systematic tendency to underestimate the IPS velocity when using power spectra with low S/N, it too can give rise to trends which shall mimic deceleration of the Solar Wind. The following simulation was done to check for the presence of such tendency. Power spectra were generated using a featureless Solar Wind model with a constant velocity along the same *l.o.s.*s as for which observations were available. A random gaussian noise, to reflect the measurement uncertainty on the power spectra, was added to make the S/N of the model spectra comparable to the observed spectra. The best fit IPS velocities for the model power spectra showed no trend for a decrease with increasing radial distance from the Sun. This rules out any systematic effects due to S/N problems.

6.6 Comparison with data from WIND

WIND is a near Earth spacecraft, launched by National Aeronautics and Space Administration (NASA) of the USA, on the 1^{st} of November 1994. The primary scientific objectives of WIND are the study of the basic plasma processes in the near Earth Solar Wind, provide baseline ecliptic plane observations to be used in conjunction with ULYSSES spacecraft (Section 6.7) and also provide complete plasma, energetic particle, and magnetic field input for magnetospheric and ionospheric studies. The scientific payloads onboard WIND, of interest to this work, include the Solar Wind Experiment (SWE) which can measure velocity, density and temperature of the Solar Wind plasma and the Magnetic Field Investigation (MFI) which provides high time resolution accurate magnetic field measurements in near-real time on a continuous basis. Apart from the payloads mentioned above, WIND has a variety of scientific instrumentation on board which performs measurements ranging from determining elemental and isotopic abundances in the Solar Wind plasma, measuring radio waves from 20 kHz to 14 MHz, measuring low frequency electric waves and magnetic field from DC to 10 kHz and provide high resolution spectroscopic survey of cosmic gamma-ray bursts and high-resolution spectroscopy of solar flares.

The average velocity of the Solar Wind measured by WIND during the period of our observations were compared with the velocities obtained close to 1 AU from our analysis. WIND measured an average velocity, $\overline{v_W}$, of 377.1 $km\ sec^{-1}$ in the period of interest. It being an Earth orbiting satellite, always samples the Solar Wind in the ecliptic. The average IPS velocity at $\theta_\odot = 0°$ at 1 AU, $\overline{v_{IPS}}(1AU, \theta_\odot = 0°)$, is $308.0 km\ sec^{-1}$ (Figure 6.1). The velocity estimated by IPS is $\sim$ 82% of $\overline{v_W}$. This difference of $\sim 70 km\ sec^{-1}$ in the two velocity estimates is large enough for the two to be considered discrepant. The following issues would contribute to this discrepancy.

6.6.1 Differences in sampling of the Solar Wind

The trajectory of the footpoint of WIND on the solar surface is shown in Figure 6.10. At any given time, WIND samples Solar Wind arising from a small patch on the solar surface. As the IPS dataset spans $\sim$ 5 solar rotations, WIND's footpoint traversed the entire longitude range 5 times, in this period. $\overline{v_W}$ is therefore an average over 5 tracks on the solar surface. IPS on the other hand is sensitive to a considerable fraction of the inner heliosphere at any given epoch, as shown in Figures 3.4 and 3.5. The average velocity profiles estimated using IPS are an average over the entire observing period and are, therefore, a more robust representative of the velocity of Solar Wind arising from the entire equatorial belt of the Sun (Figure 6.8). Thus the Solar Wind sampled by WIND is a small fraction of that sampled by IPS. $\overline{v_W}$

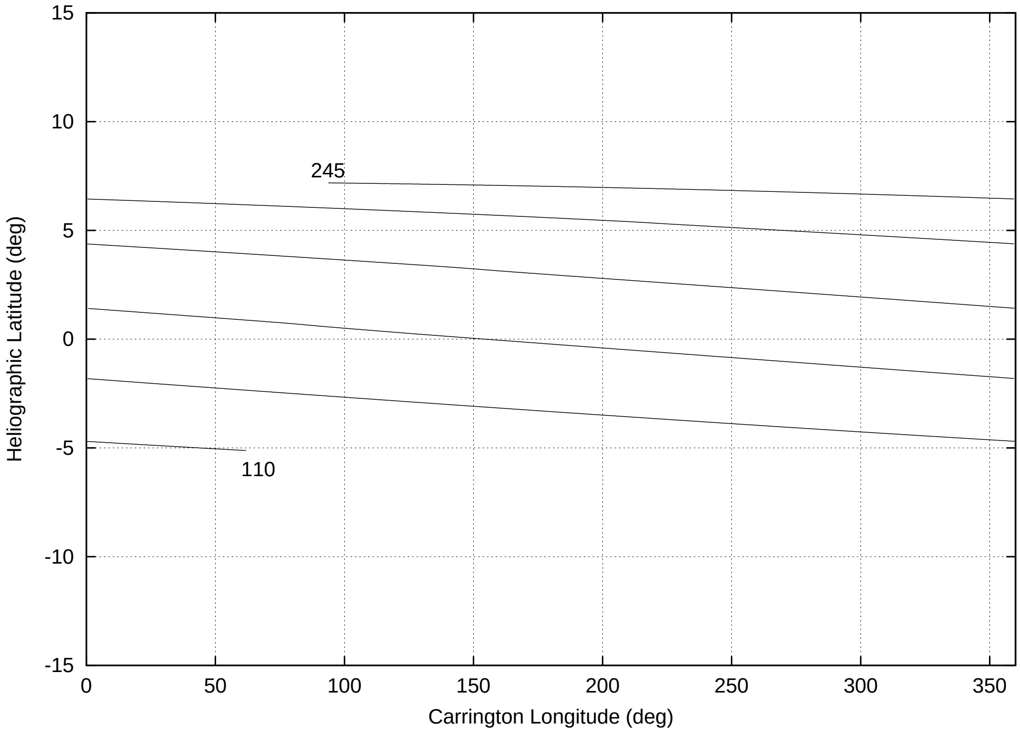

Figure 6.10: **Heliographic coordinates of WIND** – This figure presents the Carrington longitude and the heliographic latitude of WIND for Day No 110.0 to Day no 245 of 1997.

is much more prone to biases because of temporal evolution of and structure in the Solar Wind, while they get averaged out in $\overline{v_{IPS}}(1AU, \theta_{\odot} = 0°)$.

6.6.2 Heliographic latitude excursions of WIND

While the above comparison has assumed WIND to be at $\theta_{\odot}$ of 0° all through the period of interest, it actually traversed a range of $\theta_{\odot}$ from $\sim -6°S$ to $\sim 7°N$ during this period. The heliographic coordinates of the trajectory of WIND, for the period of interest, are presented in Figure 6.10 The considerable gradient in the velocity profile in this $\theta_{\odot}$ range would lead to an incorrect estimate of $\overline{v_{IPS}}(1AU, \theta_{\odot} = 0°)$. It would be more meaningful to compare $\overline{v_W}$ with velocity estimate from IPS observations averaged over the $\theta_{\odot}$ range traversed by WIND. This leads to a $\overline{v_{IPS}}(1\ AU)$ of 320.7 $km\ sec^{-1}$, reducing the discrepancy slightly to $\sim$ 15%.

6.6.3 Normalisation

IPS velocity estimates are very different in nature from the *in-situ* spacecraft measurements of the velocity of the Solar Wind. IPS measurables are a weighted average of the properties of the distribution of the Solar Wind properties along the *l.o.s.*. The weighting factor is proportional to C_n^2 which itself is proportional to $(\delta n_e)^4$. Spacecraft measurements, on the other hand, are local measurements and weight all samples equally. This basic difference in the two measurements suggests that rather than comparing the two velocities, it may be more meaningful to construct a similar weighted average from the WIND data and compare it with IPS velocities. We used the following expression to construct a weighted average of velocity measurements from WIND :

$$\tilde{v}_W = \frac{\int dt\ v_W(t)\ \ (\delta n_e(t))^4}{\int dt\ \ (\delta n_e(t))^4} \tag{6.3}$$

In the actual implementation, integration was replaced by summation because of the discreet nature of the data. We used the *rms* available on the hourly average n_e measurements from WIND as proportional to $\delta n_e(t)$ to compute $\tilde{v}_W$ and evaluated it to be 358.6 $km\ sec^{-1}$. Though $\tilde{v}_W$ moves closer to $\overline{v_{IPS}}$ (320.7 $km\ sec^{-1}$), it is still larger by $\sim$ 38 $km\ sec^{-1}$ (10.6%).

It should be pointed out that there were, on an average, 42 n_e measurements available every hour and the *rms* on them was used as δn_e. Assuming the measurements to be equally spaced, this sampling corresponds to a measurement every 87.7 *sec*. Given the average velocity of the Solar Wind measured by WIND, this duration corresponds to a length scale of $\Delta t \times \overline{v_W} = 3.3 \times 10^4$ km and *rms* from such a series probes fluctuations on length scale of 6.6×10^4 km and larger. IPS, on the other hand, is sensitive to n_e fluctuations on length scales of the Fresnel size (Section 2.3) and smaller, which for our frequency of observations is $\sim 300\ km$ (using $z = 0.6\ AU$). Hence the available measurements of fluctuations in n_e are at length scales significantly larger than the ones probed by IPS. If the spectrum of intensity fluctuations does not follow a power law with a constant coefficient, the rms on n_e estimated on different length scales will differ. A curvature in the spectrum of intensity fluctuations over the length scales of interest is likely to lead to discrepancies between the two velocity estimates.

In addition, IPS measurements are indirect, they are a model dependent estimate of the velocity of the Solar Wind, while spacecraft measurements of velocity are direct measurements, independent of any model and assumptions. It should, therefore, not be surprising to find significant differences between simple minded comparisons of the two velocity estimates. The reasons mentioned above may lead to a systematic difference between the velocities measured by IPS and WIND. In order to reconcile these differences, we have chosen to renormalise the IPS velocities at 1 AU using the WIND data.

6.7 Comparison of WIND and ULYSSES data

ULYSSES is the first spacecraft with the primary objective of characterising the heliosphere as a function of solar latitudes and it is joint endeavour of European Space Agency (ESA) and NASA. The spacecraft was launched on the 6^{th} of October 1990 and is still operational. ULYSSES remained in the ecliptic place till February 1992 when it was pushed out of it by the strong gravitational pull of Jupiter. Since then, ULYSSES has been in a polar orbit of the Sun. It reached it highest southern latitude of $80.2°$ in September 1994, crossed the ecliptic in February 1995 and reached the highest northern latitudes in September 1995. On its circumpolar orbit, ULYSSES crossed the ecliptic plane once again in May 1998. ULYSSES is the first spacecraft to provide direct measurements of polar Solar Wind. The ULYSSES payloads, of interest to the present work, are the Solar Wind Plasma Experiment which characterises the bulk flow and internal state conditions of the interplanetary plasma in three dimensions and the Magnetic Field Investigation which aims at determining the large scale features and gradients of the magnetic field. Apart from these, there are payloads onboard which deal with investigations of Solar Wind ion composition, radio studies of the Sun and Jupiter, Cosmic Rays, Gamma Ray Bursters and Gravitational Waves.

In order to look for evolution in velocity of the Solar Wind beyond 1 AU, a comparison of the average Solar Wind velocities measured by ULYSSES and WIND was done. The epoch for comparing the data from the two satellites was carefully chosen using the criterion that both the satellites should sample the Solar Wind originating at the same epoch from the same physical locations on the Sun. The Solar Wind arising from the equatorial belt on the Sun is expected to continue to propagate in the same plane, without being contaminated with Solar Wind arising from higher or lower latitudes. The epoch when ULYSSES was crossing the heliographic equator was therefore chosen for comparison with WIND data. As WIND is an Earth orbiting satellite, its trajectory remains confined to the ecliptic and is, therefore, never far from the heliographic equator.

The ULYSSES was at a latitude of $+2^\circ.0$ on 02-11-1997 (Day of year 1997 306.5) and crossed $-2^\circ.0$ on 24-01-1998 (Day of year 1997 389.5). This period corresponds to $\sim$ 3 Carrington rotation periods, and was considered long enough to obtain meaningful averages. The mean Sun-ULYSSES distance during this period was $5.36 AU$. During this period ULYSSES sampled Solar Wind originating from the equatorial region lying between $+2^\circ N$ and $-2^\circ S$ and the footpoint of its trajectory traversed the entire longitude range of 0° to 360° thrice. The mean velocity of the Solar Wind as measured by ULYSSES, $\overline{v_U}$, during this period was 355.2 $km\ sec^{-1}$.

It was assumed that Solar Wind moved with a constant velocity beyond 1 AU to the location of ULYSSES, for lack of any better information being available. Travelling at a constant velocity of $\overline{v_U}$, it would take Solar Wind 21.0 *days* to traverse a distance of 4.37 AU, the average radial distance between WIND and ULYSSES locations. The Solar Wind sampled by ULYSSES would have therefore crossed the orbit of WIND 21.0 *days* earlier. The corresponding epoch for WIND data is therefore a period 21.0 *days* earlier than that for ULYSSES, i.e. from 05-10-1997 (Day of year 1997 285.5) to 26-12-1997 (Day of year 1997 368.5). The relative locations of ULYSSES and WIND for the epochs of interest, projected on the plane of the heliographic equator, are shown in Figure 6.11. Heliographic Inertial Coordinate system, which does not rotate along with the Sun, is used to describe the relative positions of the satellites. Figure 6.12 shows the trajectories of the footpoints of the two satellites on the solar surface. WIND traverses a latitude range of $\sim 9^\circ.3$, from $6^\circ.0N$ to $-3^\circ.3S$, in this period as compared to that of 4° traversed by ULYSSES. It is also evident that the mean Heliographic Inertial longitudes of the two satellites differ by $\sim 93^\circ.7$. Though the time window in which to compare data between ULYSSES and WIND have been corrected for the propagation time delay, the effect of difference in Heliographic Inertial longitudes has not been corrected. As the data from both the satellites is being averaged for $\sim$ 3 solar rotations, the error incurred because of the difference in mean Heliographic Inertial longitudes is small. The mean velocity of the Solar Wind observed by ULYSSES in the epoch of interest, $\overline{v_U}$, is 355.2 $km\ sec^{-1}$, as compared to 358.6 $km\ sec^{-1}$ from WIND.

In order to meaningfully comparing $\overline{v_U}$ and $\overline{v_W}$, some estimate of error on the two must be obtained. The *rms* of the average velocity over the duration of a solar rotation, is a good estimate of the uncertainty of $\overline{v_W}$. Average Solar Wind velocities

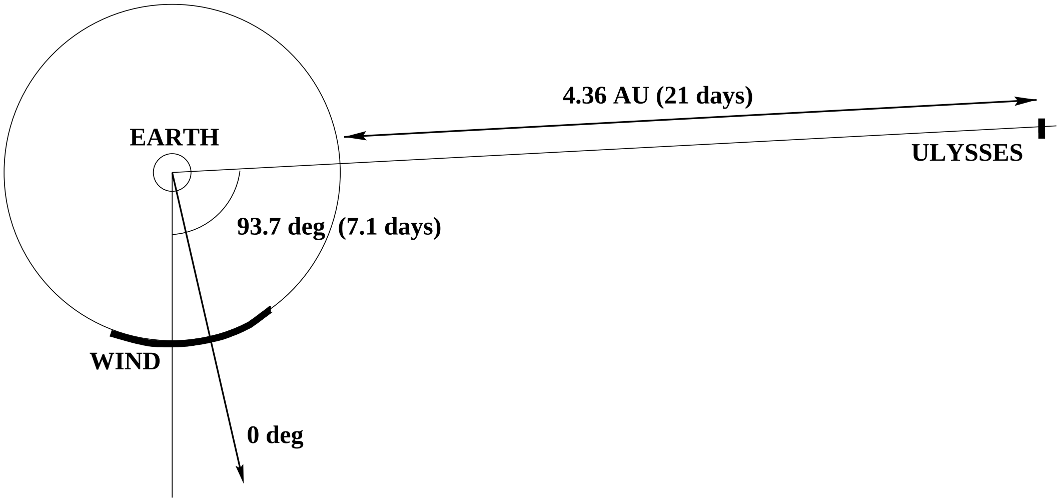

Figure 6.11: **The relative locations of ULYSSES and WIND** – The figure presents a view projected on the plane of the heliographic equator. The positions of the two satellites, during the epoch of interest, are schematically shown in Heliographic Inertial Coordinate system. The dark bands represent the distance travelled by the satellites in the duration of the period being considered. The trajectory of ULYSSES was almost perpendicular to the heliographic equator during this period as it was crossing over from the Northern hemisphere to the Southern hemisphere (Figure 6.12). The mean radial distance between ULYSSES and WIND is $4.37AU$ and the corresponding travel time, assuming constant velocity flow from $1AU$ out to ULYSSES is $21.0 days$. The mean angular separation between the two satellites is $93^\circ.7$ and it takes the Sun $7.1 days$ to rotate by this angle.

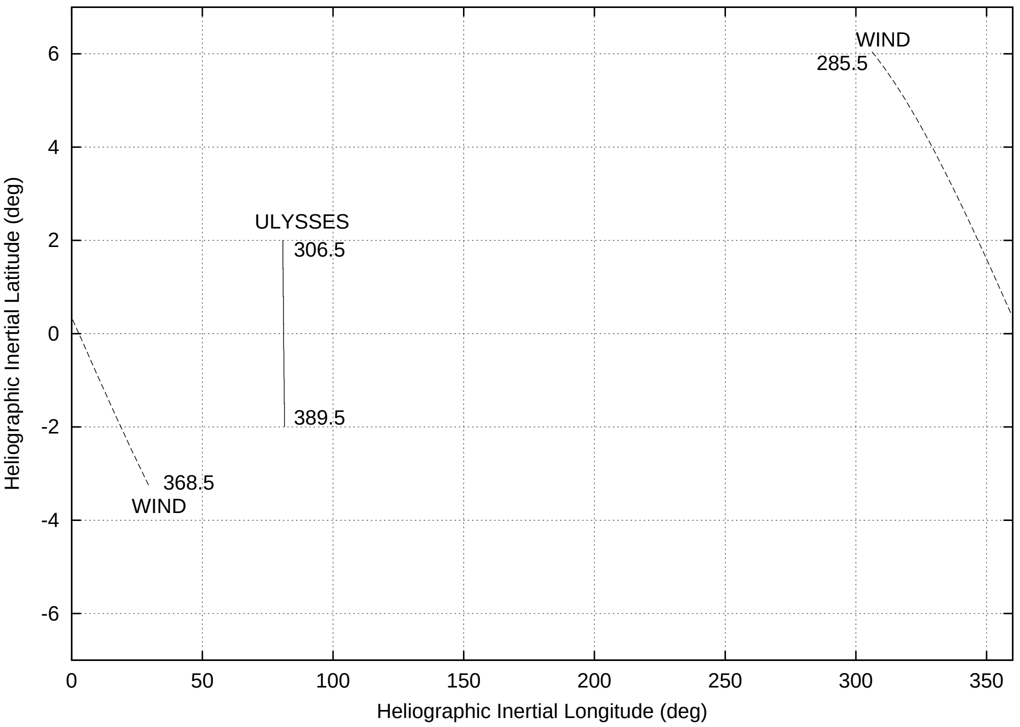

Figure 6.12: **The trajectory of ULYSSES and WIND spacecrafts** – The trajectories of ULYSSES around the epoch of its crossing the heliographic equator is shown by the solid line. The dotted line represents the trajectory of WIND. The numbers mentioned alongside the trajectories specify the epoch in units of Day of the Year with 1 Jan 1997 being day number 1.

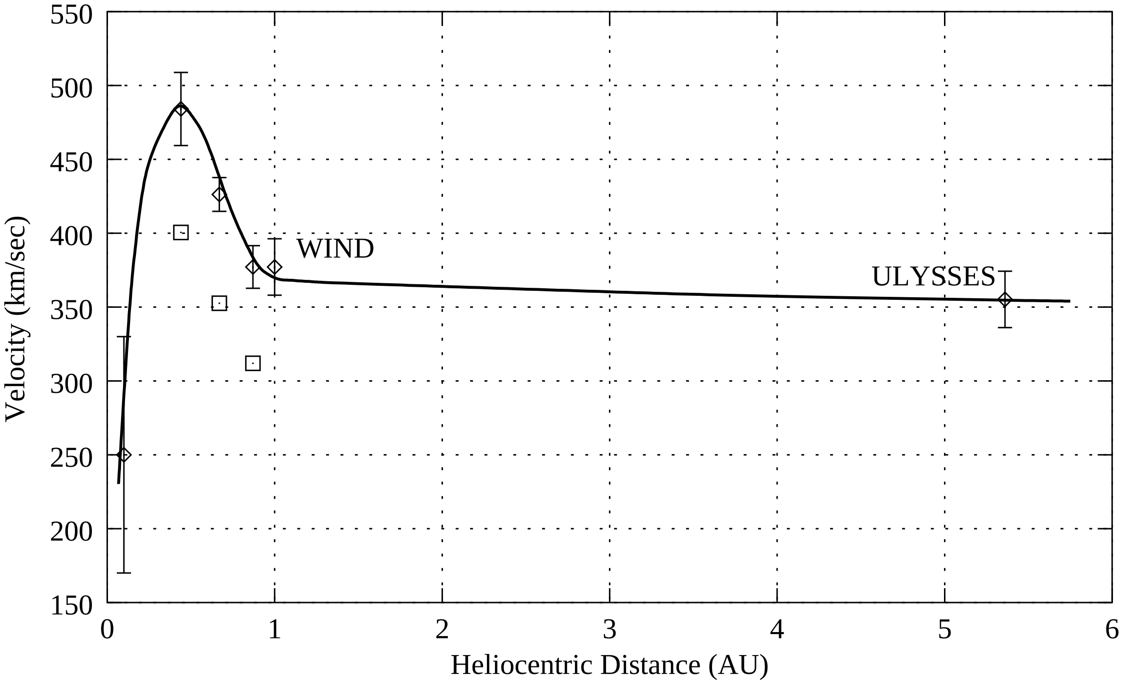

Figure 6.13: **Variation in Solar Wind velocity with heliocentric distance** – The data point at the 0.1 *AU* comes from IPS measurements at 2 and 8 *GHz*. The data points between 0.3 and 1.0 *AU* come from the present analysis and the velocity measurements from WIND and ULYSSES are marked. The points with errorbars mark the IPS velocities, normalised to velocity measured by WIND at 1 *AU*. The un-normalised values of velocity are shown with boxes. The solid line, schematically, shows the variation of the velocity of Solar Wind with heliocentric distance.

over durations of a Carrington period were computed for WIND data for a period of about a year around the epoch of interest (Carrington rotations 1923 to 1934). The *rms* of the series of average velocities so obtained, $\sigma_{\overline{v_W}}$, was used as an estimate of uncertainty in $\overline{v_W}$ and was estimated to be 19.1 $km\ sec^{-1}$. A similar estimate for ULYSSES is not possible to obtain because its orbit, unlike that of WIND, is not confined to the ecliptic plane and moves into higher latitude regions. In absence of any other estimate of $\sigma_{\overline{v_U}}$, we assume it to be similar to $\sigma_{\overline{v_W}}$.

The Solar Wind velocities, as obtained from IPS at high frequencies, our analysis and from WIND and ULYSSES observations are shown in Figure 6.13, as a function of heliocentric distance. The data point at the 0.1 *AU* represents an average value over a radial distance range of 0.07 to 0.14 *AU* and comes from IPS measurements at 2 and 8 *GHz* (Yamauchi et al., 1998). The error bar on the data point is indicative of the large spread in the measurements. The data points between 0.3 and 1.0 *AU* come from the present analysis. The measurements from WIND are plotted at 1.0 *AU* and those from ULYSSES close to 5 *AU*. IPS velocities from our analysis have been normalised to velocity measured by WIND at 1 AU and shown with points with errorbars. The un-normalised values of velocities have been shown with boxes. The solid line, schematically, shows the variation of the velocity with heliocentric distance.

6.8 Conclusions

The analysis presented earlier in this chapter clearly shows a trend for the average Solar Wind velocity to decrease with heliocentric distance. We have carefully examined the various possibilities to see if this trend is an artifact of our measurements and analysis and we find that trend is genuine. The trend can be explained by either of the following two interpretations

1. The simplest explanation is that the ambient Solar Wind decelerates as it propagates outwards. This is contrary to the expectations from most Solar Wind models, including the Parker's model, which predict a rapid acceleration of the Solar Wind close to the Sun and a slow increase in velocity as it propagates out further. Schwenn et. al (Schwenn et al., 1981) have have found a trend for increase in the velocity with radial distance (52 ± 11 $km\ sec^{-1}$ AU^{-1} in the range 0.3 – 1.0 AU) in their single epoch satellite observations. Earlier IPS studies have either found no significant trend for velocity to vary with heliocentric distance, R, (Coles, 1978) or have found a marginal decrease in velocity with R (Kojima et al., 1998), a trend similar to the one seen in our observations. The study by Coles was limited by the fact that the rms on the mean of daily velocity measurements were of the order of 100 $km\ sec^{-1}$. It should be noted that the earlier IPS observations did not have as extensive data as ours and except in the case of Kojima et. al had restricted themselves to only a P point analysis. Kojima et. al compared the average latitudinal velocity profiles in two elongation bins $6^\circ \leq \epsilon \leq 17^\circ$ ($0.1 \leq R_\odot \leq 0.3$) and $\epsilon > 17^\circ$ ($R_\odot > 0.3$) and found Solar Wind velocity to be lower at larger heliocentric distances. They concluded that the significance of the trend was "marginal", as the errors in the average speeds were quite large. In addition, at the smaller elongation bin the parts of the $l.o.s.$s with the largest IPS $l.o.s.$ weight pass through the regions of strong scattering, where the velocity estimates made assuming weak scattering approximation could be overestimated.

2. If the intrinsic velocity of the Solar Wind is not decreasing between 0.3 and 1.0 AU, there has to be some other explanation for the decrease in the IPS velocity which we observe. We have examined the possibility of analysis and observational biases and are convinced that our observations are not an artifact of such biases. A possibility which needs to be considered is that IPS is more

sensitive to structures in the Solar Wind that decelerate and hence give results which are inconsistent with spacecraft measurements. This is not unreasonable since the IPS velocity measurements are weighted by δn_e^2 while the satellite velocity measurements do not have any such weighting function associated with them. If the decelerating structures are associated with enhanced turbulence and hence higher C_n^2, the mean velocities estimated by IPS would also show a decelerating trend. The two most likely such structures known to be present in the Solar Wind are :

(a) **Co-rotating interaction regions** – Co-rotating interaction regions (CIRs) are formed due to the interaction of the faster plasma, most often from coronal holes, trying to overtake slower plasma ahead of it (Section 1.6). As the faster plasma tries to push the slower plasma, it transfers momentum and energy to the slower plasma and itself decelerates. This leads to development of regions of compression and rarefaction and the longitude profile of velocity evolves towards a rapid rise and slow decay shape. The leading edge of the CIRs is expected to have enhanced turbulence levels. A profusion of these structures would cause the IPS velocities to show a decelerating trend. While CIRs are expected to be present in the equatorial regions close to the solar minima, the WIND observations during this period, shown in Figure 6.14 do not show strong evidence for presence of co-rotating structures.

(b) **Interplanetary Disturbances** – Interplanetary Disturbances (IPDs) are the interplanetary counterparts of the Coronal Mass Ejections (CMEs). The CME rate is known to vary from $\sim 2\ day^{-1}$ close to the maxima of the solar activity cycle to about $\sim 0.75\ day^{-1}$ near the solar minima (Howard et al., 1985; St. Cyr et al., 2000) The latitudinal distribution of central latitude of CMEs also changes with the solar activity cycle, they occur over a much wider range of latitudes at times of high solar activity than at times of low activity. The latitudinal distribution always peaks at the heliographic equator and is roughly symmetric about it (Hundhausen, 1993; St. Cyr et al., 2000). The IPDs are known to be associated with regions of high turbulence and hence high C_n^2 (Gothoskar and Rao, 1999).

The IPDs due to CMEs have all the desirable properties to claim that it is the deceleration of these IPDs which is producing the trend for deceleration seen in the IPS velocity estimates. They have high C_n^2 associated with them, so the IPS velocities would be heavily weighted towards their velocities. St. Cyr et. al (St. Cyr et al., 2000) have studied the statistical properties of CMEs observed by SOHO-LASCO in the period January 1996 to June 1998, which includes the epoch of observations for

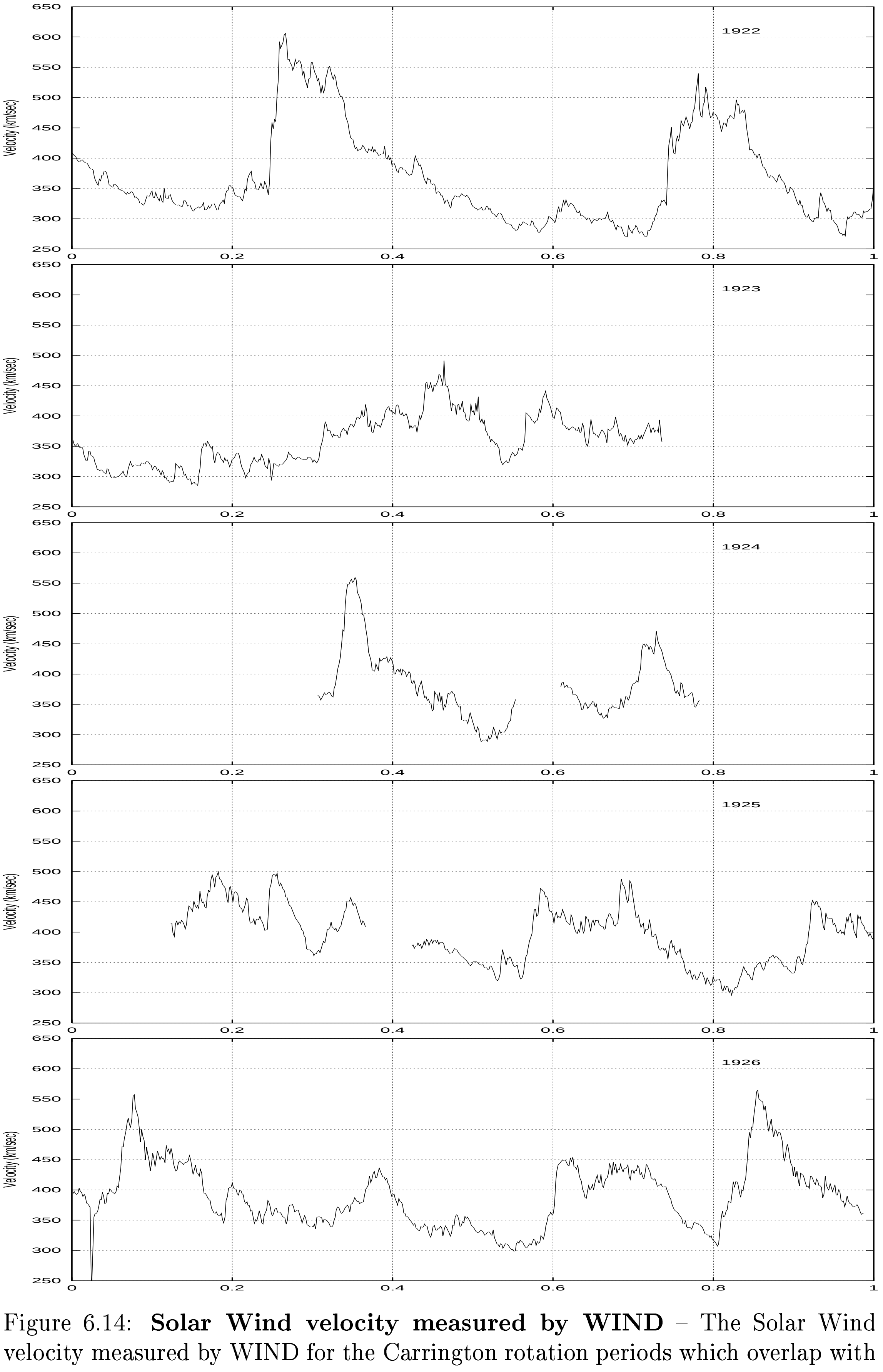

Figure 6.14: **Solar Wind velocity measured by WIND** – The Solar Wind velocity measured by WIND for the Carrington rotation periods which overlap with the present observations are shown. The X axis is phase of the Carrington rotation and varies between 0 and 1. The Y axis is velocity of the Solar Wind in $km\ sec^{-1}$. The panels show the observations for the Carrington rotations 1992 to 1926, from top to bottom.

the present work. They report the CME rate to be about 0.8 day^{-1} during our period of observations, so there was a significant number of them present. Their latitudinal distribution peaked around the heliographic equator ensures that our data-set would have sampled a large fraction of them. The reported mean and median speeds lie in the 400–500 $km\ sec^{-1}$ speed bin in the 2–32 $R_{\odot}$ region where they are observed to be accelerating still. On the other hand, the minima of the latitudinal velocity profile closest to the Sun (0.34 AU or 80 $R_{\odot}$) is $\sim$ 375 $km\ sec^{-1}$. Therefore, the CMEs and IPDs must decelerate as they propagate outwards because of interaction with the slower ambient Solar Wind.

Chapter 7

Tomographic Reconstruction Methodology

7.1 Introduction

In the presence of structure in the Solar Wind the simple featureless models are inadequate to describe the real Solar Wind, as has been discussed in Chapter 3. Tomography of the Solar Wind in the inner heliosphere, using the remote sensing technique of IPS, provides a means to reconstruct the 3D structure of the Solar Wind, under certain assumptions. There is no other technique available which can provide such detailed information about the inner heliosphere at large scales. An essential requirement for a well constrained tomographic reconstruction is that the entire physical extent of the medium be adequately sampled with numerous different perspectives (Section 3.5). In the case of IPS, the rotation of the Sun can be exploited to provide different perspectives of the same region in the inner heliosphere by observing a large number of sources for durations longer the solar rotation period. Observation of sources over a large range of elongations provides different samplings of the same physical Solar Wind as it flows radially outwards. The limitation of being confined to a single vantage point, the Earth, can be partially compensated for by using a model for the structure of the Solar Wind and by making some simplifying assumptions. The model reflects the present understanding of the Solar Wind which has been achieved over the years. The most demanding assumption required for the tomographic reconstruction is that time evolution of the Solar Wind be negligible during the period of observations used for tomographic reconstruction, typically about 27 days or more, as any change in the Solar Wind renders the data-set inconsistent.

The data-set described in Chapter 4 was used for the tomographic reconstruction exercise. Our observations were conducted at an epoch close to solar minimum, where the assumption of little time evolution has the largest probability of being satisfied. This chapter discusses our implementation of the tomographic reconstruction process and the results obtained from the simulations and the analysis of data obtained.

7.2 Methodology

7.2.1 Formulation of the problem

The problem of tomographic inversion of the observed IPS data to obtain 3D structure of the Solar Wind is not solvable in a mathematical sense. A formal tomographic inversion requires an appropriate Nyquist sampling of the medium from a large number of perspectives from different vantage points on time scales much smaller than those of variation of the Solar Wind. Though, the entire heliosphere is not simultaneously accessible to IPS, the rotation of the Sun is made use of to sample the entire inner heliosphere and therefore it takes at least as long a solar rotation period to cover the entire inner heliosphere. While IPS can provide numerous perspectives of the inner heliosphere, the vantage point is always constrained to be the Earth. It is hence necessary to pose the problem in a manner more amenable to solution.

We have posed the reconstruction problem as a χ^2 minimisation exercise. Like previous attempts at tomography using IPS data (Jackson et al., 1998; Kojima et al., 1998; Asai et al., 1998), we also considered using the values of uniform Solar Wind model fits to the observed power spectra (velocity and C_n^2) as constraints. Though, in the presence of structure in the Solar Wind, the uniform Solar Wind models are not an appropriate choice to describe the observed power spectra, the previous workers had assumed that the uniform Solar Wind model fits represent some kind of weighted average of the distribution of Solar Wind properties along the *l.o.s.*. While we agree with the observed scintillation index (and hence C_n^2) being a weighted average of the distribution of Solar Wind properties along the *l.o.s.*, we have some reservations about the validity of this assumption for the velocity arrived at using uniform Solar Wind models. If one considers a *l.o.s.* sampling a two stream feature, a single higher velocity stream superposed on a uniform background, the power spectra seen by the single station observations will show two Fresnel knees and the cross-correlation seen by the three station observations will show two peaks. The choice of the uniform Solar Wind model to describe such a situation would depend on the details of the uniform Solar Wind model fitting methodology and the personal biases of the astronomer for the single station case and the scheme used to compute the lag which is used to estimate the velocity of the Solar Wind for the three station case. While this procedure does lead to a single velocity to be associated with the observations, its physical significance is not clear. The fact that the velocity so estimated will a be weighted sum of the Solar Wind velocity along the *l.o.s.*, in the IPS sense, cannot be taken for granted. The process of describing the observations in terms of uniform Solar Wind models tries to represent the entire shape of the power spectrum or cross-correlation by a single number and therefore involves a considerable and irreparable loss of information. This process is based on interpreting the observed data in terms of an inappropriate model and therefore the conclusions arrived at by such an exercise should be taken with a pinch of salt.

In view of the shortcomings of using the uniform Solar Wind model fits to the observed power spectra for velocity, we have chosen to use the observed power spectra themselves as the constraints for the minimisation process. They are the true observables of IPS and have the desired property of being a weighted sum of the distribution of Solar Wind properties along the *l.o.s.*. They, therefore, carry the entire information of the distribution of the Solar Wind properties integrated along the *l.o.s.* as sampled by IPS and do not involve any interpretation of the data. The IPS modelling formalism, discussed in Chapter 2, also relates the physical properties of the Solar Wind plasma to the observed power spectra. It should be pointed out that the choice of using the observed power spectra as the constraints adds considerably to the complexity of the problem. As compared to using two numbers as constraints for each observations, we now have a power spectra. Every iteration of the χ^2 minimisation must now involve computing the power spectra from the present global Solar Wind model and comparing them with the observed power spectra, which is computationally a much more challenging task. One of the aims of this thesis was to study and demonstrate the feasibility of such an exercise.

The distribution of the Solar Wind parameters on a fiducial surface is treated as the χ^2 degrees of freedom of the model. Only velocity and C_n^2 of the Solar Wind are treated as free parameters, all other parameters of IPS Solar Wind model are held constant. The axial ratio, AR, is held fixed at 1.0 and α and s_i at 3.0 and 3.3 km respectively. The justification for holding these parameters fixed and for the choice of these values is provided in Section 2.6.

An attempt is made to arrive at a *best fit* model for the surface distribution of Solar Wind parameters consistent with the observed power spectra (the constraints). The number of constraints being limited, the model of the Solar Wind can have only a limited number of degrees of freedom. Consequently, the fiducial surface cannot be continuous and is represented by discreet elemental areas of finite dimensions, *pixels*. The size of the pixels, and hence the resolution of the reconstruction, depends on the number of measurements, their distribution and the stability of the reconstruction technique. These aspects are discussed later in Section 7.2.3.

The success of this formulation relies on the ability to compute the expected power spectrum of intensity fluctuations, given the distribution of the Solar Wind parameters on a fiducial surface. This is achieved in the following steps :

1. The geometry of the observations is used to compute the heliographic coordinates of the elements of each *l.o.s.* (Section 2.1 and Figure 2.2).
2. The part of the fiducial surface that contributes to the scintillations along a *l.o.s.*, is determined in a two step process.
   (a) First the best fit IPS velocity (obtained by fitting uniform Solar Wind models to the observed power spectrum) is used to locate the footpoints of the *l.o.s.* on the fiducial surface by tracing the Archimedean spiral from the elements of the *l.o.s.*. The set of pixels which correspond to the footpoints of the *l.o.s.* on the fiducial surface is determined.
   (b) Since the velocity at the footpoint pixels can be different from the best fit IPS velocity, a fine tuning of the mapping needs to be carried out. Using these pixels as the starting point, a search is conducted in the longitude space to locate the pixel whose Archimedean spiral intersects the element of the *l.o.s.*.

   The assumption that the Solar Wind flows along Archimedean spirals, which has been used here, amounts to neglecting

   (a) the tangential components of the velocity of the Solar Wind in comparison to the radial component
   (b) any evolution of the radial component of the velocity as the Solar Wind traverses out.
3. The values of velocity and C_n^2 at the pixels which contribute to *l.o.s.* are used to generate the Solar Wind properties for each of the thin screens along the *l.o.s.*. The computation of C_n^2 distribution along the *l.o.s.* assumes that $\delta n_e \propto n_e$. A constant radial outflow of the Solar Wind is also assumed, which leads to a $1/R^2$ decrease in n_e.
4. Once the distribution of Solar Wind properties along the *l.o.s.* is known, the model power spectrum is computed using the formalism presented in Chapter 2.

A quantitative estimate of how closely the model power spectra match the observations is made by computing the χ^2 of the observed and the model power spectra. The criterion for an acceptable definition of χ^2 and the definition used in this work have been presented in Sections 5.2 and 5.3.2 respectively. The χ^2 for the all the power spectra observed in the relevant period of observation are summed over to get a global χ^2, χ^2_G, for the goodness of the Solar Wind model. The χ^2_G so computed forms the quantity which is minimised. The flow-chart for the process of tomographic reconstruction is shown in Figure 7.1.

7.2.2 Generating the initial model

An initial guess for the model is required to serve as a starting point of the χ^2 minimisation process. It is desirable to arrive at a starting point as close as possible to the final model, since this reduces the likelihood of the minimisation procedure finding some other local minima and remaining confined there and also reduces the number of iterations required to converge to the final model.

The initial model, which forms the input for the χ^2 minimisation procedure, made use of the best fit uniform Solar Wind models fitted to the power spectra using the automated procedure described in Section 5.3. They represent the best description of the average Solar Wind in the direction of the *l.o.s.* in absence of any detailed information. The footpoints of the *l.o.s.*s on the fiducial surface were computed assuming that the best fit IPS velocity is the true velocity of the Solar Wind along the entire *l.o.s.*. The pixels through which the footpoints of the elements of the *l.o.s.* on the fiducial surface passed were ascertained. Since the power spectrum observed towards a *l.o.s.* is a weighted sum of the contributions from the Solar Wind along it, the best fit IPS velocity was assigned to the pixels at the footpoints of the *l.o.s.* on the fiducial surface with a weight proportional to the magnitude of contribution from the element (pixel) to the observed power spectrum. This procedure has been described in greater detail in Section 6.3. The footpoints of the elements of each *l.o.s.* describe a curve on the fiducial surface . We have considered the curve to be a band, 5° in width, and attribute the estimated velocity to the entire band. Further, a threshold value for the *l.o.s.* weight of 5% was used to limit the length of the track. All the *l.o.s.*s in the chosen period were projected on the fiducial surface and a weighted average of the contributions to each of the pixels was done to arrive at a velocity distribution on the fiducial surface which was used as the initial model. The initial model for C_n^2 distribution was computed in a similar manner by taking weighted averages of the contributions to each pixel.

7.2.3 Resolution : Constraints vs χ^2 degrees of freedom

As has been mentioned earlier, the values of velocity and C_n^2 on the fiducial surface form the degrees of freedom and the observed power spectra the constraints. The number of degrees of freedom, therefore, is given by :

$$N_{\chi^2_G} = N_{\phi_\odot} \times N_{\theta_\odot} \times 2 \tag{7.1}$$

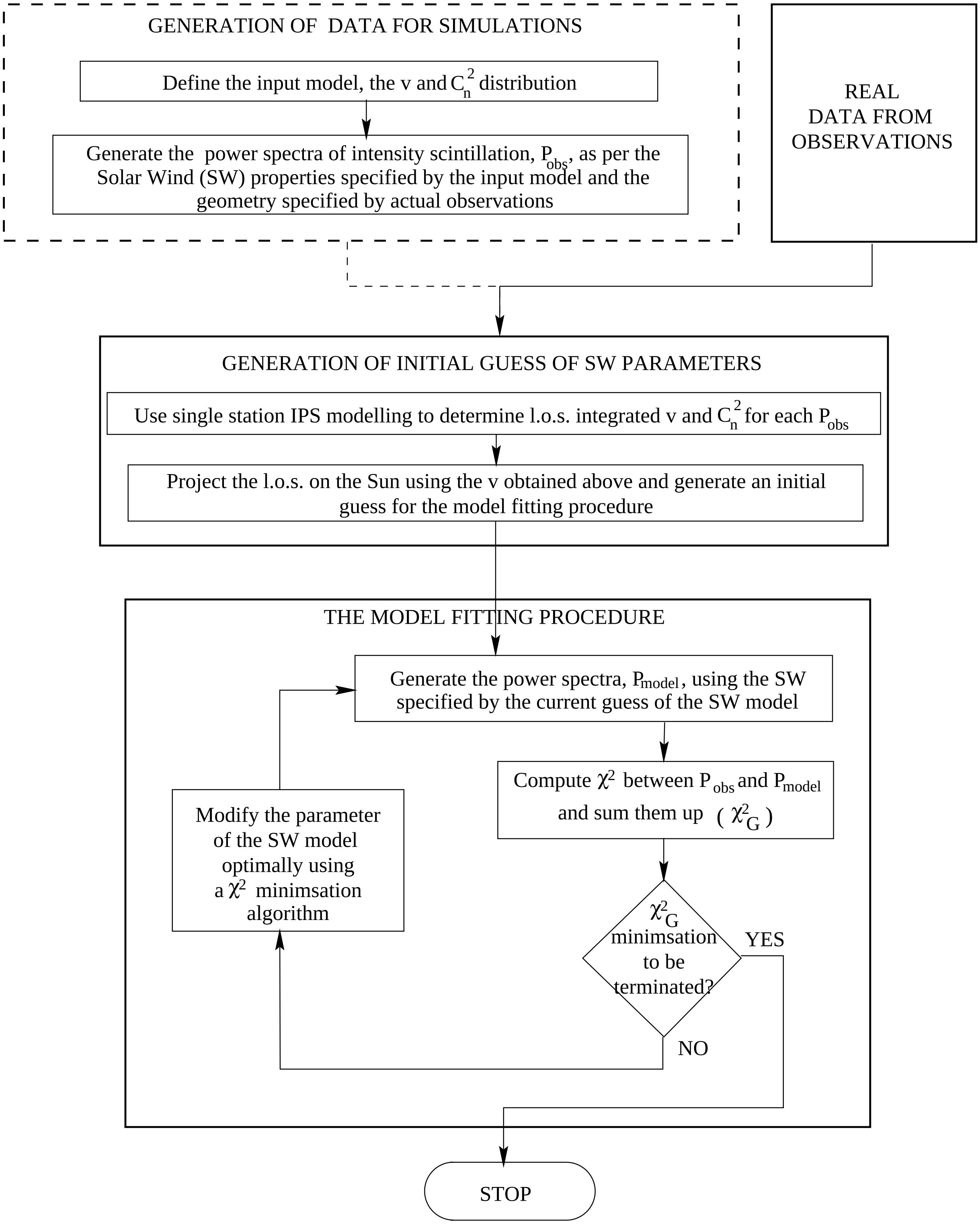

Figure 7.1: **The flow chart for the tomographic reconstruction process** – The figure shows the block diagram flow chart for our implementation of the tomographic reconstruction process. The block shown using dashed lines corresponds to the part which is used to generate the data for simulations. Both the simulated and the observed data follow exactly the same path through the reconstruction process.

where $N_{\phi_\odot}$ and $N_{\theta_\odot}$ are the number of pixels along the heliographic longitude and latitude respectively and $N_{\chi^2_G}$ is the number of χ^2 degrees of freedom for the global Solar Wind model.

The number of constraints, N_{con}, are proportional to the number of observed power spectra and it is necessary that

$$N_{con} \geq N_{\chi^2_G} \tag{7.2}$$

The number of observations (power spectra) available is typically 700 for each solar rotation and this imposes an upper limit on $N_{\chi^2_G}$ and hence the resolution of the reconstruction. The equality in equation 7.2 is the bare minimum requirement for an unconstrained fit where the number of parameters of the model is equal to the constraints available (like fitting a straight line to two data points). In order to achieve a well constrained fit, it is necessary that many constraints be available per χ^2_G degree of freedom, i. e.

$$N_{con} \gg N_{\chi^2_G} \tag{7.3}$$

The task of estimating N_{con} is complicated by the fact that one also needs to know how the constraints are distributed and how independent they are. A very large number of measurements of a few *l.o.s.*s close to each other constrain the distribution of properties on only a small part of the fiducial surface and are unlikely to result in a good global reconstruction. Further, as each of the *l.o.s.*s samples only a fraction of the fiducial surface, it constraints the properties of only those parts of the fiducial surface. This is different from the usual situation of, say, fitting a polynomial to a given set of data point where each data point constraints all the coefficients of the polynomial equally. It should be noted that each of the power spectra constraints both velocity and C_n^2 independently.

We will model $\sim 30°$ wide region of the equatorial belt. In order to achieve equal resolution along heliographic longitude and latitude, the number of pixels along the longitude and latitude axis are related as follows :

$$\frac{360°}{N_{\phi_\odot}} = \frac{30°}{N_{\theta_\odot}} \tag{7.4}$$

As the latitudes of interest are close to the equator, the decrease in the actual physical distance with latitude has been ignored.

We estimate the size of the pixels or equivalently the number of free parameters of the model using the following heuristic argument. Under the P-point assumption, each *l.o.s.* maps back to essentially a single pixel. In this assumption we can compare the number of χ^2 degrees of freedom, χ^2_G, with the number of constraints available and compute the pixel dimensions which allow there to be a reasonable number of constraints per degree of freedom, N_C as follows :

$$2\ N_{con} = N_{\chi^2_G} \times N_C \tag{7.5}$$

The 2 on the LHS in the above equation is present because each power spectrum constraints velocity and C_n^2 independently. Using equation 7.1 we can write :

$$\begin{aligned} N_{con} &= N_{\phi_\odot} \times N_{\theta_\odot} \times N_C \\ N_{con} &= \frac{N_{\phi_\odot}^2}{12} \times N_C \end{aligned} \tag{7.6}$$

We have assumed all observations to be independent and their distribution to be uniform. About 650 – 800 observations are available for the Carrington rotations 1922 – 1924, while Carrington rotation has only 536 observations available. Choosing N_C to be ~ 12, one arrives at a $N_{\phi_\odot}$ of 26 and a $N_{\theta_\odot}$ of 2. This leads to pixel of size of $13^\circ.8 \times 15^\circ$ (longitude × latitude). From the discussion in Section 6.3 it is evident that the Solar Wind has a well defined latitudinal structure which varies considerably in the equatorial region. In order to reduce the averaging due to the latitudinal structure of the Solar Wind, we have chosen to use higher resolution along $\theta_\odot$ at the cost of coarser resolution along $\phi_\odot$, keeping $N_{\chi^2_G}$ constant. We use a $N_{\phi_\odot}$ of 18 and a $N_{\theta_\odot}$ of 3, which leads to a pixel of size of $20^\circ \times 11^\circ$.

7.2.4 The χ^2 minimisation algorithm

There is no unique χ^2 minimisation algorithm which provides a satisfactory solution for all problems. The algorithm needs to be chosen to suit the problem at hand. Most χ^2 minimisation algorithms make some assumptions about the behaviour of the function being minimised and the χ^2 hypersurface in the parameter phase space. The success of an algorithm in a given situation depends on how well met are the assumptions on which it depends. The algorithms which make the least amount of assumptions tend to be more robust but also the slowest. The χ^2 minimisation algorithms which use the gradients of the function being minimised to guide the search tend to be efficient for problems which deal with smooth χ^2 landscapes with a well defined minimum. These methods are most suitable when the function being minimised is expressible in a conveniently differentiable analytic form. The blind search algorithms also work in such cases but have a slower convergence. If an analytic form is not available, one is forced to resort to numeric differentiation which is computationally expensive as it involves many function evaluations. If the number of χ^2 degrees of freedom are large, this becomes prohibitingly expensive as the gradients along each of the degrees of freedom in the multidimensional parameter phase space need to be computed. The alternative is to use unguided χ^2 minimisation algorithms, which do not require computation of the gradients but do require many function evaluations. In the presence of many local minima in the χ^2 landscape, simulated annealing methods are useful. These methods periodically add a controlled amount of noise to the current choice of the model parameters and therefore can push the minimisation process out of the shallow local minimas in which it might get stuck otherwise. We have chosen to use unguided algorithms as the function to be minimised cannot be expressed in a convenient analytic form.

A few different algorithms were tried for χ^2 minimisation. The non linear, unbounded χ^2 minimisation algorithm, the *Downhill simplex method* , due to Nelder and Mead (Nelder and Mead, 1965) was found to be quite suitable for the task. As mentioned in Section 5.3.3, this algorithm makes no special assumptions about the function being minimised and can readily be implemented for a multidimensional case. A set of $(N+1)$ noncoplanar points define a simplex in a N dimensional space. This method requires an initial simplex in the parameter phase space as a starting point and by reflecting, expanding and contracting the vertices of the simplex tries to reach the bottom of the valley in the χ^2 hypersurface. The main disadvantage of using the simplex method is that being an unguided search, it is not efficient in terms of the number of function evaluations required. As the present exercise involves a large number of χ^2 degrees of freedom ($N_{\chi^2_G} > 100$), the number of function evaluations are often exceed 3000 for a run of the χ^2 minimisation process.

7.3 Coverage of the solar surface

In order to minimise the inconsistencies within the data-set, caused by time evolution of the Solar Wind, the data-set was divided into the smallest possible intervals which gave a complete coverage of the solar surface (Carrington rotation period). Only the data within a Carrington rotation was used to constraint the reconstruction. The observations overlaps with Carrington rotation numbers 1921 to 1925. The coverage of the solar surface achieved by the observations for the four best sampled Carrington rotations, 1922 – 1925, is shown in the Figures 7.2 and 7.3. These figures show the geometric footpoints of *l.o.s.*s corresponding to the actual observations. As is evident from these figures, the equatorial belt of the solar surface is sampled very densely by the observations. The data-set satisfies the requirements for a well constrained tomographic reconstruction of having many *l.o.s.*s sample the same region. The coverage of higher and lower latitude regions is much less dense. As the primary aim of this exercise is to reconstruct the structure of the Solar Wind in the equatorial belt of the Sun, only those *l.o.s.*s whose ‘footpoints’ do not stray out of this region were used. The coverage of equatorial belt achieved by the data-set is slightly assymetric. The region best sampled by the observations is the region from $+13°$ to $-20°$, therefore, we chose this region for our attempt at tomographic reconstruction.

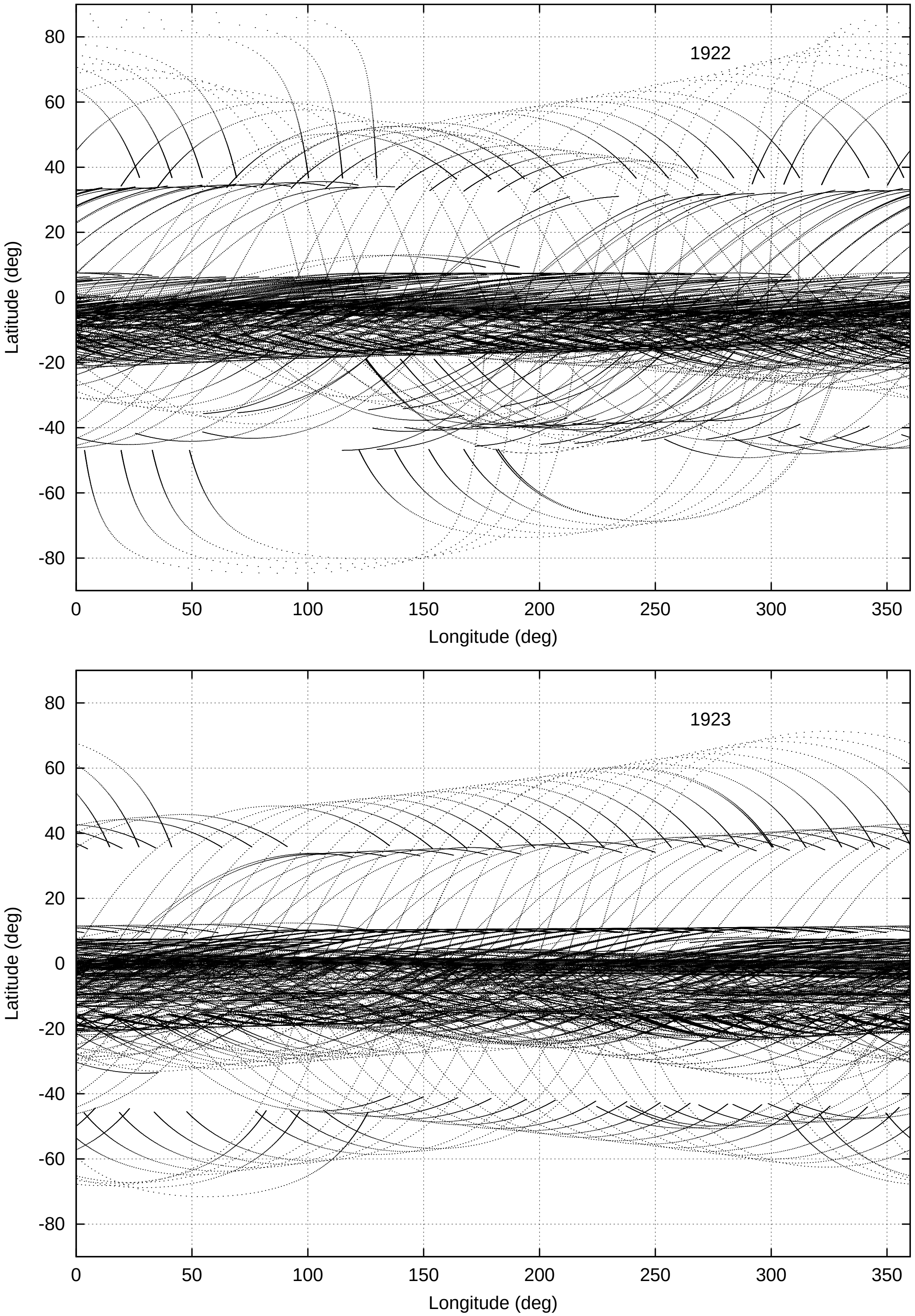

Figure 7.2: **Solar surface Coverage for Carrington rotations** 1922 **and** 1923 – The geometric footpoints of *l.o.s.*s corresponding to actual observations for Carrington rotation numbers 1922 and 1923 are shown. The X axis is Carrington longitude in degrees and the Y axis heliographic latitude. The *l.o.s.*s extending out to 2 AU from the Earth have been shown.

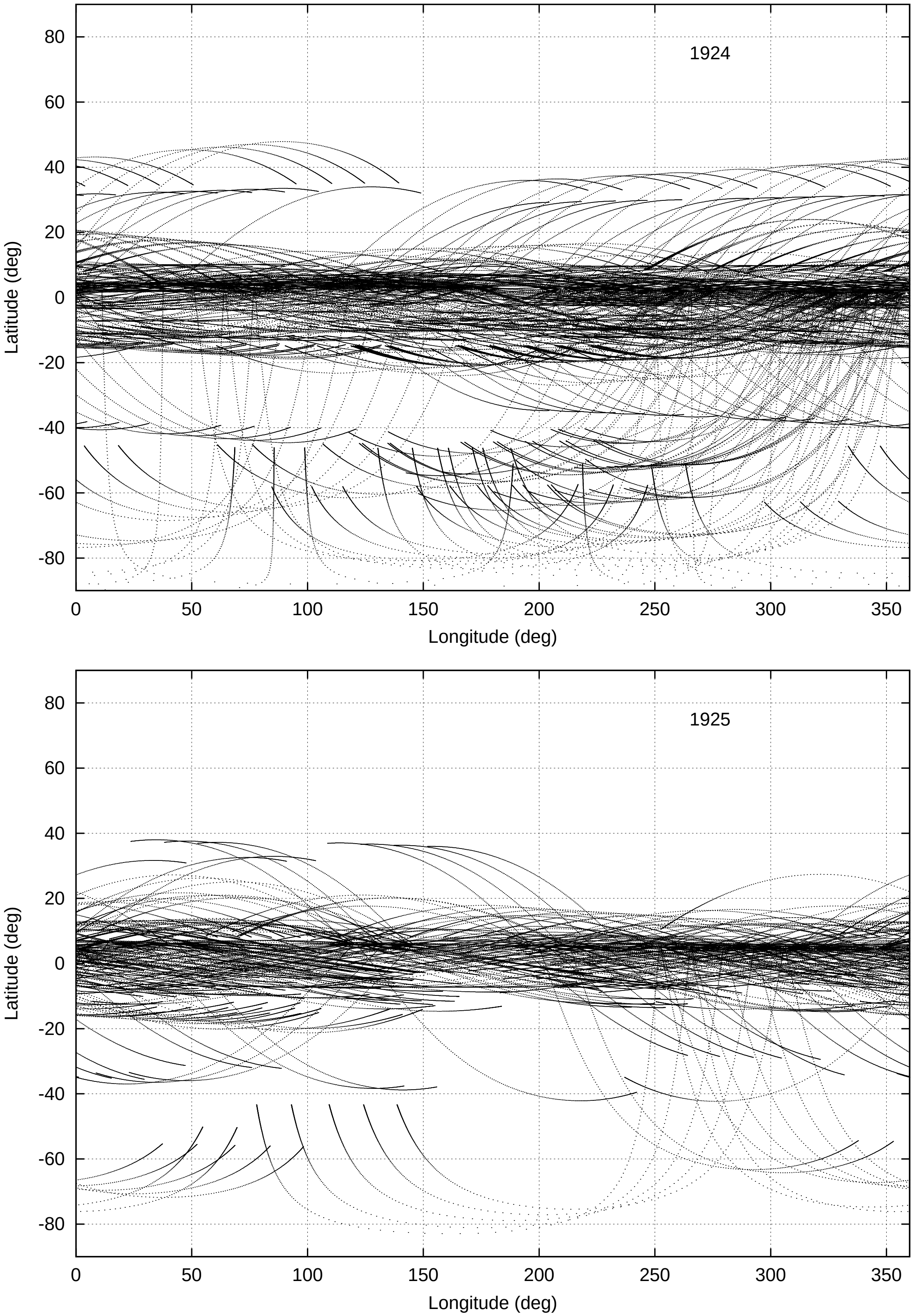

Figure 7.3: **Solar surface coverage for Carrington rotations** 1924 **and** 1925 – The figure shows the geometric footpoints of *l.o.s.*s corresponding to actual observations for Carrington rotation numbers 1924 and 1925. The plot is in the same format as figure 7.2.

7.4 Software Issues

The software required for this project was of significant complexity and volume. For such software projects, there are considerable advantages in adopting a *modular* approach. The *Object Oriented* philosophy was used as a guiding principal in the design of the software. The entire problem was broken down into large logically independent blocks. These blocks were further broken down into functionally independent smaller tasks. Most of these tasks were performed by user-callable library functions. It was attempted to build the software tasks as layers of function calls. The lowest layers of the functions handle most of the nitty-gritty of actual data processing and implement a general purpose solution for the task making as few assumptions about the data-set as possible. The higher layers provided operationally useful functionality by stringing together a set of the lower level functions and defining the details of the particular task to be performed. This approach makes complex software projects tractable by hiding most of the complexity behind function calls, allowing the software developer to focus on the comparatively small task at hand without being distracted by the rest of the paraphernalia. The individual functions were tested and debugged independently before integration with the software libraries. This approach allows the debugging of complex software to be more efficient and provides a framework for a robust software. It was ensured that a given computing task is always performed by the same piece of code. This makes it easier to maintain consistency and reduces the debug time. Several good programming practices like minimum use of global variables, meaningful variable names, error detection and warning messages, etc. were adhered to. As the task of tomographic reconstruction is computationally intensive, care was taken to optimise the software for speed and memory requirements. A fair fraction of the software developed is in form of user callable libraries which have comparatively general purpose functions.

This software was developed, debugged and integrated single handedly by the author. It was developed in the `ANSI C` programming language on `UNIX` and `GNU/LINUX` platforms. The entire code written, including the libraries, software written to test the individual functions and the final application layer, totals up to $\sim 30,000$ lines of code. The software effort has relied heavily on the availability *free software* [1].

7.5 Simulations

A large number of *test data-set* were subjected to analysis by the software developed. The term *test data-sets* refers to data-sets for which the results of the analysis are known *a priori* either quantitatively or at least qualitatively.

---

[1] Refer to `http://gnu.org` for a precise definition of *free software*

7.5.1 Aim of the simulations

These simulations were done with the following two fold aims :

1. **Validating the software** – The software required for the exercise of tomographic inversion using IPS data is of respectable complexity and considerable volume. It is inevitable that it pass through extended debugging stages, where one attempts to locate and excise all the programming errors, both logical and syntactical. In order to debug the software, the programming errors need to be recognised, located, their cause understood and removed. While correcting syntactical errors is easy as the software does not compile till they are all removed, logical errors are much more difficult to correct since they are often difficult to recognise. Simulations using test data-sets provide an effective way of recognising the presence of such errors.

2. **Assessing the effectiveness of the procedure** – It is important to assess the capabilities and limitations of the χ^2 minimisation procedure in converging towards the *true* distribution of the Solar Wind properties. It needs to be established that the analysis procedure is capable of reconstructing the structure of the Solar Wind from the IPS data which satisfies the required assumptions. The stability of the results in presence of noise in the data should also be investigated. Simulations can also be used to estimate the effects of departures from the assumptions made.

Analysis of test data-sets using the software developed and the comparison of the outcome with the known results can be used to achieve both the aims mentioned above.

7.5.2 Methodology

For the purpose of simulations, a 2D distribution of the velocity and the C_n^2 with the desired features was generated on a fiducial surface. As this fiducial surface has no constraints which limit its resolution, it was constructed at a much finer resolution of $1^\circ \times 1^\circ$ as compared to that used for the tomographic reconstruction. We refer to this distribution as the *true global Solar Wind model* and assume it to be time invariant. The distribution of the Solar Wind properties along each of the $l.o.s.$s was computed from the true global Solar Wind model assuming a constant and purely radial Solar Wind velocity. A $1/R^4$ fall in C_n^2 was assumed ($C_n^2 \propto \delta n_e^2 \propto n_e^2 \propto (1/R^2)^2$). The obtained distribution of the Solar Wind properties along the $l.o.s.$s was used to compute the theoretical power spectra for the $l.o.s.$s. The generation of the power spectra exploits the generality of the software formalism which treats individual thin screens independently, allowing for an arbitrary distribution of Solar

Wind parameters along a *l.o.s.* (Section 5.3.7). The geometry parameters of actual observations were used to specify the *l.o.s.*s used and only the observations made in the period of a Carrington rotation were used in any given simulation (Section 7.3).

The test data-sets thus generated satisfy all the assumptions made by the reconstruction process, which have been discussed in Section 3.7 and samples the inner heliosphere in exactly the same manner as the observations. The simulations were done using theoretically generated noise-free power spectra and also with power spectra to which an appropriate amount of noise had been added using equation 4.9 in Section 4.5.4, to reflect the statistical uncertainty in the measurement of the power spectrum.

The analysis procedure described in Section 7.2.1 was followed to attempt tomographic reconstruction from the simulated data. Uniform Solar Wind models were used to estimate the best fit velocity and C_n^2 for the generated power spectra using the the automated procedure described in Section 5.3. These best fit IPS velocities and C_n^2 for individual *l.o.s.*s were used to arrive at a global initial guess for the tomographic reconstruction procedure as discussed in Section 7.2.2. The χ^2 minimisation procedure was started using the initial guess as the starting point and was allowed to continue till it converged to a reconstruction.

The Downhill simplex χ^2 minimisation algorithm (Section 7.2.4) which we have chosen proceeds by reducing the step sizes by which it varies the parameters of the model as it approaches the minima, in an attempt to reduce the volume the parameter phase space which encloses the minima towards which it is converging. This leads to a increasingly shallow decrease in χ_G^2 as the minimisation progresses. It is necessary to decide a criterion to terminate the minimisation process in order to finish it in a reasonable amount of time. We used a Silicon Graphics Origin 200 machine for our simulations and each iteration of the global χ^2 minimisation procedure took close to 30 *sec*. As each of the simulations ran for a few thousand iterations, the computing time requirements for each of the simulations are of a few tens of hours. As the χ_G^2 decrease tapers off the number of iterations required for significant gains in reconstruction quality become very large, we therefore terminate the minimisation process at a stage when further iterations lead to little gains. We have chosen to terminate the minimisation process when the fractional decrease in χ_G^2 over a cycle drops below 1%.

The simulated data followed exactly the same path through exactly the same software as the real observed data. The only difference is that the correction for the contribution to the IPS velocity due to Earth's motion along it's orbit (Section 5.3.6) is not required for simulated data. The simulations, therefore, test out the entire data path through the software and provide a quantitative means of estimating the performance of the reconstruction procedure.

7.6 Results of simulations

A variety of Solar Wind models were used for simulations, ranging from an artificial featureless model to more realistic models with large scale velocity and C_n^2 features. All simulations discussed in this section use the geometry parameters of the actual observations conducted during the Carrington rotation number 1923 to sample the heliosphere. Tomographic reconstruction is applied only to an equatorial belt extending from 13° to -20°. As discussed in Section 7.2.3, a pixel size of $20^\circ \times 11^\circ$ (longitude×latitude) has been used. The equatorial region of interest therefore has 18 pixels along longitude and 3 along latitude. Thus, the global Solar Wind model has $18 \times 3 = 54$ degrees of freedom each for velocity and C_n^2. The total number of observations whose *l.o.s.*s remain confined in the equatorial region are 739, each constraining velocity and C_n^2 independently. The results for featureless Solar Wind models and for Solar Wind models with structure are presented separately.

7.6.1 Featureless Solar Wind models

Featureless models were used to test if the basic machinery of the χ^2 minimisation procedure was in order. As the uniform Solar Wind models used to estimate the IPS velocities and C_n^2 for the individual power spectra provide an adequate description for a featureless true global Solar Wind model, the initial guess generated from the best fit IPS velocity and C_n^2 estimated for individual *l.o.s.*s is expected to be very close to the true distribution. These featureless models were used to look for any systematics in the final Solar Wind model arrived at, which could be an artifact of the analysis procedure or the sampling of the inner heliosphere. These simulations were also used to check for the presence of instabilities in the χ^2 minimisation procedure, in the sense of oscillations developing on subjecting a smooth model to tomographic reconstruction.

The simulations were carried out according to the procedure described in Section 7.5.2. The results of the simulations are presented in Table 7.1. The results are presented in form of the ratio of the average velocity arrived at by the minimisation procedure, $\overline{v_M}$, to the true value of the velocity, v_D. The proximity of this ratio to unity is a measure of how well the minimisation procedure is able to reproduce the true value. The *rms* of v_M was computed over the fiducial surface and its ratio to v_D is also presented. As the true model is a constant all over the fiducial surface, the *rms* of v_M, σ_{v_M}, represents the fluctuations in the global Solar Wind model and is a measure of uncertainty in the value of the v_M. A small value of σ_{v_M}/v_D implies that the tomographic reconstruction has yielded satisfactory results. Results are presented in a similar manner for C_n^2 as well.

The results shown in Table 7.1 validate the software developed for the global χ^2

Table 7.1: **Results of global Solar Wind model χ^2 minimisation simulations : Featureless models** – The first column specifies if the simulations had noise added to them, the second column gives the ratio of the mean best fit velocity to the true velocity used and the third column gives the ratio of *rms* of the best fit velocities to the true velocity in percentage. Columns four and five present the same information for C_n^2 as columns two and three for velocity. The last column gives the number of iterations for the χ^2 minimisation procedure to converge.

Noise Added	$\overline{v_M}/v_D$	σ_{v_M}/v_D %	$\overline{C^2_{n\ M}}/C^2_{n\ D}$	$\sigma_{C^2_{n\ M}}/C^2_{n\ D}$ %	No. of Iterations
No	0.9998	0.08	1.0002	0.06	683
Yes	1.0026	0.34	1.0012	0.78	55

minimisation procedure and demonstrate that the procedure works remarkably well for the featureless Solar Wind model. For the noise-free simulations, the mean values of the results of the minimisation procedure differ from the true values by $\sim 0.02\%$ for both velocity and C_n^2 and the uncertainties in the values of the velocity and C_n^2 are $\sim 0.08\%$ and 0.06%, respectively. On adding an appropriate amount of noise to the power spectra, to reflect the statistical uncertainty in their measurement, the mean values of velocity and C_n^2 differ by less than 0.3% from the true value. While the uncertainty in the value of the velocity increases to 0.34% that for C_n^2 to 0.78%. The small percentage of uncertainty in the values of fit parameters indicates that the uncertainty in the final model is not dominated by the noise on the data. While the noise-free simulation required 683 iterations to reach the termination criterion, the simulation with noise took 55 iterations.

The χ^2 for the global Solar Wind model, χ^2_G, corresponding to the initial guess for the simulations without noise and with noise were 0.284 and 95.23 respectively. The final value of χ^2_G for these two cases arrived at by the tomographic minimisation procedure were 0.281 and 95.07. As the initial model hardly differs from the true global model, one does not expect a further significant decrease in χ^2_G. It should be noted that χ^2_G with and without the addition of noise differ by ~ 100. This provides a useful estimate of the contribution of the measurement uncertainty in the power spectra to χ^2_G.

We define a χ^2_{GN} as χ^2_G normalised to the number of observations used to constrain the reconstruction :

$$\chi^2_{GN} = \frac{\chi^2_G}{N_{con}} \tag{7.7}$$

χ^2_{GN} for the noise-free and noise added simulations were 4×10^{-4} and 0.13, respectively. For comparison, the average χ^2 obtained from fitting uniform Solar Wind models to the individual power spectra, χ^2_U, were 9×10^{-4} and 0.07 for the noise-free and the noise added cases, respectively. While χ^2_{GN} is about a factor of two smaller than the average χ^2_U for the noise free case, the reverse is true for the noise added case. Such small values of χ^2_{GN} and χ^2_U imply that the fits are good and there is not much to choose between the fits on the basis of the χ^2 values, it is, however, instructive to understand the differences in the final χ^2.

In the case of noise-free data, the only source of uncertainty on the fit parameters for individual spectra is the uncertainty in the best model fit values due to the termination the χ^2 minimisation process beyond some threshold when determining the best fit uniform Solar Wind models. As the initial guess is made by projecting all the *l.o.s.*s observed in a Carrington rotation on the fiducial surface and taking a weighted mean of contributions from different *l.o.s.*s, many uniform Solar Wind model fits get averaged over to produce the initial model. If this uncertainty is a zero mean gaussian random variate, the averaging involved in the process of making the initial guess shall reduce the fluctuations due to it and lead to smaller values of χ^2_{GN}. On the other hand, the dominant cause of uncertainty in the case of noise added power spectra is the measurement uncertainty in them. As each of the spectra are individually fitted to arrive at the best fit uniform Solar Wind models for them, the best fits are influenced by the particular realisation of noise on the spectra. One can visualises the spectrum to be a sum of two separate parts, the true spectrum and the noise because of measurement uncertainty. The individual fits to the spectra fit to the sum of both in the noise added case and therefore try to fit the noise as well. The individual fitting to the spectra allows for much greater freedom to fit the measurement uncertainty as compared to the global Solar Wind model, resulting in χ^2_{GN} to be larger than χ^2_U for noise added data.

In addition, we have imposed a termination criterion to stop the χ^2_G minimisation process when further iterations lead to diminishing returns (Section 7.5.2). This has been done because of limitations of computing power and time and does not reflect the inability of the minimisation process to achieve the desired minimum value of χ^2_G. It is theoretically possible for the χ^2_G to be exactly 0.0 for the noise-free simulation. As the χ^2_G hypersurface in the parameter phase space is smooth, in absence of noise, and is expected to have a unique minima, we expect to asymptotically approach a value of 0.0 for χ^2_G if we allow the minimisation process to proceed. For the simulation which incorporates the presence of noise, it is theoretically not possible to achieve a value of 0.0 for χ^2_G. The imperfections of the tomographic reconstruction and the imposed termination criterion for the χ^2_G minimisation process also contribute to yielding a larger value of χ^2_{GN} as compared to the average χ^2_U.

No large scale systematic features, which could imply presence of artifacts, due to either the analysis procedure or the sampling of the heliosphere or both, were seen in the final Solar Wind model. The final reconstruction resembles the true global model very well and no tendency for a smooth model to 'break-up' into oscillations manifests itself. Thus the global χ^2 minimisation works satisfactorily for the cases of featureless global Solar Wind models.

7.6.2 Solar Wind models with features

The ability of the global χ^2 minimisation procedure to recover the structure of the Solar Wind sampled by IPS observations was studied by using global Solar Wind models with large scale features. We tried to estimate the strength of the weakest feature which the simulations could detect and also tried to estimate the effective resolution which the reconstruction could provide. Another important issue is the effect of the resolution of the reconstruction on χ^2_G. The real Solar Wind has a continuous distribution while the reconstruction process deals with a discreet fiducial surface which has a finite grid size, or equivalently, a finite resolution. As a discreet distribution can represent a continuous one only in an approximate manner, there is a need to estimate the errors incurred due to quantisation. While the variations on spatial scales smaller than the grid size cannot be represented on the fiducial surface, variations on spatial scale much larger than the grid size are not effected by the coarseness of the resolution. If the scale size of the features is similar to the grid size, the lack of resolution has a significant effect. A coarsening of the resolution (or increase in grid size) beyond the scale sizes of features in the Solar Wind leads to an increase in χ^2_G because the variations in the true model get averaged over on the fiducial surface. The χ^2_G can thus be thought of as having contributions from two independent sources, the measurement uncertainty on the power spectra, $\chi^2_{G\ Noise}$, and the resolution of the reconstruction, $\chi^2_{G\ Resolution}$ apart from the contributions due to imperfections in the tomographic reconstruction.

$$\chi^2_G = \chi^2_{G\ Noise} + \chi^2_{G\ Resolution} + \chi^2_{G\ Tomography} \tag{7.8}$$

Several Solar Wind models with varying feature strengths and separations were used to study these issues. One of the simulations, using a Solar Wind model with a single strong feature on the fiducial surface, is discussed in considerable detail and the results obtained from the others are presented briefly.

Simulations with a single feature

To estimate the effectiveness of the reconstruction procedure in locating the peak and the width of the features on the fiducial surface, a simple Solar Wind model with a single strong feature was used. A gaussian feature of half width 30° along longitude was placed at a longitude of 150° and the model was held constant along latitude. The feature had a velocity peak of 600 $km\ sec^{-1}$ and a C_n^2 peak of 2×10^{13} above the background and was superposed on a uniform velocity and C_n^2 background of 400 $km\ sec^{-1}$ and 10^{13}, respectively. This global Solar Wind model is referred to as model D in the text.

In order to estimate the magnitude of $\chi^2_{G\ Resolution}$ for this model, the true global Solar Wind model was smoothed to the resolution provided by the reconstruction ($20^\circ \times 11^\circ$). This coarse resolution global Solar Wind model was used to compute the power spectra along the various *l.o.s.*s as detailed in Section 7.5.2. χ^2 was computed between the power spectra so obtained and the spectra computed using the original high resolution true global Solar Wind model. The sum of this χ^2 over all the 739 power spectra in the Carrington rotation of interest is $\chi^2_{G\ Resolution}$ and was computed to be 186. $\chi^2_{G\ Noise}$ was estimated to be $\sim$ 100 in Section 7.6.1. Thus the minimum value of χ^2_G which the tomographic reconstruction can be expected to achieve for case of noise-free simulations is $\sim$ 190 ($\chi^2_{G\ Resolution}$) and that for noise added case is $\sim$ 290 ($\chi^2_{G\ Resolution} + \chi^2_{G\ Noise}$).

The simulations were carried out according to the procedure laid out in Section 7.5.2. The first step in the reconstruction process is to estimate the best fit uniform Solar Wind model parameters for the power spectra which are used later to compute the initial guess for the global χ^2 minimisation procedure. The best fit uniform Solar Wind model velocities obtained for the power spectra are shown in Figure 7.4 as a function of the χ^2 of the fit. Note that the Y axis is in log scale. In order to show more clearly the distribution of points in Figure 7.4, the histograms of velocity and χ^2 distribution are shown in Figure 7.5. It should be pointed out that while only the observations made during the Carrington rotation number 1923 were used to constrain the tomographic reconstruction, Figures 7.4 and 7.5 show the entire data-set. As the feature in the Solar Wind model is confined to a small part of the fiducial surface, most of the *l.o.s.*s sample a featureless Solar Wind, which is fitted very well by the featureless Solar Wind IPS models. The large cluster of points close to a velocity of 400 $km\ sec^{-1}$ with low values of χ^2 corresponds to such *l.o.s.*s. The same data points form the large population in the velocity histogram around 400.0 $km\ sec^{-1}$ and the lowest χ^2 bin in the χ^2 histogram. The *l.o.s.*s which sample the feature have power spectra which deviate from the featureless Solar Wind spectra and the fits to them, therefore, have larger χ^2 values. As the uniform Solar Wind model is not an appropriate model for such power spectra, the interpretation of the best fit velocities estimated for such spectra is not clear, as has been discussed in Section 7.2.1. Though it is not appropriate to associate a single velocity with such spectra, because of the variations in properties of the Solar Wind along the *l.o.s.*, most of the IPS studies in the past have assumed that the best fit IPS velocity represents some kind of weighted average of the Solar Wind parameters

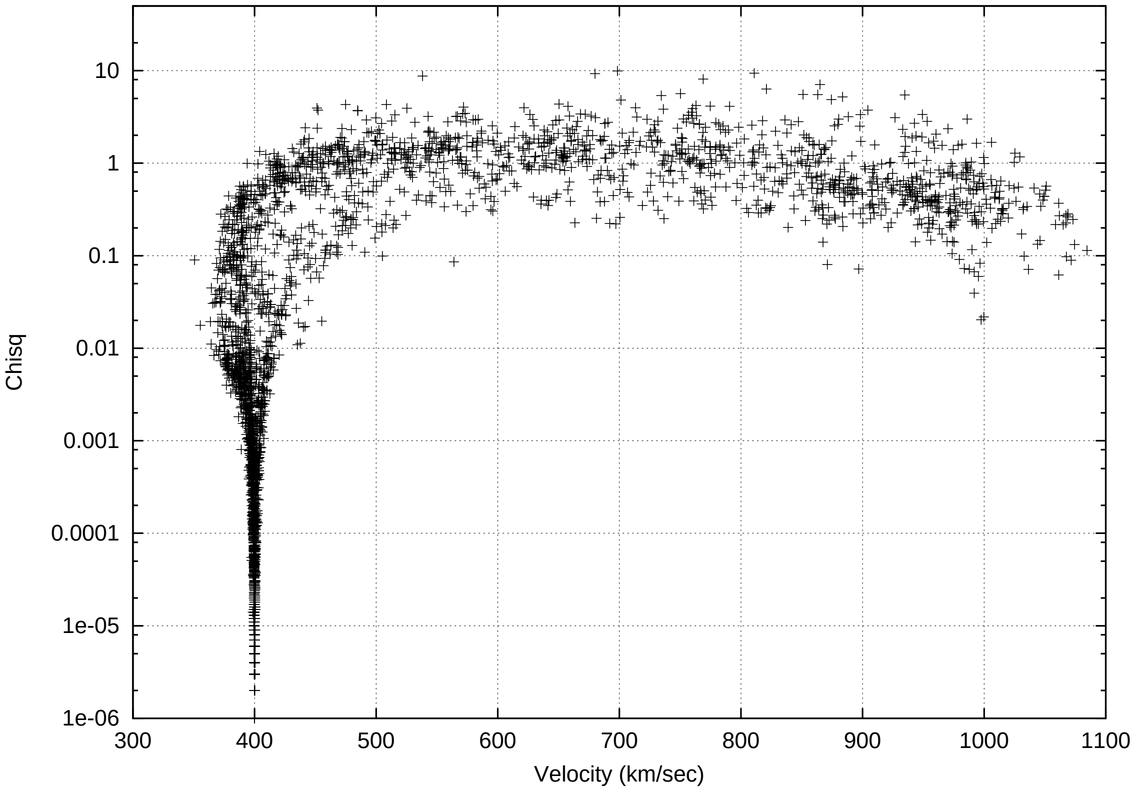

Figure 7.4: **Velocity vs χ^2: Solar Wind model D** – The X axis shows the best fit uniform Solar Wind model velocity for the simulated power spectra and the Y axis the χ^2 for the model fit. The Y axis is plotted in log scale. The large cluster of points close to 400 $km\ sec^{-1}$ on the X axis with low values of χ^2 come from the $l.o.s.$s which sample only the featureless part of the Solar Wind model D and are hence fitted well with uniform Solar Wind models. The points at velocities ranging from $\sim$ 375–1100 $km\ sec^{-1}$ with larger values for χ^2 come from $l.o.s.$s which sample the feature as well.

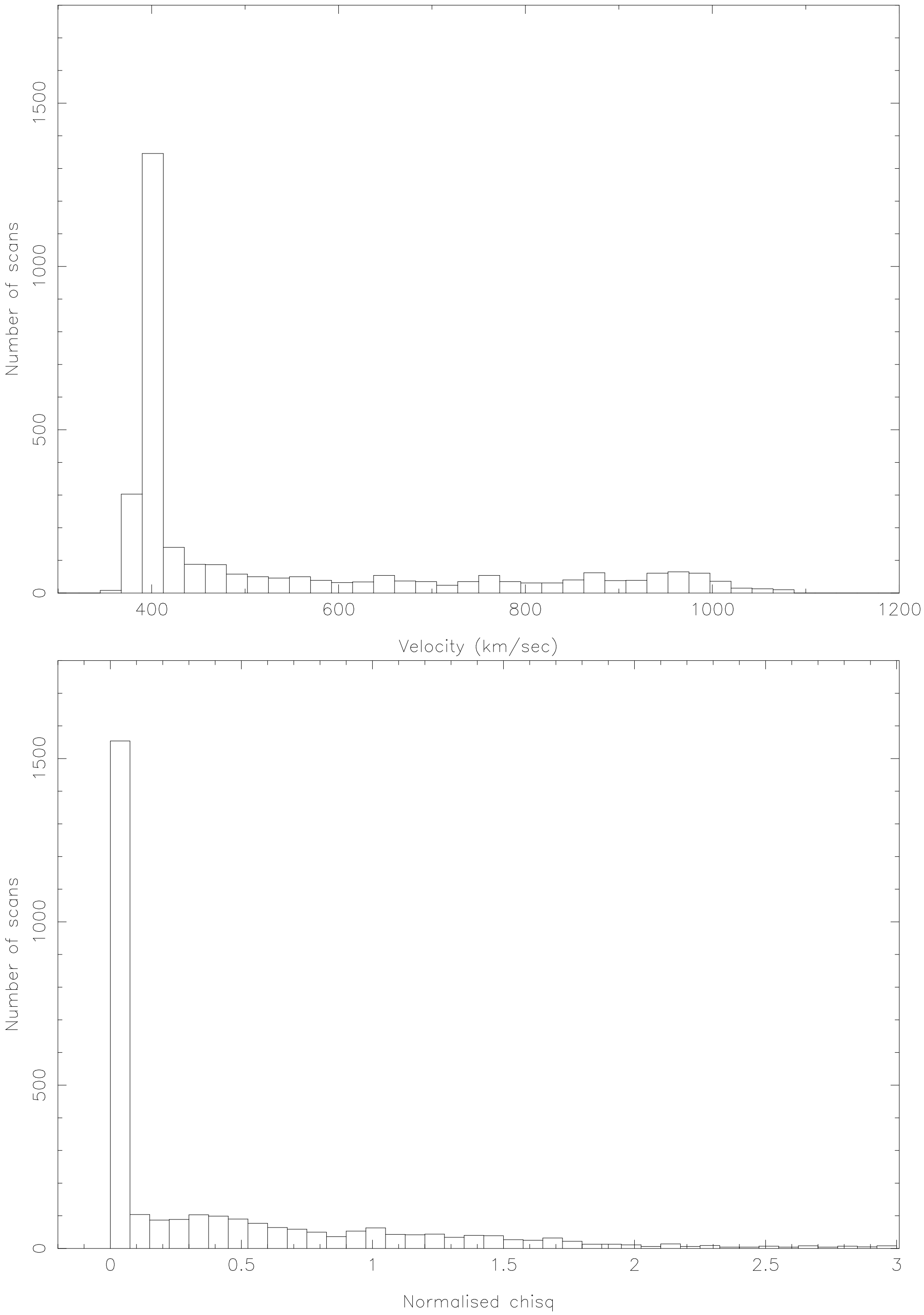

Figure 7.5: **Velocity and χ^2 histograms : Solar Wind model D** – The first panel shows the distribution of the best fit uniform Solar Wind velocities estimated for model D and the second panel the distribution of the χ^2 of the uniform Solar Wind model fit. The large cluster of points at 400 $km\ sec^{-1}$ in the first panel and at χ^2 values close to 0.0 come from the *l.o.s.*s which sample only the featureless part of the model D.

along the *l.o.s.*. We find that the best fit velocities for these power spectra range between $\sim$ 375.0–1100.0 $km\ sec^{-1}$, depending upon the relative contributions of the background and the gaussian feature. While in most cases the velocity for the best fit uniform Solar Wind model does lie in the right range for it to be a weighted mean, the weighting function which has been used to arrive at it is by no means clear. The slight decrease in the values of χ^2 close to velocities of 1000.0 $km\ sec^{-1}$ is due to the fact the P-points of these *l.o.s.*s sample the peak the the gaussian feature, these *l.o.s.* are, hence, so dominated by the it that the deviations from featureless model become small in comparison. The population of power spectra which are fitted with velocities ranging from 375–1100 $km\ sec^{-1}$ form the long tail of the χ^2 histogram shown in Figure 7.5.

The results of the reconstruction procedure for velocity and C_n^2, for the Solar Wind model just described, are shown in Figures 7.6 and 7.7, respectively. Each of the three panels in Figure 7.6 shows the true global Solar Wind velocity model which was used to generate the power spectra (dotted line), the initial guess which was computed using the generated power spectra (dashed line) and the reconstruction which the χ_G^2 minimisation process arrived at (solid line). The top panel shows the reconstruction for the latitude bin 13° – 2°, the middle panel for the bin 2° – $-9°$ and the bottom panel for the bin $-9°$ – $-20°$. Figure 7.7 shows the results of the reconstruction procedure for C_n^2 in the same format as Figure 7.6. To provide favourable circumstances for the reconstruction process to converge, these simulations used noise-free data.

The figures show that the reconstruction is able to recover the shape of the initial model to a very satisfactory level for velocity while the match between the original model and the reconstruction for C_n^2 is not as good. A longitudinal offset between the true model and the velocity reconstruction is seen in the middle and the bottom latitude bins. The magnitude of this shift is about half a longitude pixel width and is a manifestation of the limited resolution of the reconstruction. The poorer reconstruction for C_n^2 global model as compared to that for velocity model suggests that the χ_G^2 is more sensitive to deviations in the velocity model as compared to those in the C_n^2 models.

It should also be noticed that the reconstruction matches the true model most closely for the middle latitude bin and the match is comparatively poorer for the top and the bottom latitude bins. This is a consequence of differences in the density of sampling of the fiducial surface achieved by the observations. From Table 7.2 it is evident that while the number of *l.o.s.*s which pass through a given pixel in the middle latitude bin lie in the range 120–150, those which pass through the top latitude bin vary between 60–90 for the bottom bin they lie in the range 40–55. Therefore, the top and the bottom bins are comparatively poorly constrained and this explains the poorer match of the reconstruction with the true model.

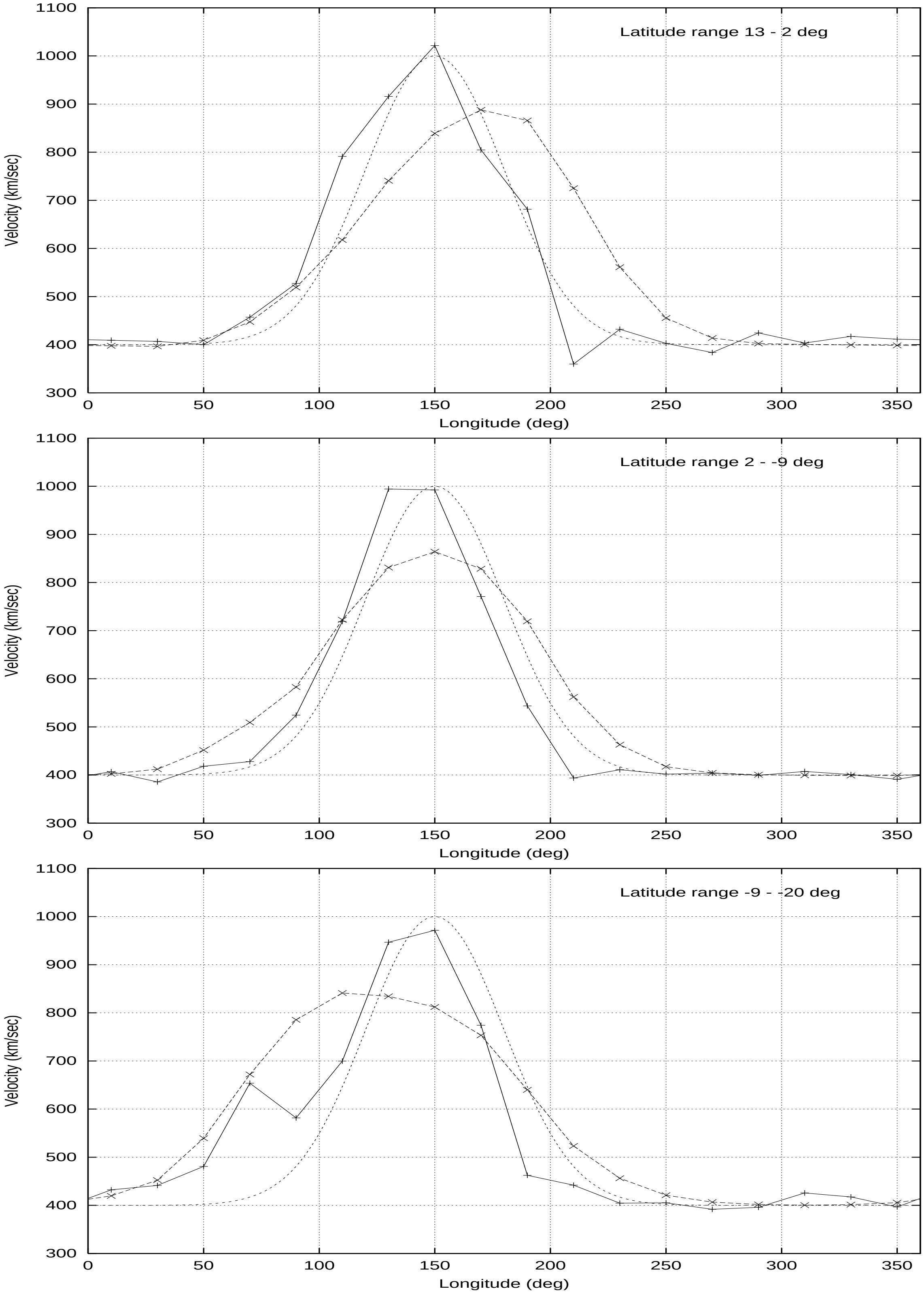

Figure 7.6: **Velocity reconstruction for model D (noisefree data)** – The X axis for each of the panels is Carrington longitude and the Y axis the velocity. The first panel shows the velocity reconstruction for the top latitude bin (13° to 2°), the second panel for the middle latitude bin (2° to $-9°$) and the third one for the bottom latitude bin ($-9°$ to $-20°$). The true global Solar Wind model is shown by the dotted lines, the initial guess by the dashed lines and the tomographic reconstruction by the solid line.

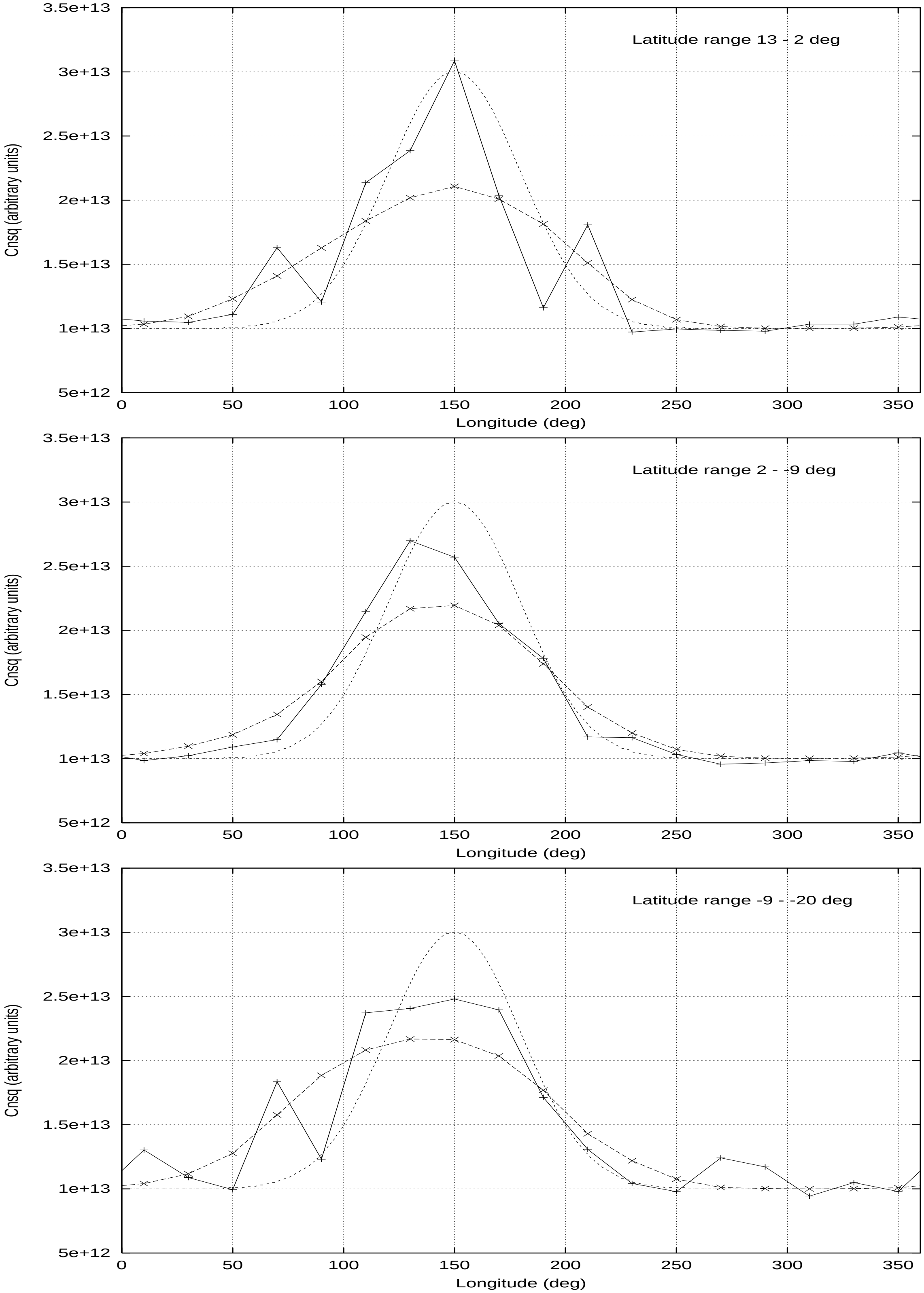

Figure 7.7: C_n^2 **reconstruction for model D (noisefree data)** – The X axis for each of the panels is Carrington longitude and the Y axis the C_n^2. The figure is in the same format as 7.6.

Table 7.2: **Distribution of constraints : Model D** – The table lists the number of *l.o.s.*s crossing each of the pixels on the fiducial surface. It should be noted that the middle latitude bin is sampled most densely and the bottom one most poorly.

		Longitude pixel no. and mid point value								
Latitude pixel no. and range		1	2	3	4	5	6	7	8	9
		10°	30°	50°	70°	90°	110°	130°	150°	170°
1	13° – 2°	84	79	81	72	77	77	76	75	74
2	2° – −9°	149	154	149	133	127	132	130	150	150
3	−9° – −20°	39	38	35	32	47	55	56	46	46
		10	11	12	13	14	15	16	17	18
		190°	210°	230°	250°	270°	290°	310°	330°	350°
1	13° – 2°	63	62	62	63	67	77	92	96	89
2	2° – −9°	123	119	118	137	141	140	147	146	144
3	−9° – −20°	45	49	52	48	40	43	47	49	44

Figure 7.8 shows the decrease in χ^2_G as the global minimisation proceeds. The first 110 $((N_{\phi_\odot} \times N_{\theta_\odot} + 1) \times 2)$ points in the plot show the χ^2_G for the vertices of the simplex used for the reconstruction process. The decrease in the χ^2_G by about 80.7% (from 1232.6 to 238.3) implies that the reconstructed model is a much better description of the data-set as compared to the initial model. As has been discussed in the beginning of this section, even for a perfect reconstruction, the errors due to coarseness of the fiducial surface impose a lower limit on the achievable value of χ^2_G and the expected value of this limit has been indicated on the plot. The success of the tomographic reconstruction lies in achieving a value of χ^2_G as close to this limit as possible. The χ^2_G minimisation process did not hit the termination criterion in $\sim 2,500$ iteration (corresponding to $\sim 1 day$ of computer run time) and was terminated by hand due to limitations of computing time and resources. While the simulation had not reached the minimum achievable value of χ^2_G by then, the trend for a decrease in χ^2_G was still continuing. Judging by the difference of ~ 50 between the χ^2_G achieved by the reconstruction and the minimum achievable value and the continuing trend for χ^2_G to decrease one expects that had the reconstruction process been allowed to continue for a few more days, it would ultimately reach significantly closer to the minimum achievable value. The residual difference between the minimum achievable value of χ^2_G and the value achieved is a measure of the errors or uncertainties associated with reconstruction process and the lowest χ^2_G achieved by our reconstruction can be treated as a gross upper limit for these uncertainties. The minimisation process arrives at the best values of the degrees of freedom to which χ^2_G is more sensitive earlier on in the minimisation process. As χ^2_G seems

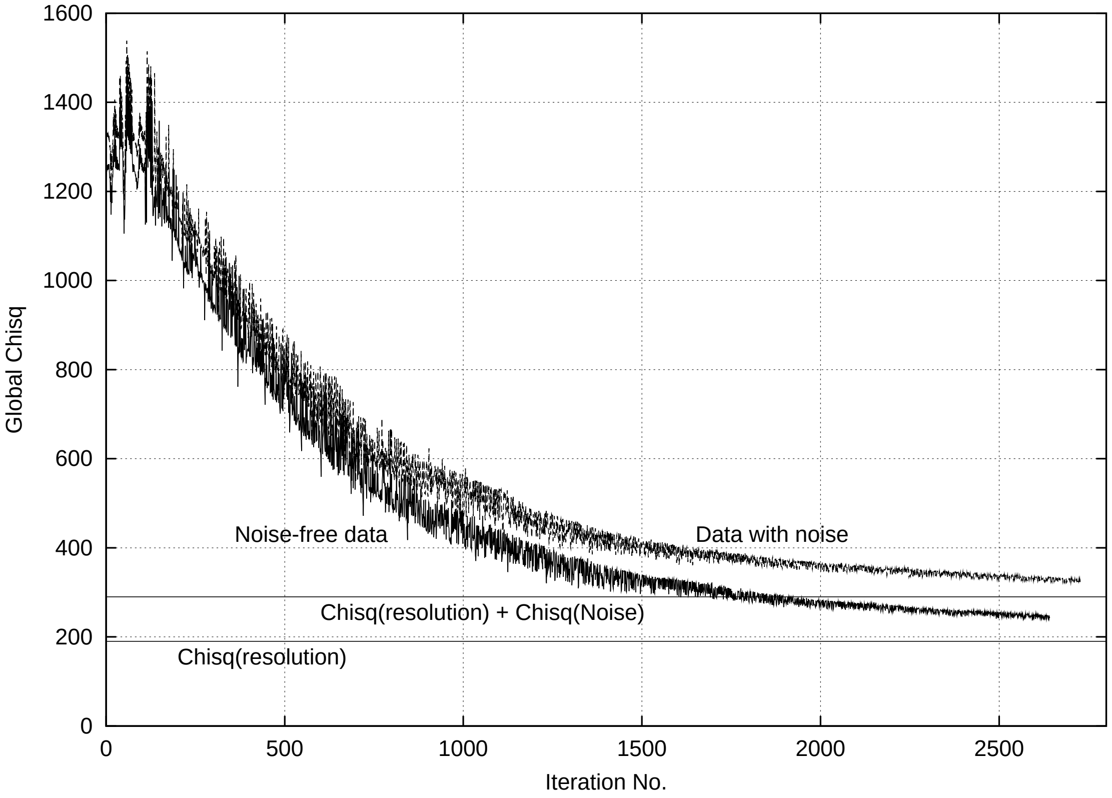

Figure 7.8: **Reduction in χ_G^2 achieved by tomographic reconstruction for model D** – The figure shows the decline in χ_G^2 with the progress of the global χ_G^2 minimisation process for both noisefree and noise added simulations. The first 110 points represent the χ_G^2 for the starting simplex. The minimum achievable value of χ_G^2 for the noisefree reconstruction is marked by line labelled *Chisq(resolution)* and that for the noise added reconstruction by the line labelled *Chisq(resolution) + Chisq(Noise)*.

more sensitive to velocity than to C_n^2, a satisfactory velocity reconstruction had been achieved by the time the minimisation was terminated. The quality of C_n^2 reconstruction could have been improved by allowing the minimisation process to continue. Thus, given enough computing resources and time, we believe, that the χ_G^2 minimisation process would have converged to the proper global Solar Wind model.

The performance of the reconstruction process was studied in considerable detail. To study how well the power spectra from the tomographically reconstructed global Solar Wind models agree with the input model spectra, the χ^2 between the spectra obtained from the reconstruction and the true model was compared with the χ^2 between the individual spectra of the true model and the spectra obtained from the true model smoothed to the reconstruction resolution, which suffers the same increase in χ^2 due to lack of resolution. This comparison is shown in Figure 7.9 with both the X and the Y axes plotted in log scales and the $X = Y$ line is indicated. The points on X axis represent the expected values of χ^2 at the resolution of the reconstruction. If the imperfections in the reconstruction process are not large, the values of χ^2 obtained for individual spectra from the tomographic reconstruction (Y axis) should be close to the values on the X axis. The clustering of points close to the $X = Y$ line points to the fact that the individual power spectra have been fitted reasonably well. It should be pointed out that the data points on the Y axis which go down to very low values of χ^2 ($\sim 10^{-5}$) arise from the power spectra which sample only the featureless part of the fiducial surface and hence a decrease in resolution of the reconstruction has no effect on them at all. On the other hand, the reconstruction, being imperfect, has small departures from the true global Solar Wind model because of which even the featureless part of the reconstructed fiducial surface, has some small variations in velocity and C_n^2 values and hence the *l.o.s.*s which sample it have a larger χ^2 associated with them. Therefore, there are only a few power spectra the χ^2 for which is lower than ~ 0.01 on the X axis. Thus the global Solar Wind model which has been arrived at by the reconstruction procedure compares well with the true global model smoothed to the same resolution as the reconstruction.

We have verified that the spectra from from the tomographic reconstruction were considerably better than the uniform Solar Wind models in describing the model power spectra. The χ_{GN}^2 for the global Solar Wind model was computed to be 0.32 and is about 40% smaller than the average value of χ_U^2 of 0.49. A detailed comparison of the χ^2 for the individual power spectra is presented in figure 7.10. The X axis shows the χ^2 computed between the power spectra obtained from tomographic reconstruction and the true model and the Y axis shows the χ^2 computed between the uniform Solar Wind models fits and the true model. Both the X and the Y axes are plotted in log scales and the $X = Y$ line is indicated. As in Figure 7.9, there are points on the Y axis which go down to very low values of χ^2 ($\sim 10^{-5}$), which

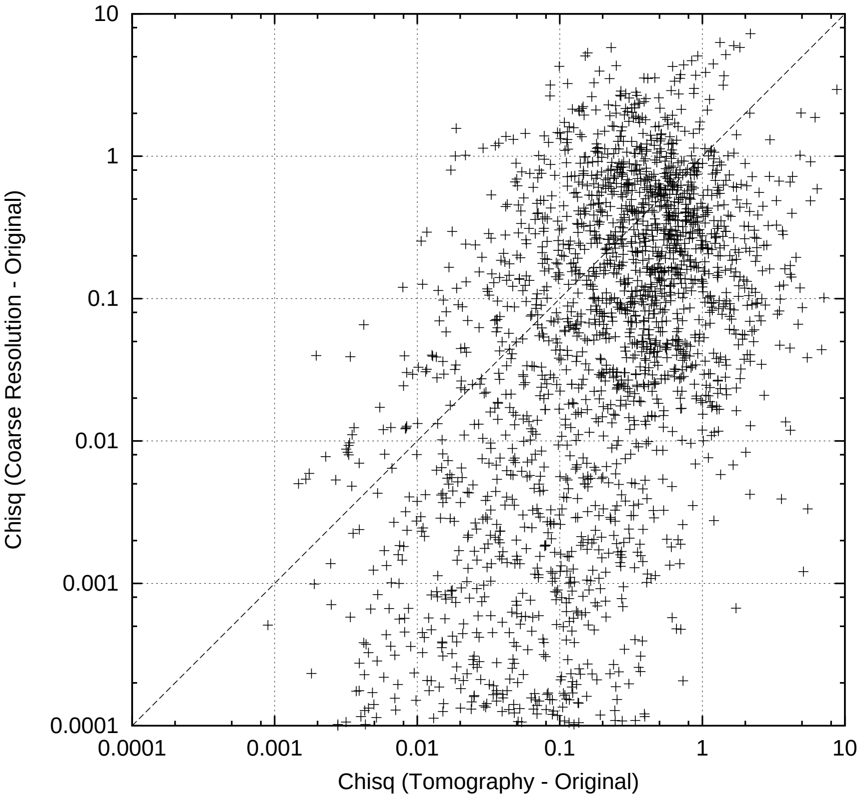

Figure 7.9: **Assessing the quality of the tomographic reconstruction** – The X axis shows the χ^2 for individual power spectra computed between the power spectra obtained from tomographic reconstruction and the original spectra computed from the true global Solar Wind model. The Y axis shows the χ^2 for individual power spectra computed between the power spectra obtained from the true global Solar Wind model smoothed to same resolution as the reconstruction and the true global Solar Wind model. The $X = Y$ line is marked and both X and Y axes are plotted on log scale. The clustering of points close to the $X = Y$ line at high χ^2 indicates that the tomographic reconstruction process is not far off from the best it could be expected to do.

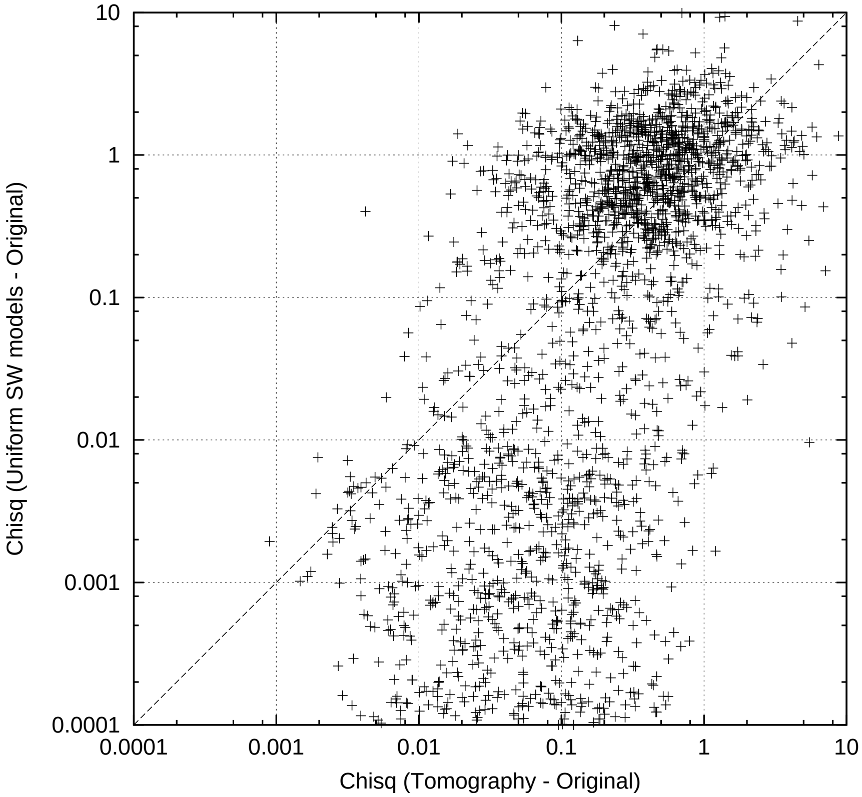

Figure 7.10: **Comparison of χ^2 from tomographic reconstruction and uniform Solar Wind models** – The X axis shows the χ^2 for individual power spectra computed between the power spectra obtained from tomographic reconstruction and the original spectra computed from the true global Solar Wind model, as in Figure 7.9 and the Y axis shows the χ^2 obtained for the best fit uniform Solar Wind models estimated for the power spectra. Both X and Y axes are plotted on log scale and the $X = Y$ line is marked. The fact that most of the points in the dense cluster of points at large values of χ^2 lie above the $X = Y$ line implies that the spectra generated from the tomographically reconstructed global Solar Wind model offer a better description of the data as compared to the best fit uniform Solar Wind models for the power spectra.

sample only the featureless part of the fiducial surface and are therefore adequately described by uniform Solar Wind models. The imperfection in the tomographic reconstruction cause these spectra to have larger values of χ^2 along the X axis. It should be noted that in the cluster of points at high χ^2 values, most of the points lie above the $X = Y$ line (i.e. in the $Y > X$ regime). Thus the power spectra generated from the tomographic reconstruction provide a significantly better representation for the *l.o.s.*s which sample the feature on the fiducial surface. This is not surprising since there are *l.o.s.*s which have disturbed spectra which cannot be fitted with by the uniform Solar Wind models but are being addressed to by the tomographic reconstruction.

Fitting uniform Solar Wind models to individual power spectra can be thought of using one degree of freedom for velocity and C_n^2 per spectrum and these fits are not consistent with a global distribution of the Solar Wind properties. On the other hand, tomographic reconstruction relies upon a global model for the Solar Wind properties and therefore has only as many degrees of freedom for velocity and C_n^2 as the number of resolution elements on the fiducial surface. For the simulation under discussion, the uniform Solar Wind models had 739 degrees of freedom for velocity and C_n^2 each while the global χ_G^2 minimisation approach had only 54 (18×3). It is worth highlighting that in spite of using about an order of magnitude fewer degrees of freedom, the global χ^2 minimisation approach is able to give a better description of the observed power spectra.

In order to test the quality of the reconstruction in the presence of noise, the simulation using the same model (model D) as described earlier was done with an appropriate amount of noise added to the power spectra, reflecting the measurement uncertainty in them. The velocity and C_n^2 reconstruction for this simulation are shown in Figures 7.11 and 7.12, respectively. The figures show that the quality of the reconstruction has not worsened in any significant manner due to inclusion of the effects of measurement uncertainty on the power spectra for the middle latitude bin while the top and the bottom bins have suffered some deterioration in the quality of the reconstruction. This is not unexpected as the number of constraints available for the top and bottom latitude bins are much smaller than those for the middle bin.

Figure 7.8 shows the progression of χ_G^2 for the global Solar Wind model as the minimisation process proceeds. The χ_G^2 decreases by 75.5% (from 1303.2 to 319.2) implying that the reconstructed model is a much better description of the data-set as compared to the initial model. The minimum achievable values of χ_G^2, estimated earlier in this section, has also been plotted. The simulation failed to hit the termination criterion in about 1 *day* of computer run time ($\sim$ 2600 iterations) and was terminated by hand. While the value of χ_G^2 arrived at by the minimisation was larger than the minimum achievable value, the trend for a decrease in χ_G^2 was still continu-

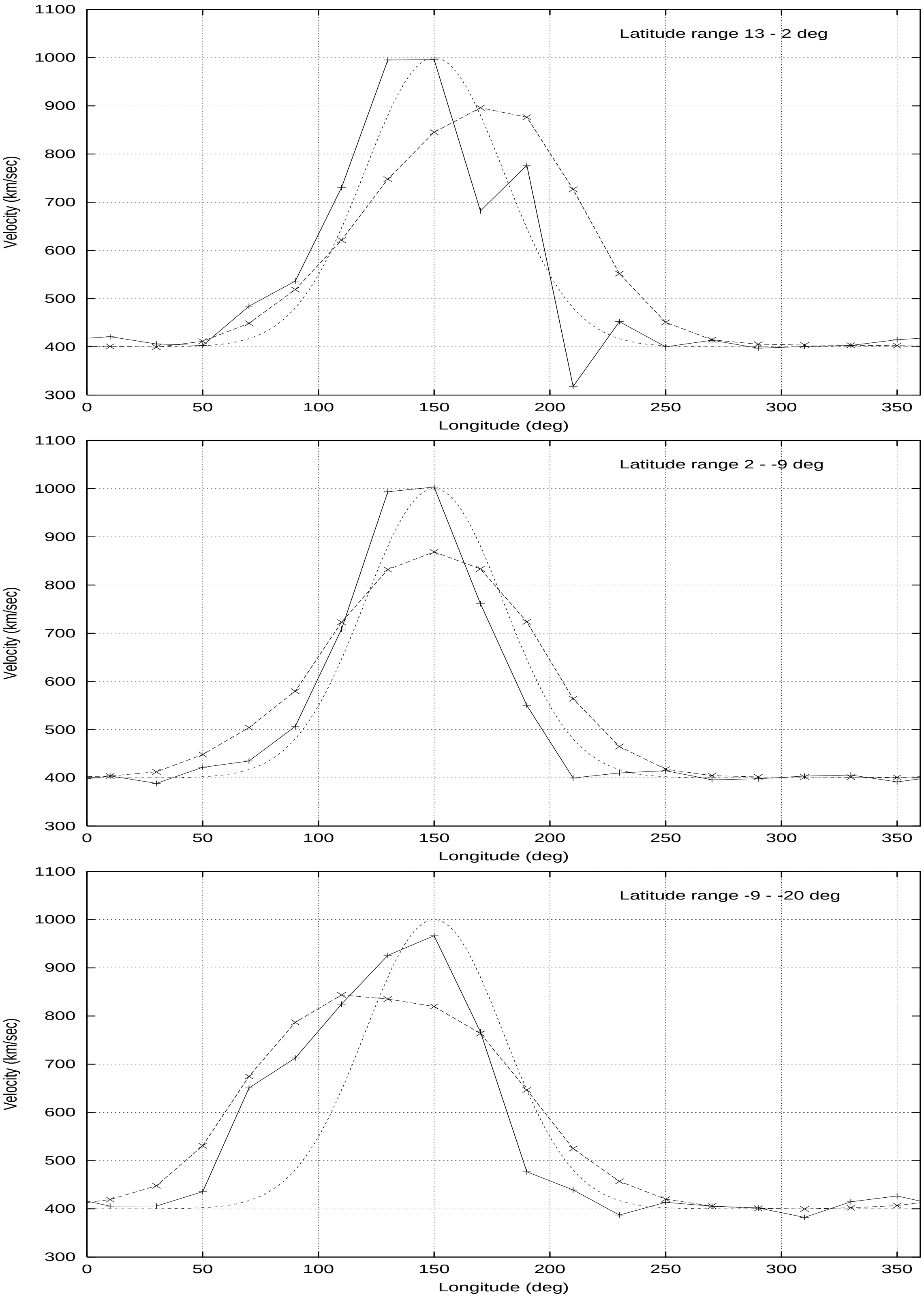

Figure 7.11: **Velocity reconstruction for model D (noise added data)** – The figure shows the results of the tomographic reconstruction for velocity for model D incorporating the noise to reflect the measurement uncertainty on the power spectra. The figure is in the same format as Figure 7.6.

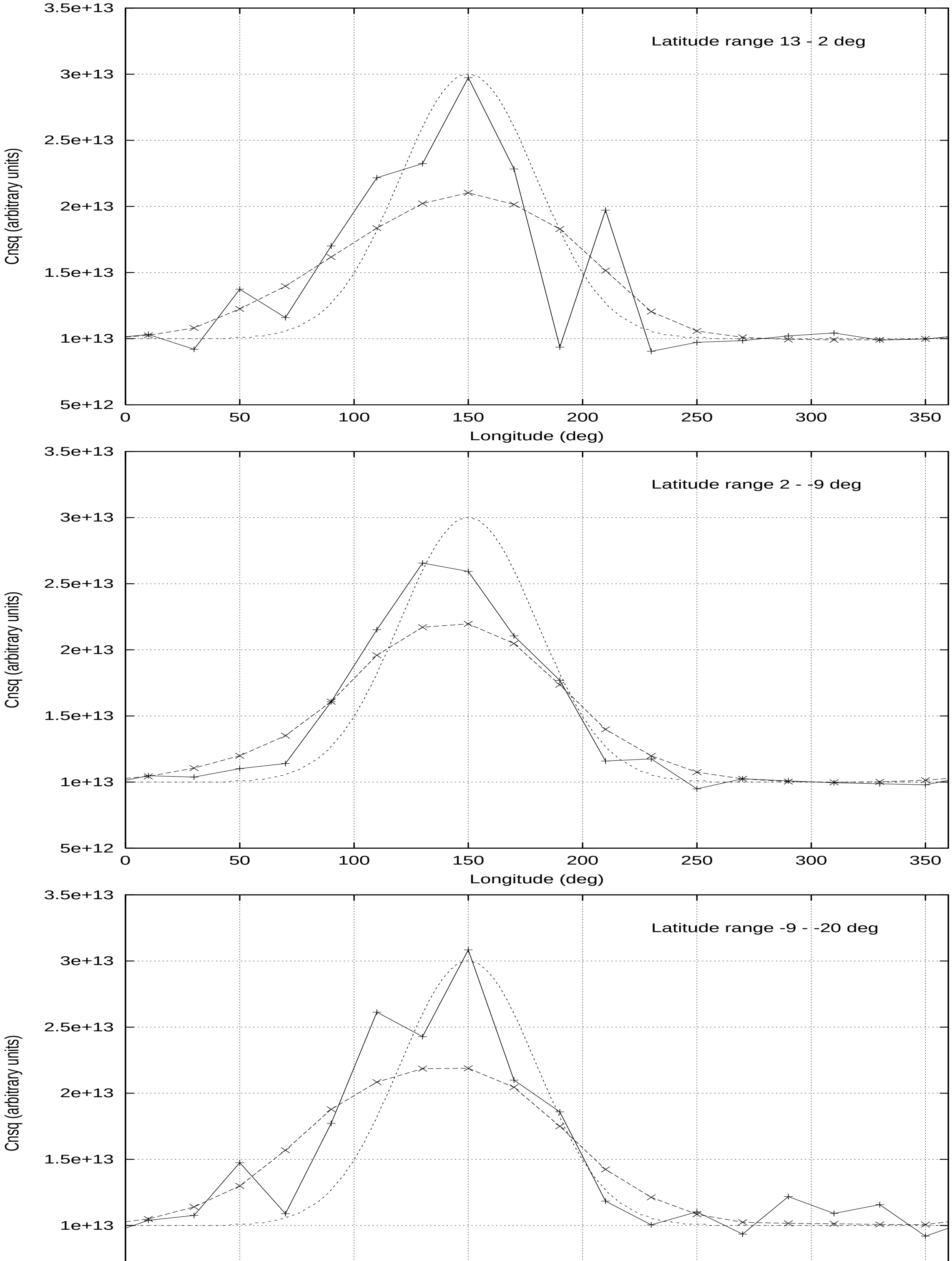

Figure 7.12: C_n^2 **reconstruction for model D (noise added data)** – The figure shows the results of the tomographic reconstruction for C_n^2 for model D incorporating the noise to reflect the measurement uncertainty on the power spectra. The figure is in the same format as Figure 7.7

ing. The difference between the χ^2_G achieved by the reconstruction and the minimum achievable value is $\sim$ 35. This gives a generous upper bound on the contribution of the reconstruction process itself to χ^2_G. As in case of the noise-free simulation, the trend for χ^2_G to decrease was continuing when the minimisation was terminated. One, therefore, expects that had the reconstruction process been allowed to continue, it would ultimately reach closer to the minimum achievable value, though the time take to achieve it would be few days. Also the C_n^2 reconstruction quality would have improved with further iterations of the minimisation.

The reconstruction process was thus found to be able to recover the locations, widths and amplitudes of the velocity and C_n^2 feature to a very satisfactory level though the C_n^2 reconstructions were not as good the ones for velocity. The performance for the C_n^2 feature can be improved by allowing the minimisation process to continue further for time scales of days. The χ^2_G minimisation procedure is performing well and the inability to achieve the lowest attainable χ^2_G values is because of limitations of computing resources and time. The power spectra computed from the reconstructed fiducial surface provide a better description for the power spectra which sample the feature on the fiducial surface as compared to the uniform Solar Wind model fits. The simulations were also tested for stability of reconstruction by perturbing the starting simplex used. Different starting simplexes led to very similar final reconstructions and χ^2_G values and so the reconstruction process was found to be stable against perturbations to the initial value of the simplex.

Simulations with two features

After having tested the efficiency and reliability of reconstruction process for a single feature in the presence of noise, many more simulations with more than one feature were carried out to estimate the strength of the weakest feature which the simulations can reliably detect and to get some estimate of the resolution of the simulations. All these simulations had an appropriate amount of noise added to them (to incorporate the measurement uncertainty in the observed power spectra). The models used had structure only along the longitude axis and were invariant along the latitude axis.

Simulations were done with models having two velocity and C_n^2 features superposed on a uniform background. While one of the features was of the same strength as in the earlier simulations (velocity of 600 $km\ sec^{-1}$ and C_n^2 of 2×10^{13}), the strength of the other feature was scaled down to half, quarter and one eight of it (300, 150 and 75 $km\ sec^{-1}$ and C_n^2 values of 10^{13}, 5×10^{12} and 2.5×10^{12}, respectively). These models are identified by the labels E1, E2 and E3 respectively. The features were superposed on a velocity background of 400 $km\ sec^{-1}$ and a C_n^2 background of 10^{13}.

The results of the simulations are shown in Figures 7.13 – 7.18. In all

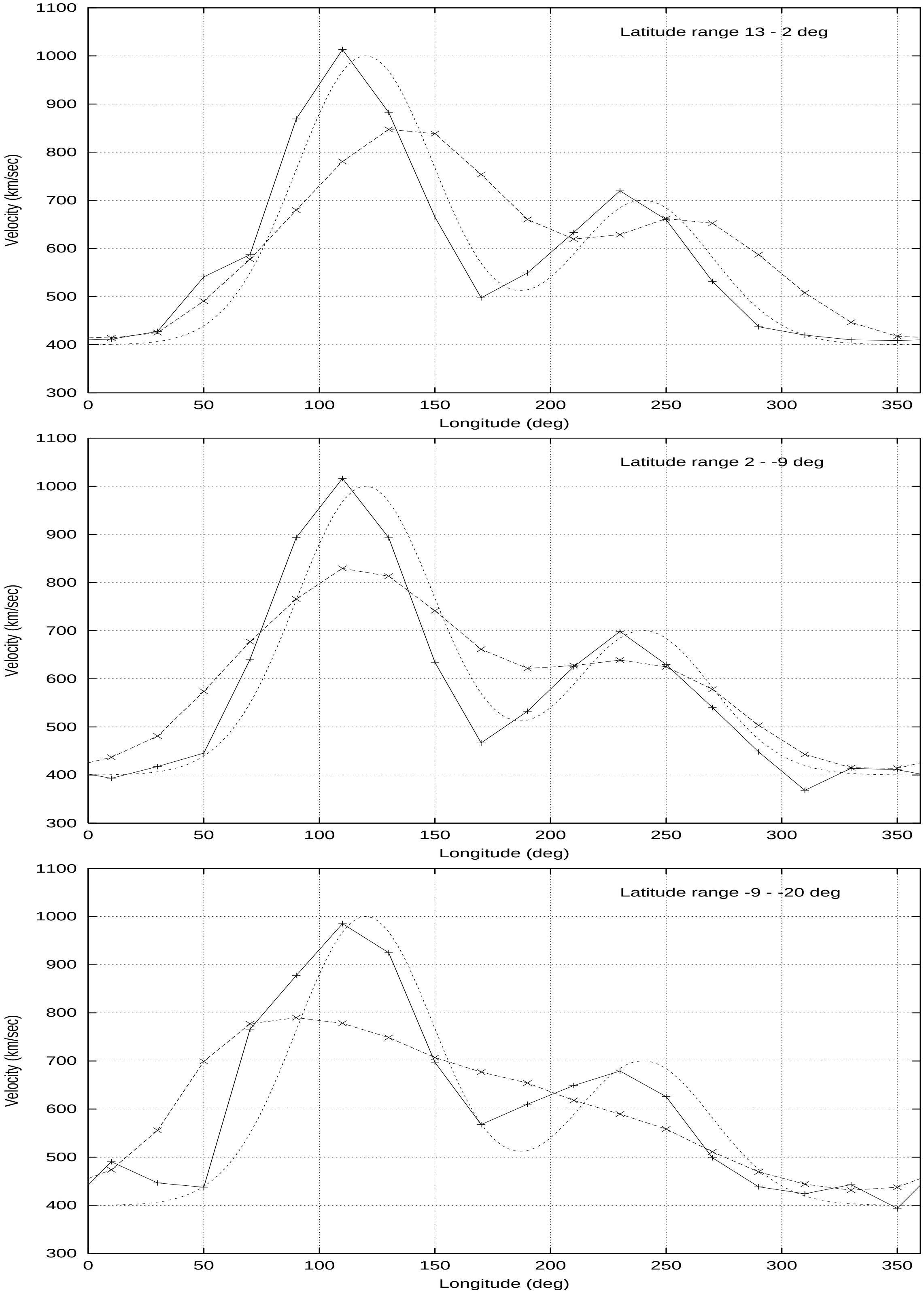

Figure 7.13: **Velocity reconstruction for model E1** – The figure shows the results of the tomographic reconstruction for velocity for model E1 incorporating the noise to reflect the measurement uncertainty on the power spectra. The figure is in the same format as Figure 7.6.

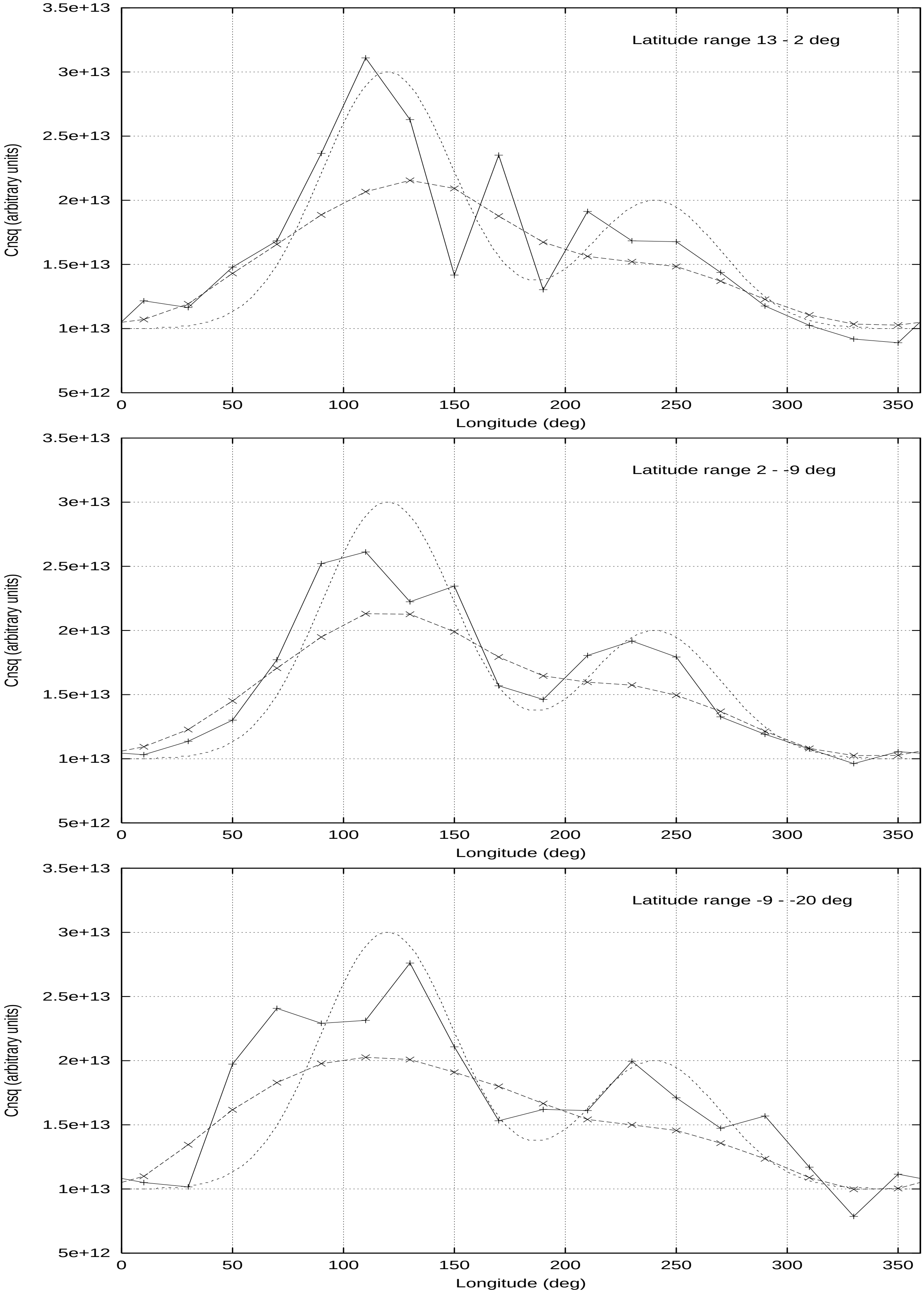

Figure 7.14: C_n^2 **reconstruction for model E1** – The figure shows the results of the tomographic reconstruction for C_n^2 for model E1 incorporating the noise to reflect the measurement uncertainty on the power spectra. The figure is in the same format as Figure 7.7

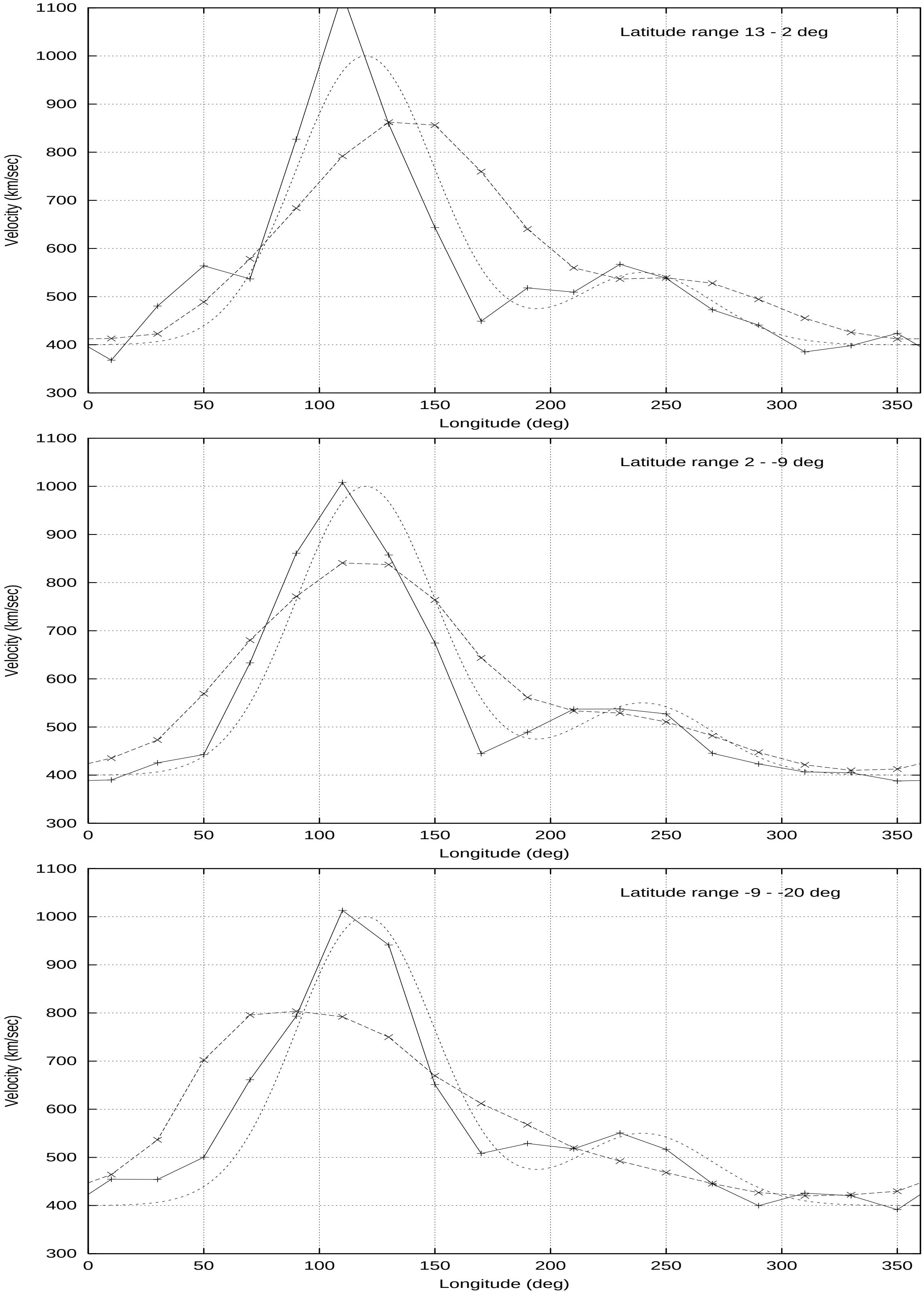

Figure 7.15: **Velocity reconstruction for model E2** – The figure shows the results of the tomographic reconstruction for velocity for model E2 incorporating the noise to reflect the measurement uncertainty on the power spectra. The figure is in the same format as Figure 7.6.

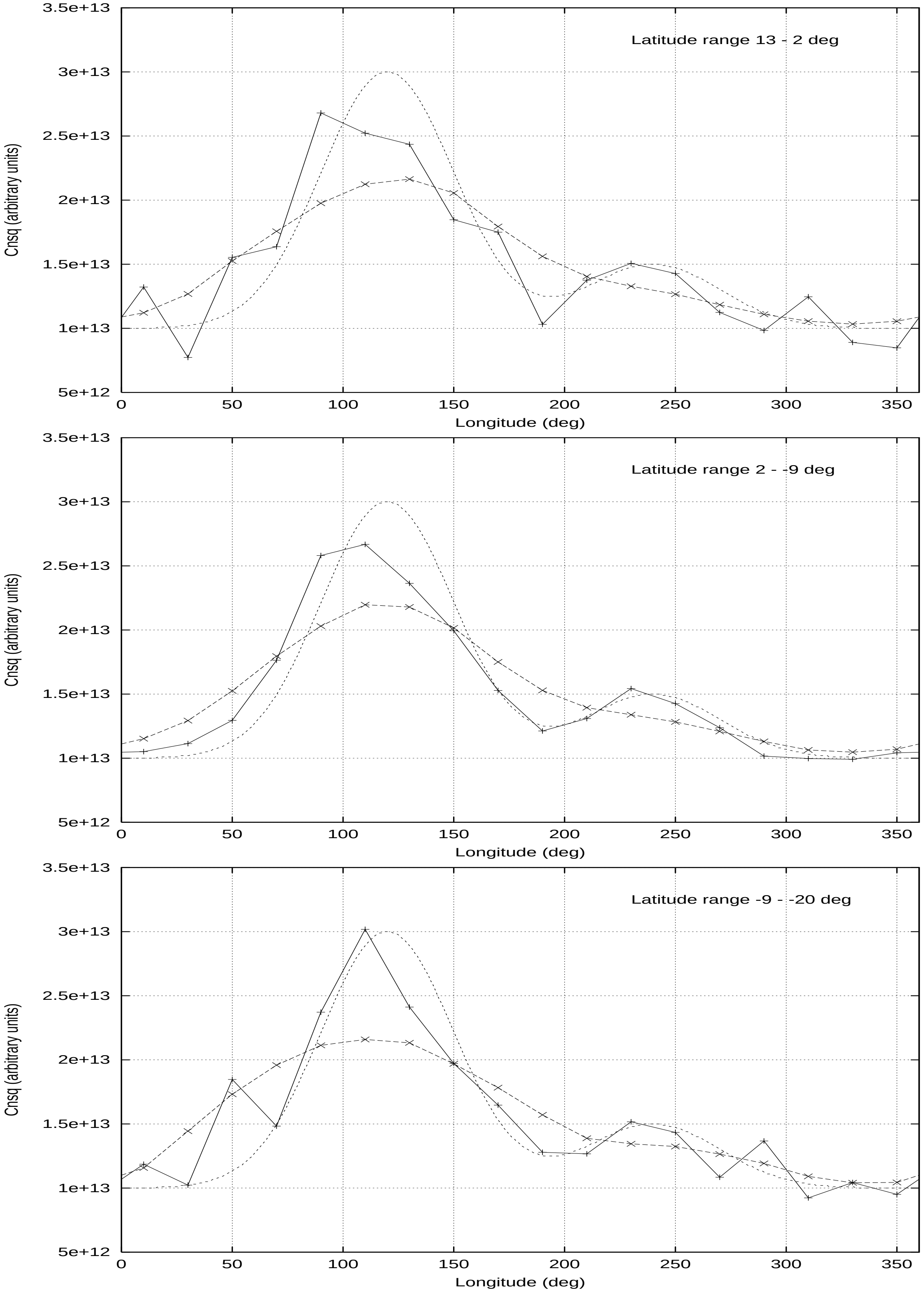

Figure 7.16: C_n^2 **reconstruction for model E2** – The figure shows the results of the tomographic reconstruction for C_n^2 for model E2 incorporating the noise to reflect the measurement uncertainty on the power spectra. The figure is in the same format as Figure 7.7

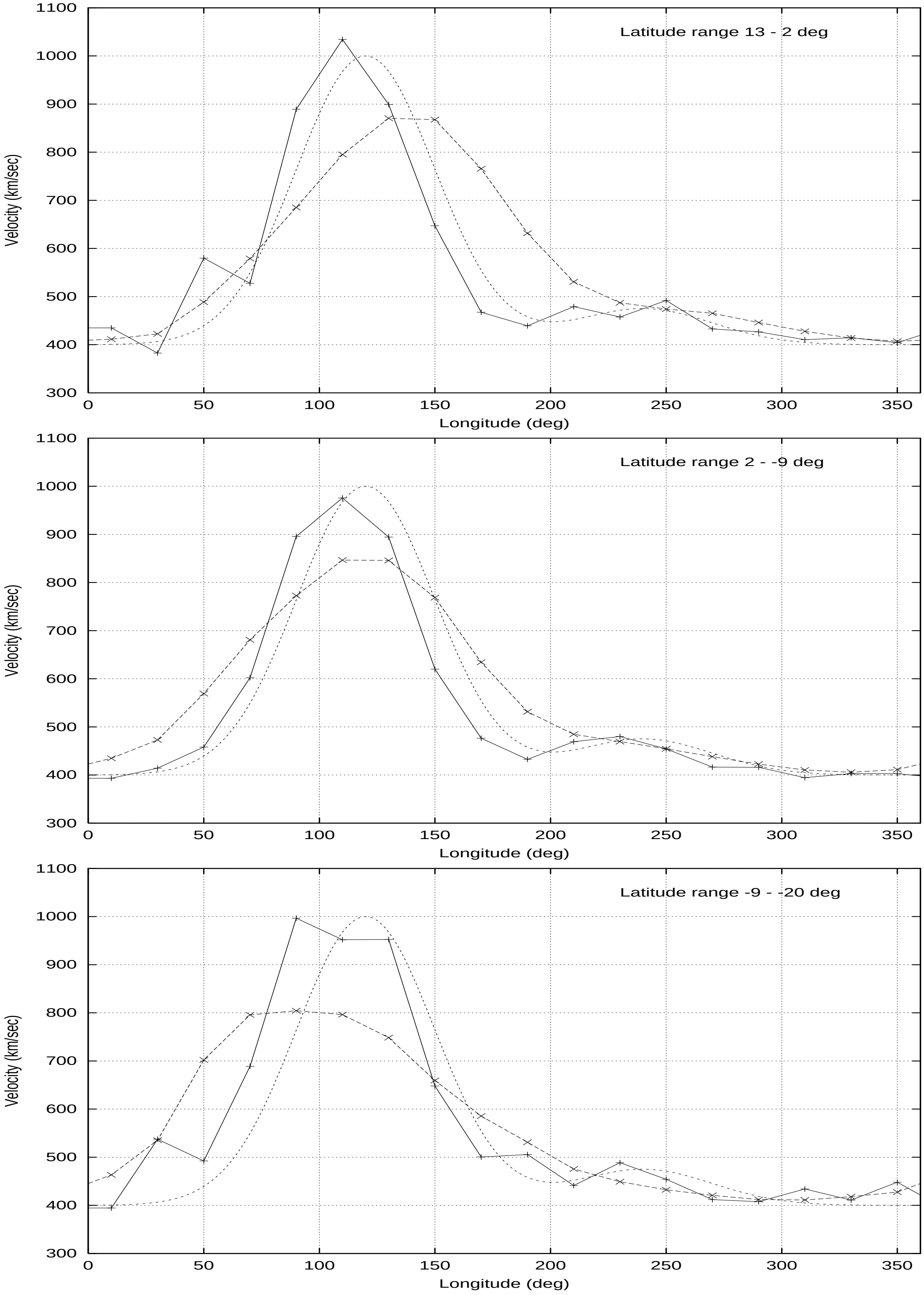

Figure 7.17: **Velocity reconstruction for model E3** – The figure shows the results of the tomographic reconstruction for velocity for model E3 incorporating the noise to reflect the measurement uncertainty on the power spectra. The figure is in the same format as Figure 7.6.

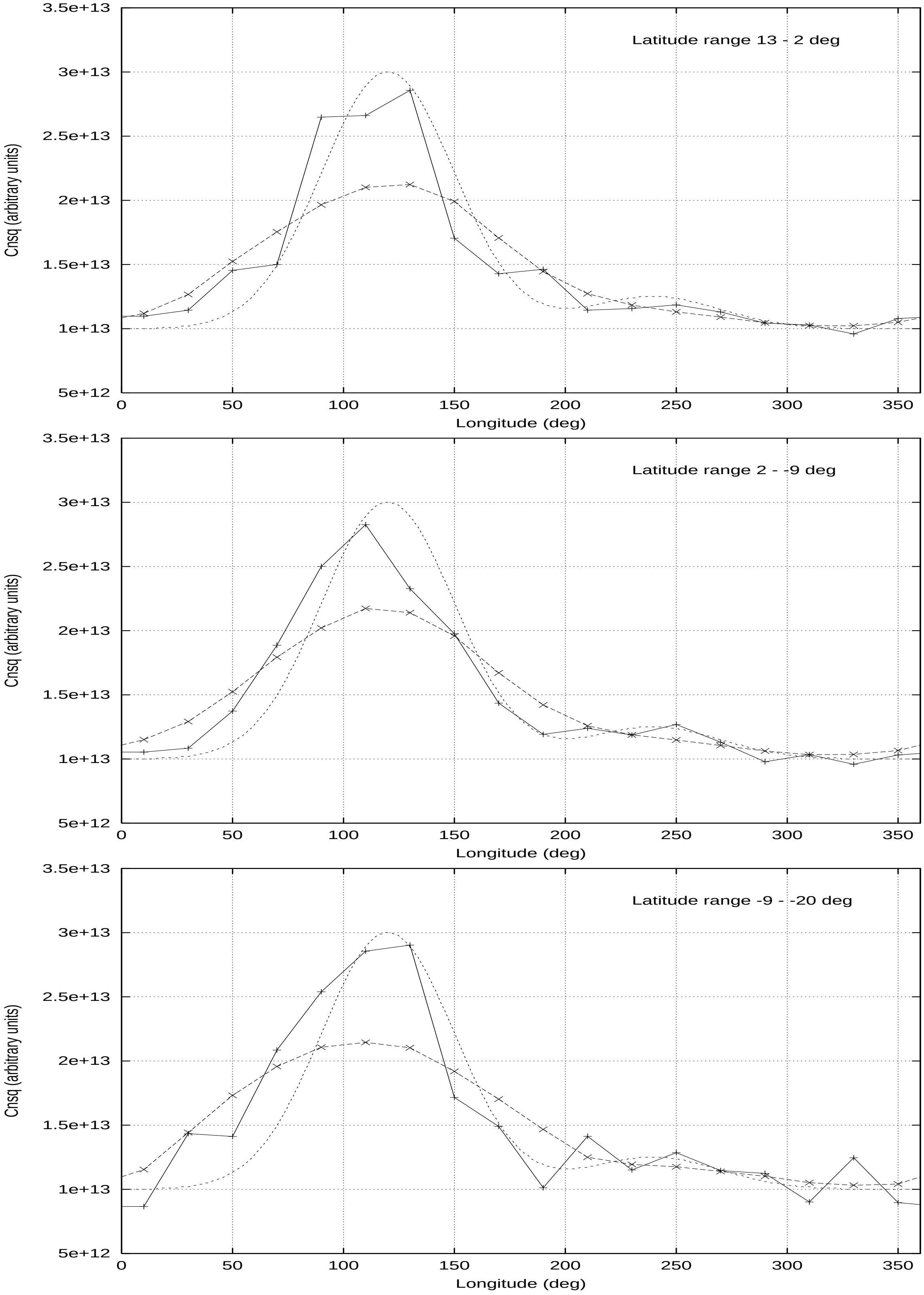

Figure 7.18: C_n^2 **reconstruction for model E3** – The figure shows the results of the tomographic reconstruction for C_n^2 for model E3 incorporating the noise to reflect the measurement uncertainty on the power spectra. The figure is in the same format as Figure 7.7

Table 7.3: **Results of global Solar Wind model χ^2 minimisation simulations : Models with two features** – The first column gives the label to identify the simulation, the second column list the average χ^2 of the uniform Solar Wind model fits, χ^2_U, the third column the χ^2 per power spectra from the tomographic reconstruction, χ^2_{GN}, the fourth column the % decrease in the χ^2_G achieved during the reconstruction process and the last column gives the number of iterations for which the reconstruction was allowed to run. Models E1, E2, E3, F1 and F2 all incorporate the effect of measurement uncertainty in the power spectra. The status at an intermediate stage of reconstruction is also given for models E2 and E3 to illustrate the increasingly shallow decline in χ^2_G.

Model	χ^2_U	χ^2_{GN}	% decrease in χ^2_G	No. of iterations
D (without noise)	0.49	0.32	80.7	2533
D (with noise)	0.57	0.43	75.5	2619
E1	0.64	0.45	74.4	2899
E2 (final)	0.59	0.35	77.4	3899
E2 (intermediate)		0.37	76.1	2953
E3 (final)	0.58	0.36	76.7	3587
E3 (intermediate)		0.38	75.9	2933
F1	0.24	0.31	63.2	1675
F2	0.40	0.32	70.8	2953

the cases the reconstruction was able to satisfactorily reproduce the true velocity model for the middle latitude bin. The velocity reconstruction was able to detect the presence of the fainter feature and reproduce them in a reasonable manner for the other two bins for models E1 and E2 while for the model E3 the reconstruction was less satisfactory. For C_n^2 the reconstructions were not as good as the velocity reconstructions and followed the same trend of the middle latitude bin showing the best match with the true model and the other two latitude bins deviating by larger amounts. Models E1 and E2 reproduced the fainter feature with a reasonable degree of fidelity, the matches for model E3 were not than satisfactory.

A summary of the results of the simulations is given in Table 7.3. The first column identifies the simulation, the second column gives χ^2_U, the third column χ^2_{GN}, the fourth one the percentage decrease in χ^2_G achieved by the simulation and the last one the number of iterations for which the minimisation was allowed to proceed. The table shows that the χ^2_U lies in the range 0.58–0.64 for the three models (E1, E2 and E3) and decreases as the strength of the weaker feature is reduced. The final values of χ^2_{GN} achieved by the reconstruction lie in the range 0.36–0.45 and are smaller than the respective values of χ^2_U. Each of the reconstructions achieved a reduction in χ^2_G in the range 74 – 77%. In order to illustrate the shallow drop in χ^2 with increasing iterations, the results for models E2 and E3 are also shown at an intermediate stage of minimisation. The minimisation for model E2 had achieved a decrease of 76.1% in χ^2_G by $\sim$ 3000 iterations and the $\sim$ 1000 subsequent iterations could only push it by about another one percent to 77.4%.

In order to estimate the effective resolution available in the reconstruction, the following simulations were done. A Solar Wind model with two features of equal strength and a separation of 60° was used. The features had a strength of 300 $km\ sec^{-1}$ in velocity and 10^{13} in C_n^2 above the background and the model did not have any structure along the latitude axis. Both the features were chosen to be gaussians with a half width of 20° and were superposed on a background of 400 $km\ sec^{-1}$ in velocity and 10^{13} in C_n^2. This model is referred to as model F1 in Table 7.3. The results of the simulation are shown in Figures 7.19 and 7.20 for velocity and C_n^2, respectively. The separation between the two features was chosen to three pixel widths, the minimum separation required between the two features so that they can be resolved by the simulation. While the velocity reconstruction is able to pick up the two features in the middle latitude bin, it is not seen clearly in the top and the bottom latitude bins. The C_n^2 reconstruction shows signatures of the presence of the two features in the top and the middle latitude bins but not in the bottom latitude bin which has the poorest C_n^2 reconstruction. Thus the middle latitude bin, which has been sampled best by the observations, is able to detect the presence of two distinct features 3 pixels apart.

Another simulation which used a Solar Wind model with two features of unequal strengths and half widths was done. The strengths of the velocity features were 400 and 200 $km\ sec^{-1}$ while those of the C_n^2 features were kept equal at a value of 10^{13}. The half width of the higher velocity feature was 10° while that of the other one was 20° and the two features were separated by 30° (one and a half pixel width). This model is labelled as model F2 in Table 7.3. The results for velocity and C_n^2 are shown in Figures 7.21 and 7.22, respectively. While the velocity reconstruction is a significant improvement over the initial guess, it is not able to capture the detailed shape of the initial model used to generate the power spectra in any of the latitude bins. The C_n^2 reconstruction also fares similarly. This is not unexpected, as the size of one of the features is smaller than the pixel size on the fiducial surface and the other feature has the same half width as the pixel size, the fiducial surface has too coarse a grid size to be able to represent the model well. The χ^2_G, however, reduces by 70.8% during the course of the minimisation procedure and the achieved χ^2_{GN} of 0.32 also compares favourably with an average χ^2_U of 0.40.

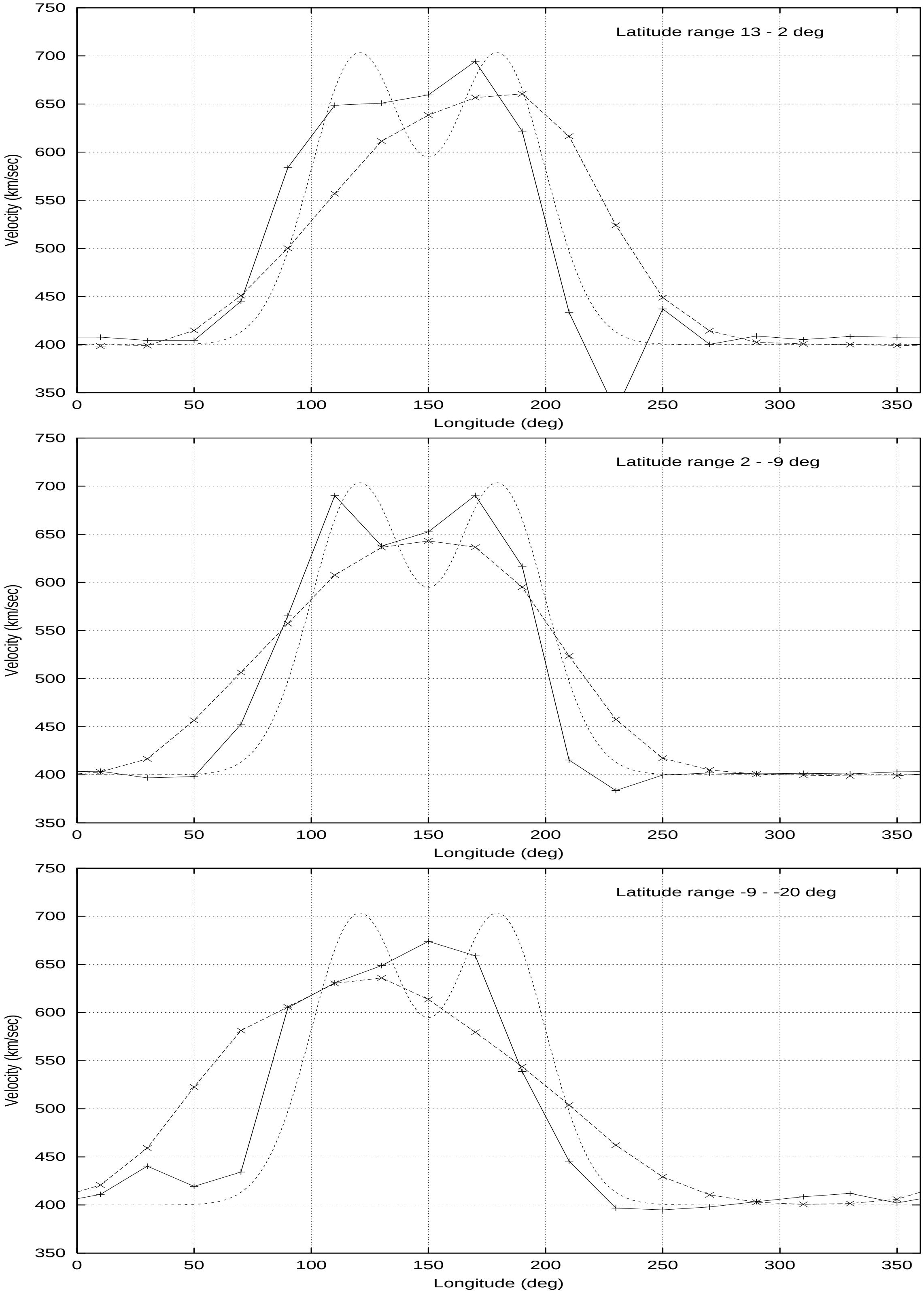

Figure 7.19: **Velocity reconstruction for model F1** – The figure shows the results of the tomographic reconstruction for velocity for model F1 incorporating the noise to reflect the measurement uncertainty on the power spectra. The figure is in the same format as Figure 7.6.

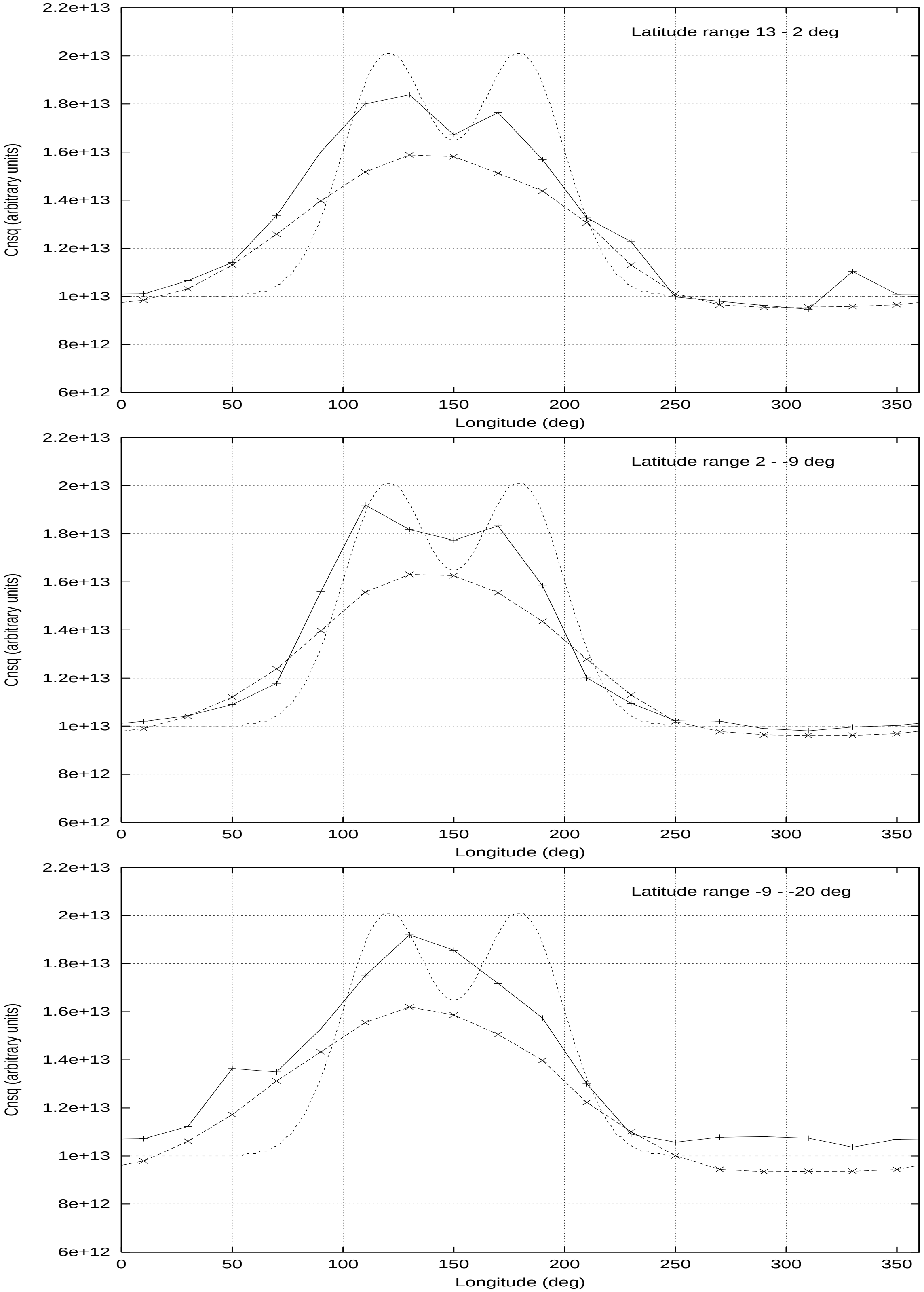

Figure 7.20: C_n^2 **reconstruction for model F1** – The figure shows the results of the tomographic reconstruction for C_n^2 for model F1 incorporating the noise to reflect the measurement uncertainty on the power spectra. The figure is in the same format as Figure 7.7

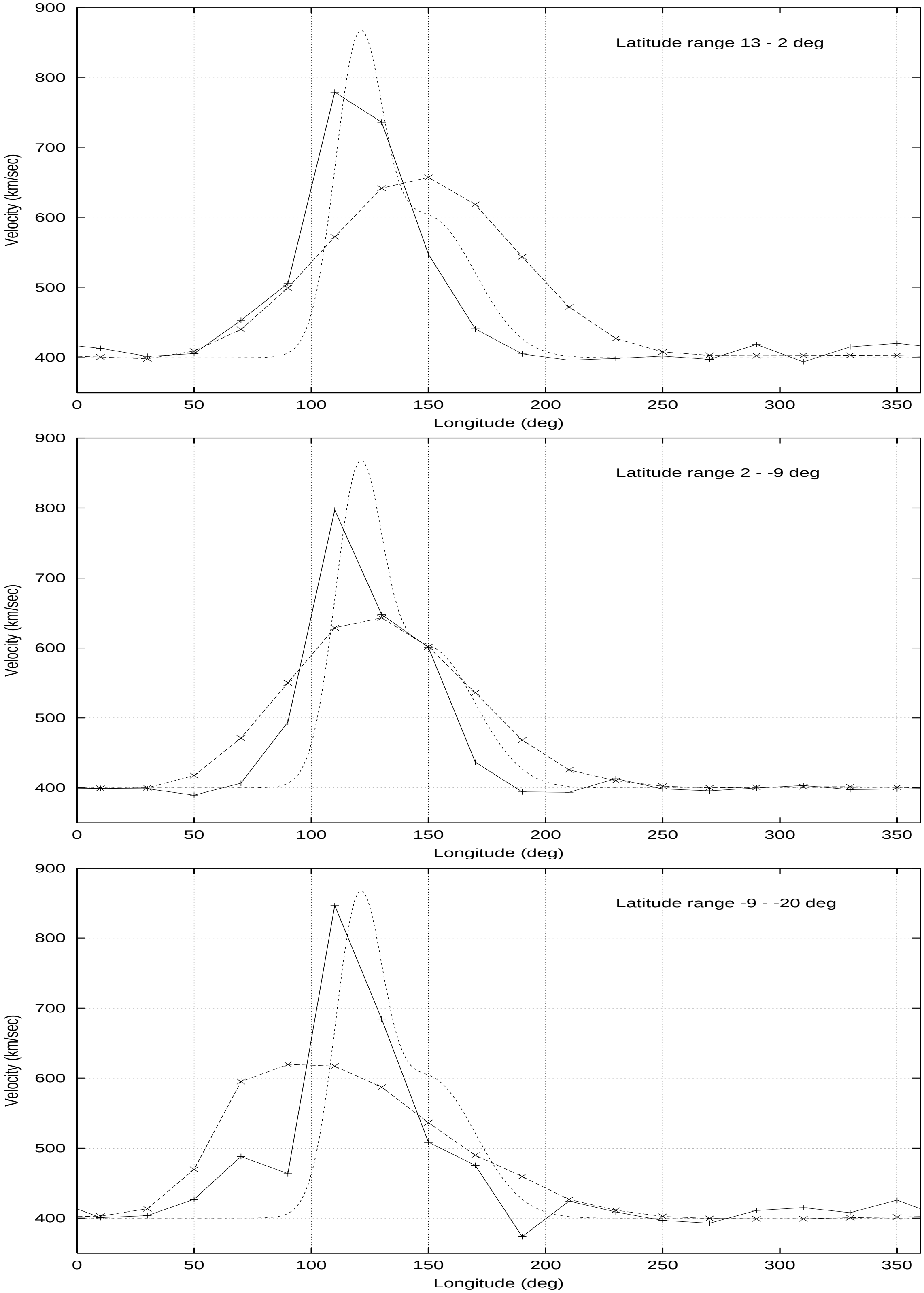

Figure 7.21: **Velocity reconstruction for model F2** – The figure shows the results of the tomographic reconstruction for velocity for model F2 incorporating the noise to reflect the measurement uncertainty on the power spectra. The figure is in the same format as Figure 7.6.

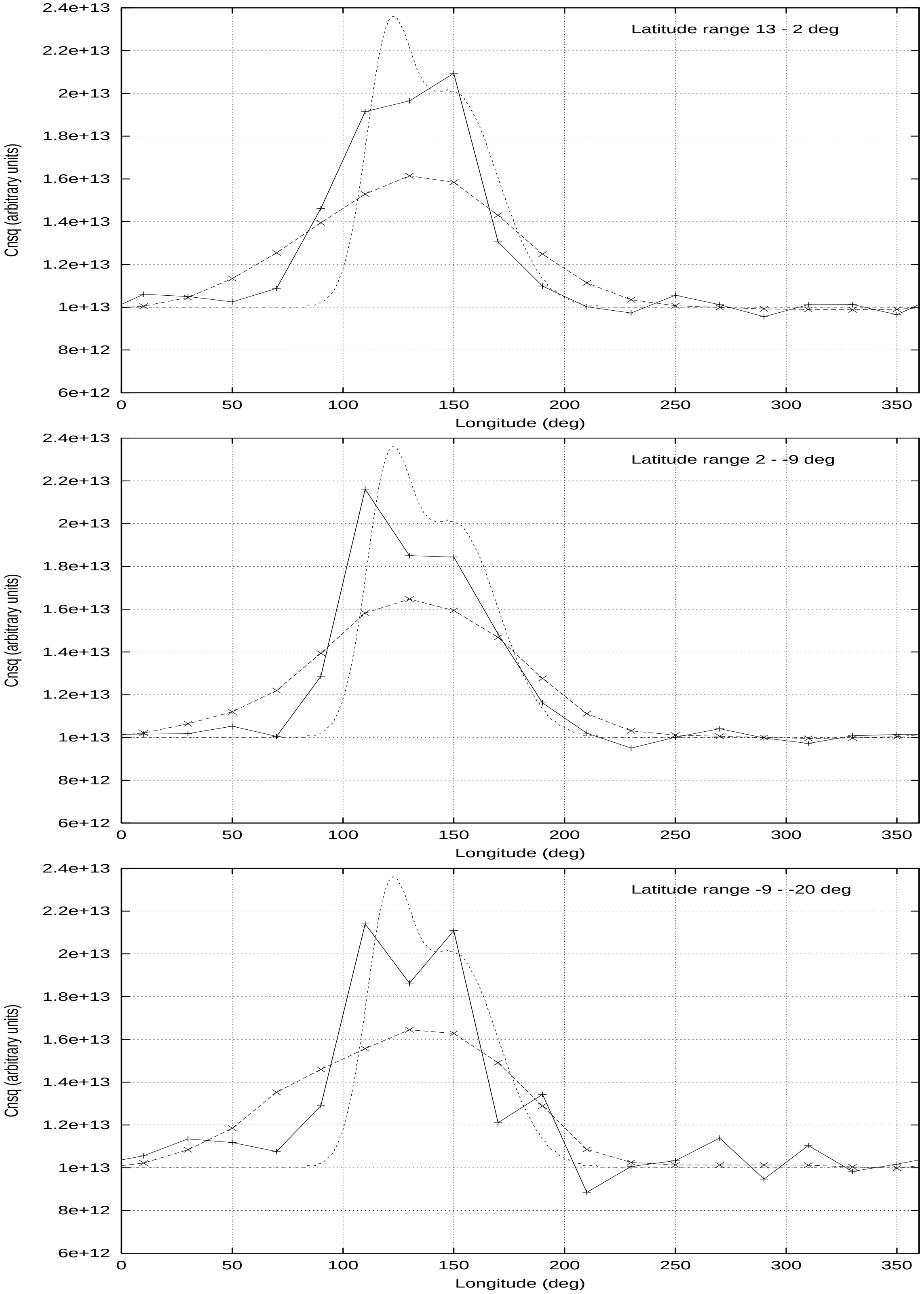

Figure 7.22: C_n^2 **reconstruction for model F2** – The figure shows the results of the tomographic reconstruction for C_n^2 for model F2 incorporating the noise to reflect the measurement uncertainty on the power spectra. The figure is in the same format as Figure 7.7

Conclusions from simulations

1. **The featureless models** – The featureless Solar Wind models were appropriately reconstructed by the tomographic reconstruction methodology. Of course, the convergence to the right model was assured in this case as the initial guess was practically the true model itself. The main reasons for this exercise were to validate the software developed, check for any systematic effects due to, say, sampling of the heliosphere and to see if the reconstruction has some instability which leads it away from the true model. The reconstruction remained stable, both with and without the noise being incorporated.

2. **Models with one feature** – These simulations were done to test the convergence of the reconstruction to the true global model in the most conducive circumstance of noisefree data which satisfies all the assumptions made by the reconstruction process. While the reconstruction was quite close to the true model, there were some deviations from the true model. The velocity reconstruction was closer to the true model as compared to the C_n^2 reconstruction and the middle latitude bin, which is sampled most densely by the observations, showed the best reconstructions. The deviations from the true model can be regarded as the noise or uncertainty associated with the reconstruction procedure. While these deviations can certainly be reduced by allowing the minimisation process to continue for longer, they may not completely disappear. The quality of the reconstruction did not deteriorate significantly on incorporating the measurement uncertainty in the observed power spectra for the middle latitude bin. This suggests that the presence of noise in the data does not affect the reconstruction process seriously in presence of a sufficient constraints. The reconstructions for the other two, comparatively less constrained latitude bins, showed some deterioration in the reconstruction quality. The reconstruction found to converge to the same true global Solar Wind model on perturbing the initial simplex.

3. **Models with two features** – The simulations show that the dynamic range of the reconstruction is not uniform over the entire fiducial surface, while the middle latitude bin could reproduce velocity features one eighth the strength of the stronger feature (75 $km\ sec^{-1}$), the top and the bottom bins could reproduce only features only a quarter of the strength of the stronger one (150 $km\ sec^{-1}$). The C_n^2 features of only a quarter of the strength of the stronger feature could be reproduced in the reconstruction in a respectable manner. The simulations are able to resolve out features separated by three pixel widths in the middle latitude bin for both velocity and C_n^2 reconstructions. In C_n^2 reconstructions the presence of two different features is discernible in top latitude bin as well while the bottom latitude bin is unable to resolve

it.

The set of simulations which have carried out clearly show that the problem of reconstructing the distribution of the Solar Wind properties using the IPS data-set obtained is invertible. These simulations incorporate measurement uncertainty on the observed power spectra in a realistic manner and the data-set was generated assuming no time evolution and a purely radial propagation with a uniform velocity. The reconstruction process has been found to be stable to perturbations of the starting simplex.

7.7 Results from data

The observed data-set was divided into periods of Carrington rotations and the data from each Carrington rotation was subjected to tomographic analysis. Our data-set provides good coverage of the solar equatorial belt for four Carrington rotations, 1922–1925 (Section 7.3 and Figures 7.2 and 7.3).

Of these rotations, rotation number 1923 corresponds to the period of least activity on the Sun. Few signatures of significant activity have been reported in Solar Geophysical Data Reports for this period and the WIND velocity measurements also show little fluctuations during the entire period (Figure 6.14). The prominent Earth directed CME which occurred on 12^{th} May 1997 falls in rotation 1922. While we have used the data from all the rotations for tomographic inversion, we discuss the results for the rotation 1923 in detail as we expect the least amount of time evolution in this period. The success of tomographic reconstruction depends on the degree to which the assumption of little or no time evolution is satisfied, therefore, known transients and sudden fluctuations were removed from the data. For all sources which had more than 10 observations, the mean and rms of the g time series was computed and all the data points differing from the mean by amounts larger than 3σ were not used for tomographic reconstruction.

The initial guess for this period was arrived at using the procedure described in Section 7.2.2. Our procedure to generate the initial guess is quite similar to that adopted by earlier attempts at tomographic reconstruction of the Solar Wind using IPS (Jackson et al., 1998; Kojima et al., 1998; Asai et al., 1998). The main differences between their work and the present attempt lie in our restricting the reconstruction to only an equatorial belt on the solar surface and our having many more constraints per degree of freedom of the global Solar Wind model. A detailed comparison with these attempts is presented in Section 7.9. As the final reconstruction achieved by the earlier attempts is not very different from their initial guess (Section 7.9), it may not be unreasonable to compare our initial guess with other observations of the Sun to look for correlated large scale structures.

The tomographic reconstruction was carried out in the same manner as for the simulations described in the previous Section and is detailed in Section 7.5.2. Figures 7.23 and 7.24 show the velocity and C_n^2 reconstruction for the rotation number 1923. The reconstructions look quite reasonable, the velocity reconstruction is able to pick out significant structure from a featureless initial guess and the structures vary smoothly across the three latitude bins. The progression of χ_G^2 with iteration number is shown in figure 7.25. It is immediately noticed that the magnitude of starting value of χ_G^2 for the case of real data $(12,178.4)$ is much larger than that obtained for simulations $(\sim 1,000)$. This points to there being basic differences between the real data and the simulations. The χ_G^2 minimisation achieves a reduction of 25.3% in χ_G^2 (from $12,178.4$ to $9,101.8$) and made use of 739 *l.o.s.*s. We expect contributions from measurement uncertainty and resolution to χ_G^2 to be about 300 – 400, on the basis of conclusions drawn from earlier simulations.

The average χ_U^2 for the power spectra was 0.50, while χ_{GN}^2 was 12.3, more than an order of magnitude larger. As has been mentioned in Section 7.6.2, fitting individual power spectra with independent uniform Solar Wind models can be thought of as using N_{con} (739 for the present case) degrees of freedom each for velocity and C_n^2 to describe the data. On the other hand, the global Solar Wind model uses only $N_{\phi_\odot} \times N_{\theta_\odot}$ (54 for the present case) degrees of freedom each for velocity and C_n^2. As fitting uniform Solar Wind models makes use of more than an order of magnitude larger numbers of degrees of freedom and the uniform Solar Wind models also provide a reasonable description of the observed power spectra, it is only expected that they give smaller average χ^2 for the fits. It is important to realise that the independent uniform Solar Wind models are inconsistent with a global model of the solar surface, which is exactly what tomographic reconstruction tries to address. We expect variability and the slow time evolution of the Solar Wind to be the most likely cause of the large observed value of χ_G^2 discuss it in detail in Section 7.8.

In order to check for the stability of the reconstruction, we re-started the minimisation process with a different starting simplex. The final reconstruction arrived at, in the second run, was rather different from the first one but the χ_G^2 for both of them were quite close to each other. A few more simulations with differing starting simplexes were done and they resulted in differing reconstructions with similar values for χ_G^2 (within 10% of one another). The results from two of them are presented in figures 7.26 and 7.27. Though the different reconstructions do not match well with each other, all of them show a tendency for an excess in velocity in the middle and the bottom latitude bins in the longitude range 150°–300°. The strength and the widths of the velocity excess differ from one reconstruction to another and it seems to break up in some of them. Similarly there is a strong C_n^2 feature in the same longitude range in the bottom latitude bin. As the χ_G^2 for different reconstructions using the same data are close to each other, there is no justification for believing

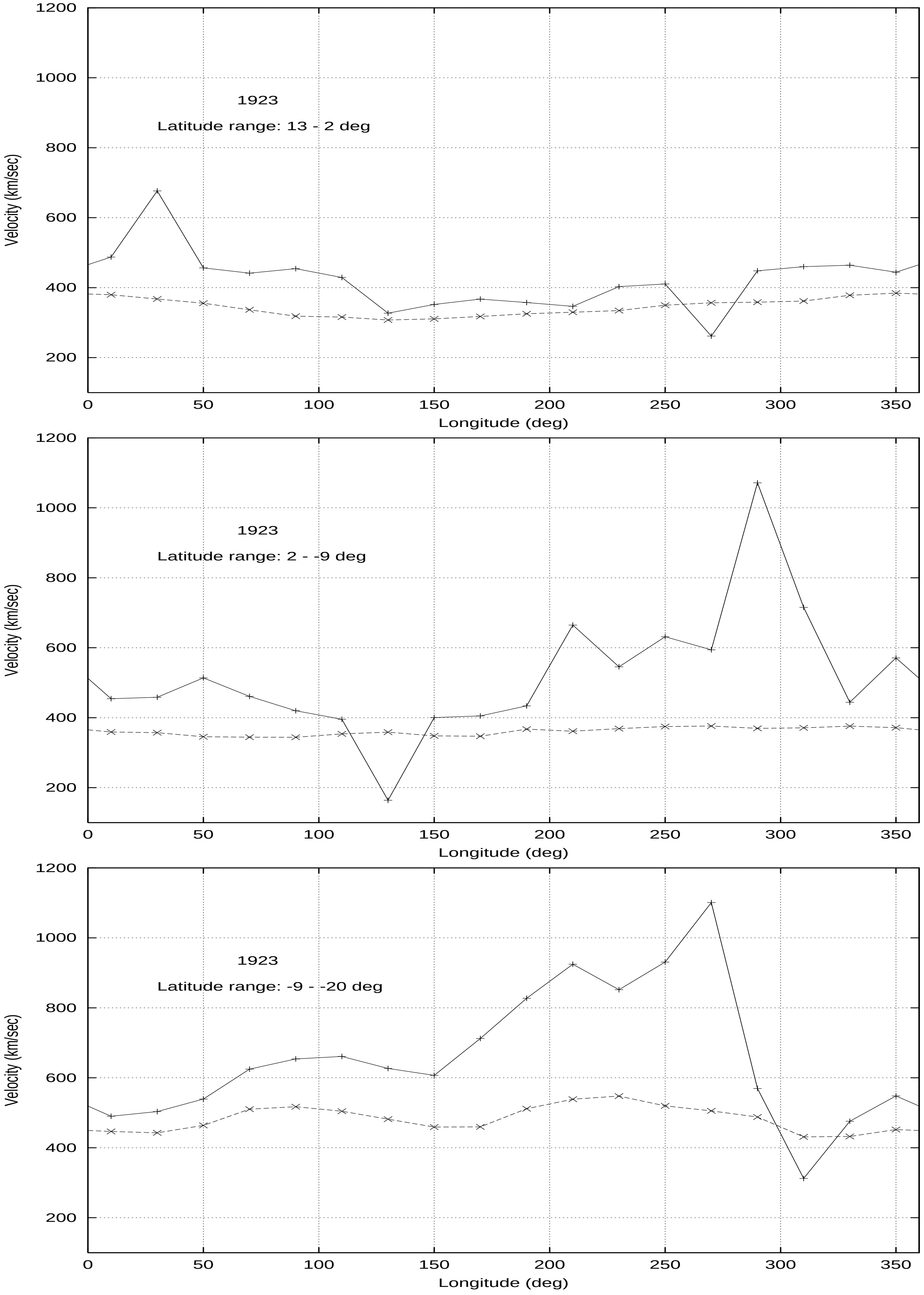

Figure 7.23: **Velocity reconstruction for Carrington rotation 1923** – The figure shows the results of the tomographic reconstruction for velocity for Carrington rotation 1923. The dashed line shows the initial guess for the global χ_G^2 minimisation process and the solid line the final reconstruction arrived at by it.

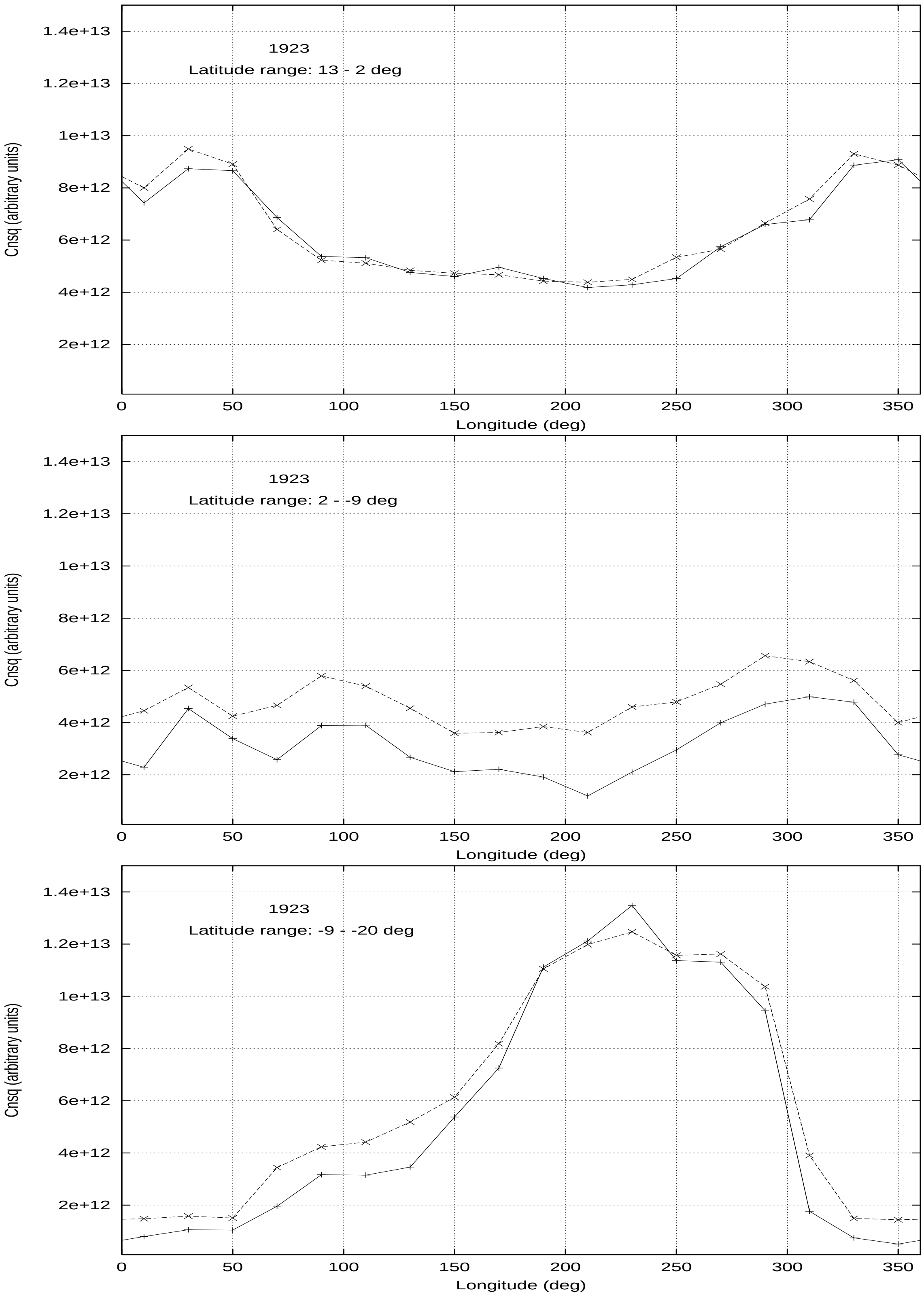

Figure 7.24: C_n^2 **reconstruction for Carrington rotation 1923** – The figure shows the results of the tomographic reconstruction for C_n^2 for Carrington rotation 1923. The dashed line shows the initial guess for the global χ_G^2 minimisation process and the solid line the final reconstruction arrived at by it.

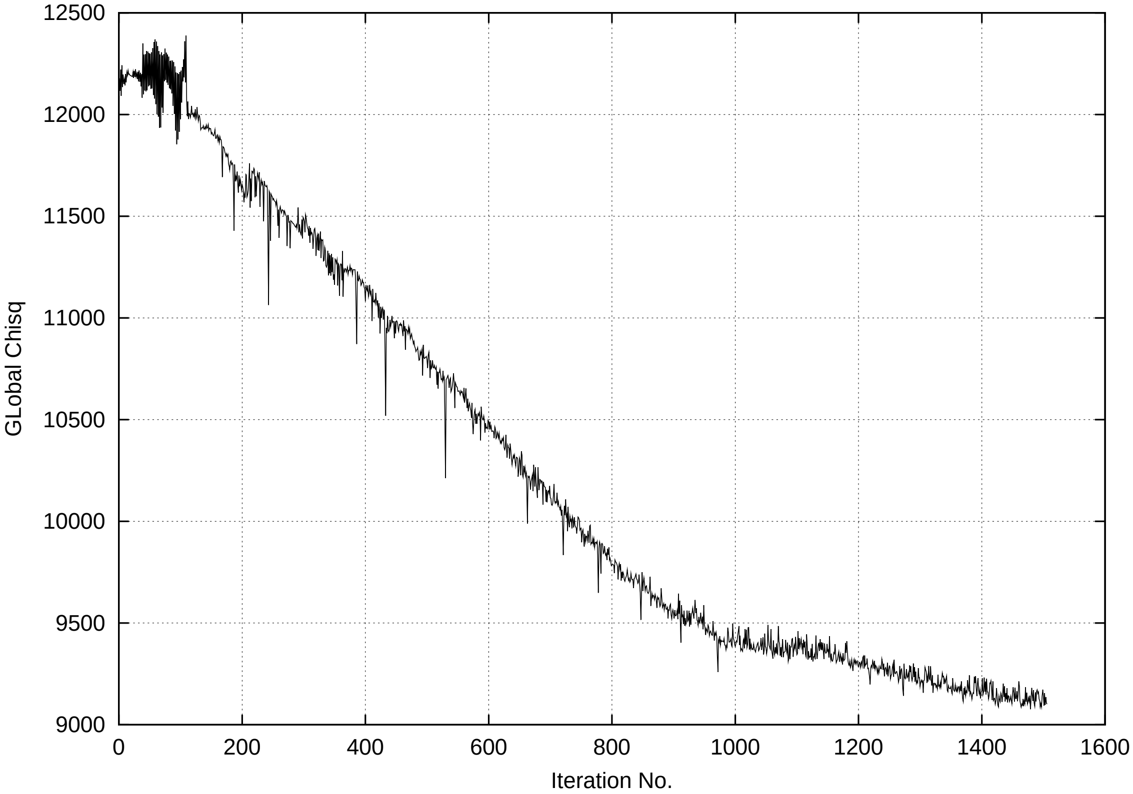

Figure 7.25: **Reduction in χ_G^2 achieved by tomographic reconstruction for Carrington rotation 1923** – The figure shows the decrease in the χ_G^2 as the global χ_G^2 minimisation proceeds. As in Figure 7.8, the first 110 points represent the χ_G^2 for the starting simplex.

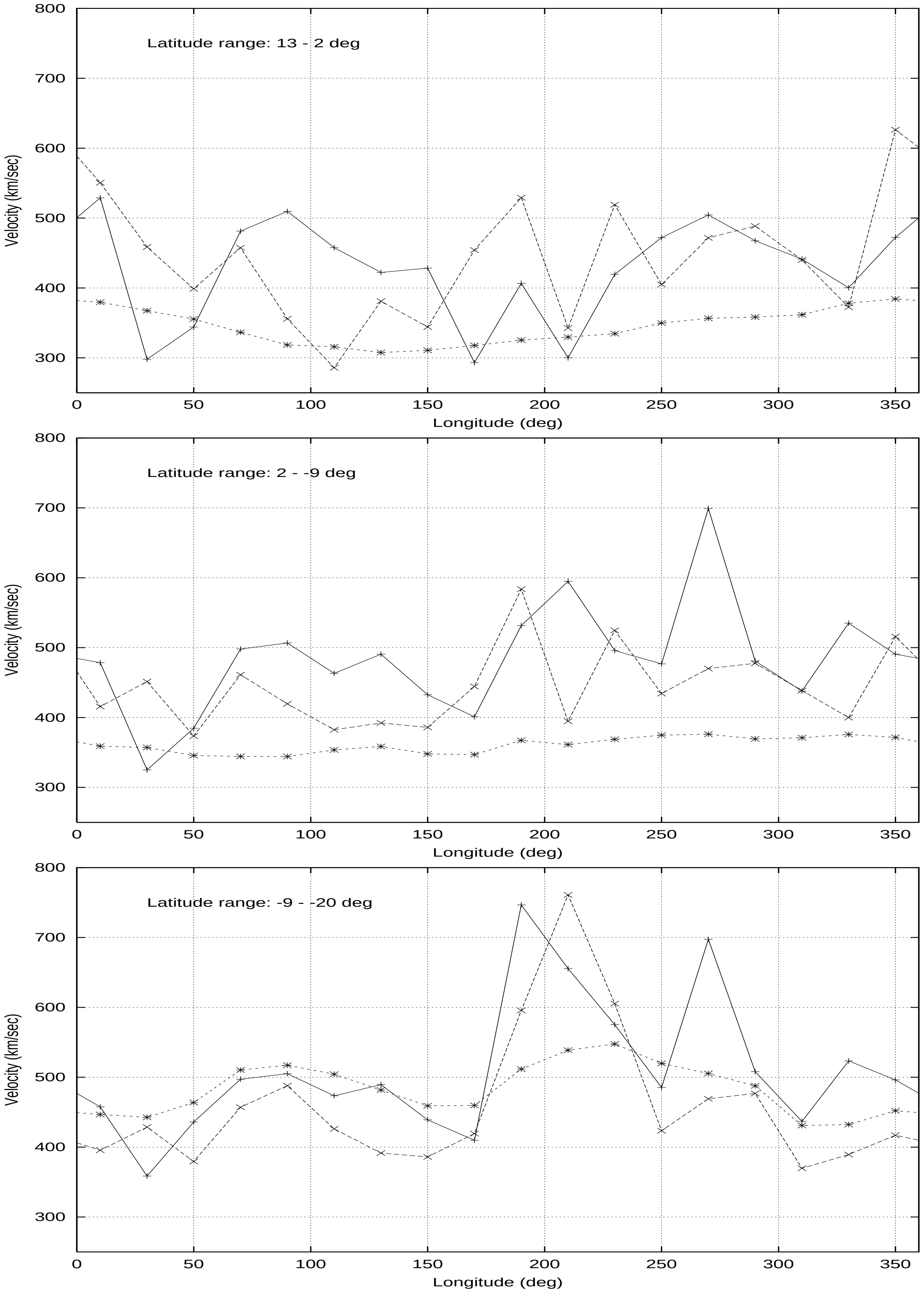

Figure 7.26: **Some more velocity reconstructions for Carrington Rotation 1923** – The solid and the dashed lines show two different tomographic reconstructions for Carrington rotation 1923. The initial guess is shown by the dotted line.

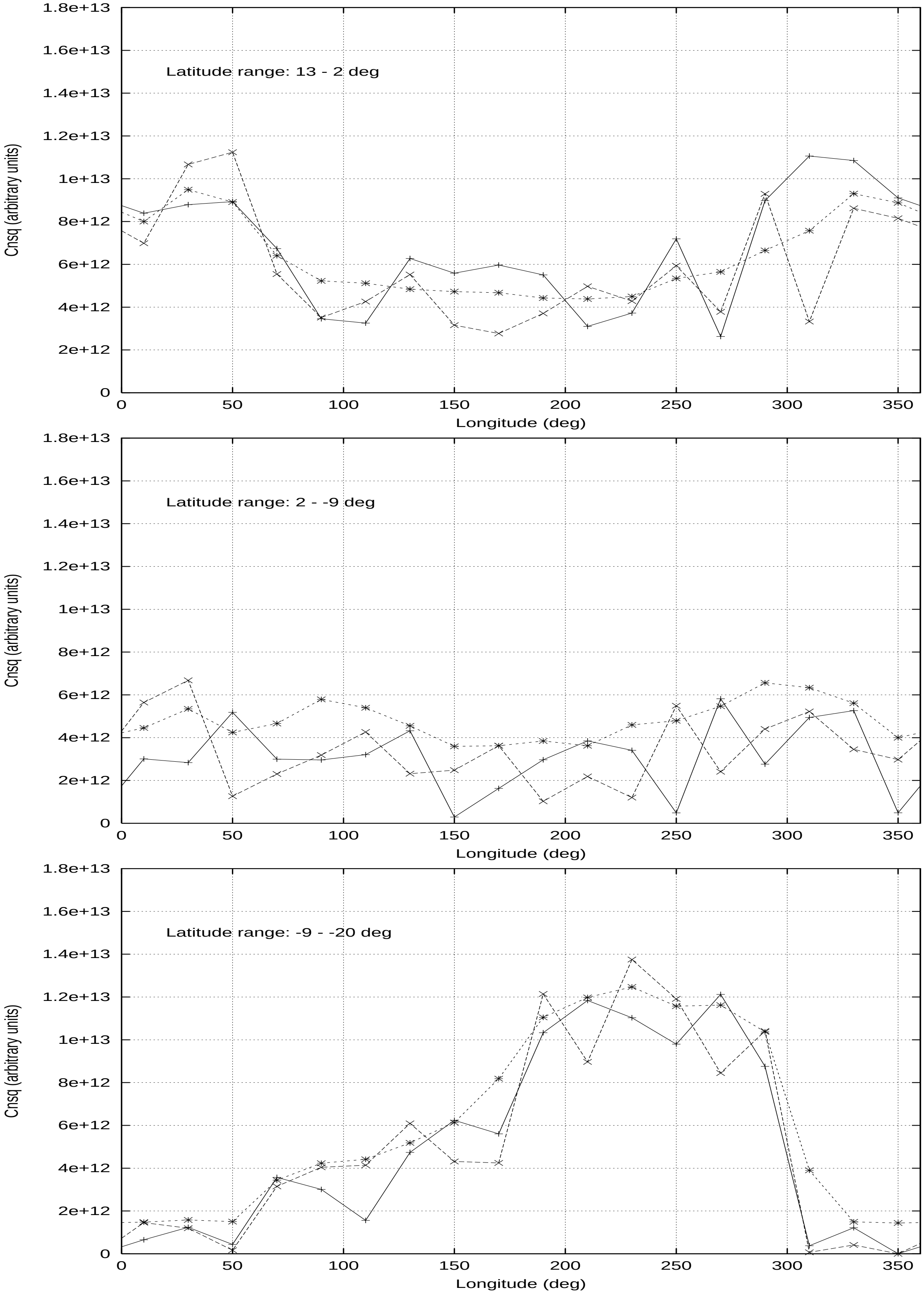

Figure 7.27: **Some more C_n^2 reconstructions for Carrington Rotation 1923** – The solid and the dashed lines show two different tomographic reconstructions for Carrington rotation 1923. The initial guess is shown by the dotted line.

one any more than the other.

The white light coronograph synoptic map for Carrington rotation 1923 from the LASCO instrument on board SOHO spacecraft are shown for comparison with our reconstruction of the heliosphere in figure 7.28. The most prominent features seen in the synoptic maps are the CMEs which correlate very well between the synoptic maps at the three different radial distances ($2.5, 3.0$ and $4.5\ R_\odot$) both on the East and the West limb. There is an enhancement in intensity at roughly the same location as the prominent C_n^2 feature in the bottom latitude bin between 150° and 300°. There is little correspondence between the synoptic maps of the East and the West limbs, except for the feature close to longitude 290° on the East limb and 305° on the West limb. The possibility that the correspondence is due to two CMEs being launched from around the same site spaced by half a solar rotation cannot be ruled out.

The velocity time series measured by the WIND spacecraft projected at the same fiducial surface as the reconstruction is also shown for comparison in figure 7.29. Solar Wind has been assumed to be travelling with a constant radial velocity in order to project the measurements at the radial distance of the fiducial surface. There is a large data gap in the velocity time series from WIND for Carrington rotation 1923 (second panel) in the $\phi_\odot$ range where the most prominent velocity feature in the middle latitude bin occurs. It is difficult to make a case of a correlation between the velocities seen by WIND and the ones arrived at by the tomographic reconstruction.

The velocity and C_n^2 tomographic reconstructions for Carrington rotation 1992 are shown in figures 7.30 and 7.31, respectively and the LASCO white light coronographs synoptic map for the same rotation in figure 7.32. There were 797 observations available for this Carrington rotation and the reconstruction achieved a decrease in χ_G^2 of 23.2 % (from $12,237.5$ to 9396.0) in 3169 iterations. The values of χ_{GN}^2 and χ_U^2 for this rotation are 11.8 and 0.65, respectively. WIND velocity measurements show two well defined peaks in this rotation, the first one in the $\phi_\odot$ range 70°–110° and the other one in 240°–300°. The first of these is associated with an Earth directed CME which was launched from the Sun on the 12^{th} of May 1997. Our velocity reconstruction shows two regions of enhancement in roughly the same locations in the middle latitude bin. The velocity feature at in the 70°–110° $\phi_\odot$ range in also seen in the top latitude bin and is accompanied by a C_n^2 enhancement as well which shows a trace of continuing down to the middle bin. The most prominent feature in the bottom latitude bin is a C_n^2 enhancement which is associated with a low velocity feature. The fact that the reconstruction is able to produce a velocity excess in the same location as the site of the CME leads to the conclusion that the attempts to flag the data which was affected by transients have not been completely successful in removing the effects of this event. As this was an Earth directed CME, it would effect all the $l.o.s.$s in that period and unless we flag all the observations in

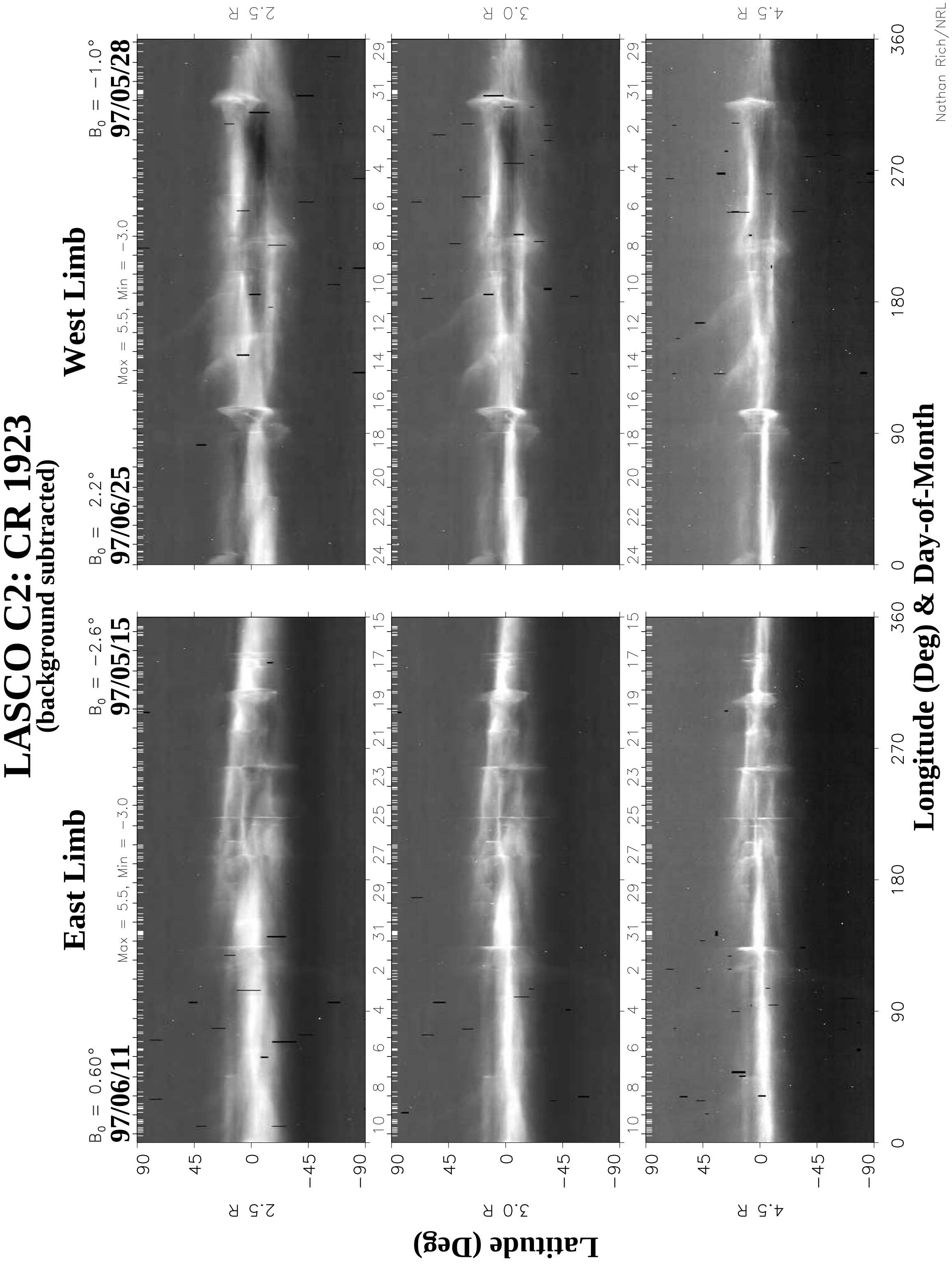

Figure 7.28: **LASCO Synoptic map for Carrington rotation 1923** – The figure shows the background subtracted LASCO Synoptic maps which present the coronal structure at 2.5, 3.0 and 4.5 $R_\odot$ for both the East and the West limb of the Sun for Carrington rotation 1923. The X axis is heliographic longitude and the days of observation which correspond to a given longitude are also mentioned. The Y axis is the heliographic latitude and the grey scale the white light intensity.

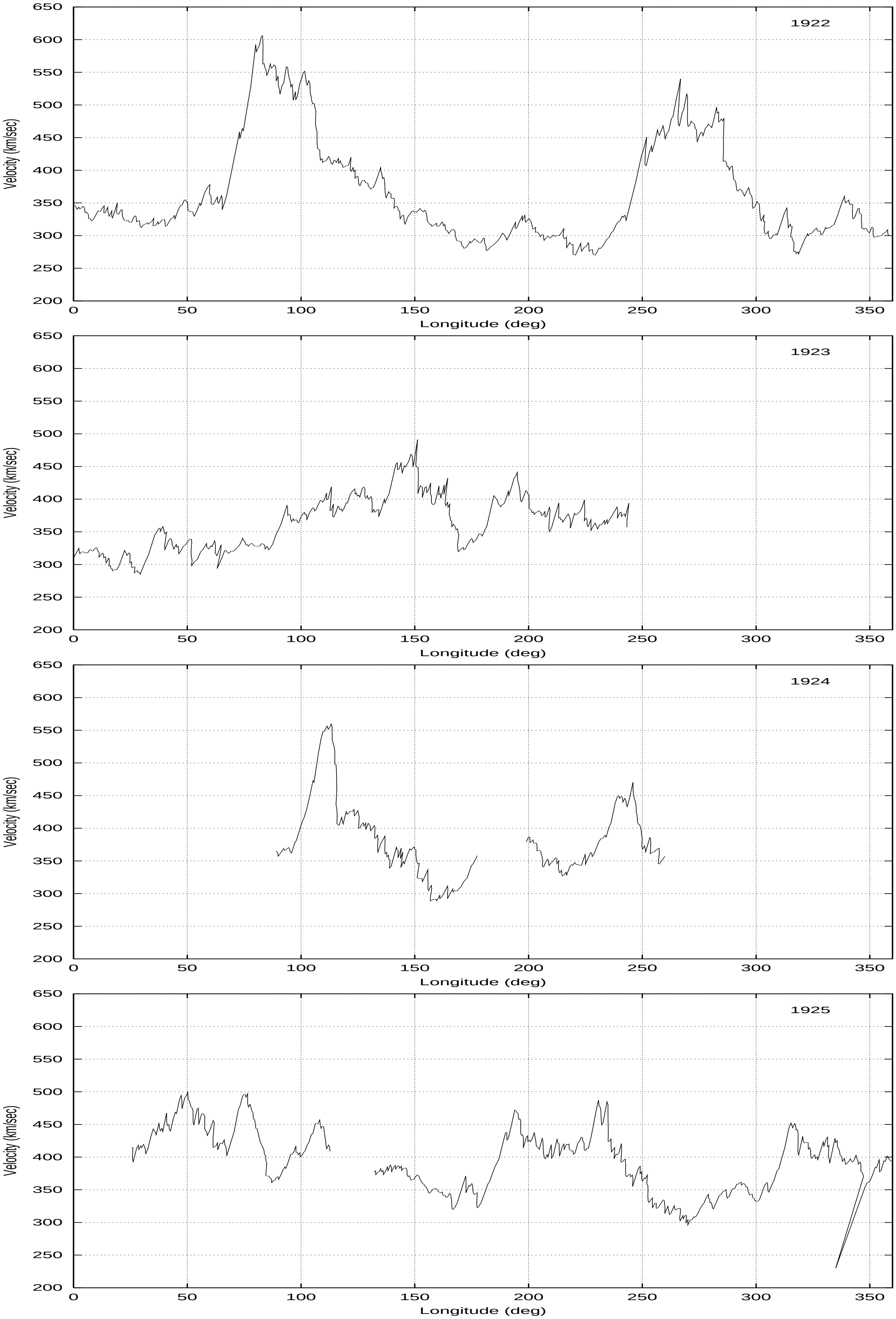

Figure 7.29: **Solar Wind velocity measured by WIND** – The X axis is the Carrington longitude and the Y axis the velocity of the Solar Wind in $km\ sec^{-1}$. The panels show the observations for the Carrington rotations 1992 to 1925, from top to bottom.

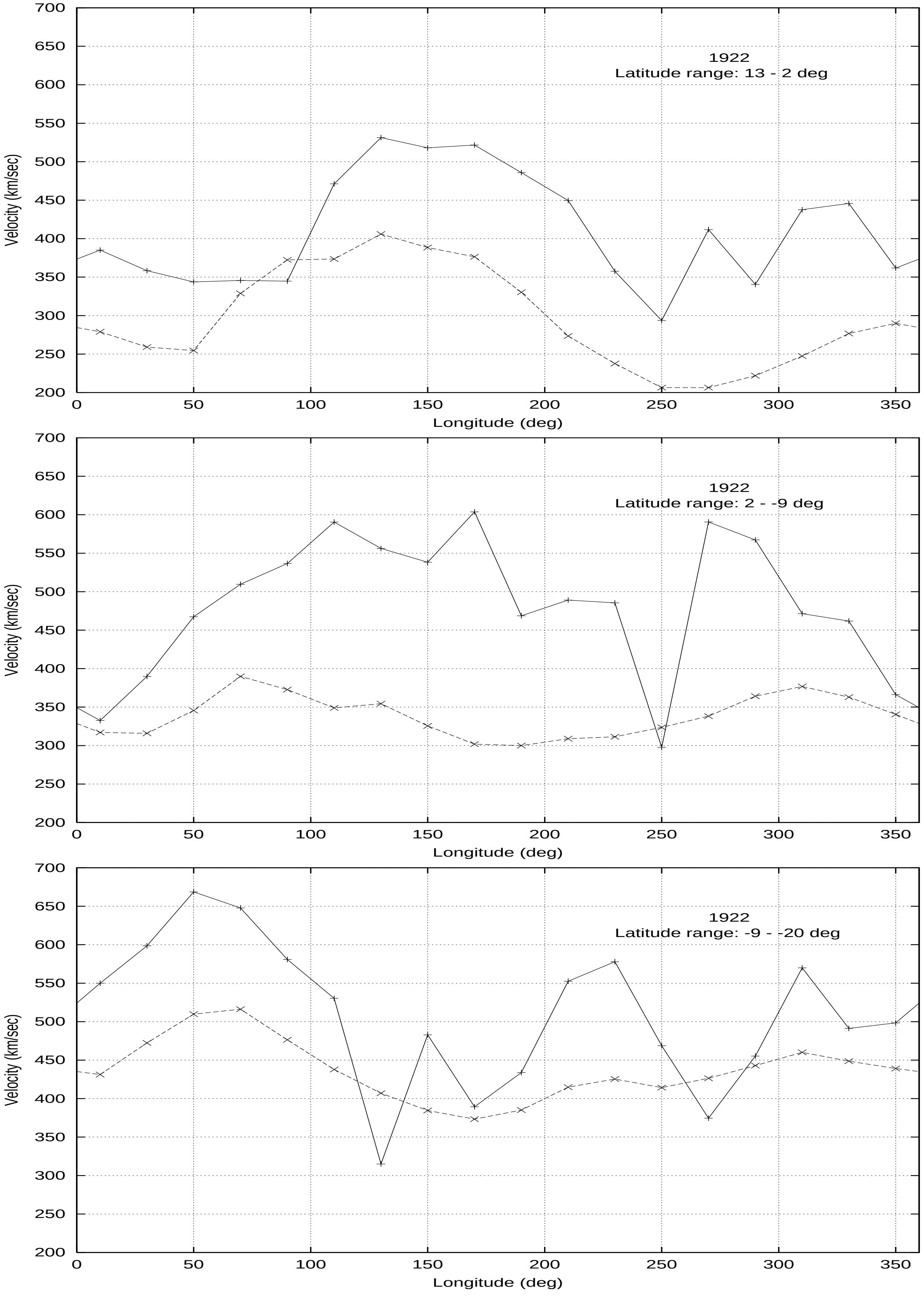

Figure 7.30: **Velocity reconstruction for Carrington rotation 1922** – The figure shows the results of the tomographic reconstruction for velocity for Carrington rotation 1922. The dashed line shows the initial guess for the global χ^2_G minimisation process and the solid line the final reconstruction arrived at by it.

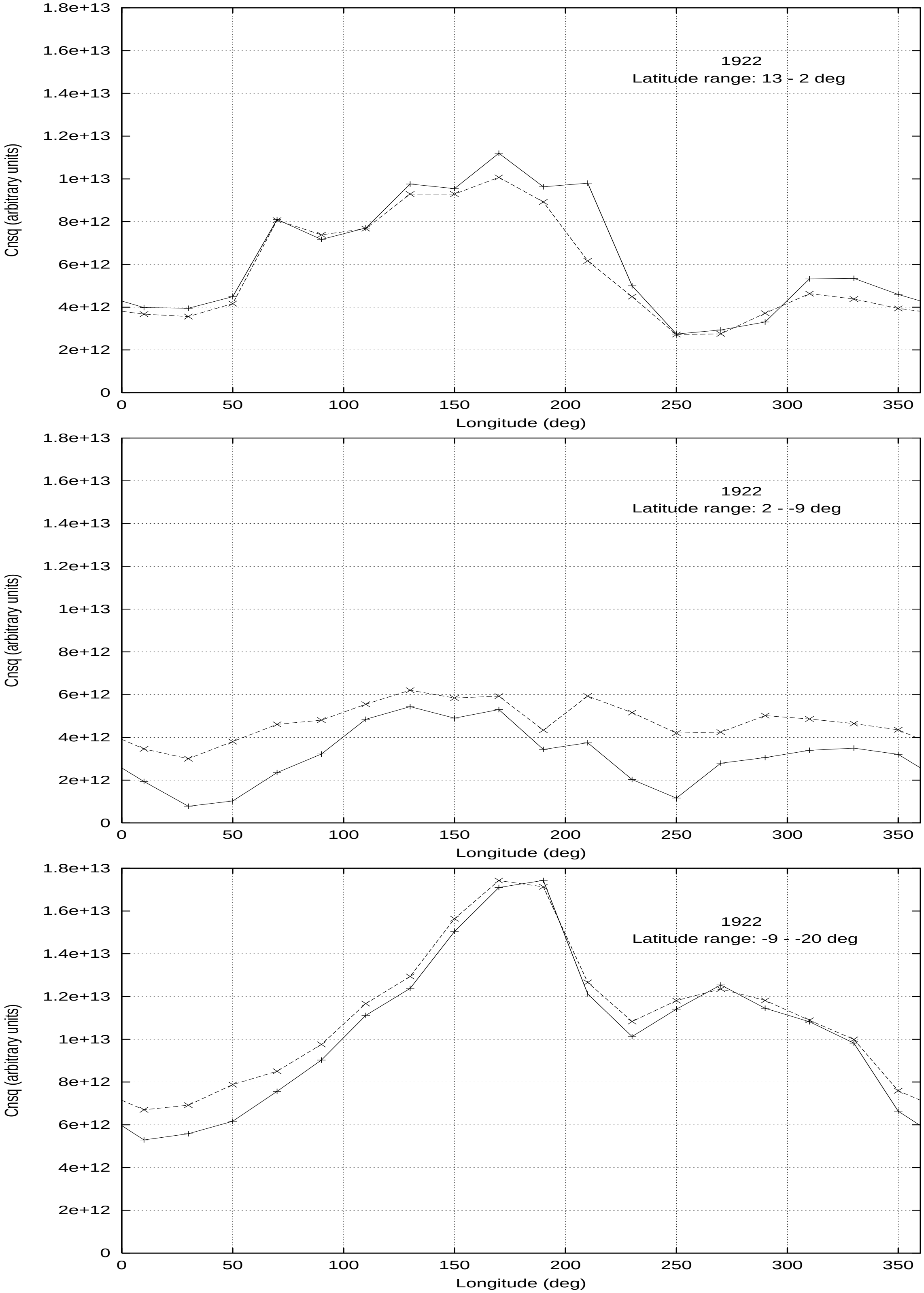

Figure 7.31: C_n^2 **reconstruction for Carrington rotation 1922** – The figure shows the results of the tomographic reconstruction for C_n^2 for Carrington rotation 1922. The dashed line shows the initial guess for the global χ_G^2 minimisation process and the solid line the final reconstruction arrived at by it.

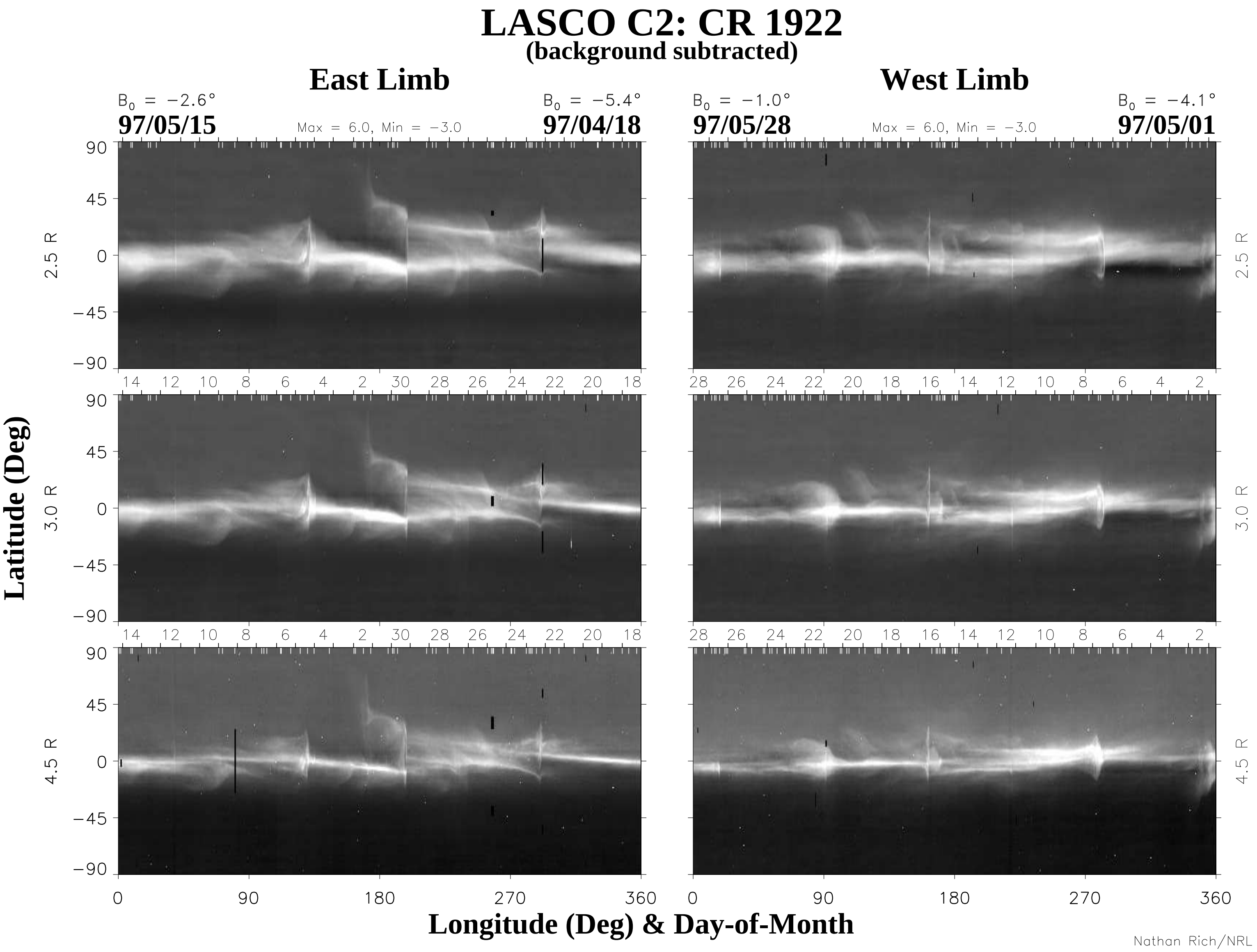

Figure 7.32: **LASCO Synoptic map for Carrington rotation 1922** – The figure shows the LASCO synoptic maps for Carrington rotation 1922 in the same format as Figure 7.28.

that period, the transient affected data cannot be removed. While the *l.o.s.*s which were worst affected by the transient have been flagged, the remaining *l.o.s.*s still retain enough information about it to make it appear in the reconstruction.

The reconstructions for Carrington rotation 1924 are shown in figures 7.33 and 7.34 for velocity and C_n^2 respectively and the corresponding LASCO white light synoptic map in figure 7.35. This rotation made use of 636 *l.o.s.*s and achieved a decrease of 22.7% in χ_G^2 (from $9,512.3$ to $7,348.9$) in 3796 iterations. The values of χ_{GN}^2 for this rotation was 11.6 and that for χ_U^2 was 0.46. The middle latitude bin shows a very strong peak in the $\phi_\odot$ range 50°–100°, associated with a weaker dip in the C_n^2. The magnitude of the peak is so large ($1,800\ km\ sec^{-1}$) that it much more likely to an artifact than a true feature. In addition, if it were real it will be seriously affected by the inability of the Solar Wind model used to incorporate the interaction of the slow and the fast wind. There is no data available from WIND in the corresponding $\phi_\odot$ range but there is a velocity peak of much smaller magnitude close to it. The top latitude bins remains largely featureless in both velocity and C_n^2 while the bottom bin shows velocity bump close at $\phi_\odot$ 210°.

The results of the reconstruction procedure for Carrington rotation 1925 are shown in figures 7.36 and 7.37 for velocity and C_n^2 respectively and figure 7.38 shows the corresponding LASCO white light synoptic map. The reconstruction achieved a reduction in χ_G^2 of 28.9% (from $11,822.9$ to $8,398.6$) in 4563 iterations and had 536 *l.o.s.*s available. The χ_{GN}^2 for this rotation was 15.7 and χ_U^2 was 0.48. The WIND velocity measurements for this rotation do not show any prominent structure, there is a small velocity enhancement in the $\phi_\odot$ range 18°–230° followed by a velocity dip. A somewhat similar feature is seen in the middle latitude bin of the velocity reconstruction arrived at and it seems to continue to the top latitude bin. There is a prominent C_n^2 excess in the top latitude bin in the $\phi_\odot$ range 70°–180°.

In order to give an estimate of the density of the coverage of the solar surface we show the number of *l.o.s.*s passing through each pixel for each of the Carrington rotations in Figure 7.39. They usually lie in the range 50–150.

It should be noted that the nature of measurements provided by the coronograph synoptic maps or satellite plasma measurements is very different from IPS measurements. Though the coronograph synoptic observations cover the entire solar surface, the measurements which contribute to each longitudinal strip come only from two epochs, once when the region is at the East limb and half a rotation later when it is at the West limb and the two are used to construct individual synoptic maps. So synoptic maps are essentially a collage of the projections of the solar corona at the limbs of the Sun on the sky plane, taken at successive epochs during a solar rotation. Each longitude bin in a synoptic map is sampled at one point in time, and therefore is sensitive to day to day variations in the corona. The differences between the local

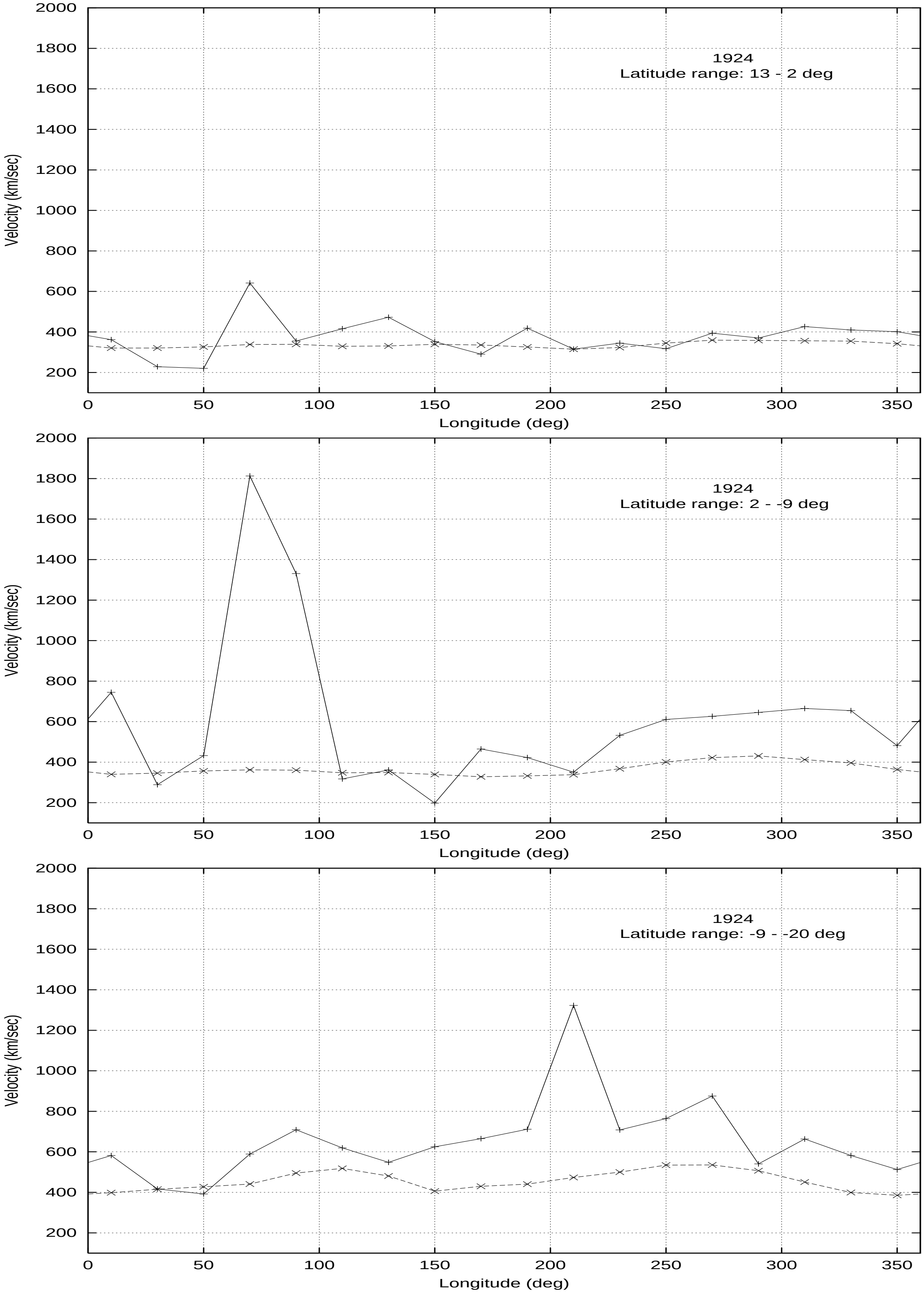

Figure 7.33: **Velocity reconstruction for Carrington rotation 1924** – The figure shows the results of the tomographic reconstruction for velocity for Carrington rotation 1924. The dashed line shows the initial guess for the global χ_G^2 minimisation process and the solid line the final reconstruction arrived at by it.

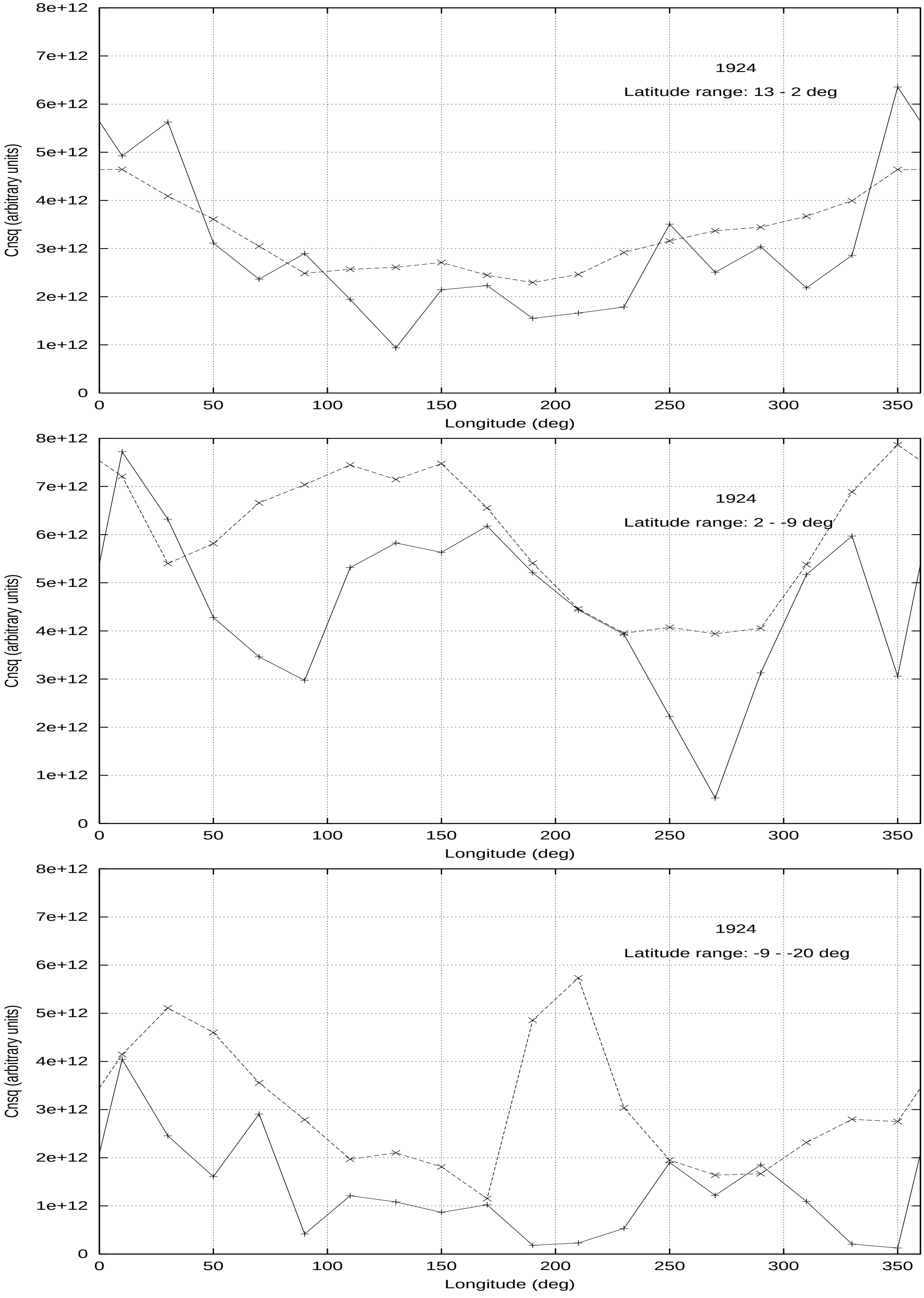

Figure 7.34: C_n^2 **reconstruction for Carrington rotation 1924** – The figure shows the results of the tomographic reconstruction for C_n^2 for Carrington rotation 1924. The dashed line shows the initial guess for the global χ_G^2 minimisation process and the solid line the final reconstruction arrived at by it.

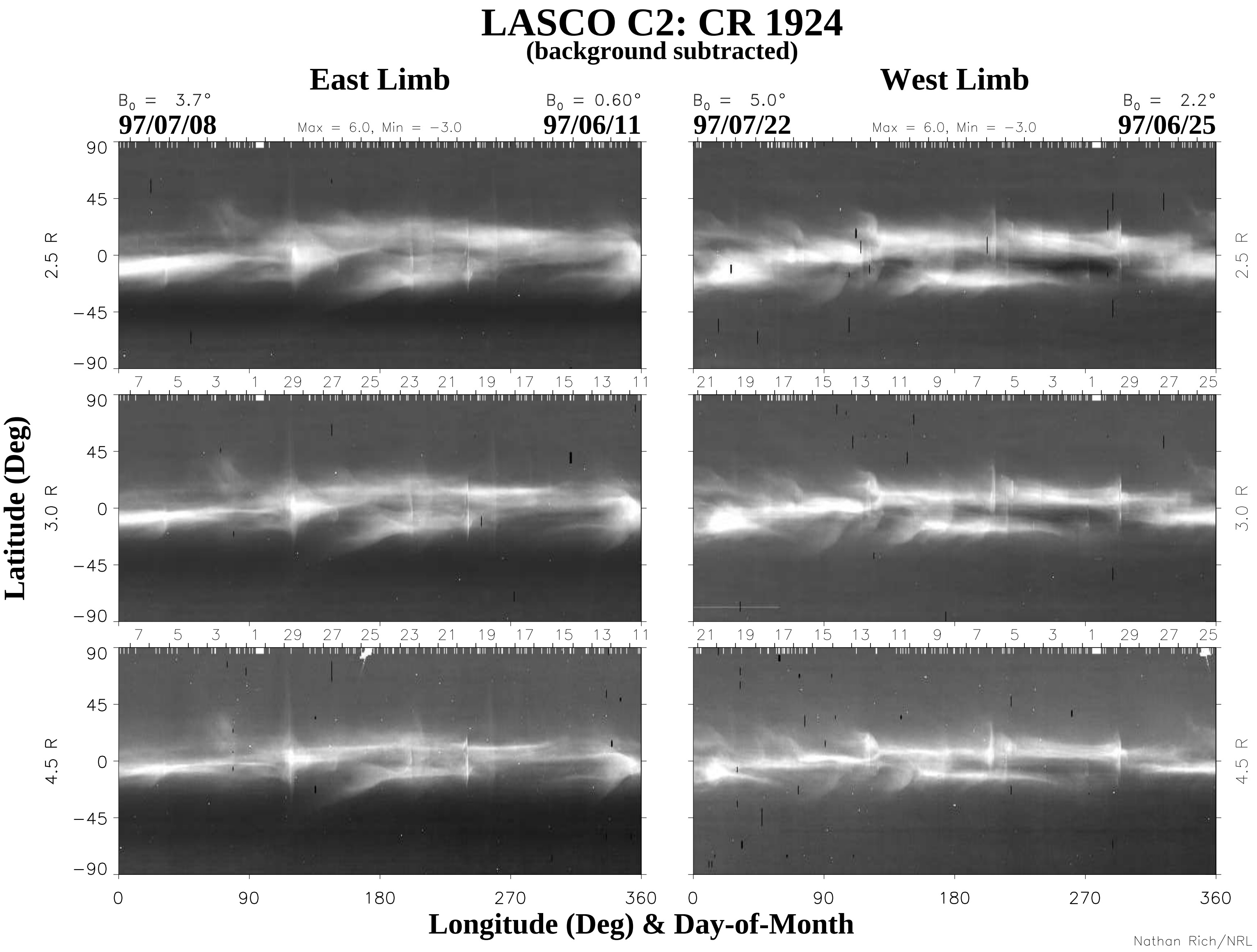

Figure 7.35: **LASCO Synoptic map for Carrington rotation 1924** – The figure shows the LASCO synoptic maps for Carrington rotation 1924 in the same format as Figure 7.28.

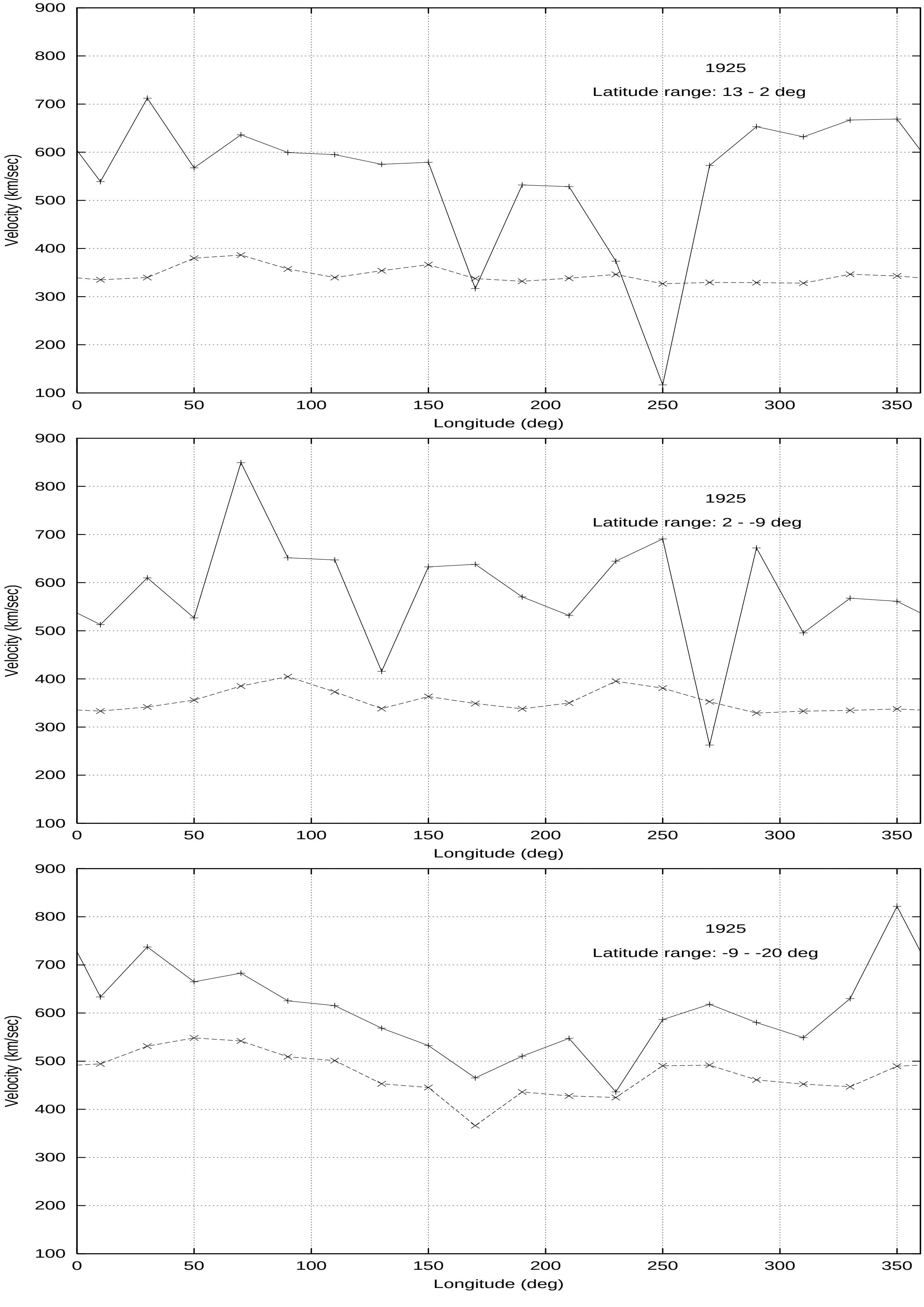

Figure 7.36: **Velocity reconstruction for Carrington rotation 1925** – The figure shows the results of the tomographic reconstruction for velocity for Carrington rotation 1925. The dashed line shows the initial guess for the global χ^2_G minimisation process and the solid line the final reconstruction arrived at by it.

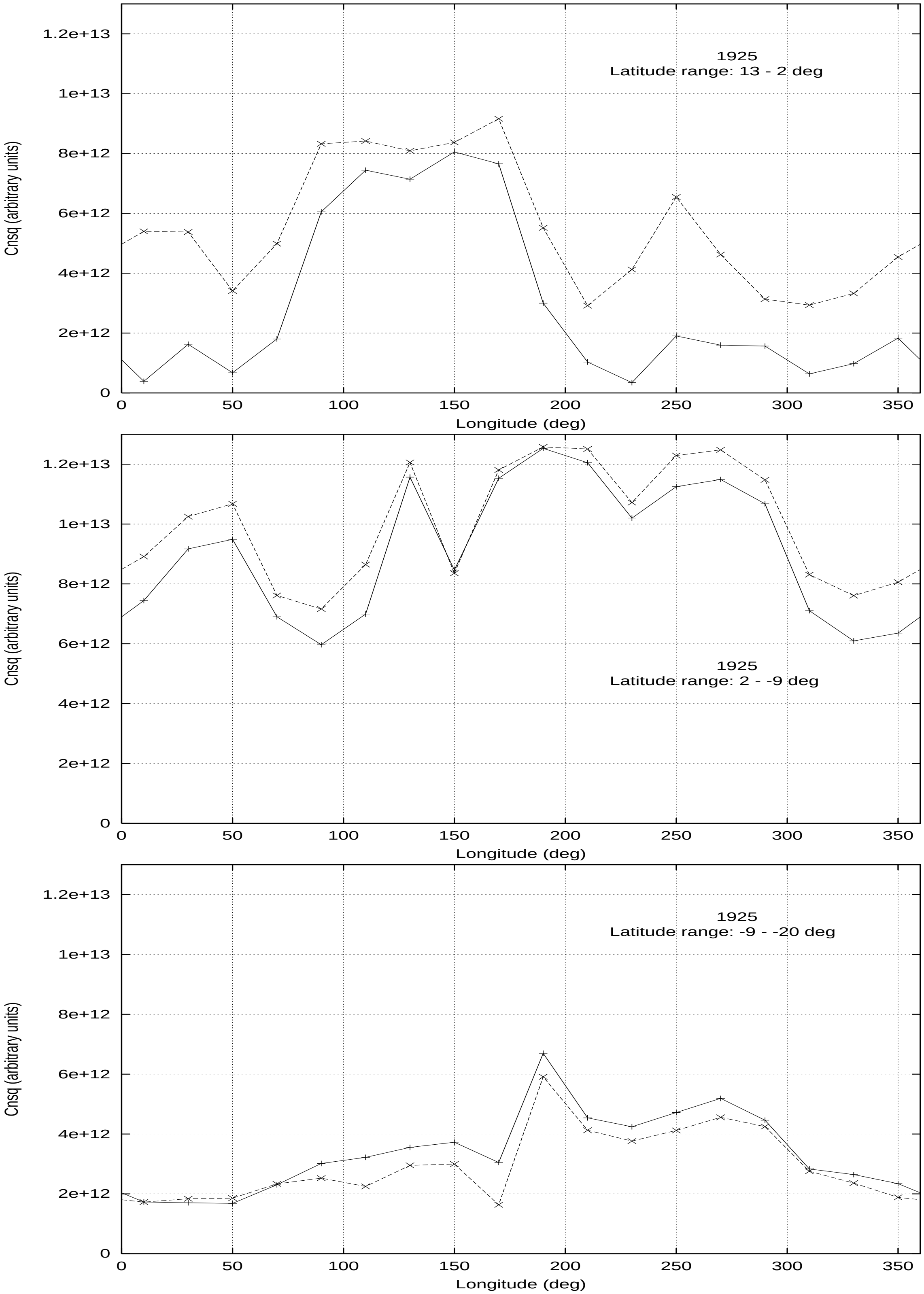

Figure 7.37: C_n^2 **reconstruction for Carrington rotation 1925** – The figure shows the results of the tomographic reconstruction for C_n^2 for Carrington rotation 1925. The dashed line shows the initial guess for the global χ_G^2 minimisation process and the solid line the final reconstruction arrived at by it.

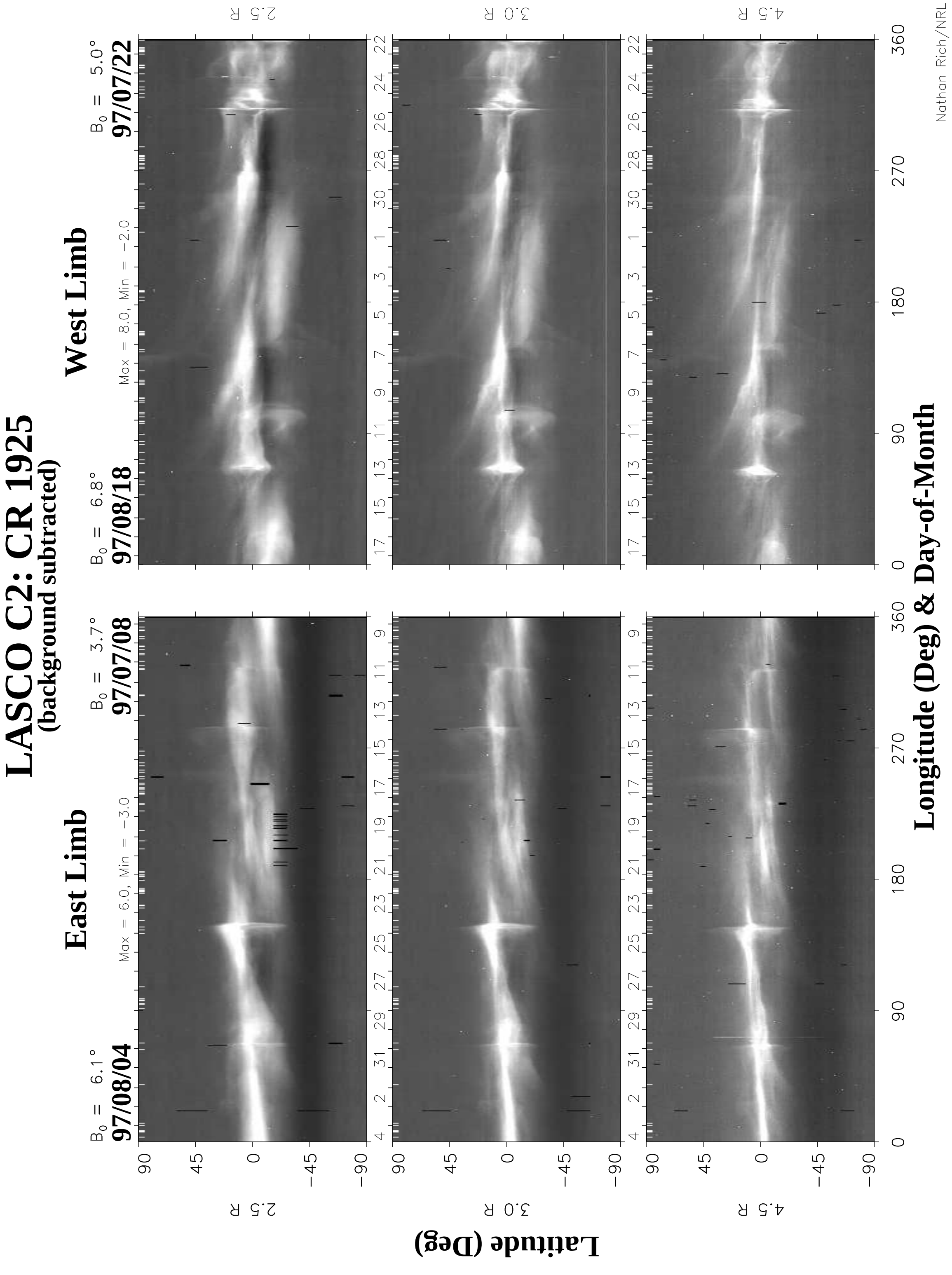

Figure 7.38: **LASCO Synoptic map for Carrington rotation 1925** – The figure shows the LASCO synoptic maps for Carrington rotation 1925 in the same format as Figure 7.28.

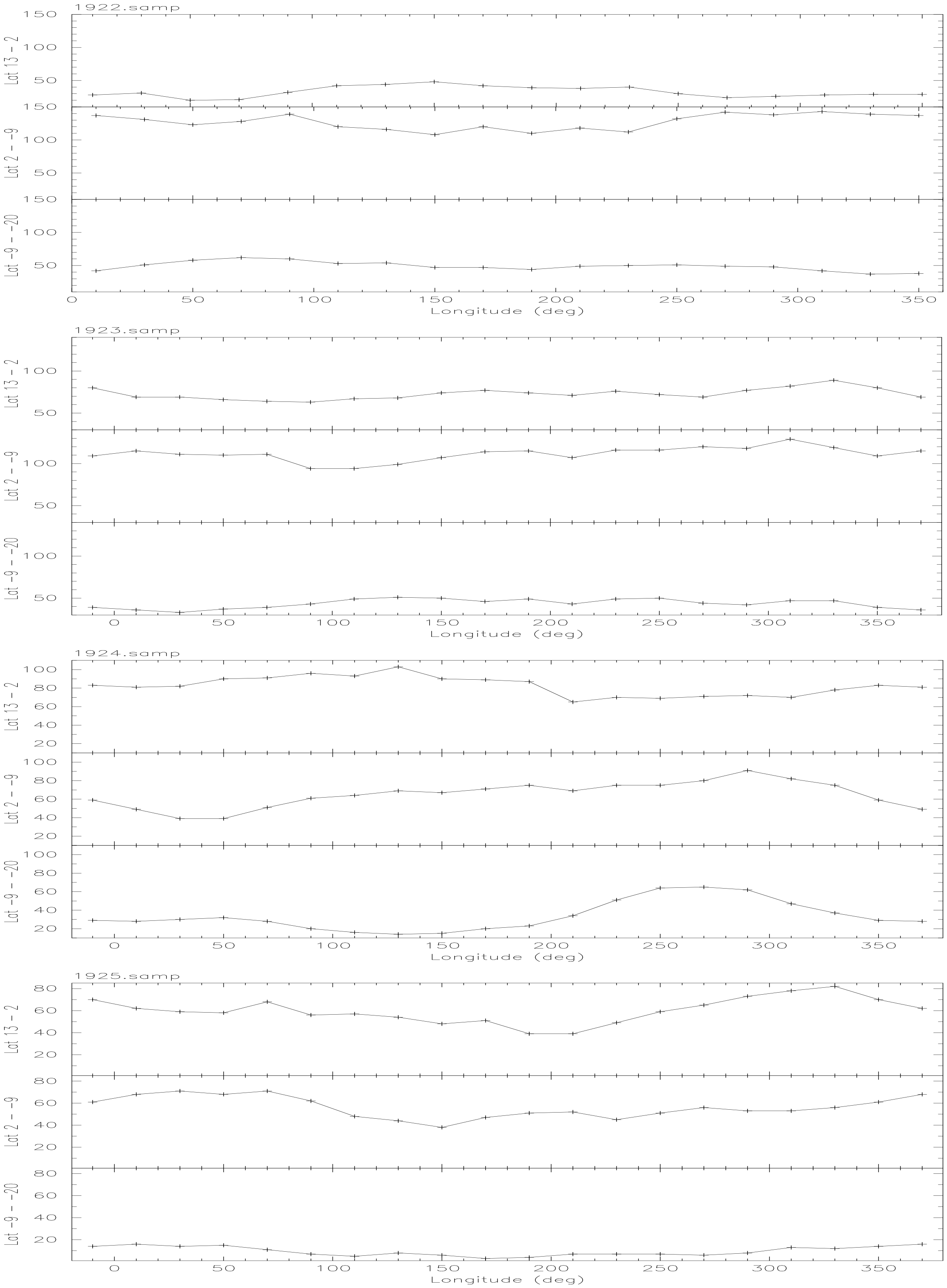

Figure 7.39: **The density of coverage for Carrington rotations 1925–1925** – The figure shows the number of *l.o.s.*s crossing each of the pixels on the fiducial surface for all the Carrington rotations for which the tomographic reconstruction was attempted. The three curves in the first panel correspond to the top, middle and the bottom latitudinal bin from top to bottom for Carrington rotation 1922. The X axis is Carrington longitude and the Y axis the number of *l.o.s.*s which cross a given pixel. The second, the third and the fourth panels correspond to observations for the Carrington rotations 1923, 1924 and 1925, respectively.

nature of satellite sampling and IPS observations have been discussed in sufficient detail in Section 6.6. IPS observations on the other hand, sample a large fraction of the heliosphere at any given time and the fiducial surface constructed using IPS tomography is an average over this large fraction of the heliosphere for the period of a solar rotation. It thus measures a representative average of the entire heliosphere and is not sensitive to the variations due to fluctuations on short time scales.

Some more experiments were performed by taking the reconstruction arrived at by the minimisation, replacing the most prominent feature in the reconstruction by interpolated values on either sides of the feature and using the distribution of Solar Wind properties so obtained as the initial guess for the reconstruction process. If the prominent feature is really required to describe the data, the χ^2 minimisations procedure should be able to put it back in. The prominent feature did not appear in the reconstruction and the entire reconstruction bore little resemblance to the starting model. A similar exercise using simulated data, with one component on an uniform background, where we started from a completely featureless model, was able to pick out the feature required by the data. While the reconstruction, in this case, was not as good as that obtained on starting from the proper initial guess, the feature was unmistakably present. This leads to the conclusion that for real data the, the χ^2 minimisation is much more unstable and the minimisation process needs more 'guidance' and that choice of a good starting guess is important. We had hoped that a larger number of observations which translate into a large number of constraints will lead to more stable reconstructions but it has not turned out to be so.

7.8 Discussion

The inability of our data and analysis to give stable tomographic reconstructions even though the simulations and the earlier attempts were successful was a cause for concern. We have spent considerable amounts of time in trying to understand the poorer stability of the reconstruction. Possible explanations which we consider include the following.

1. The χ^2_G obtained for real data is much much larger than that for simulations (about 1.5 orders of magnitude). This implies that the Solar Wind model arrived at is a much poorer representation of the real data as compared to the simulations. The following causes are expected to contribute to this :

    (a) Significant time variations, during the course of the observations, would lead to large deviations from the average model. Under such circumstances, an average model may be an inadequate or even an inappropriate description of the data. The time variations seen in the Solar Wind span a large range of time scales, from a few hours to many days. The short time scale variations (few hours to a day) are a manifestations of intrinsic fluctuations in the properties of the Solar Wind and usually only a subset of these can be associated with known CMEs. The long time scale changes, on the other hand, are slow variations in the intrinsic, usually large spatial scale, structure of the corona. The short time scale variations can be thought of as random fluctuations superposed on the average model for the distribution of the Solar Wind properties and contribute additive noise to the data. While the simulations have been found to be stable in the presence of zero mean additive noise due to measurement uncertainty, there is no assurance that the noise due to intrinsic fluctuations in the real data has to be zero mean. In fact, as most of the fluctuations show higher values of velocity and C_n^2, we expect the noise due to small time scale fluctuations to be biased towards positive values. The strength of this noise depends on the level of activity on the Sun and can be large enough to cause the average model to have such a large *rms* on it that the concept of an average model no longer remains useful. Slow variations should not be thought of as simply contributing additive noise because the variations due to them are systematic in nature and not stochastic. These variations will also lead the average model to have a large *rms* associated with it. Thus, significant time variations cause considerable departures from the average model which lead to a large value for χ^2_G.

An examination of IPS model fit parameters obtained for *l.o.s.* towards various sources, shown in Figures 5.17 to 5.29, shows the presence of both short and long time scale variations. Time variations seen in the data can either be due to transient events or due to stable co-rotating structures passing through the *l.o.s.* to a source. The variations due to the latter reason do not cause any damage as the analysis procedure maps them back to the proper place on the Sun but the intrinsic variations would render the data-set inconsistent. While co-rotating structures can give rise of variations on the time scales of few days, they are not expected to give rise to short time scale variations, the short term variations seen must necessarily be intrinsic. The plots of IPS model fit parameters of *l.o.s.*s which contribute to a few randomly chosen pixels, for the Carrington rotation 1923, are shown in Figures 7.40–7.42. These plots show a significant amounts of time variations in the uniform Solar Wind model parameters determined for the observed power spectra.

(b) A simplistic model which does not take into account the interaction be-

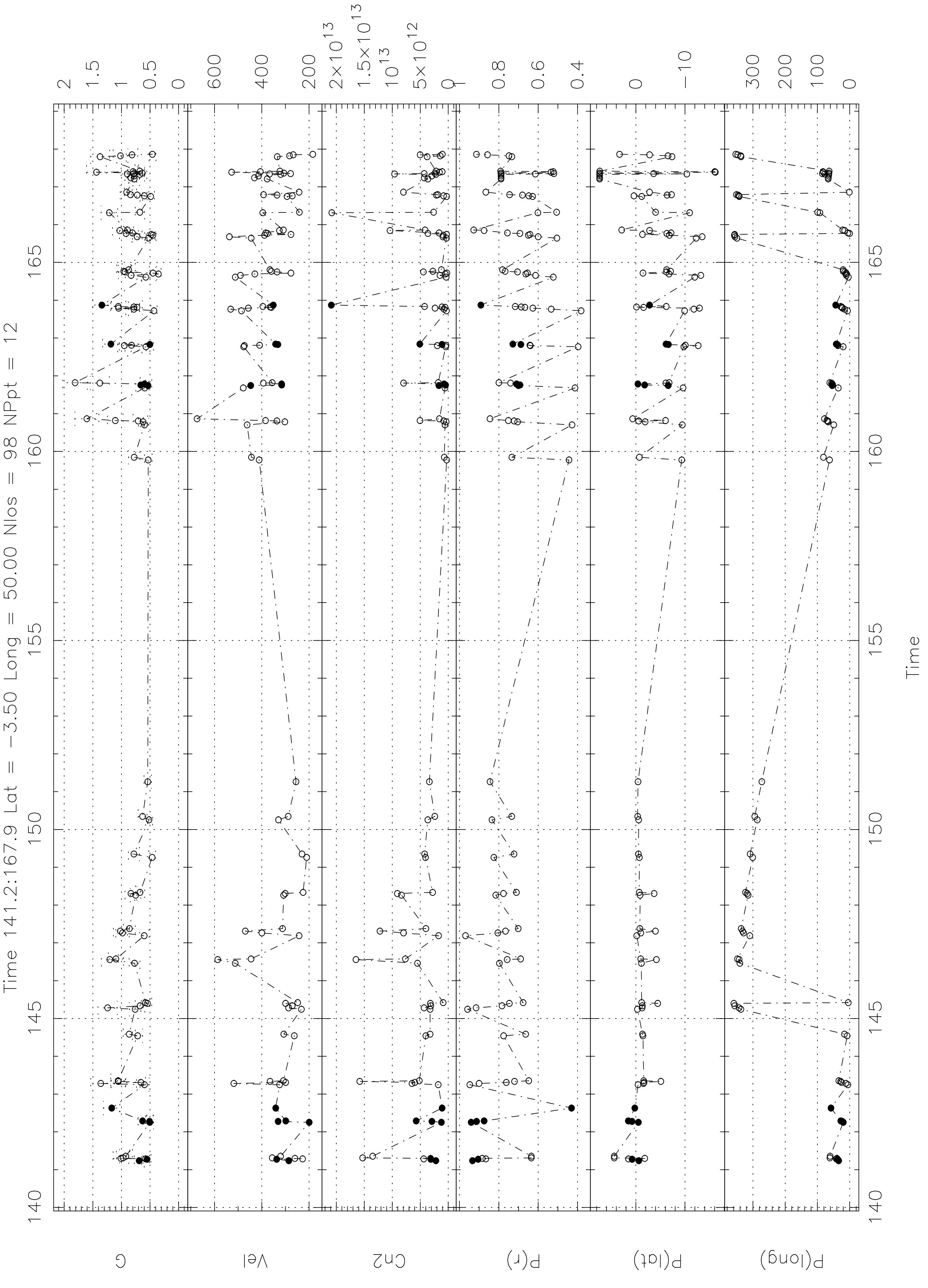

Figure 7.40: **Contributions to a pixel on the fiducial surface – 1** – The figure shows the time series of the uniform Solar Wind parameters estimated for all the *l.o.s.* which pass through the pixel centred at heliographic latitude, $\theta_{\odot}$, of $-3^{\circ}.5$ and a Carrington longitude of 50° in Carrington rotation number 1923. The X axis shows the time (Day of year 1997). The first panel on the Y axis shows the g value, the second and the third the uniform Solar Wind model velocity and C_n^2. The next three panels show the heliographic coordinates of the P-point of the *l.o.s.* to give some information about the geometry of the *l.o.s.*. The *l.o.s.*s whose P-points maps back to this pixel are shown with filled circles while the others are shown with open circles.

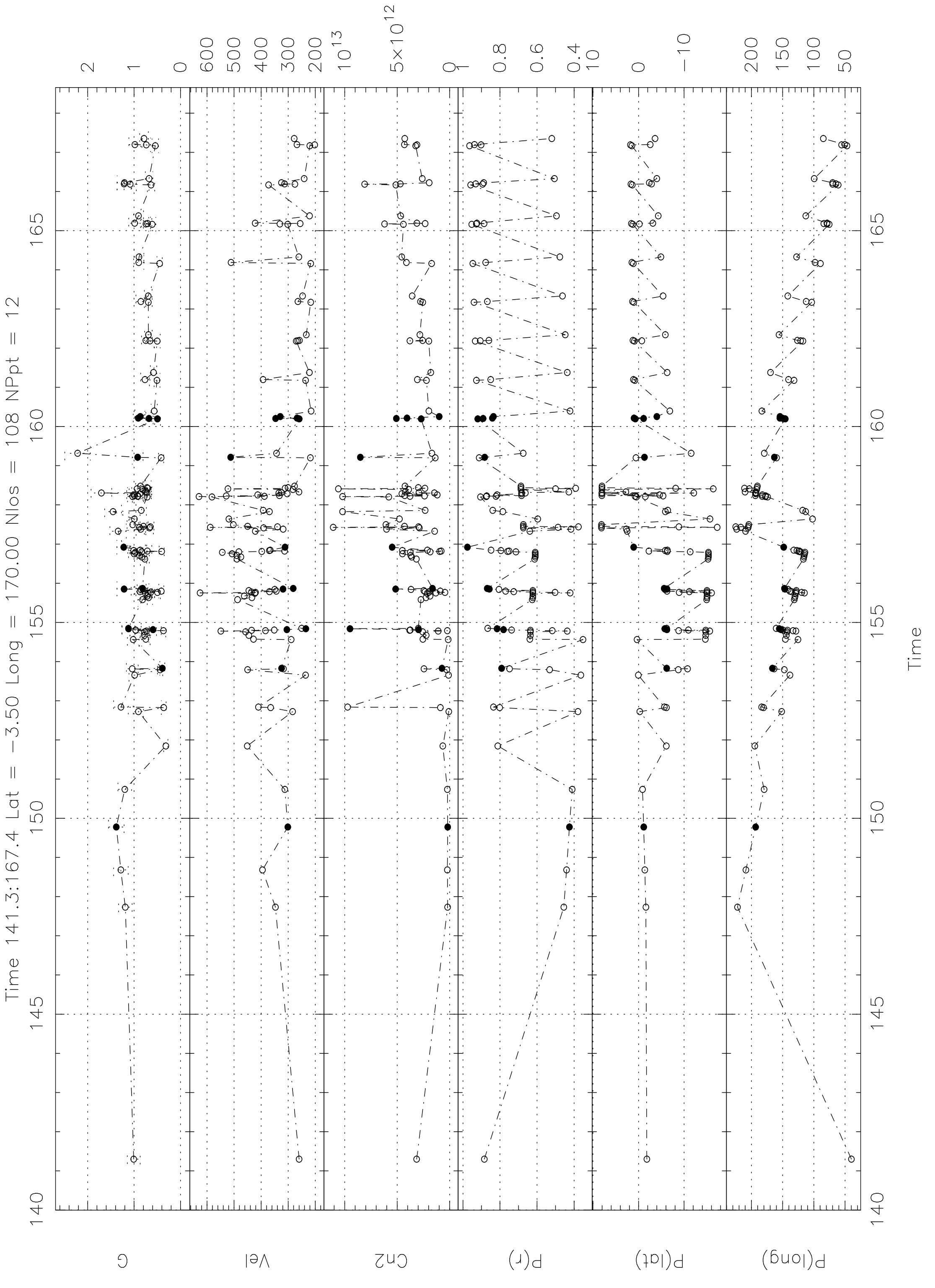

Figure 7.41: **Contributions to a pixel on the fiducial surface – 2** – The figure shows the time series of the uniform Solar Wind parameters estimated for all the *l.o.s.* which pass through the pixel centred at heliographic latitude, $\theta_\odot$, of $-3^\circ.5$ and a Carrington longitude of 170° in Carrington rotation number 1923. The figure is in the same format as Figure 7.40.

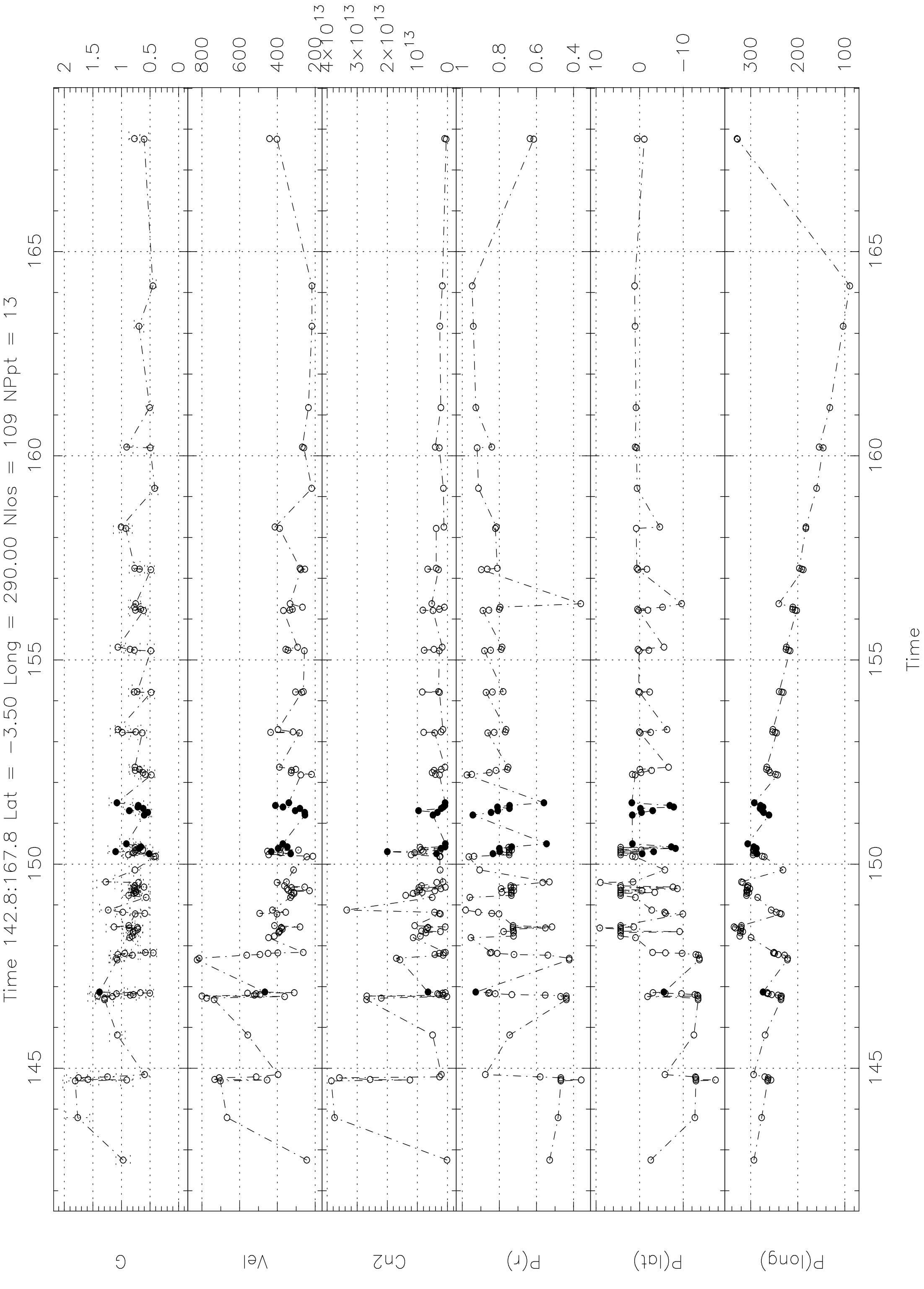

Figure 7.42: **Contributions to a pixel on the fiducial surface – 3** – The figure shows the time series of the uniform Solar Wind parameters estimated for all the *l.o.s.* which pass through the pixel centred at heliographic latitude, $\theta_\odot$, of $-3^\circ.5$ and a Carrington longitude of 290° in Carrington rotation number 1923. The figure is in the same format as Figure 7.40.

tween the slow and the fast Solar Wind has been used and the Solar Wind velocities have been assumed to be purely radial and constant as a function of heliocentric distance. This inadequacies of the model can reflect as an increase in the χ_G^2.

   (c) There is significant latitudinal structure in the data on length scales smaller than the model resolution. This lack of resolution will also add to the χ_G^2 obtained.

2. The minimisation converges to the same correct model for the simulations using different starting simplexes but it does not do so for the real data. The simulated data was manufactured to satisfy the time stationarity assumption made by the reconstruction process and used the same prescription for propagation of the Solar Wind as the reconstruction process. Different runs of the minimisation process on the real data using different starting simplexes converged to different models which had comparable χ_G^2 but few similarities. This is indicative of the fact that χ_G^2 hypersurface, in the model parameter phase space, has numerous valleys of similar depth. We can try to understand the χ_G^2 landscape in terms of the following scenario. If there were no time variations in the Solar Wind, and in the hypothetical case of infinite signal to noise measurements with infinite resolution, the average model for the Solar Wind would be a perfect description of the data-set. Extrapolating our conclusions drawn from simulations using rather simple models, we expect, the χ_G^2 landscape to have a well defined global minima in such situations. Of course, any real life data-set has a finite S/N and resolution and therefore there will be some contributions to χ_G^2 due to coarseness of the resolution and measurement uncertainties. These contribution to χ_G^2 add to the ideal χ_G^2 landscape filling in the minima and making the smooth variations in the χ_G^2 landscape noisy. From our simulations, we do not expect this effect to be large enough to seriously affect the reconstruction process. The presence of short time scale variations contributes an independent non-zero mean additive noise, an estimate for the amplitude of which is not easily available. This will distort the features in the χ_G^2 landscape and if its amplitude is large enough, it may even mask the original features in the χ_G^2 landscape for the ideal invariant Solar Wind model. The slow variations in the Solar Wind provide yet another additive piece to the χ_G^2 which is not expected to have noise like characteristics as it arises because of systematic variations and is not assured to be zero mean either. If the slow variations are significant, this piece will have a large amplitude and can also distort and maybe mask the features in the ideal χ_G^2 landscape. Our minimisation process sees a χ_G^2 which is a sum of all these contributions and therefore is effected by all the issues discussed above. A cut across the expected χ_G^2 landscape for the real observations is shown schemat-

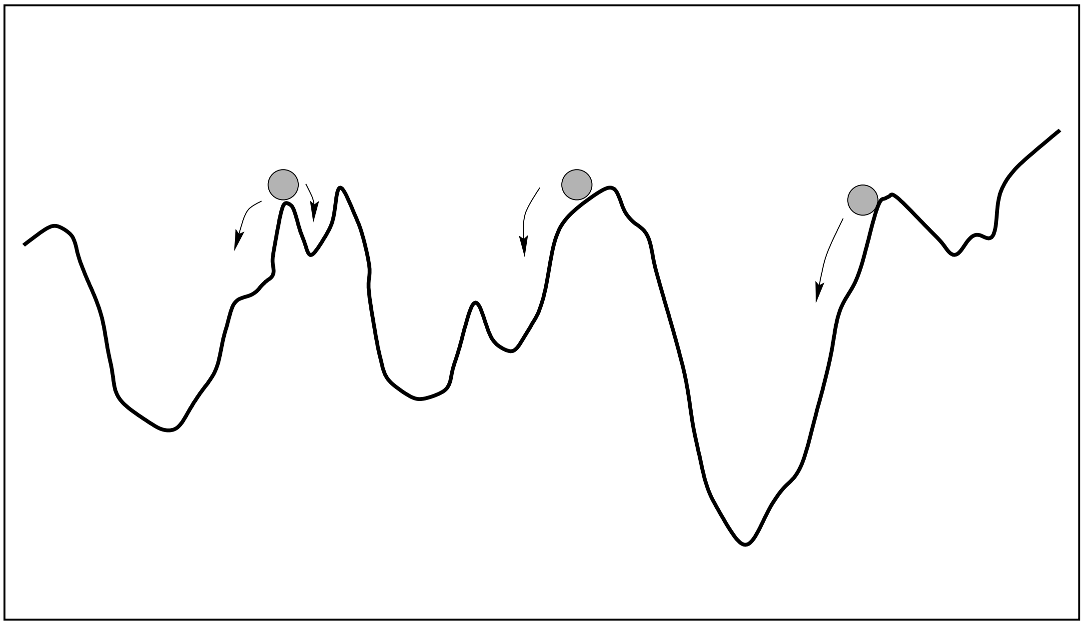

Figure 7.43: χ^2_G **landscape** – A schematic illustration of a cut across the χ^2_G landscape is shown. The different initial guesses are represented by filled circles. A multiplicity of valleys of similar depths causes different initial guesses to climb down into different valleys leading to non-unique solutions.

ically in figure 7.43. The simplex descends into the minima it happens to wander into and different starting simplexes descend into different χ^2_G valleys. There are, thus, fundamental differences in the χ^2_G hypersurface corresponding to the simulated data and the real data and the apparent lack of stability in the tomographic reconstruction is due to the existence of a multiplicity of local χ^2_G valleys.

3. Due to constraints of time and computing resources, we have used a termination criterion to stop the minimisation process if the fractional decrease in the χ^2_G over a cycle of the minimisation process falls below 1%. It is worth noting that most often, the minimisation procedure was stopped before it reached the termination criterion for simulations, as the progressive decrease in χ^2_G was very shallow, but it always hit the termination criterion in minimisations runs using real data. The trend for decrease of χ^2_G was present in almost all the minimisations runs using the real data even when the termination criterion was reached. This raises the possibility that had the minimisation process been allowed to continue it would have improved upon the model and the differences between different reconstructions might have become smaller. In the most optimistic case, different starting simplex could have been trying to reach the same global valley from different paths and because the minimisa-

tion process was terminated early, the different starting simplexes have led to different looking reconstructions, though we believe this to be quite unlikely.

4. It was noticed that often the final model had a jaggered or saw-tooth like appearance. This pattern develops slowly from the smooth initial model and keeps on getting more pronounced as the minimisation proceeds. This may be interpreted to mean that the χ^2 minimisation is not sensitive to these oscillations, or they are *invisible* to it. In this sense, it implies that the degrees of freedom of the model are ill constrained or are larger in number than are required by the data. In order to test this, the reconstruction procedure was repeated with the same data-set but with the number of degrees of freedom of the model reduced to half by reducing the resolution of the reconstruction. The resultant model still showed the saw-tooth like patterns. This is in contrast to the expectations from the simulations (model E1), which had shown that the middle latitude bin has sufficient resolution to discern the presence of features three pixels apart.

   There are some issues about different observations qualifying as independent constraint. Different observations of the same source in rapid succession are independent only in the sense that the noise on them is uncorrelated, they do not convey any independent information about the Solar Wind they sample. How different should the *l.o.s.*s be in order to qualify as independent constraints is a question which has not been addressed. As this work has assumed all the observations to be valid independent constraints, the number of constraints may have been overestimated. In the present data-set the latitude range corresponding to the middle pixel is the most densely sampled by the *l.o.s.* (Figure 7.39) and we believe that it is quite unlikely that even in this range the model is ill constrained.

7.9 Comparison with others similar exercises

Apart from the early *g*-maps from Cambridge group (Tappin et al., 1983, 1984; Hewish, 1990), the first systematic attempt at making tomographic reconstruction was presented in a series of papers by the groups at University of California, La-Jolla, USA (UCSD group) and Solar-Terrestrial Environment Laboratory, Nagoya University, Japan (STELab group) (Jackson et al., 1998; Kojima et al., 1998; Asai et al., 1998). In the first of these papers the authors use 81.5 MHz scintillation index (g) measurements along with three-four station IPS velocity measurements of the STELab group to make a composite picture of the distribution of the velocity and density on the Sun for the observing period June 1994 to September 1994 (Carrington rotations 1884 to 1886). They had $\sim$ 5000 measurements of g and $\sim$ 600 measurements of velocity per Carrington rotation. The authors used the measured g values and the velocity estimates from the four station observations as inputs to constrain the reconstruction process. The velocity and g values were projected back to the Sun to generate an initial model using a procedure similar to the one used by us. The initial model of velocity and density distribution on a fiducial surface was modified iteratively to reduce the difference between the observed quantities (velocity and density) and the model prediction. They assume radial velocities for the Solar Wind and the interaction between the fast and the slow wind is approximated by merging together the Archimedean spirals when they tend to intersect and applying conservation of mass and momentum. The next two papers describe the attempts of STELab group at tomographic reconstruction of the Solar Wind properties using the STELab three-four station velocity measurements alone. As they do not have any independent information of n_e (m or g observations), they use an empirical power law relation between δn_e and velocity ($\delta n_e(z) = v^{\gamma}(z)$ with $\gamma = 0.5$). This relationship was noticed by Kakinuma et. al (Kakinuma et al., 1982) and the last in the series of these papers provides additional confirmation for this relationship. These authors use a Solar Wind model with constant radial velocities. Their analysis covers the Carrington rotation periods 1988-1901 and the observations from all the three Carrington rotations are put together to make a single reconstruction.

In both these works a basic assumption which is made is that velocity and C_n^2, either from the single station power spectra fitting or from three-four station cross-correlation analysis, are a weighted mean of these quantities along the *l.o.s.* with a weight factor that can be calculated from the known distribution of C_n^2 along the *l.o.s.* and the Fresnel filter. While the assumption is true for relating C_n^2 with observed scintillation index, we have serious reservations in using such an assumption for the velocity. The effect of a non-uniform velocity distribution along a *l.o.s.* is to distort the shape of the power spectrum and equivalently the cross-correlation function (CCF) between two stations. Using this distorted CCF or power spectrum to estimate the velocity is fraught with unspecifiable systematic errors. The situation is clearly visualised is we consider a *l.o.s.* sampling two different velocity streams of comparable C_n^2. The spectrum shows a two stream structure which is not rare and can be fitted with either of the velocities or a sum of the two kind of spectra. By forcing the entire spectrum to be fitted with a single uniform Solar Wind model spectrum generally gives an unsatisfactory fit since we are fitting power spectra with Solar Wind models whose intrinsic shapes are different. While the velocity of the best fit spectrum usually lies between the two velocities, it is by no means clear that the fitted velocity is a weighted average of the velocity distribution along the *l.o.s.* with the *l.o.s.* weighting function appropriate for IPS. A similar situation holds for two or more station observations of the CCF. The effect of the two streams with different velocities is to distort the shape of the CCF and produce two peaks in it. The information of velocity distribution along the *l.o.s.* is in the shape of the CCF and can be retrieved by trying to model the shape of the CCF, as has been demonstrated by Grall et. al (Grall et al., 1996; Grall et al., 1995). Fitting a single velocity to the observed CCF by estimating a time delay, using a peak or the mid point at half the peak value, looses this information and yields a number which is very difficult to interpret as being a weighted mean of the velocity along the *l.o.s.*.

For this reason, we have preferred to use the actual measured power spectra as the constraints for the tomographic reconstruction procedure. While this is attractive in view of mathematical rigour, we were aware that this makes the problem much more complex since now instead of fitting two numbers per observation, this requires us to model the entire power spectrum and reproduce its magnitude and shape. Since the approach we have taken has never been demonstrated before, we carried out simulations to verify the viability of this approach. We were encouraged by the reasonable success shown by the simulations but were not satisfied with the reconstructions using real data. This raises questions about the apparent success of the earlier methods. For reasons given below we feel that the earlier attempts were more akin to our initial guess and formalism did not allow the model to deviate much from the initial guess.

Another major difference between the earlier attempts and ours is the number of constraints in the reconstruction. The reconstruction by Jackson et. al used ~ 600 velocity measurements and ~ 5000 g measurements and they attempted a reconstruction of velocity and density over the entire solar surface with a resolution of $10^\circ \times 10^\circ$. The reconstruction has ~ 400 resolution elements giving an average of ~ 10 constraints per pixel for density and less than 2 per pixel for velocity. In contrast, we have typically ~ 700 simultaneous measurements of velocity and scintillation index for every Carrington rotation. However, we have confined our observations to the equatorial belt in order to maximise the overlap between footpoints of different *l.o.s.*s on the fiducial surface and have chosen our resolution to have ~ 10 constraints per pixel. When the number of constraints per pixel is of the order of unity, one can easily make a model for the distribution of velocity on a fiducial surface which is consistent with all the observations, but one has no means of checking whether the spatial structures seen in the model reflect actual stable spatial structures on the Sun or whether time variations of the Solar Wind are being reflected as spatial variations. Our data, having many more constraints per pixel, can actually to separate spatial and temporal variations. Our data (Figures 7.40–7.42) indicates that there are considerable temporal variations and because of this our reconstruction does not do as well on real data as in simulation. While the temporal fluctuations are not unexpected, we had hoped that with many constraints per pixel at an epoch close to the solar minima, we would be able to achieve a stable reconstruction. However, this not borne out, which raises the question of how reliable and stable are other earlier reconstructions (unless, of course, we have been singularly unlucky in having a considerable activity during our observations).

The algorithm used by these groups performs a guided search and progressively reduces the differences between the data and the model. However no estimate of the 'goodness' of the model in representing the data (χ^2) and its improvement with progression iterations of the minimisation algorithm has been presented. Judging from a figure which is presented in the first of these three papers, the maximum fractional corrections to the initial model are always smaller than $\sim 10\%$ for velocity co-ordinate corrections and less than $\sim 2\%$ for velocity model deviations and they are practically zero beyond 15 iterations. As the corrections to the model are small, this leads to the conclusion that the final reconstruction should be quite close to the initial model itself.

7.10 Possible improvements

There are many possible improvements which can be incorporated in the analysis procedure adopted, most of which deal with second order effects and can lead to small improvements over the present procedure. As the basic methodology used for tomographic reconstruction has been validated by the simulations, these effects can be incorporated to improve the reconstruction for more realistic simulations. While we do not believe that any of these have been the primary limitations for the present work, we list them for academic interest and completeness.

1. A shortcoming of the present analysis is that it neglects the interaction between the Solar Wind streams moving with different velocities. In our analysis, the velocities are assumed to remain constant with heliocentric distance and the Archimedean spirals for Solar Wind moving with different velocities can pass through one another. While this makes negligible difference to the radial propagation of the Solar Wind if the velocity differences between the Solar Wind arising from neighbouring areas on the Sun are not large, especially in view of the coarse resolution afforded by the reconstruction, their effects cannot be ignored in presence of large velocity contrasts. The absence of radial evolution of velocity has been assumed only because of its ease of implementation, the shortcomings of this choice are well known. As this model is not an appropriate description of reality, it would contribute to the observed data-set seeming inconsistent with the model.

   The interaction between the slow and the fast streams in the Solar Wind leads to development of a considerable structure and significant radial evolution.

Incorporating the interaction of Solar Wind in a rigorous manner involves doing magnetohydrodynamics (MHD) in a turbulent medium. This is a subject of active research its own right and lies outside the scope of this work.

While it would be difficult to incorporate the interaction of the Solar Wind in a rigorous manner, it can be incorporated in a phenomenological manner using a variety of schemes. The simplest of these would be to assume that the intersecting Archimedean spirals colasce and move outwards with a velocity arrived at using conservation of momentum. More complicated schemes can also be implemented with, an increasing degree of sophistication, which track the Archimedean spirals from one fiducial surface to another close by one and rather than wait for the Archimedean spirals to intersect before they are colasced, the mass and momentum distribution on the later fiducial surface can be obtained from the earlier one depending on the tendency of adjacent spirals to crowd together or move away from one another using an empirical scheme. Work in this direction is in progress.

Another, purely empirical, approach to incorporating radial evolution of Solar Wind would be to make independent initial models at small and large elongations and interpolate between them to estimate the average radial evolution effects. This approach has the disadvantage that it yields a single prescription to account for radial propagation effects while they are known to be dependent on the magnitude of velocity contrast in the neighbouring regions.

2. Our reconstruction has a resolution of 11° in heliographic latitude, $\theta_{\odot}$. It has been shown that Solar Wind has a well defined latitudinal structure which varies by $\sim 100\ km\ sec^{-1}$ over the resolution length scales in the equatorial belt (Section 6.3). The coarseness of the resolution afforded by the reconstruction, forces the systematic variation within the resolution element to be represented by an average constant number. It would be possible to reduce the damages due to this by taking into account the known average latitudinal variation of the velocity across the pixel dimensions.

3. A given pixel on the fiducial surface receives contributions from *l.o.s.* observed over a large fraction of the solar rotation period. Every heliographic longitude is sampled twice by IPS *l.o.s.*s in a solar rotation, once when observing sources on the East of the Sun and then half a rotation later when observing sources on the West. One can construct models using observations only on the East or the West of the Sun and compare the two to look for signatures of slow time scale evolution of the average properties of the Solar Wind. This can provide a limited amount of information about the time evolution of the Solar Wind structure which can be built into the Solar Wind model.

4. We have used an un-guided minimisation the *Downhill simplex* algorithm for

χ^2 minimisation without simulated annealing. Inclusion of simulated annealing in the minimisation process gives a periodic random *kick* to the model parameters, the frequency and magnitude of which are user defined quantities. These methods reduce the probability of remaining stuck in a shallow minima. Given the χ^2 landscape for the problem at hand, this is does not offer any assurance of leading to the global minima but the minimisation process may have better chances of reaching the deepest local minima.

One can also use guided minimisation methods where the initial model is modified on the basis of the differences between the model and the observed data. While these methods do not assure convergence to the global minima, their advantage lies in the fact that they provide a much faster convergence as compared to un-guided minimisation algorithms.

5. We have used the elemental areas on the fiducial surface, pixels, as degrees of freedom of the Solar Wind model. Our reconstructions using the data often show jaggered features. These features appear with such regularity that they are unlikely to be real. An alternative approach would be to use a set of spherical harmonics to represent the equatorial belt of the solar surface. The use of spherical harmonics as degrees of freedom is likely to yield smoother reconstructions.

6. In a real life situation, there are likely to be significant differences in the number of $l.o.s.$s which constrain different parts of the fiducial surface. The reconstruction, therefore, is not likely to be equally well constrained over the entire fiducial surface. A systematic study of the reliability of the reconstruction in presence of non-uniform distribution of constraints should be done.

Chapter 8

Conclusions

IPS tomography of the inner heliosphere offers an opportunity to reconstruct the average large scale distribution of Solar Wind. In spite of the fact that a successful tomographic reconstruction can yield valuable information which is not obtainable by any other means, the complexity of the problem and the lack of suitable datasets have led to there being few such attempts. The only other attempts at IPS tomography have been by the UCSD and the STELab groups who have used the index values, g, from the Cambridge 81.5 MHz telescope and the velocities from Nagoya multi-station observations at 327 MHz.

8.1 Tomographic reconstruction of the Solar Wind

8.1.1 Formulation of the problem

We formulate the problem in terms of a χ^2 minimisation exercise with the observed power spectra as the constraints for the reconstruction process and the distribution of the physical properties of the Solar Wind (velocity and C_n^2) on a fiducial surface as the free parameters of the model. The χ^2 minimisation is expected to lead to a best fit surface distribution most consistent with the observations. Earlier attempts at tomography of the Solar Wind (Jackson et al., 1998; Kojima et al., 1998; Asai et al., 1998) have used the IPS velocities estimated using the cross-correlation analysis obtained from the multi-station IPS observations as the constraints for the reconstruction procedure. The process of assigning a single velocity to the Solar Wind along a $l.o.s.$ loses the information of the distribution of Solar Wind properties along the $l.o.s.$ which is contained in the shape of the cross-correlation function (CCF) between different stations. The velocities obtained from such analysis are not assured to be the appropriate $l.o.s.$ integrated velocities and their use is fraught with unspecifiable systematics. Our approach does not suffer from such drawbacks as we use the true observables of IPS (power spectra), which are the appropriate *l.o.s.* integrated measure of the distribution of Solar Wind properties, as the constraints for the reconstruction process and do not involve any interpretation in terms of unsuitable Solar Wind models.

8.1.2 Simulations

Our formulation of the problem of tomographic reconstruction increased the complexity of the problem many fold over the previous attempts as rather than model only two numbers (velocity and g) for each observation, it required us to model the entire power spectra and reproduce its area and shape. Since such a formulation of the problem had not been used before, we did an extensive set of simulations to validate the software developed and convince ourselves of the viability of the formulation. Another aim of the simulations was to check if the sampling of the heliosphere provided by our observations was sufficient for a reliable reconstruction. The results from our simulations show that this formulation is able to reconstruct the true structure of the Solar Wind models to a satisfactory level for data which satisfied the assumptions made by the reconstruction process. The simulations were tested for effects of noise due to measurement uncertainty in the power spectra and were not found to be seriously affected by it. Stability of the reconstructions to perturbations to the starting point for the reconstruction process was also tested and they were found to be stable to such perturbations. These simulations were used to arrive at useful estimates of the contributions of various sources of errors and uncertainties to the χ^2_G for the global Solar Wind model fit.

8.2 Observations and analysis

8.2.1 The data-set

An extensive set of IPS observations with a good coverage of the equatorial belt on the Sun was made using the Ooty Radio Telescope, India (ORT) at 327 MHz. The data comprises of $5,418$ observations of individual scintillating sources and calibrators, spans ~ 5 Carrington rotations and used $\sim 1,500$ hrs of telescope time. The observed sources were selected from the list of known scintillators which has been built up at the ORT over the years. Most of the observations were confined to a heliographic latitude range of $\pm 15^\circ$ and an elongation range of 20°–80°. The epoch of observation was close to the minima of the solar activity cycle (April to August 1997) and overlaps with Carrington rotations 1921–1925. This data-set has been used for tomographic reconstruction of the Solar Wind using our formulation.

8.2.2 Automated best fit uniform Solar Wind model estimation

One of the achievements of this work has been to develop an automated procedure for estimating the best fit uniform Solar Wind models for the observed power spectra and demonstrate its effectiveness. The task of 'fitting' the spectra has traditionally been done by visual examination. It is a rather tedious exercise and allows the possibility of human errors and biases creeping in as it is difficult to maintain similar levels of objectivity while handling large databases. The automated procedure, on the other hand, provides a uniform objective criterion for fitting the spectra and relieves the astronomers of considerable drudgery. Often, when IPS is used to study the IPDs, only the disturbed spectra, which are a small fraction of the total number of observed power spectra, are of interest. This procedure provides an efficient means for picking out such observations as the IPDs spectra are expected to have significant departures from the uniform Solar Wind and therefore have poorer fits or large χ^2. The procedure thus provides a very useful tool for analysing large databases and forms an integral part of the simulations mentioned above.

8.2.3 Results of tomographic reconstruction

While the simulations lead to stable reconstructions, we found that reconstructions using the observed power spectra were not so stable. Though there were some broad similarities between different reconstructions for the same Carrington rotation which started from different starting simplexes, there were also significant differences between them. Most of the reconstructions had similar values for the final global χ^2 and therefore they all seem equally believable according to the χ^2 criteria. While comparison of the reconstructions with Solar Wind velocity measured by WIND did show some correlations, those with white light coronograph synoptic maps from LASCO-SOHO did not show any obvious correlations. The considerable difference in the nature of these measurements and IPS tomographic reconstruction should be borne in mind while making these comparisons.

The failure of our formulation to achieve convincing unique solutions with real data imply that some of the tomography assumptions are not valid and there are considerable differences in the χ^2 landscape for the observed and the simulated data. The fact that the simulated data are insensitive to perturbations of the starting point of the reconstruction process suggests the presence of a global minima which the minimisation process descends into. Of course, because of the noise associated with the reconstruction process itself, the reconstruction differs from the true model by some amount, but all the different reconstructions tend to approach the true model. The multiplicity of local minima for observed power spectra suggests that there are basic differences between the simulated and observed data. A strong indicator of the difference is that the global χ^2 for the initial guess and the final reconstruction is more than an order of magnitude larger for the observed power spectra than that for the simulations The most likely reason for the differences is that while the data for simulations was 'manufactured' to satisfy all the assumption, the observed data does not adhere to these assumptions.

The assumption of little or no time evolution during the course of a solar rotation is a rather demanding one. Though the our period of observations was close to the minima of solar activity cycle and would qualify as a 'quite' period according to most criteria, we believe that significant time evolution took place during the course of a Carrington rotation. While slow time evolution leads to the data-set being rendered inconsistent for a tomographic reconstruction, the transients act like noise in the data. If the χ^2 due to these effects is comparable to or larger than the χ^2 due to the time invariant features, the final χ^2 landscape may lead to a unique reconstruction, besides the reconstruction arrived at may not reflect the true average structure of the Solar Wind. The lack of stability of our reconstructions should be interpreted as indicative of existence of non-unique solutions. SOHO-LASCO reported ~ 0.8 CMEs per day during our epoch of observations (St. Cyr et al., 2000). Given their latitudinal distribution, our data-set would sample almost all of them and this could be one of the many causes of inconsistencies in the data-set.

8.3 Radial evolution of Solar Wind

The dense coverage of the equatorial Solar Wind achieved in our data-set makes it a useful data-base for studying the radial evolution of the Solar Wind properties. We have studied the radial evolution of the Solar Wind velocity in this work. Our work has revealed a trend for the average equatorial IPS velocities to decrease with heliocentric distance. As this trend is different from expectations, we have performed a careful analysis and are convinced that the observed decrease is not an artifact due to the presence of some biases in the data-set or analysis procedure. The IPS velocity measurements are heavily weighted in favour of structures which are associated with significant amounts of turbulence (and hence higher C_n^2), because of the *l.o.s.* weight function. The observed trend can, therefore, be explained by the presence of structures which have higher levels of turbulence associated with them and which decelerate as they propagate outwards. Coronograph observations of CMEs during our epoch of observations (St. Cyr et al., 2000) show that IPDs due to CMEs fulfil all these requirements and we believe that slowing down of IPDs is the cause for the observed deceleration seen in the equatorial Solar Wind. We feel that this effect has not been seen earlier because of the lack of a suitable data-set.

The weighting of IPS velocities by a function proportional to $(\delta n_e)^4$ would also explain why the average *in-situ* velocity measurements from spacecrafts, which are not biased in this manner, may not show such a trend.

8.4 Future prospects of IPS tomography

8.4.1 Need for better S/N observations

IPS tomography aims at providing a global model for the distribution of Solar Wind properties in the inner heliosphere using the observed IPS power spectra as the constraints. For a good reconstruction it is necessary that the primary observable which is used for the tomographic reconstruction has enough information about the distribution of the Solar Wind which tomography can try to unravel. During the course of this analysis, we realised that the uniform Solar Wind models provide an adequate model for many of the observed power spectra primarily because most often the sensitivity and the reliability of the observations are not sufficient to discern the deviations from the uniform Solar Wind models.

Though the mean and the median χ^2 for the best fit uniform Solar Wind model to the observed power spectra are significantly less than unity (Section 5.5 and Figure 5.3), their distribution shows a systematic increase in χ^2 as the S/N of the observed power spectra increases. The χ^2 being a measure of the *significance* of the deviations of the model from the data, this trend implies that as the S/N of the power spectra improves, the significance of the deviations of the uniform Solar Wind model from the observed spectra increases.

Therefore, in order to make measurements which are sensitive to the structure in the Solar Wind, the S/N on the measurements of power spectra needs to be improved. This can be achieved by a variety of means - observing for longer durations, increasing the collecting area and the bandwidth of observations. The present IPS data acquisition system at the Ooty Radio Telescope uses only 4 MHz of the total 12 MHz of the signal bandwidth available, so an improvement of $\sqrt{3}$ in S/N, while maintaining the same observing duration, is achievable with a reasonable effort.

8.4.2 Tomography as a routine investigation tool

A fair amount of experience and insight was gained during this exercise about tomographic reconstruction using IPS data. We feel that though success in this exercise offers lucrative results, rigorous tomography of the type we have attempted, is not viable as a routine investigation tool. The assumption of little or no time evolution during the course of the observations which is necessarily required by this exercise is likely to met, if at all, for only very brief periods close to the minima of the solar activity cycle. The observational effort required to obtain a data-set suited for a tomographic reconstruction is enormous and necessarily requires a dedicated good sensitivity telescope.

Given the fact that even in the quietest parts of the solar cycle CMEs launched at the rate of about one per day, the problem of tomographic inversion will not become any more amenable to a non-unique reconstruction even if higher S/N observations are available. This bottleneck can be overcome only by ensuring that the entire heliosphere is sampled adequately on time scales shorter time scales of its variations. This cannot be achieved while being confined to the single vantage point of the Earth. Space radio telescopes with large collecting areas spread, say, all along the Earth's orbit can reduce the time taken to sample the entire heliosphere substantially and enable reliable tomography.

In spite of the bleak prospects of the success of rigorous IPS tomography, the subject is sufficiently interesting and the information it can yield cannot be obtained by any other means. It can certainly be used for qualitative estimates of the approximate 3D structure of the Solar Wind in conjunction with information from a variety of other sources both close to the Sun and at 1 AU which can be used as additional constraints.

Till the time we reach a stage where it takes much shorter durations to cover the entire heliosphere, using the data from spacecrafts which can provide different perspectives of the heliosphere with sufficient S/N to be sensitive to the structure along the IPS $l.o.s.$s, this technique cannot be used as a routine means of investigation of the Solar Wind.

Bibliography

Alfven, H. (1977). Electric currents in cosmic plasmas. *Reviews of Geophysics and Space Physics*, 15:271–284.

Ananthakrishnan, S., Tokumaru, M., Kojima, M., Balasubramanian, V., Janardhan, P., Manoharan, P. K., and Dryer, M. (1999). "study of solar wind transients using ips". In *AIP Conf. Proc. 471: Solar Wind Nine*, pages 321+.

Ananthkrishnan, S., Balasubramanian, V., and Janardhan, P. (1995). "latitudinal variation of solar wind velocity". *Space Science Reviews*, 72:229+.

Armstrong, J. and Coles, W. (1972). Analysis of three station inteplanetary scintialltion. *Journal of Geophysical Research*, 77:4607+.

Armstrong, J. W., Coles, W. A., Rickett, B. J., and Kojima, M. (1990). Observations of field-aligned density fluctuations in the inner solar wind. *Astrophysical Journal*, 358:685–692.

Armstrong, J. W. and Woo, R. (1981). Solar wind motion within 30 r solar radii - spacecraft radio scintillation observations. *Astronomy and Astrophysics*, 103:415–421.

Asai, K., Kojima, M., Tokumaru, M., Yokobe, A., Jackson, B. V., Hick, P. L., and Manoharan, P. K. (1998). Heliospheric tomography using interplanetary scintillation observations. iii - correlation between speed and electron density fluctuations in the solar wind. *Journal of Geophysical Research*, 103:1991+.

Balasubramaniam, V. (1997). *Private communication.*

Belkovich, O. I., Sidorov, V. V., Filimonova, T. K., and Nugmanov, I. S. (1997). Tomographic method for meteor-flux determination from radar observations. *Astronomicheskii Vestnik*, 31:477+.

Bhandari, S. M., Ananthakrishnan, S., and Rao, A. (1974). Structure of 194 southern declination radio sources from interplanetary scintialltions. *Australian Journal of Physics*, 27:121–128.

Bird, M. K. and Edenhofer, P. (1990). Remote sensing observations of the solar corona. In *Physics of the Inner Heliosphere : Part 1 - Large Scale Phenomena*, pages 13–98.

Blessing, R. and Dennison, P. (1972). *Proceedings of the Astronomical Society of Australia*, 2:84+.

Bourgois, G., Daigne, G., Coles, W. A., Silen, J., Turunen, T., and Williams, P. J. (1985). Measurements of the solar wind velocity with eiscat. *Astronomy and Astrophysics*, 144:452–462.

Bruno, R., Villante, U., Bavassano, B., Schwenn, R., and Mariani, F. (1986). "in-situ observations of the latitudinal gradients of the solar wind parameters during 1976 and 1977". *Solar Physics*, 104:431–445.

Budden, K. G. and Uscinski, B. J. (1970). *Proc. Roy. Soc. Lond. A.*, 316:315+.

Celnikier, L. M., Harvey, C. C., Jegou, R., Moricet, P., and Kemp, M. (1983). A determination of the electron density fluctuation spectrum in the solar wind, using the isee propagation experiment. *Astronomy and Astrophysics*, 126:293–298.

Cohen, M. H., Gundermann, E. J., Harris, D. E., and Zeissig, G. (1968). Structure of scintillating radio sources. *Astronomical Journal*, 73:171+.

Coles, W. A. (1978). Interplanetary scintillation. *Space Science Reviews*, 21:411–425.

Coles, W. A. and Harmon, J. K. (1978). Interplanetary scintillation measurements of the electron density power spectrum in the solar wind. *Journal of Geophysical Research*, 83:1413–1420.

Coles, W. A. and Harmon, J. K. (1989). Propagation observations of the solar wind near the sun. *Astrophysical Journal*, 337:1023–1034.

Coles, W. A. and Kaufman, J. J. (1978). Solar wind velocity estimates from multi-station ips. *Radio Science*, 13(3):591–597.

Coles, W. A. and Rickett, B. J. (1976). Ips observations of the solar wind speed out of the ecliptic. *Journal of Geophysical Research*, 81:4797–4799.

Cormack, A. M. (1964). *Journal of Applied Physics*, 34:2908.

Cronyn, W. M. (1970). PhD thesis, University of Maryland.

Cronyn, W. M. (1972). Density fluctuations in the interplanetary plasma: Agreement between spaceprobe and radio scattering observations. *Astrophysical Journal Letters*, 171:L101–+.

Davila, J. M. (1994). Solar tomography. *Astrophysical Journal*, 423:871+.

Dennison, P. and Hewish, A. (1967). The solar wind outside the plane of the ecliptic. *Nature*, 213:343+.

Ekers, R. D. and Little, L. T. (1971). The motion of the solar wind close to the sun. *Astronomy and Astrophysics*, 10:310+.

Gapper, G. R., Hewish, A., Purvis, A., and Duffett-Smith, P. J. (1982). Observing interplanetary disturbances from the ground. *Nature*, 296:633–636.

Gosling, J. T. (1997). The solar wind.

Gothoskar, P. and Rao, A. P. (1999). "on observing mass ejections in the interplanetary medium". *Solar Physics*, 185:361–390.

Gothoskar, P. B. (1994). *IPS observations of variability in the Solar Wind.* PhD thesis, University of Bombay.

Grall, R. R., Coles, W. A., and Klinglesmith, M. T. (1995). Observations of the solar wind speed near the sun. In *Solar Wind Conference*, pages 61+.

Grall, R. R., Coles, W. A., Klinglesmith, M. T., Breen, A. R., Williams, P. J. S., Markkanen, J., and Esser, R. (1996). Rapid acceleration of polar solar wind. *Nature*, 379:429–432.

Hewish, A. (1990). Ips imaging and short-term solar-terrestrial predictions. In *Proceedings of Workshop at Leura, Australia, October 1989, National Oceanic and Atmospheric Administration, Environmental Research Laboratories, Boulder, Colorado*, pages 81–101.

Hewish, A., Scott, P. F., and Wills, D. (1964). *Nature*, 203:1214+.

Hick, P. P. and Jackson, B. V. (1998). Three-dimensional tomography of heliospheric features using thomson scattering data. *Proceedings of SPIE Conference*, 3442:87–93.

Howard, R. A., Sheeley, N. R., Michels, D. J., and Koomen, M. J. (1985). "coronal mass ejections - 1979-1981". *Journal of Geophysical Research*, 90:8173–8191.

Hundhausen, A. J. (1972). *"Coronal Expansion and Solar Wind".* Coronal Expansion and Solar Wind, XII, 238 pp. 101 figs.. Springer-Verlag Berlin Heidelberg New York. Also Physics and Chemistry in Space, volume 5.

Hundhausen, A. J. (1993). "sizes and locations of coronal mass ejections - smm observations from 1980 and 1984-1989". *Journal of Geophysical Research*, 98:13177+.

Intriligator, D. S. and Neugebauer, M. (1975). A search for solar wind velocity changes between 0.7 and 1 au. *Journal of Geophysical Research*, 80:1332–1334.

Intriligator, D. S. and Wolfe, J. H. (1970). Preliminary power spectra of the interplanetary plasma. *Astrophysical Journal Letters*, 162:L187–+.

Jackson, B. V., Hick, P., Kojima, M., and Yokobe, A. (1997). Heliospheric tomography using interplanetary scintiallation observations. *Advances in Space Research*, 20:23–26.

Jackson, B. V., Hick, P. L., Kojima, M., and Yokobe, A. (1998). Heliospheric tomography using interplanetary scintialltion observations 1. combined nagoya and cambridge data. *Journal of Geophysical Research*, 103(A6):12049–12067.

Jain, P., Ralston, J. P., and Frichter, G. M. (1999). Neutrino absorption tomography of the earth's interior using isotropic ultra-high energy flux. *Astroparticle Physics*, 12:193–198.

Kakinuma, T., Washimi, H., and Kojima, M. (1973). On the analysis of the observations of interplanetary scintillations obtained with three spaced receivers. *Publications of the Astronomical Society of Japan*, 25:271+.

Kakinuma, T., Washimi, H., and Kojima, M. (1982). Three dimensional distribution of the solar wind velocity deduced from ips observations. In et. al, S. M. A., editor, *Proceedings of STIP Symposium on Solar Radio Astronomy, Interplanetary Scintiallation and Coordination with Spacecraft*, pages 153–162.

Kojima, M. and Kakinuma, T. (1990). Solar cycle dependence of global distribution of solar wind speed. *Space Science Reviews*, 53:173–222.

Kojima, M., Tokumaru, M., Watanabe, H., Yokobe, A., Asai, K., Jackson, B. V., and Hick, P. L. (1998). Heliospheric tomography using interplanetary scintillation observations. ii - latitude and heliocentric distance dependence of solar wind structure at 0.1-1 au. *Journal of Geophysical Research*, 103:1981+.

Laigle, M. and Hirn, A. (1999). Explosion-seismic tomography of a magmatic body beneath mount etna: Volatile discarge and tectonic control of volcanism. *Geophysical Research Letters*, 26:2665+.

Leinbach, H., Ananthakrishnan, S., and Detman, T. (1994). The utility of interplanetary scintillation maps in forecasting geomagnetic activity: A study based on single-station data from cambridge, united kingdom. *NOAA Technical Memorandum, ERL SEL-83.*

Little, L. T. (1968). *Planetary and Space Science*, 16:749+.

Little, L. T. and Hewish, A. (1968). Radio source structure derived from interplanetary scintillation. *Monthly Notices of the Royal Astronomical Society*, 138:393–406.

Lovelace, R. V. E., Salpeter, E. E., Sharp, L. E., and Harris, D. E. (1970). Analysis of observations of interplanetary scintillations. *Astrophysical Journal*, 159:1047+.

Madau, P., Meiksin, A., and Rees, M. J. (1997). 21 centimeter tomography of the intergalactic medium at high redshift. *Astrophysical Journal*, 475:429+.

Manoharan, P. K. (1991). *Study of Solar Wind using Single-Station Interplanetary Scintillation*. PhD thesis, University of Bombay.

Manoharan, P. K. (1996). "solar activity dependence of interplanetary disturbances". *Astrophysics and Space Science*, 243:221+.

Manoharan, P. K. (1997a). *Private communication*.

Manoharan, P. K. (1997b). "solar cause of interplanetary disturbances observed in the distance range 0.24-1 au". *Geophysical Research Letters*, 24:2623+.

Manoharan, P. K. and Ananthakrishnan, S. (1990). Determination of solar-wind velocities using single-station measurements of interplanetary scintillation. *Monthly Notices of the Royal Astronomical Society*, 244:691–695.

Manoharan, P. K., Ananthakrishnan, S., Dryer, M., Detman, T. R., Leinbach, H., Kojima, M., Watanabe, T., and Kahn, J. (1995). "solar wind velocity and normalized scintillation index from single-station ips observations". *Solar Physics*, 156:377–393.

Manoharan, P. K., Kojima, M., Gopalswamy, N., Kondo, T., and Smith, Z. (2000). "radial evolution and turbulence characteristics of a coronal mass ejection". *Astrophysical Journal*, 530:1061–1070.

Manoharan, P. K., Kojima, M., and Misawa, H. (1994). The spectrum of electron density fluctuations in the solar wind and its variations with solar wind speed. *Journal of Geophysical Research*, 99:23411+.

Marians, M. (1975). Computed scintillation spectra for strong turbulence. *Radio Science*, 10:115–119.

Marians, M. (1975). *Theory of Scintillation due to Propagation through a Turbulent Medium*. PhD thesis, University of California, San Diego.

Nelder, J. A. and Mead, R. (1965). *Computer Journal*, 7:308–313.

Panasyuk, A. V. (1999). Three-dimensional reconstruction of uv emissivities in the solar corona using ultraviolet coronagraph spectrometer data from the whole sun month. *Journal of Geophysical Research*, 104:9721–9726.

Phillips, J. L., Bame, S. J., Barnes, A., Barraclough, B. L., Feldman, W. C., Goldstein, B. E., Gosling, J. T., Hoogeveen, G. W., McComas, D. J., Neugebauer, M., and Suess, S. T. (1995). "ulysses solar wind plasma observations from pole to pole". *Geophysical Research Letters*, 22:3301–3304.

Plunkett, S. P., Thompson, B. J., Howard, R. A., Michels, D. J., St. Cyr, O. C., Tappin, S. J., Schwenn, R., and Lamy, P. L. (1998). Lasco observations of an earth-directed coronal mass ejection on may 12, 1997. *Geophysical Research Letters*, 25:2477+.

Press, W. H., Teukolsky, S. A., Vellerling, W. T., and Flannery, B. P. (1992). *Numerical Recipies in C: The Art of Scientific Computing.* Cambridge University Press, second edition edition.

Purvis, A., Tappin, S. J., Rees, W. G., Hewish, A., and Duffett-Smith, P. J. (1987). The cambridge ips survey at 81.5 mhz. *Monthly Notices of the Royal Astronomical Society*, 229:589–619.

Radon, J. (1917). *Ber. Verh. Sachs. Acad. Wiss.*, 69:262.

Rao, A. P. (1975). *A study of Interplanetary Scintillation at 327 MHz.* PhD thesis, University of Bombay.

Rao, A. P., Ananthakrishnan, S., Balasubramanian, V., Coles, W. A., and Oberoi, D. (1995). Very long baseline ips observations of the solar wind speed in the fast polar streams. In *Solar Wind Conference*, pages 94+.

Ruffini, G., Cardellach, E., Flores, A., Cucurull, L., and Rius, A. (1998). Ionospheric calibration of radar altimeters using gps tomography. *Geophysical Research Letters*, 25:3771+.

Rumsey, V. H. (1975). Scintillations due to a concentrated layer with a power-law turbulence spectrum. *Radio Science*, 10:107–114.

Salpeter, E. E. (1967). Interplanetary scintillations. i. theory. *Astrophysical Journal*, 147:433+.

Schwenn, R. and Marsch, E., editors (1990a). *Physics of the Inner Heliosphere : Part 1 - Large Scale Phenomena.* Springer Verlag.

Schwenn, R. and Marsch, E., editors (1990b). *Physics of the Inner Heliosphere : Part 2 - Particles, Waves and Turbulence.* Springer Verlag.

Schwenn, R., Mohlhauser, K. H., Marsch, E., and Rosenbauer, H. (1981). Two states of the solar wind at the time of solar activity minimum - part two - radial gradients of plasma parameters in fast and slow streams. In *Solar Wind Conference*, pages 126+.

Scott, S. L., Coles, W. A., and Bourgois, G. (1983). Solar wind observations near the sun using interplanetary scintillation. *Astronomy and Astrophysics*, 123:207–215.

St. Cyr, O. C., Howard, R. A., Sheeley Jr., N. R., Plunkett, S. P., Michels, D. J., Paswaters, S. E., Koomen, M. J., Simnett, G. M., Thompson, B. J., Gurman, J. B., Schwenn, R., Webb, D. F., Hildner, E., and Lamy, P. L. (2000). Properties of coronal mass ejections: Soho-lasco observations from january 1996 to june 1998. *Journal of Geophysical Research*.

Swarup, G., Sarma, N. V. G., Joshi, M. N., Kapahi, V. K., Bagri, D. S., Damle, S. H., Ananthakrishnan, S., Balasubramanian, V., Bhave, S. S., and Sinha, R. P. (1971). Large steerable radio telescope at ootacamand (ooty), india. *Nature Physical Science*, 230(185).

Swindell, W. and Barrett, H. H. (1977). Computerized tomography: taking sectional x rays. *Physics Today*, 30:32–41.

Tappin, S. J., Hewish, A., and Gapper, G. R. (1983). Tracking a major interplanetary disturbance. *Planetary and Space Science*, 31:1171–1176.

Tappin, S. J., Hewish, A., and Gapper, G. R. (1984). Tracking a high-latitude corotating stream for more than half a solar rotation. *Planetary and Space Science*, 32:1273–1281.

Tatarsky, V. I. (1961). *Wave Proapagation in a Turbulent Medium*. Dover Publications.

Tatarsky, V. I. (1971). *The Effects of the Turbulent Atmosphere on the Wave Propagation*. Israel Programme for Scientific Translators.

Thompson, B. J., Plunkett, S. P., Gurman, J. B., Newmark, J. S., St. Cyr, O. C., and Michels, D. J. (1998). Soho/eit observations of an earth-directed coronal mass ejection on may 12, 1997. *Geophysical Research Letters*, 25:2465+.

Tokumaru, M., Kondo, T., Mori, H., and Tanaka, T. (1994). Solar wind motion near the sun derived from simultaneous interplanetary scintillation observations at 2 ghz and 8 ghz. *Journal of Geomagnetism and Geoelectricity*, 46:835–849.

Tsapin, A. I., Storrie-Lombardi, M. C., McDonald, G., and Nealson, K. H. (1999). Application of computer tomography (ct) for search of life in extreme environments. In *Bioastronomy 99: A New Era in Bioastronomy. 6th Bioastronomy Meeting - Kohala Coast Hawaii - August 2-6, 1999*, pages E100–+.

Unti, T. W. J., Neugebauer, M., and Goldstein, B. E. (1973). Direct measurements of solar-wind fluctuations between 0.0048 and 13.3 hz. *Astrophysical Journal*, 180:591–598.

Uscinski, B. J. (1977). *The Elements of Wave Proapagation in Random Media*. McGraw Hill Book Company.

Vitkevich, V. V. and Vlasov, V. I. (1970). *Soviet Astronomy*, 13:669+.

Vrielmann, S. and et al. (1998). Next generation tomography: Accretion disks as they "really" are. In *ASP Conf. Ser. 137: Wild Stars in the Old West*, pages 410+.

Woo, R. and Armstrong, J. W. (1979). Spacecraft radio scattering observations of the power spectrum of electron density fluctuations in the solar wind. *Journal of Geophysical Research*, 84:7288–7296.

Yakovlev, O. I., Efimov, A. I., Razmanov, V. M., and Shtrykov, V. K. (1980). Inhomogeneous structure and velocity of the circumsolar plasma based on venera-10. *Soviet Astronomy*, 24:454+.

Yamauchi, Y., Kojima, M., Tokumaru, M., Misawa, H., Mori, H., Tanaka, T., Takaba, H., Kondo, T., and Manoharan, P. K. (1996). Micro-turbulence in the solar wind at 5-76 rs observed with interplanetary scintillation. *Journal of Geomagnetism and Geoelectricity*, 48:1201–1217.

Yamauchi, Y., Tokumaru, M., Kojima, M., Manoharan, P. K., and Esser, R. (1998). A study of density fluctuations in the solar wind acceleration region. *Journal of Geophysical Research*, 103:6571+.

Yamauchi, Y., Tokumaru, M., Kojima, M., Manoharan, P. K., and Esser, R. (1999). "radial evolution of micro-turbulence in the solar wind observed with interplanetary scintillation". In *AIP Conf. Proc. 471: Solar Wind Nine*, pages 473+.

Zidowitz, S. (1999). Coronal structure of the whole sun month: A tomographic reconstruction. *Journal of Geophysical Research*, 104:9727+.